DEFORMATION-BASED ALLEVIATION OF IRRADIATION EFFECTS IN PROTON IRRADIATED NANOCRYSTALLINE CU-10AT%TA ALLOY

by

Priyam Vivek Patki

A Dissertation

Submitted to the Faculty of Purdue University

In Partial Fulfillment of the Requirements for the degree of

Doctor of Philosophy

School of Materials Engineering

West Lafayette, Indiana

December 2020

THE PURDUE UNIVERSITY GRADUATE SCHOOL

STATEMENT OF COMMITTEE APPROVAL

Dr. Janelle P. Wharry, Co-chair

School of Materials Engineering

Dr. Maria Okuniewski, Co-chair

School of Materials Engineering

Dr. Anter El-Azab

School of Materials Engineering

Dr. Yaqiao Wu

Boise State University & Center for Advanced Energy Studies, ID

Approved by:

Dr. David F. Bahr

To my late grandparents,

Thank you for always having motivated and supported

me in my pursuit for higher education.

ACKNOWLEDGMENTS

First and foremost, I would like to thank my advisor Prof. Janelle Wharry for taking me on as a student and guiding me throughout my graduate studies. I am lucky to have had such a patient and dedicated advisor as you. I am so grateful to have worked with you, you have made me a better writer as well as a better researcher. Thank you for supporting and believing in me throughout this journey. I would also like to thank my committee members – Dr. Okuniewski, Dr. El-Azab and Dr. Wu for their input and advice to help me make this research better.

I would like to thank my family for supporting me throughout the journey. Aai and Baba, thank you for being my pillars throughout this journey. Priyal, Mahi, and Ilina you are the best sisters I could ask for and best of luck for your individual journeys. I would also like to thank Vinay kaka and Aditi kaku without whose support my journey to USA would not have been possible. I would like to thank my late grandparents for instilling in me the importance of higher education and motivating me to go see the world. I would like to thank Priyal for taking utmost care of my furry brother, Rancho. I miss him a lot.

I would also like to appreciate Aakanksha and her furry baby Emma for supporting and bearing with me through the ups and downs during my graduate life. Also, I would like to thank my extended family Kunal, Rohan, Rahul and Ashay for bearing me as a captain in all those dota games. We are almost out of the trench! I would also like to thank my group members, Kayla and Keyou for keeping the lab lively with all the banter and gossip. Best of luck to the rest of group members, hang in, you guys are almost there!

The research presented in this thesis was carried out at MaCS, CAES, ID. I would like to thank Jatu Burns, Alyssa Bateman and Megha Dubey for their help with the FIB experiments and Joanna Taylor for her help with scheduling experiment time at CAES. A special thanks to Dr. Yaqiao Wu for his help with the microstructure characterization on the TEM and APT, as well as his help with the TEM *in situ* mechanical testing. Thank you to Dr. Mukesh Bacchav from INL for teaching me to use the APT analysis software. Thank you to the Army Research Lab for providing the material.

This research was sponsored in part by Prof. Wharry's startup funds at Purdue University and by the US DOE Office of Nuclear Energy under DOE Idaho Operations Office Contract DE-AC07-05ID14517, as part of the Nuclear Science User Facilities experiment 18-1168

TABLE OF CONTENTS

LIST OF TABLES

LIST OF FIGURES

NOMENCLATURE

Al	Aluminum
R_0	APT tip radius
c	atomic fraction of the solute
N	Atomic number density
Z	Atomic Number of the element
At%	Atomic percentage composition
α	Barrier strength coefficient
BCC	Body Centered Cubic
b	Burger's vector
℃	Celsius
$\Delta\sigma_y$	Change in yield stress
q	Charge per incident ion
Cr	Chromium
V	Collection Voltage
C_s	Concentration of defect sinks
C_i	Concentration of interstitials
C_v	Concentration of vacancies
Cu	Copper
K_0	Defect production rate
Dpa	Displacements per lattice atom
F	Evaporation Field
FCC	Face Centered Cubic
FEG	Field Emission Gun
FIB	Focused Ion Beam
σ_0	Friction Stress
FWHM	Full Width Half Maximum
Ga	Gallium
d	grain size of the material
k	Hall-Petch constant
Hz	Hertz frequency
HPT	High Pressure Torsion
ICF	Image Compression Factor
λ	Interparticle spacing
Fe	Iron
Φ	Irradiation flux
K	Kelvin
keV	Kilo electron-volt
kV	kilo-Volt
Kr	Krypton
LEAP	Local Electrode Atom Probe
MeV	Mega electron-volt
T_m	Melting Temperature
M_xC_y	Metal Carbide precipitate
μC	Micro-Coulomb
μm	Micrometers/Microns
Mo	Molybdenum
NC	Nanocrystalline
nm	Nanometer
Ns	Nanoseconds
Ni	Nickel

Nb	Niobium
N	Number density of the material
τ_{oro}	Orowan Strengthening
ODS	Oxide Dispersion Strengthened
O	Oxygen
pA	Pico-ampere
pJ	Pico-joules
Pt	Platinum
PKA	Primary Knock-on Atom
R_d	Rate of displaced atoms
τ_{RoM}	Rule of Mixtures strengthening
SPD	Severe Plastic Deformation
G	Shear Modulus
μ	Shear Modulus of material
Si	Silicon
Ag	Silver
τ_{ss}	Solid Solution strengthening
β	Solid Solution strengthening constant
SFT	Stacking Fault Tetrahedra
Ta	Tantalum
Ti	Titanium
W	Tungsten
V	Vanadium
x	Volume fraction
Wt%	Weight percentage composition
Xe	Xenon
σ_y	Yield strength of material
Y	Yttrium
ASTM	American Standard for Testing of Materials
ACOM	Automated Crystal Orientation Mapping
r	Average size of the dispersed particle
BFTEM	Bright Field Transmission Electron Microscopy
CAES	Center for Advanced Energy Studies
f*	Effective volume fraction of dispersed particles
EELS	Electron Energy Loss Spectroscopy
EFTEM	Energy Filtered Transmission Electron Microscopy
ECAE	Equal Channel Angular Extrusion
$d_{erosion}$	Erosion distance for maximum distance of atoms near the matrix interface to be removed
α	Grain boundary energy constant
D_g	Guinier diameter
HRTEM	High Resolution Transmission Electron Microscope
K_{iv}	Interstitial-vacancy recombination rate

d_{max}	Maximum distance between two solute atoms for them to be considered as a cluster
L	Maximum distance of non-solute atoms surrounding the confirmed clustered atoms
N_{min}	Minimum number of atoms in a cluster for the group of clustered atoms to be considered as a cluster
ε	Misfit strain between matrix and solute
MD	Molecular Dynamics
N_{nc}	Number density of nanoclusters
Order	Number of ions within d_{max} distance
N_c	Number of nanoclusters indexed
PED	Precession Electron Diffraction
R_g	Radius of Gyration
K_{is}	Rate of loss of interstitials to sinks
K_{vs}	Rate of loss of vacancies to sinks
M	ratio of uniaxial yield strength to resolved shear strength
ROI	Region of Interest
D	Resultant grain size
STEM	Scanning Transmission Electron Microscope
p,q	Solute-dislocation interaction constants
$\tau_{\#}$	Strength of individual component
TEM	Transmission Electron Microscope
f	Volume fraction of the nanoclusters
V_T	Volume of APT tip

ABSTRACT

Advancements in fabrication of immiscible alloy has allowed the development of high temperature stable nanostructures. One such system is the nanocrystalline Cu-10at%Ta alloy system which has been shown to maintain its nanocrystalline structure up to temperatures of $0.7T_m$, owing to the Ta nanoclusters which act as Zener pinning point and hinder grain boundary motion. High mechanical strength, high temperature stability and increased sink strength for point defects due to high volume of grain boundary volume and Cu-Ta interface boundary volumes, make it a candidate material for nuclear applications. To study the effects of radiation the material is proton irradiated at 500℃ up to a dose of 1 dpa and to study the mechanical response of the material, TEM in situ pico-indentation intermitted with Automated Crystal Orientation Mapping (ACOM) is used. Post irradiation, microstructure analysis using transmission electron microscope reveals limited grain growth and absence of irradiation induced defects in the Cu grains due to a combination of high sink volume in the material and the high irradiation temperature. TEM analysis also reveals Ostwald Ripening of Ta particles > 20 nm and Atom Probe Tomography (APT) cluster analysis shows ballistic dissolution of Ta particles < 2.5 nm which leads to supersaturation of Ta in the Cu matrix as Ta is immiscible in Cu. A closer look at the nanostructure during deformation of the alloy using TEM in situ pico-indentation reveals refining of the Ta particles > 20 nm in both as-received and irradiated sample due to a dislocation glide mediated mechanism. In the proton irradiated sample, the TEM in situ mechanical test also results in the formation of Ta particles at the grain boundaries due to the supersaturated Cu matrix after irradiation and due to the transport of Ta atoms along the grain boundaries showing effects of radiation can be alleviated via deformation.

1. INTRODUCTION

Advancements in material fabrication techniques has led to the creation of nanocrystalline metal alloys. Nanocrystalline alloys has sparked interest in the scientific community as these materials exhibit exceptional properties unseen in bulk counterparts [1–3]. Impressive mechanical properties of nanocrystalline alloys make it a candidate material for use in extreme environments. But nanocrystalline alloys tend to lack thermal stability meaning the microstructure is altered due to thermal effects alone. This can be observed in nanocrystalline Cu which exhibits grain growth at room temperature due to low melting temperature of Cu (T_m = 1085°C) and unstable grain boundaries [4,5]. Attempts to stabilize the grain boundaries has been made using solute atoms to reduce grain boundary energy as well as through the mechanism of solute drag resulting in stabilizing of nanostructured alloys up to $0.45T_m$ [6]. Recent attempts on creating thermally stable nanostructured alloys by alloying between immiscible components has proven to be successful for temperatures up to $0.8T_m$ [7–9].

The solute atoms in an immiscible alloy stabilize the grain boundary in two different ways: reduction of grain boundary energy by solute segregation at the grain boundary and the other is by the solute drag in which the solute atoms act as obstacles for grain boundary migration [10]. Cu-10at%Ta is one such immiscible alloy system which has been tailored to contain Ta nanoclusters (size < 10 nm) which act as Zener pinning points and pin the grain boundary. This also stops grain boundary migration due to thermal effects giving the alloy a thermally stable nanostructure at elevated temperatures of $0.8T_m$ [11].

As nanocrystalline alloys contain a high volume of defect sinks in the form of grain boundaries and interphase boundaries, they may prove to be excellent materials for use in a radiation environment [12–19]. Studies on radiation effects on nanocrystalline Cu and Cu alloys

have shown these materials to exhibit grain growth [13,20–24]. Hence, the introduction of Ta nanoclusters in the material might make the Cu matrix more stable under irradiation as it not only provides additional defect sink areas but also as they are pinning the Cu grain. But studies on precipitation strengthened alloys and dispersion strengthened alloys has shown precipitates/nanoclusters to not be stable and undergo morphological changes under irradiation, e.g., nanoclusters in Oxide Dispersion Strengthened (ODS) alloys [25]. Study of the stability of these Ta nanoclusters under irradiation will provide an insight into tailoring radiation resistant materials.

Studies on effects of deformation on immiscible alloy system [26,27] has shown the components to undergo chemical mixing and nucleation of newer clusters by the process of dislocation glide mediated random walk. Wire drawing of Cu-V alloy [28] has shown mixing at the interface whereas High Pressure Torsion (HPT) experiments on Cu-Nb system [29] has shown precipitation of Nb clusters after deformation. This unique behavior of immiscible alloys under deformation provides us an opportunity to devise a route to mitigate radiation effects on the Ta particles.

In this study, the material has been ion irradiated to study the effects of irradiation. The main drawback of this method is the shallow depth of damage created in the material after ion irradiation which disallows any bulk mechanical testing method. To target the small region of damage in the material Transmission Electron Microscope (TEM) *in situ* mechanical testing has proven to be highly effective. While this mechanical testing method does provide quantitative information, it also provides qualitative information about the deformation processes in the material via recorded video outputs. These mechanical tests can be carried out in various geometries such as compression pillars [30–32], tensile testing [33], pico-indentation [34] or four-point bend tests [35]. As this is

an *in situ* mechanical test, these tests can be combined with the various microstructure characterization techniques such as composition analysis, Scanning TEM, High Resolution TEM or Crystal Orientation Mapping techniques. The combination of these techniques would allow us to get a closer look at the deformative processes in the material.

In this thesis, we will be using Transmission Electron Microscope (TEM) and Atom Probe Tomography (APT) techniques to study the effects of proton irradiation on the Cu-10at%Ta alloy. We will also be studying the effects of deformation on the Ta particles via TEM *in situ* Pico-indentation intermitted with Automated Crystal Orientation Mapping (ACOM) system.

2. BACKGROUND

Nanostructured alloys are becoming popular due to their superior mechanical and physical properties as compared to their bulk counterparts. These alloys can be single or multi-phase composing of nano-sized microstructure features typically less than 100 nm in size. These materials have an increased volume of atoms near grain boundaries and interface boundaries due to which these materials exhibit unique properties. One such enhanced feature is the strength of the material, which can be explained by the Hall-Petch relationship [36,37], which correlates the yield strength of the material to its crystal grain size, as shown in Eq. 2.1.

$$\sigma_y = \sigma_0 + \frac{k}{\sqrt{d}} \qquad \text{(Eq. 2.1)}$$

Where, σ_y is the yield strength of the material, σ_0 is the friction stress, k is a constant, and d is the grain size of the material. As can be observed, this is an inverse relationship between the yield strength of the material and the grain size. Therefore, with decreasing grain size, the yield strength of the material increases. Currently, there are limitations to the industrial application of nanocrystalline material mainly due to fabrications techniques (such as electro-deposition, vapor deposition), which cannot be adapted for large scale production. Still, there are other physical limitations, one such being grain growth at room temperature [4]. Based on the Hall-Petch relationship discussed above, grain growth would lead to a decrease in the strength of the material. Hence, there is a need to tailor nanostructured alloys, which can exhibit stable grain size to retain their enhanced mechanical strength.

2.1 Radiation mechanics in materials

To meet the energy needs of today, nuclear reactors are being designed to operate at higher temperature for better thermodynamic efficiency. Which means structural materials in nuclear reactors would be exposed to higher radiation damage doses and higher temperatures [38,39]. Irradiation is bombardment of energetic particles on to the lattice atoms of the material. Upon impact, the energetic particle imparts energy on to the lattice atom. If the imparted energy is enough, the lattice atom gets knocked out of the lattice. This knocked out atom is known as the primary knock-on atom (PKA). This leads to formation of a vacancy and interstitial point defect pair known as the Frenkel pair defect. The bombarded energetic particle goes on to create several other PKA while the PKA goes on to create secondary collisions. This process is known as the damage cascade formation during irradiation as shown in Fig. 2.1.

The point defects formed during this process, evolve to form irradiation induced defects such as dislocation loops, stacking fault tetrahedra or voids/bubbles [40]. The formation of these defects leads to change in mechanical properties of the material as they act as hurdles to dislocation motion. The formation of these defects is based on the point defect balance equation as shown in Eq. 2.2 and 2.3.

$$\frac{dC_v}{dt} = K_0 - K_{iv}C_vC_i - K_{vs}C_vC_s \quad \text{(Eq. 2.2)}$$

$$\frac{dC_i}{dt} = K_0 - K_{iv}C_vC_i - K_{is}C_iC_s \quad \text{(Eq. 2.3)}$$

Where, C_i, C_v and C_s are the concentration of interstitials, vacancies and defect sinks respectively, K_0 is the defect production rate, K_{iv} is the interstitial vacancy recombination rate and K_{vs} and K_{is} is the rate of loss of vacancies and interstitials to defect sinks, respectively. Defect sinks are generally microstructural features such as grain boundaries, incoherent phase boundaries,

amorphous regions, or coherent precipitates. Based on Eq. 2.2 and 2.3, as the rate of accumulation of point defects is negatively proportionate to sink concentration, increasing the sink volume in materials would make the material radiation tolerant. Therefore, nanocrystalline alloys seem attractive materials for use in nuclear reactor environment as they would be more tolerant to radiation damage due to the increased volume of grain boundary volume as compared to their bulk counterparts. But nanocrystalline materials under irradiation have been known to behave differently with respect to radiation and hence it is important to study the effects of radiation on nanocrystalline material.

2.1.1 Effects of radiation on nanostructured alloys

Even though nanostructured alloys have a higher volume of grain boundary, these materials tend to show very less grain size stability under irradiation environment as well. Nita et al. [13] performed room temperature proton irradiation on nanocrystalline Ni and nanocrystalline Cu-Al_2O_3 alloy and observed grain refinement in nc Ni but grain growth in the nc Cu alloy. Studies have also shown that grain boundaries may not be the best sink source as they over time during irradiation get saturated with defects leading to loss in efficiency of annihilating point defects [41,42]. But duplex systems having FCC-BCC interface boundaries have proven to be unlimited source of defect sinks [43–45]. Hence, the best way forward to tailor make stable nanocrystalline materials in high temperature and radiation environment is to create a nanocrystalline alloy with dispersed nanoclusters for high temperature stability as well as having incoherent phase boundaries for a better irradiation induced defect sink.

Due to advancement in manufacturing alloys, scientists can create alloys with components which are not miscible in each other also known as immiscible alloys. Immiscible alloys are alloys of elements which have a positive heat of mixing. These alloys can be alloyed following various manufacturing routes such as chemical vapor deposition, electrodeposition, ball milling and ion beam mixing. For creating temperature stable nanostructured alloys, doping with an immiscible solute element to stabilize grain boundaries has proven to be very effective [46–50]. Immiscible solute elements exhibit a tendency to segregate at the grain boundaries which effectively reduce the free energy at the grain boundaries and stabilize them to retard the process of grain growth. These solute elements also stabilize grain boundaries by the solute drag effect which basically is the drag effect created by the solute atoms while moving with the grain boundary. These immiscible solute atoms also form dispersed nano-precipitates which act as barrier to grain boundary motion by acting as Zener pinning points [51]. Therefore, the Cu-Ta immiscible system has been gaining interest due to the negligible solubility of either element in each other as well as due to the different crystal structures of the two components i.e., Cu has Face Centered Cubic (FCC) crystal structure, whereas Ta has Body Centered Cubic crystal structure.

2.2 Copper-Tantalum Alloy System

In this research, we will be studying the Cu-10at%Ta alloy system provided by the Army Research Lab, Maryland. This alloy has been prepared by high energy ball milling and then processed through Equal Channel Angular Extrusion (ECAE). The details of the manufacturing process have been discussed in section 3. Powders of Cu and Ta in the appropriate amounts are ball milled to achieve a homogeneous mixed powder of Cu and Ta. Ball milling causes ballistic disordering and reordering due to vacancy supersaturation due to the continuous plastic deformation of the powders allowing the formation of a solid solution of Cu and Ta. During ball

milling, the ball mill is cryogenically cooled to hinder thermal diffusion of atoms and ensure proper mixing. Heat treatment and the severe plastic deformation process results in a unique nanocrystalline microstructure with FCC Cu grains, BCC Ta phases and small Ta nanoclusters [52,53].

The thermal stability of this alloy system has piqued the interests of researchers to study this system. Fig. 2.2. shows a molecular dynamics simulation of nanocrystalline Cu versus nanocrystalline Cu-Ta alloy system both raised to a temperature of 1200 K for 18 ns. NC Cu shows rapid grain growth whereas NC Cu-Ta shows negligible change in grain size. This is due to the Ta nanoclusters which pin the grain boundary and impede thermal grain boundary migration [54]. A TEM *in situ* thermal treatment experiment done by Rajagopalan et. al. [55] shows the microstructural stability of the nanoclusters for temperatures up to 400℃ (673 K) where 4% change in Cu grain size was observed while the Ta phases and the nanoclusters exhibit stability.

Another reason for studying this alloy system is its superior mechanical properties as compared to its individual nanocrystalline counterpart. Multiple mechanical tests were carried out by Darling et. al. [11] and compared with nanocrystalline Cu and nanocrystalline Ta counterparts [56–60] as shown in Table 2.1. As observed in Table 2.1, the Cu-Ta alloy system exhibits thrice the hardness of nanocrystalline Cu. This alloy system has also proven to resist creep at elevated temperatures of 873 K [53], as a steady state creep of 10^{-6} s^{-1} was observed which is 6 to 8 orders of magnitude lesser than most of the nanostructured alloys. Due to the enhanced strength of the Cu-Ta alloy system, this material is being considered for use in extreme environments as structural materials such as that of nuclear reactors.

2.3 Effects on the stability of dispersed nanoclusters

As the mechanical and physical properties of the material are highly dependent on the stability of the nanoclusters, it is important to study the response of these nanoclusters/precipitates in similar systems under radiation. Most seen effects on nanoclusters are with respect to the nanocluster size, density, volume fraction, chemistry, and crystal structure. Table 2.2, 2.3 and 2.4 summarize studies from the literature differentiated based on the irradiating particles and list the change in size and density of the nanoclusters.

2.3.1 Nanocluster Size and Density

The most common observed change for nanoclusters under irradiation is the change in size and density of nanoclusters post irradiation. Wharry et. al. [25] were unable to find a relation between nanocluster size and density with respect to total dose and temperature so in this study we plotted Total Dose Vs Temperature Vs Dose Rate for different irradiating particles in Fig. 2.3(a-c) and 2.4(a-c) to see if any trend could be found. These plots show consistent behavior in nanocluster evolution as change in nanocluster size and density is consistently observed with ion irradiation. But stability is observed for neutron irradiation with a total dose up to 75 dpa beyond which change in nanocluster size and density is observed under neutron irradiation. Ribis et. al. [61–63] after neutron irradiation of MA957 up to a dose of 50 dpa at 412°C observed stability in nanoclusters whereas after increasing the dose to 75 dpa at 430°C observed decrease in nanocluster density and increase in size.

Neutron irradiation experiments have a lower dose rates allowing sufficient time for the alloy matrix to heal before another damage cascade is formed and hence stability of nanoclusters

is observed in most of the neutron irradiation experiments as compared to ion irradiations which have high dose rates.

The plots in Fig. 2.3 & 2.4 suggest that nanocluster evolution is greatly affected by the irradiating particle due to difference in scattering cross-section and cascade size. Even though trends due to type of irradiating particle are observed there is no discernible trend which would explain the growth or coarsening of the nanoclusters. But experiments with temperature lower than room temperature all exhibit dissolution of nanoclusters.

2.3.2 Chemistry

With the advent of atom probe tomography studying nanocluster composition has become extremely easy but due to the lower detection efficiency of APT studying the stoichiometry of compounds present in the clusters is still difficult hence relative compositions between the as received and irradiated samples are studied.

Studies on ODS alloys have shown both increase and decrease in Y:Ti ratio in the nanocluster post irradiation. Wharry et. al. [25] plotted change in Y:Ti ratio with respect to dose and temperature (Fig. 2.5) to find a critical temperature of 500°C below which the ratio decreases and above which the ratio increases. Wharry et. al. [25] suggests this phenomena due to the higher bond strength of Y in Y_2O_3 which increases the displacement energy of Y with respect to Ti, therefore at high temperatures this displacement energy reduces and therefore Y:Ti ratio decreases. In Fe-9wt%Cr ODS alloy, [64] observe an increase in Y:Ti ratio after proton irradiation at 400°C suggesting preferential displacement of Ti whereas stable Y:Ti ratio is observed by [65,66] after proton irradiation with same dose but at a temperature of 500°C suggesting equal displacement of both Y and Ti.

Studies on Ni super alloy have shown the formation of unstable and non-stoichiometric precipitates due to radiation enhanced mechanisms. Ji-Jung Kai and Lee [67] show formation of $M_{23}C_6$ precipitate in solution annealed Alloy 600 due to 1 MeV proton irradiation for doses of 0.5 to 5 dpa at 450°C at a dose rate of 4×10^{-5} dpa/s even when the stable carbide precipitate is M_7C_3 in Alloy 600 attributed to the increase in Cr diffusion towards the nanoclusters due to irradiation.

2.3.3 Crystal Structure

Due to the nanoscale size of these nanoclusters they normally tend to be coherent with the matrix and contribute to the thermal stability of the material and the incoherent nanoclusters act as effective dislocation pinning points. They are also effective defect sinks due to the high interfacial energy between nanocluster and matrix. Hence it is of utmost importance to study the crystal structure of the nanoclusters.

Chen et. al. [68] compared coherent interfaces versus incoherent interfaces before and after irradiation in neutron irradiated Fe-12Cr ODS alloy and observed the coherent nanoclusters to grow towards a critical size whereas the incoherent nanoclusters dissolved with decreasing temperature. Bazarbayev et. al. [69] observe dissolution of precipitate after proton irradiation in Alloy 600 which is attributed to disordering of γ′ precipitate similarly amorphization of oxide nanoclusters has been observed. Lescoat et. al. [70] also found a critical temperature for amorphization to occur for DY ODS alloy for 1.2 MeV Kr^+ irradiation up to 45 dpa to be at 500°C (Fig. 2.6).

2.4 Factors affecting dispersed nanoclusters/precipitate stability

During irradiation namely two competing effects of irradiation affect the stability of the dispersed nanoclusters/precipitates i.e the ballistic dissolution and the radiation enhanced diffusion.

The following section discusses these processes.

2.4.1 Ballistic Dissolution

Ballistic dissolution is the expulsion of atoms from the nanoclusters resulting in the coarsening or dissolution of the nanoclusters due to head on collisions or due to the damage cascades formed due to the irradiating particle. Ballistic dissolution can be split into two phenomena: recoil dissolution is the ejection of the primary knock-on atom from the cluster due to the irradiating particle and disordering dissolution is disordering of nanocluster atoms due to the damage cascade and both these phenomena lead to the coarsening of the nanocluster.

Studies in literature have shown that ballistic dissolution mechanism can be isolated by carrying out low temperature irradiation experiments so that thermal diffusion is absent. Certain et. al. [71] carried out nickel ion irradiation of 14YWT ODS steel at -75°C and 100°C to a dose of 100 dpa and observed complete dissolution of nanoclusters less than 20 nm size. Similar results were seen by Sencer et. al. [72] when they carried out proton irradiation of Alloy 718 at a temperature of 32°C to 55°C to a dose of 0.6 dpa and 13.4 dpa where complete dissolution of γ' and γ'' precipitates was observed. An example of ballistic dissolution can be seen in Fig. 2.7.

Though Ballistic dissolution leads to coarsening of nanoclusters, it sometimes also leads to homogeneous nucleation of smaller nanoclusters which is caused due to first ejection of solute particles into the matrix around the parent nanocluster. The solute particles form a solid solution due to enhanced solubility of solute particles due to irradiation which nucleate and form smaller clusters once the irradiation is stopped. This is observed as smaller nanoclusters surrounding a bigger nanocluster and is known as the haloing effect and goes on until the parent nanocluster is completely dissolved.

2.4.2 Irradiation Enhanced Diffusion

Diffusion is governed by the probability of a lattice atom finding a neighboring vacancy. As irradiation leads to formation of vacancies in the lattice which is in excess of the vacancies due to thermal effects, which increases the probability of a lattice atom to find a neighboring vacancy leading to increase in diffusivity of the alloy atoms by interstitial or vacancy diffusion, leading to change in size and chemistry of the nanoclusters.

Irradiation enhanced diffusion can lead to both shrinkage and growth of nanoclusters depending on the concentration gradient between the nanocluster and the surrounding matrix for solute atoms or create stoichiometric or non-stoichiometric nanoclusters. This has been observed by Song et. al. [73] where long ranged ordered NiAl precipitates are formed in Ni super alloys which isn't observed when the alloys are just heat treated. These precipitates were observed to grow in size with increasing dose in alloy 718 [73].

2.5 Cluster evolution phenomenon

The equilibrium condition between ballistic dissolution and irradiation enhanced diffusion governs the stability of the nanocluster as they take place simultaneously. When these two factors aren't at equilibrium phenomenon such as Ostwald ripening, Homogeneous Nucleation and multiple mechanisms taking place simultaneously have been observed. The next section details these special case phenomena.

2.5.1 Ostwald Ripening

Ostwald ripening is the process by which the larger nanoclusters undergo growth caused by dissolution of the smaller nanoclusters as they are thermodynamically unstable. Smaller nanoclusters have more interfacial surface energy and to reduce this interfacial energy the

nanoclusters diffuse towards bigger nanoclusters resulting in a more thermodynamically stable phase. It should be kept in mind that only incoherent precipitates undergo growth [68]. Lescoat et. al. [74] observed Ostwald ripening of nanoclusters in Fe-18wt%Cr ODS alloy after Fe ion irradiation up to 150 dpa at 500°C as shown in Fig. 2.8.

This phenomenon can be modeled based on the Ostwald-Freundlich equation using the Gibbs-Thompson equation for precipitate growth. Studies have shown that growth of larger incoherent precipitates is due to the dissolution of smaller coherent nanoclusters hence conserving mass. The effect of Haloing is opposite of Ostwald ripening as bigger precipitates reduce in size which leads to nucleation of smaller nanoclusters which then grow by Ostwald ripening when they reach critical radius. Chen et. al. [68] has made attempts to model irradiation induced evolution of nanoclusters by combining Gibbs-Thompson model for Ostwald ripening to explain growth of nanoclusters and ballistic dissolution.

Ostwald ripening scales by $\phi^{1/3}$ where ϕ is the irradiation flux [61,74]. Molecular dynamics has shown how irradiation leads to Ostwald ripening of nanoclusters [75]. First amorphization of smaller nanoclusters takes place due to damage cascades which increases their solubility into the matrix. Similar disordering takes places at the interface of bigger phases which in turn increases it defect sink capability due to which the amorphized smaller clusters end up going to the bigger phase leading to precipitate growth.

2.5.2 Homogeneous Nucleation

Homogeneous nucleation is the process by which formation of newer nanoclusters takes place and is caused due to the super saturation of solute atoms which grows to a critical radius beyond which growth due to Ostwald ripening can occur. The process of haloing is an example of

homogeneous nucleation where smaller nanoclusters are formed around the parent precipitate after recoil ejection of solute particles from the parent nanoclusters. This mechanism has to be coupled with another mechanism to explain nanocluster evolution due to irradiation.

Nucleation has been observed in Martensitic phases of ODS Steel alloys, Allen et. al. [76,77] irradiated Ferritic/Martensitic Fe-9Cr ODS Steel with 5 MeV Ni ions with a dose rate of 1.4×10^{-3} dpa/s at 500°C-700°C temperature to total dose of 150 dpa resulted in the formation of smaller nanoclusters leading to strengthening of the matrix. Similarly Ji-Jung Kai and Lee observed formation of smaller 1 nm precipitates in solution annealed alloy 600 post proton irradiation [67]. An example micrograph of homogeneous nucleation can be seen in Fig. 2.9.

2.5.3 Multiple Mechanisms

Other than Ballistic dissolution none of the other mechanisms have been isolated and are said to take place simultaneously to be consistent with what is being observed in the literature. For example: Akasaka et. al. [78] neutron irradiated MA957 ODS alloy at 700°C to a dose of 100 dpa and observed decrease in the number density of nanoclusters signifying ballistic dissolution of nanoclusters and simultaneous increase in average size of the precipitate indicating Ostwald ripening of the nanoclusters. As we have seen earlier haloing effect is also a combined effect of ballistic ejection of solute atoms leading to homogeneous nucleation and Ostwald ripening of the newer formed nanoclusters to an equilibrium size.

2.6 Strengthening mechanisms in Nanocrystalline materials

Majority of the strengthening of nanocrystalline materials comes from the Hall-Petch effect, but when it comes to nanocrystalline alloys, strengthening can also be due to solid solution strengthening [79], Orowan strengthening [80] or rule of mixture strengthening [81].

Solid Solution Strengthening for nanocrystalline materials can be achieved through formation of equilibrium or non-equillibrium solution (Immiscible alloy systems). This is similar to bulk materials except for the fact that nanocrystalline material manufacturing process allow the alloying of immiscible solutes as well. The amount of solid solution strengthening can be judged based on Eq. 2.4.

$$\tau_{ss} = \beta G \varepsilon^{p} c^{q} \quad \text{(Eq. 2.4)}$$

Where, τ_{ss} is the strengthening due to solid solution, β is a constant, G is the shear modulus, ε is the misfit strain between the matrix and the solute atom, c is the atomic fraction of the solute and p & q depend on the solute-dislocation interaction [82].

When the material consists of nanoclusters or dispersed secondary phases smaller than the graian size of the matrix, Orowan type strengthening takes place in the material [80]. When such small particles are present in the matrix grains, the dislocations are pinned due to these particles which act as obstacles to dislocation motion. This type of strengthening can be quantified using Eq. 2.5.

$$\tau_{oro} = \frac{Gb}{2\pi}\left\{\frac{\ln(\lambda)}{\lambda}\left[\frac{\ln(2r)}{\ln(\lambda)}\right]^{1.5}\right\} \quad \text{(Eq. 2.5)}$$

Where, τ_{oro} is the increase in stress due to Orowan strengthening, G is the shear modulus, b is the burger's vector, r is the average size of the dispersed particles and λ is the interparticle spacing based on the effective volume fraction (f*) of the dispersed particles given by Eq. 2.6.

$$\lambda = 2r\left(\sqrt{\frac{\pi}{4f^{*}}} - 1\right) \quad \text{(Eq. 2.6)}$$

For a separate secondary phase of similar or bigger size as compared to the matrix grain size, the strengthening effect can be quantified using the rule of mixtures. The rule of mixture dictates that each phase contributes its individual strength to the overall strength of the material based on its volume fraction in the material and for duplex system is given by Eq. 2.7.

$$\tau_{RoM} = (1 - x)\tau_1 + (x)\tau_2 \quad \text{(Eq. 2.7)}$$

Where, τ_{RoM} is the increase in stress due to strengthening by rule of mixtures, x is the volume fraction of one of the alloying components and τ_1 and τ_2 are strength of individual components in the alloy. This can be extended to alloys with more than two components as well. Though there is no certainty that rule of mixtures is an appropriate relation for judging the strength of the material, it serves as a standard for the strength of the material.

These strengthening mechanisms have been found to individually contribute towards the strength of the nanocrystalline alloys as well as contribution of multiple strengthening mechanisms has also been observed [11,83–85]. Systems with multiple strengthening mechanisms tend to show higher strength, possibly due to the interaction of the various mechanisms with each other [11,86]. For example, Darling et al. [11] explained the strength of Cu -Ta alloy system using Hall-Petch Relationship due to nanocrystallinity and Rule of Mixtures Strengthening due to presence of Ta particles comparable to size of Cu grain in the system whereas in the Cu -W system [83] which consists of nanoclusters of W, Orowan type strengthening is also taken into account. Therefore, any change in the microstructure of the alloy would directly impact the mechanical properties of the material.

2.7 Effects of radiation on the mechanical response of materials

Irradiation has been known to cause hardening of the material due to the irradiation induced point defects which lead to the formation of defect clusters such as stacking fault tetrahedra, dislocation loops or voids/bubbles. There are two types of hardening in material, i.e. source hardening and friction hardening.

Source hardening is referred to the increase in stress to unpin a dislocation on to its slip plane. In irradiated BCC materials, source hardening is caused due to the impurity atoms. For the Frank-read source to move, the dislocation lines need to be unpinned from impurity atoms which requires a larger stress and is indicated by a drop in the yield stress after the dislocation line is unpinned. In FCC materials, source hardening is due to presence of irradiation induced defects in the surrounding of a Frank-read source which increases the stress needed for loop expansion or multiplication. But after the threshold stress is overcome the irradiation induced defects are destroyed and the deformation can occur at a lower level [40].

Friction hardening is referred to as the opposition to motion of the dislocation on its slip plane due to obstacles. This is normally the stress required for continuous plastic deformation. This resistance is mainly due to dislocation-dislocation interaction or dislocation-feature interacture for features such as defect clusters, precipitates, and voids. The dislocation-dislocation interaction due to their individual stress fields is referred to as long range stresses whereas the interaction of dislocations with obstacles is referred to as short range stresses. Unlike long range stresses, short range stress occurs only when the dislocation interacts with the obstacle as shown in Fig. 2.10. Cu being FCC generally tends to show formation of stacking fault tetrehedra [13,87–89] which mainly contribute to hardening via friction hardening. The amount of hardening a

material undergoes due to the presence of obstacles can be calculated using the Orowan's dispersed barrier strengthening model [40] as shown in Eq. 2.8.

$$\Delta\sigma_y = \alpha M \mu b \sqrt{Nd} \quad \text{(Eq. 2.8)}$$

Where, $\Delta\sigma_y$ is the change in yield stress, α is the barrier strength coefficient (depends on the geometry of the barrier), M is the ratio of uniaxial yield strength to resolved shear strength [90], μ is the shear modulus of the material, b is the burger's vector, N is the number density of the obstacle and d is the average size of the obstacle. Each type of obstacle has a different α value depicting the effectiveness of the barrier, therefore α=1 represents a perfectly hard barrier.

Various studies have shown that irradiation of Cu leads to the formation of Stacking Fault Tetrehedra [88,89,91–93]. Nita et al. [13] proton irradiated nanocrystalline Cu-Al_2O_3 alloy at room temperature and observed the formation of SFT as well as Zinkle et al. observed formation of SFTs in Cu after neutron irradiation. This suggests that the hardening of the material will also depend on the formation of SFTs post irradiation. But the formation of these defects highly depends on the irradiating temperature as well. Zinkle et al. [94] explored the formation of irradiation induced defects at various temperatures and found that above 186℃ there was no formation of stacking fault tetrehedra in Cu grains. The high temperature increases point defect annihilation by mutual recombination and therefore no SFTs are observed.

2.8 Deformation response in immiscible alloys systems

With respect to radiation, as we are doing a high temperature ion irradiation, we are more likely to see change in the nanocluster morphology rather than formation of irradiation induced defects. To alleviate the effects of irradiation, annealing has been the go to choice, but annealing might lead to changes in the microstructure of the alloy due to nanocluster evolution during

irradiation. Therefore, we need to explore a different route to lighten the effects of irradiation on the material.

Experimental studies for deformation response of immiscible alloys are known to show phenomena such as phase thinning and nucleation during deformation. Also referred to as self-organization of solutes during deformation, this phenomenon is highly dependent on the rate of shear induced mixing and thermally activated diffusion [95,96]. This phenomenon was first demonstrated in a simulation for various immiscible alloys under Severe Plastic Deformation (SPD) at elevated temperatures [97] where they observed chemical mixing in the alloy. Later, it was first confirmed in the Cu – Ag alloy system which was formed by ball milling for chemical mixing of the alloy components [98].

Studies on Cu – Nb alloy system have shown the Nb BCC precipitates go towards an equilibrium size of 10 nm under low temperature High Pressure Torsion experiment irrespective of the initial microstructure [29] as shown in Fig. 2.11. This phenomenon has been simulated for Cu-Nb and Cu-V alloy systems, and was found to be due to removal of atoms by dislocations due to shear force developed at the fcc-bcc interface of Cu and Nb/V [26,27]. The removed atoms are then carried away from the parent phase due to dislocation glide and helps explain the reduction in size of large phases. This process was found to be in competition with nucleation of newer solute phases due to athermal grain boundary relaxations and their growth due to transport of solute atoms along superdiffusive pathways such as grain boundaries [29].

There have also been other explanations for these behaviors such as fracturing of the precipitate due to co-deformation of the Cu and Nb phases [99,100] or by atomic shuffling [101]. The process of co-deformation of Nb phase has been demonstrated in the accumulative roll

bonding of Cu – Nb laminates [102]. Post accumulative roll bonding the samples were put through High Pressure Torsion (HPT) in which the co-deformed structures eventually fractured to form well distributed Nb precipitates [103]. The process of atomic shuffling explains the thinning of Nb by the process of dislocations in Cu penetrating through the Cu – Nb interface leading to amorphization and eventual thinning of the Nb phase [101]. Though these mechanisms explain the thinning of the phases, none of them predict the nucleation of newer phases after deformation at low temperatures.

Recent studies detailing large scale molecular dynamics simulations of deformation at low temperatures on Cu – Nb/V/Ta systems tries to explain the thinning of the precipitates and formation of new smaller clusters [27]. The simulations showcased formation of an amorphous layer between the Cu grain and Nb/V/Ta precipitates as shown in Fig. 2.12. The formation of the amorphous interface allows the transport of Ta atoms across the interface into the Cu matrix by dislocation glide. They emphasized that the transport of these atoms is not due to atoms being carried away by dislocations but due to relative displacements of atoms resulting in the atoms being separated from the parent phase. On the other hand, Cu atoms did not diffuse into the Ta precipitate. Ashkenazy et al. [27] tracked these atoms and their trajectories during the deformation process and found that these atoms are very far from their initial position. Fig. 2.13(a) shows their initial and final position after deformation and Fig. 2.13(b) shows the zigzag trajectories of these atoms which signify the transport of these atom through dislocation glide. For Cu-Ta alloy system they found that the formation of newer Ta clusters is not due to fracturing of the Ta precipitate but due to the single emission of atoms from Ta precipitate which due to dislocation glide segregate to form newer Ta clusters.

Ashkenazy et al. [27] also performed large scale molecular dynamic to check the evolution of microstructure of the alloy based on the initial concentration of the solutes. They found that below a certain solute concentration i.e. 1at% for Nb, 5at% for V and 0.3at% for Ta, the alloy post deformation consisted of a single FCC phase whereas anything above those concentrations resulted in the formation of a separate FCC phase and a separate BCC phase. They also observed that above a certain initial concentration i.e. 9at% for Nb, 8at% for V and 24at% for Ta, instead of formation of two different phases, the system would completely amorphize.

As immiscible alloys tend to go towards a certain equilibrium size of precipitates irrespective of the initial microstructure, the deformation route represents a possible mechanism of lessening the non-equilibrium effects of irradiation in case of nanocluster evolution.

Table 2.1: Mechanical Properties of CuTa alloy in comparison to NC pure Cu and NC pure Ta [11]

Property	Cu-10Ta 700ºC	NC Pure Cu	NC Pure Ta
Vickers Hardness Testing	3.75	2.55 1.35 1.05	4.10[d] 2.50[d]
Shear Punch Testing	0.69	0.42[a]	-
Quasistatic compression testing	1.10	0.80[b] 0.45[b] 0.35[b]	1.30[e] 0.90[e]
Dynamic Compression	1.47	0.88 – 0.55[c]	2.00 1.20[e]
Compression Yield Stress	1.23	0.85 0.45 0.35	1.36 0.83
Shear Yield Stress	0.62	0.43 0.23 0.18	0.68 0.42

[a] Nanocrystalline Cu with grain sizes 5 nm, 70 nm and 250 nm respectively
[b] Nanocrystalline Cu with grain size 74 nm
[c] Nanocrystalline Cu with grain sizes 35 nm and 300 nm
[d] Nanocrystalline Ta with grain size 56 nm and 160 nm
[e] Nanocrystalline Ta with grain size 44 nm and 250 nm

Table 2.2: Summary of Proton irradiation experiments adapted from [25] with additional data points for Ni Alloys.

Material	Energy	Irradiation dose (dpa)	Irradiation Temp (°C)	Dose rate (dpa/s)	NC density	NC size	Reference
9Cr ODS	2 MeV	3	500	0.00001	Stable	Decrease	[65,66]
9Cr ODS	2 MeV	3.7	400	0.000005	Decrease	Increase	[64]
14YWT	2 MeV	3	400	0.000005	Increase	Increase	[71]
9Cr ODS	2.6 MeV	1	525	0.000005	Decrease	Decrease	[104]
Inconel 600 MA	1 MeV	5	450	0.00004	Stable	Increase	[67]
Inconel 600 SAS	1 MeV	5	450	0.00004	Increase	Increase	[67]
Alloy 718	2 MeV	7	500	0.0001	Dissolution	Dissolution	[69]
Alloy 625 P	2 MeV	2.1	360	0.00000648	Increase	n.s	[73]
Alloy 725	2 MeV	2.5	360	0.0000077	Increase	n.s	[73]
Alloy 718	2 MeV	2.5	360	0.0000077	Stable	n.s	[73]
Alloy X750	2 MeV	2.5	360	0.0000077	Stable	n.s	[73]
Alloy 718	600-800 MeV	0.6	44	0.0000001	Dissolution	Dissolution	[72]
Alloy 718	800 MeV	10	250	0.00000027	Dissolution	Dissolution	[105]
Alloy 718	800 MeV	13.4	55	0.0000001	Dissolution	Dissolution	[106]

Table 2.3: Summary of Fe ion irradiations adapted from [25] with additional data points for Ni alloys

Material	Energy	Irradiation dose (dpa)	Irradiation Temp (°C)	Dose rate (dpa/s)	NC density	NC size	Reference
12Cr ODS	3.5 MeV	100, 200	325, 475, 625	-	Decrease at 625°C. Stable at 475°C	Decrease	[68]
18Cr ODS	0.5 MeV	75, 150,	500	-	Decrease	Increase	[74]
14Cr ODS	500 keV	150	500	0.0064	Decrease	Increase	[61]
9Cr ODS	5 MeV	3, 100	500	0.0001	Decrease 3dpa. Stable for 100dpa	Decrease	[31]
14Cr ODS	1.8 MeV	100	-83	0.003	Dissolution	-	[107]
14Cr ODS	5 MeV	150	500, 700	0.003	Decrease	Decrease	[107]
18Cr ODS	150 keV	4, 23, 38, 45	500	-	Stable	Stable	[108]
12Cr ODS	24 MeV	4.4	RT	-	Stable	Stable	[109]
9Cr ODS	5 MeV	50	400	0.0001	Decrease	Stable	[110]
14Cr ODS	14 MeV	30	600	-	Stable	Increase	[60]
SOC-1	-	60	650	0.0005	Stable	Stable	[111]
316 ODS	10.5 MeV	20	380	0.0011	Decrease	Decrease	[112]
F82H	10.5 MeV	20	380	0.0011	Decrease	Decrease	[112]
Eurofer 97	0.5 – 2 MeV	2	400	0.0001	Stable	Stable	[113]
K1	6.4 MeV	150	670	0.001	Stable	Stable	[111]
K4	6.4 MeV	20 - 150	500, 670 & 700	0.001	Stable	Stable	[111]
MA957	500 keV	150	500	0.00065	Decrease	Increase	[61]
Alloy 718SA	3.5 MeV	10	200	0.00155	Dissolution	Dissolution	[114]
Alloy 718PH	3.5 MeV	10	200	0.00155	Dissolution	Dissolution	[114]

Table 2.4: Summary of Neutron Irradiation experiments adapted from [25] with an additional data point for Ni alloy

Material	Energy	Irradiation dose (dpa)	Irradiation Temp (ºC)	Dose Rate (dpa/s)	NC density	NC size	Reference
9Cr ODS	Fast	3	500	0.0000001	Decrease	Decrease	[65,66,110]
9Cr ODS	Fast	33	420-835	0.0000001	Stable	Stable	[115]
12Cr ODS	Fast	33	420-835	0.0000001	Stable	Stable	[115]
MA957	Fast	3	600	0.00000037	Stable	Stable	[116]
MA957	Fast	50	412	0.0000013	Stable	Stable	[61–63]
MA957	Fast	75	430	0.0000013	Decrease	Increase	[61–63]
MA957	Fast	100	502-709	0.00000118	Decrease	Increase	[78]
MA957	Fast	2, 6	325	0.0000001	-	Stable	[117]
MA957	Fast	110	412-670	-	Stable	Stable	[118]
MA957	Thermal	2, 5.5	325	-	Stable	Stable	[119]
F94	Fast	2.5-15	400-530	0.0000001	Stable	Stable	[78]
F95	Fast	2.5-15	400-530	0.0000001	Stable	Stable	[78]
DY	Fast	81	400-580	0.0000013	Decrease	Decrease	[120]
DY	Fast	75	400-480	0.0000013	-	Decrease	[121]
DY	Fast	81	400-580	0.0000013	Decrease	Decrease	[122]
1 DS	Fast	10.5-21	450-530	-	Decrease	Decrease	[123]
1 DK	Fast	10.5-21	450-530	-	Decrease	Increase	[123]
M93	Fast	2.5-15	400-530	-	Stable	Stable	[78]
14YWT	Fast	3	500	0.0000001	Increase	Decrease	[71]
Eurofer 97 ODS	Fast	32	330	-	Increase	Dissolution	[124,125]
Alloy 718	Spallation	0.1	72	0.0000001	Dissolution	n.s	[72]

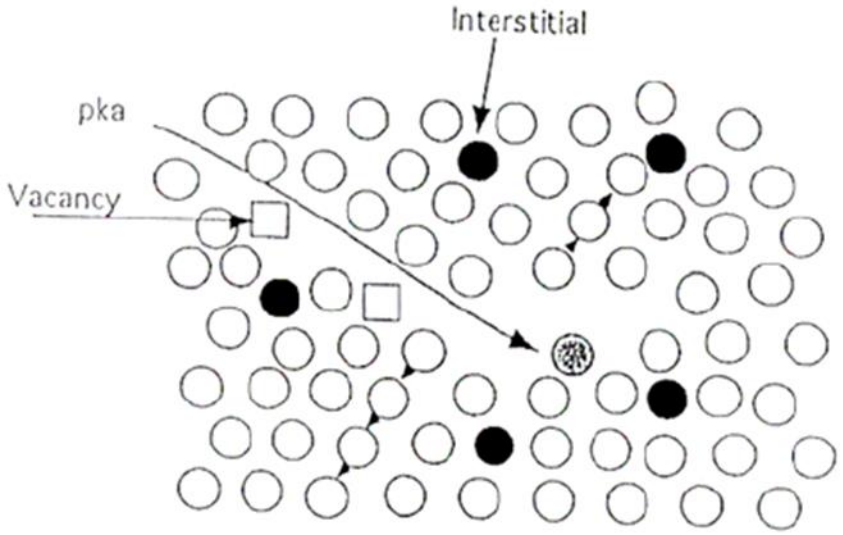

Figure 2.1: This image depicts the formation of Frenkel pairs due to the Primary Knock on Atom formed due to the bombardment of an energetic particle which leads to the formation of a damage cascade.

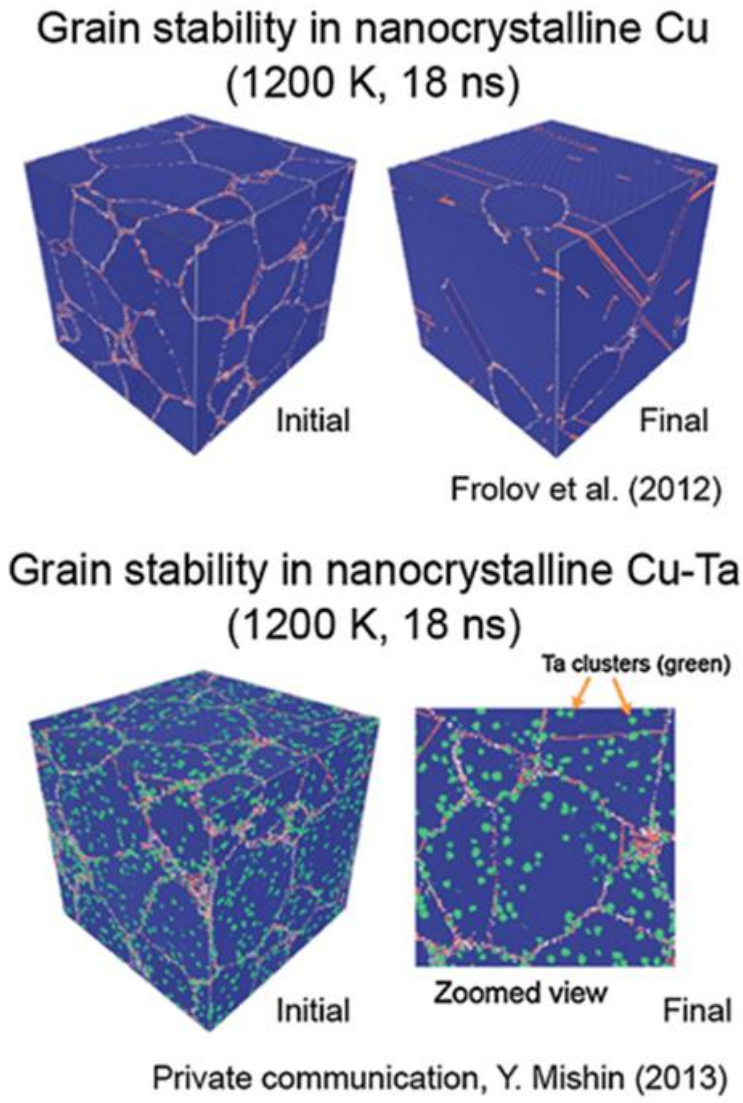

Figure 2.2: A molecular dynamics simulation which compares the response of nanocrystalline Cu to nanocrystalline Cu-Ta alloy system. It can be observed that the nanocrystalline Cu - Ta system does not show any grain growth when subjected to 1200K for 18 ns signifying its superior grain stability at elevated temperatures [6].

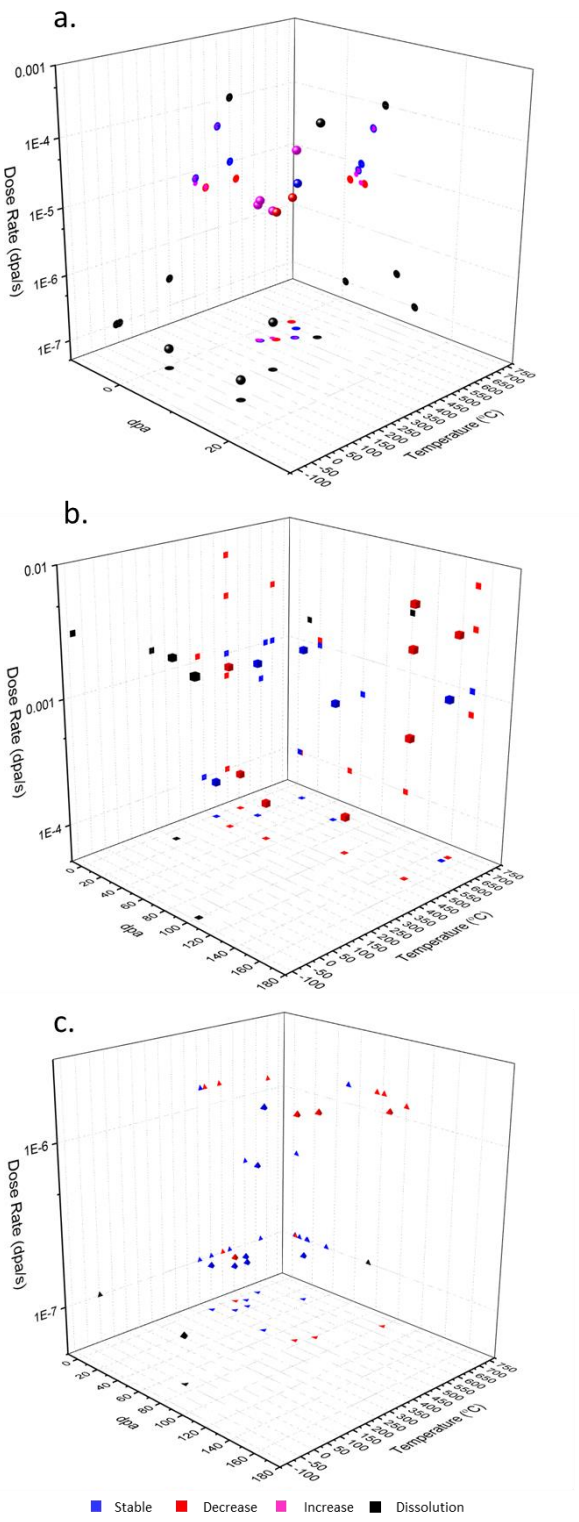

Figure 2.3: Change in Nanocluster density plotted as function of dose rate vs dose vs temperature for a. Proton Irradiation Experiments, b. Fe-ion Experiments and c. Neutron Irradiation Experiments.

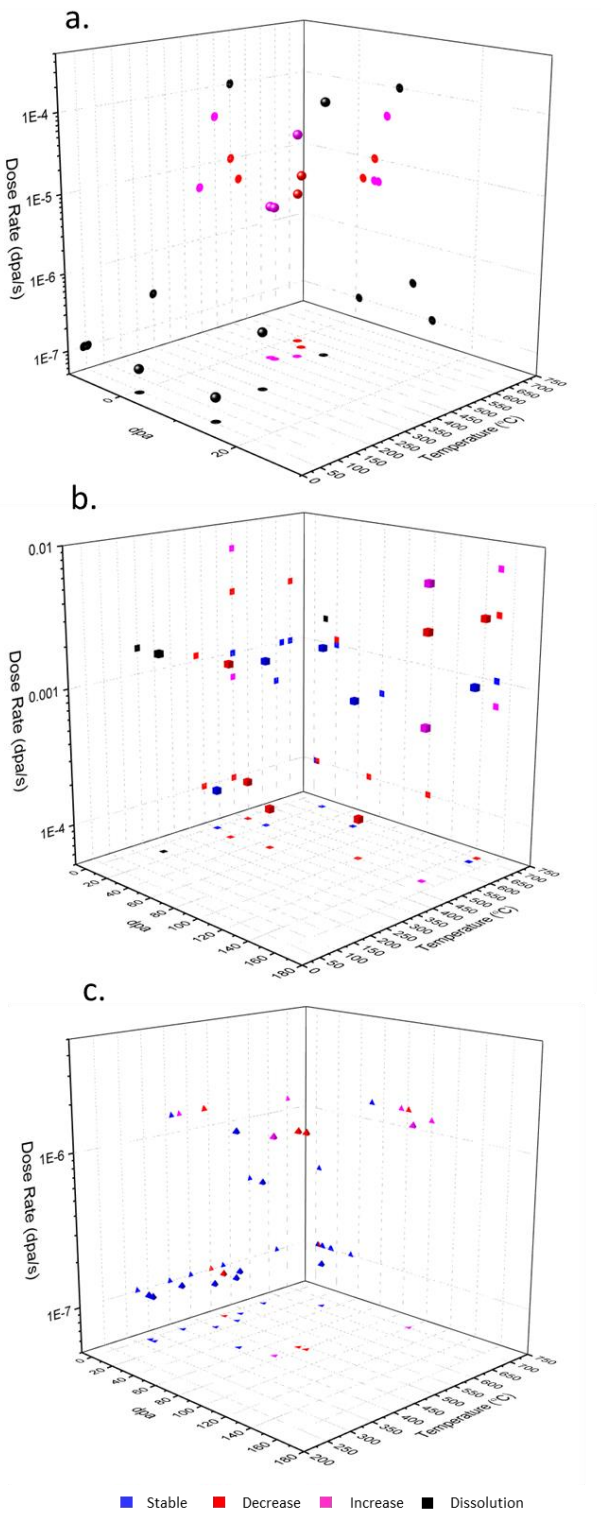

Figure 2.4: Change in Nanocluster size plotted as function of dose rate vs dose vs temperature for a. Proton Irradiation Experiments, b. Fe-ion Irradiation Experiments and c. Neutron Irradiation Experiments.

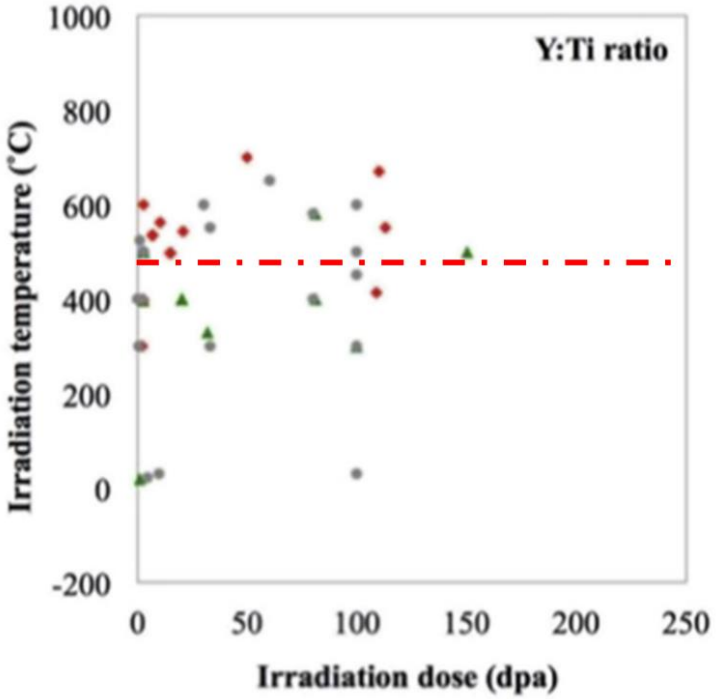

Figure 2.5: Adapted from [25]. Shows the change in Y:Ti ratio as a function of Temperature Vs Dose. The red dashed line shows the critical temperature above which Y:Ti ratio decreases and below it Y:Ti ratio increases.

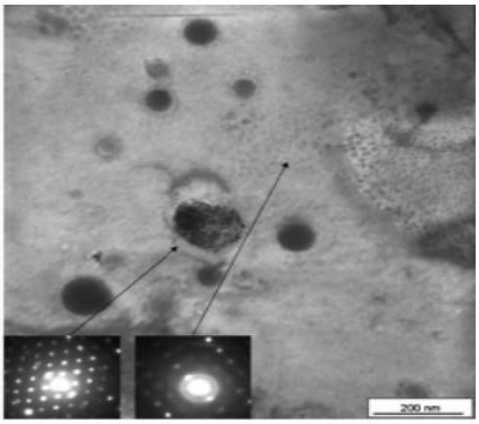

Figure 2.6: DY ODS alloy after 92 MeV Xe ion irradiation [70] Some nanoclusters stay crystalline while some undergo disordering as is seen in the diffraction pattern.

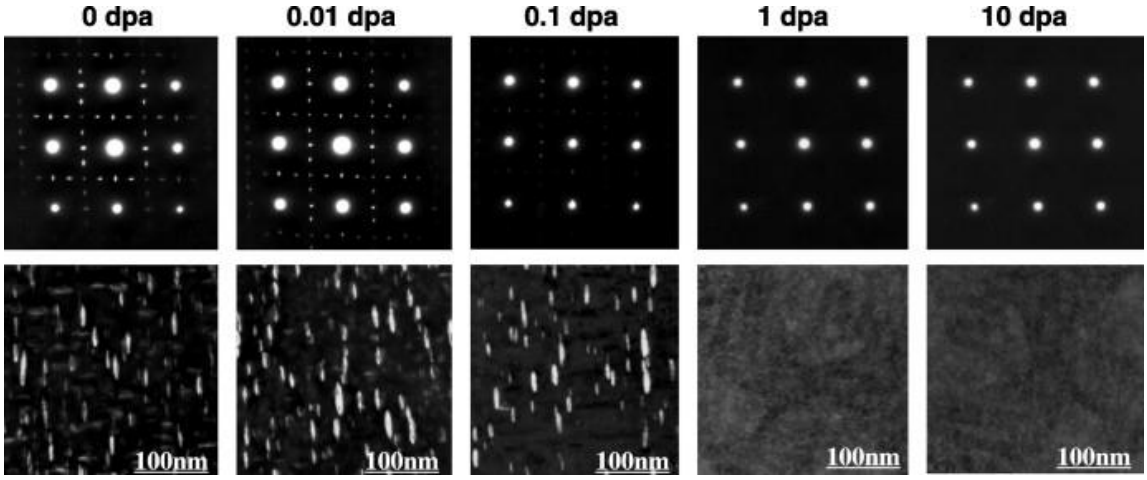

Figure 2.7: Ballistic dissolution observed by [114] with increasing dose after Fe ion irradiation. The ballistic dissolution is observed by loss of diffraction pattern for γ'/γ'' precipitates as the dose increases.

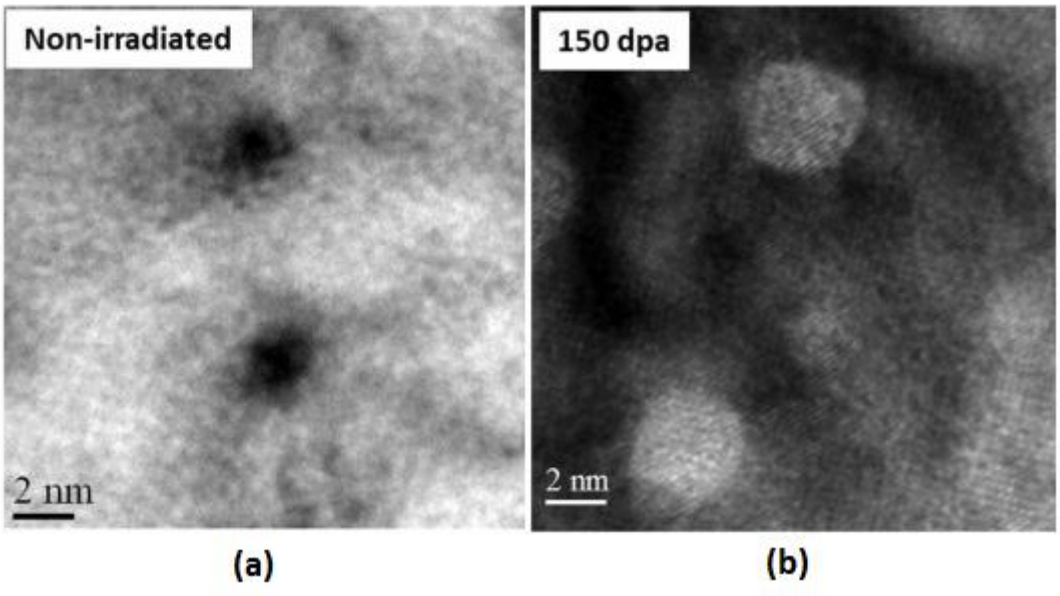

Figure 2.8: Ostwald ripening of nanoclusters post irradiation observed by [74] after Fe ion irradiation at 500°C (a) Non irradiated sample (b) irradiated up to 150 dpa sample.

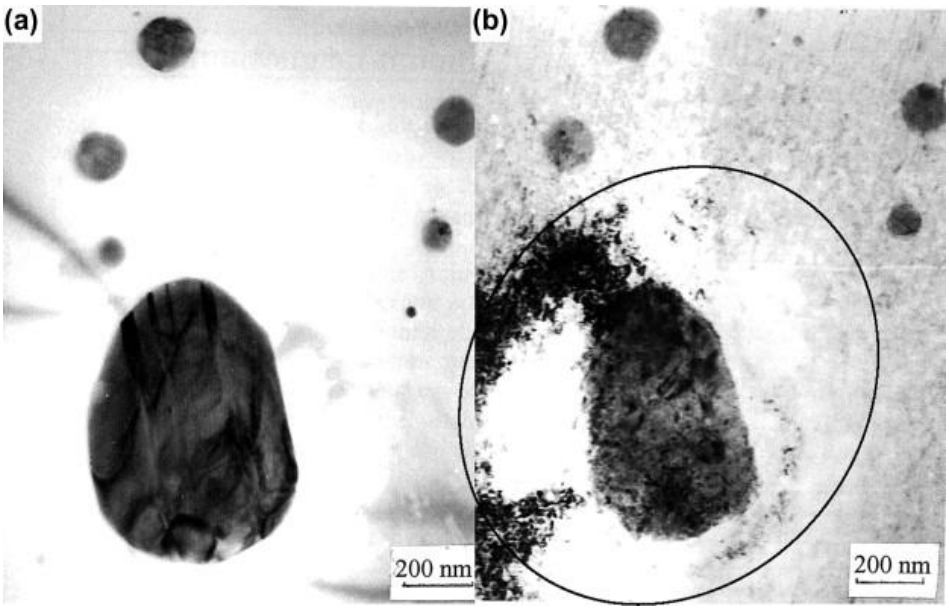

Figure 2.9: TEM micrograph from [122] of EM10 ODS material a. As received condition b. After electron irradiation up to 100 dpa showing formation of smaller nanoclusters around the parent nanoclusters also called as "haloing" effect.

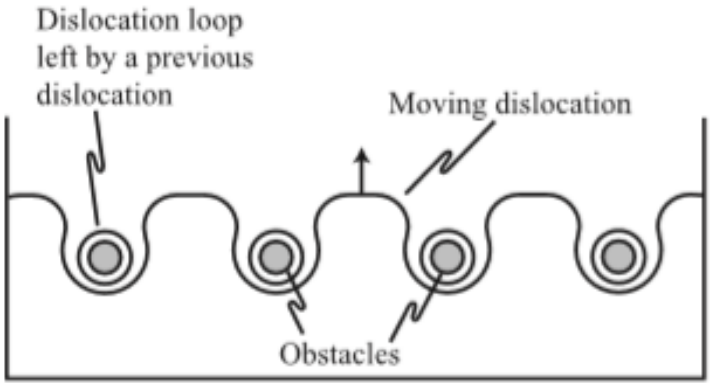

Figure 2.10: A schematic showing the interaction of dislocations with precipitates [40]. The pinning of dislocations due to precipitates falls under friction hardening short stresses.

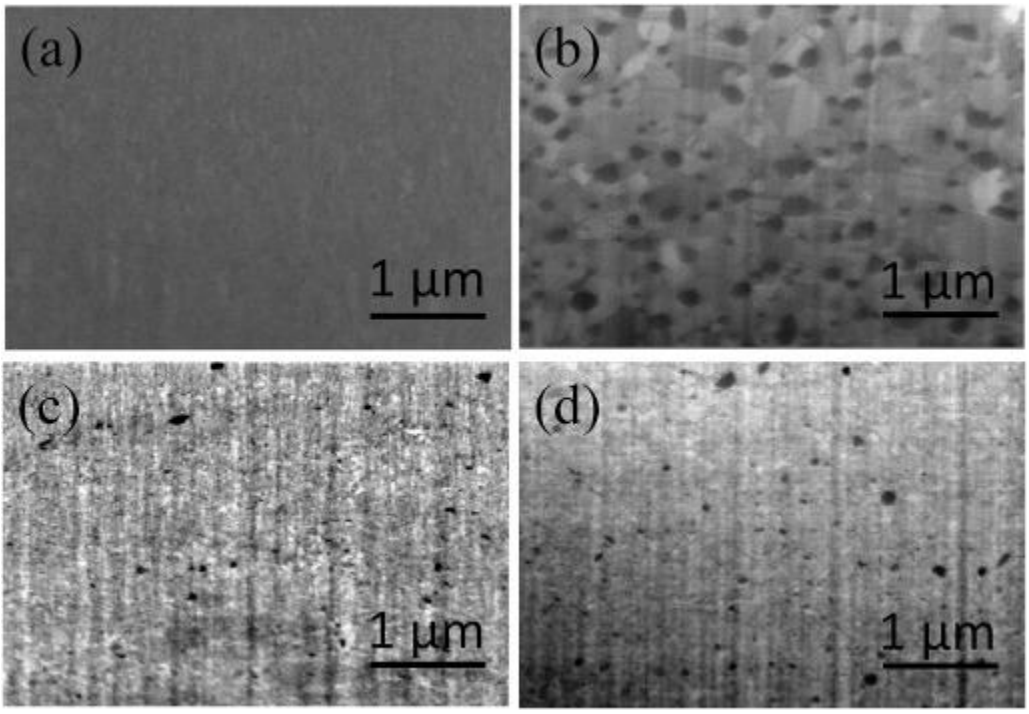

Figure 2.11: A study on Cu- Nb alloy system [29] which shows that irrespective of the initial microstructure, after HPT the Nb precipitates go towards an equilibrium size of 10 nm.

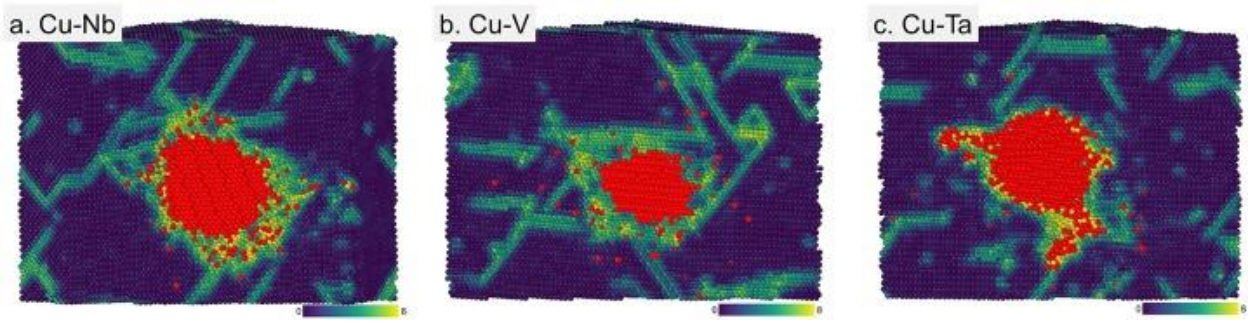

Figure 2.12: This is an image showing the centro-symmetry of atoms in [27]. The atoms marked red represent atoms belonging to the solute atoms whereas the dark blue to yellow scale represents the crystallinity of the atom. Dark blue color represents the atoms occupying a perfect crystal lattice position whereas yellow represents the low symmetry atoms signifying the amorphous region.

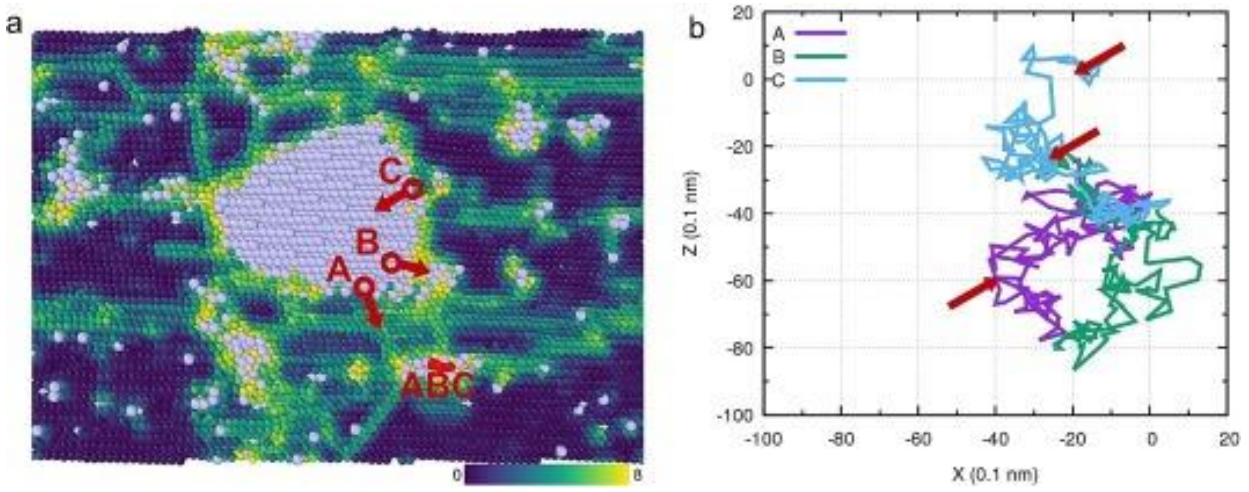

Figure 2.13: (a) Shows the initial and final position of solute atoms A, B and C which segregate via dislocation glide to form a new Ta cluster. (b) Shows the trajectories of atom A, B and C. The zigzag pattern signifies transport of atoms due relative displacement of atoms from each other via dislocation glide. [27]

3. METHODS

In this section we discuss the different techniques for alloy preparation, proton irradiation, polishing, microstructure characterization techniques and mechanical testing experiments. This section also discusses the use of analysis software for atom probe tomography cluster analysis and automated crystal orientation mapping software.

3.1 Alloy Manufacturing

Bar of size 2 mm × 40 mm × 2 mm was provided by the Army Research Laboratory, MD, and has been prepared by high energy ball milling powders of 76wt% of Copper (Cu) and 24wt% Tantalum (Ta) to achieve a composition of Cu-10at%Ta. The powders are loaded into the ball mill with hardened steel vials and 440C stainless steel balls, which have a 10 to 1 ball to powder ratio by weight in the Argon atmosphere to limit contamination. The ball milling is done for continuous 8 hours while being cooled using liquid nitrogen (~ -196℃). The nitrogen cooling impedes thermal diffusion of Cu and Ta atoms allowing proper mixing of the powders and formation of a homogeneous Cu-Ta solid solution which otherwise is immiscible in each other. The ball-milled powders are consolidated in a Nickel 201 canister and subjected to Equal Channel Angular Extrusion process in an Argon environment of temperature 700℃ with an extrusion angle of 90° as shown in Fig 1. This is repeated 4 times with each time the solid bar being rotated by 90° resulting in a total strain of 450% in the sample. For more details on the manufacturing process, the reader should refer to [11].

3.2 Irradiations

The proton irradiation was performed at the Michigan Ion Beam Laboratory at the University of Michigan, Ann Arbor. The irradiation condition has been summarized in Table 3.1.

3.2.1 Sample preparation for irradiation experiment

From the sample provided by ARL, a sample of size 2 mm × 21 mm × 2 mm was used for proton irradiation by electrical discharge machining and the rest was saved for analyzing the as-received microstructure. This sample is first mechanically polished using SiC polishing pads starting from 240 grit to 4000 grit. This sample was then electropolished using 10% perchloric acid + 90% methanol solution kept between -30°C -40°C for 20 secs. During the electropolishing the sample is made anode and there is a platinum mesh which is made cathode. A potential difference of 35V is applied between the anode and cathode to assist in electropolishing. The polishing is complete once a mirror finished sample is obtained.

3.2.2 Proton Irradiation

The irradiation experiment was carried out on the 1.7 MV General Ionex Tandetron accelerator at the Michigan Ion Beam Laboratory (MIBL), Ann Arbor, MI by Dr. Matthew Swenson in 2013. The sample is mounted on the typical sample stage shown in Fig. 3.2. The empty space around the sample is filled with Indium liquid for efficient heat application throughout. This assembly is secured using a hold down plate, which holds the sample in place as well as prevents any leakage of the Indium liquid. The temperature is monitored using thermocouples which are spot welded onto the sample.

The assembly stage was inserted at the end of the beamline chamber (Fig. 3.3), and the chamber is electrically isolated from the accelerator beamline for accurate collection of charge from the

irradiation. The chamber is pumped to maintain a vacuum pressure of 1.3×10^{-5} Pa. Rectangular shaped Ta aperture plates are used such that the irradiation area covers the sample as well as the guide bars on each side (Fig. 3.4).

The sample was then irradiated with 2 MeV protons at 500℃. The temperature is maintained by a combination of resistance heating and air cooling. The proton beam was raster scanned at a frequency of 2061 Hz in the vertical direction and 255 Hz in the horizontal direction on the sample. Post irradiation, the charge collected was found to be 0.13 μC. The next section details the process of determining the damage profile due to the irradiation.

3.2.3 SRIM calculations

The damage profile due to proton irradiation can be calculated using Stopping Range for Ions in Matter (SRIM) 2013 program. SRIM uses the Monte-Carlo method to estimate the interaction of energetic particles in matter. For the SRIM simulation, the damage calculations are done in Quick Kinchin-Pease Mode as it has been shown to predict the damage profile than the Full cascade calculation mode more accurately. A layer of 25 μm composing of Cu 90at% and Ta 10at% with a calculated atomic density of 9.7 g/cm^3. The displacement energies for Cu and Ta are chosen to be 23 eV and 32 eV based on ASTM Handbook. The simulation is run for 1,000,000 ions to get a smooth damage profile. Post simulation, a vacancy.txt is obtained, which consists of a depth profile for vacancies created by the direct impact of ions and secondary vacancies created by displaced atoms. Both vacancies are added to obtain the total vacancies generated during the simulation, which is R_d. The charge collected during the irradiation experiment can be used to calculate the damage profile. Every μC equates to 1 count for the irradiation experiment, i.e., 10^6 counts/C

$$\frac{counts}{dpa} = \frac{NqA\left(\frac{counts}{C}\right)}{R_d} \quad \text{(Eq. 3.1)}$$

Where N is the atomic number density, q is the charge per incident ion, in this case, it is 1.6×10^{-19} C/p$^+$ for protons, A is the area of the aperture used for irradiation (1 cm^2), and R_d is obtained from the SRIM simulation. Fig. 3.5 shows the calculated irradiation damage profile. The peak damage is at 22 µm, and our target dose of 1 dpa is between 12 µm to 15 µm. We avoid analyzing our sample at the surface as the surface is a big sink to irradiation-induced defects as well as at the peak damage area as there is a lot of ion implantation and heat deposited in this region during the irradiation.

3.3 Polishing

3.3.1 As-received sample

The sample piece sawed off before the irradiation process is used for analyzing the as-received microstructure and mechanical properties. The sample is mechanically polished using SiC polishing paper starting from 240 grit till 2000 grit. This sample is further polished using 3 µm and 1 µm diamond slurry to obtain a mirror finish. This sample is used for sample preparation for TEM lamellas, APT needles, and TEM in situ mechanical testing.

3.3.2 Proton irradiated sample

Post irradiation, the irradiated surface of the sample is untouched. For the preparation of lifting out APT needles from the depth of the sample rather than from the surface and milling till 12 µm which would result in deposition of Ga in large quantities, a side adjacent to the irradiated surface is polished. A dummy piece of the same alloy is pasted right beside the proton irradiated sample to avoid curving of the edge adjacent to the irradiated sample, and a proper flat edge can be retained.

This sample is then mechanically polished similarly to the as-received sample by using SiC polishing pads from 240 grit till 2000 grit and then polishing using diamond slurry. Fig. 3.6 represents a schematic of the polished surfaces on both the samples.

3.4 Focused Ion Beam (FIB) sample preparation

The sample preparation for TEM and APT samples was done on the FEI (Now ThermoFischer Scientific) Quanta 3D FEG located at either Center for Advanced Energy Studies (CAES), Idaho or at Purdue University, West Lafayette, IN. The sample preparation steps for TEM lamella preparation, APT needles and TEM in situ mechanical testing samples has been outlined ahead.

3.4.1 Transmission Electron Microscope (TEM) lamella

The lamellas are prepared using the procedure outlined by [126], where the lamellas are lifted out from the surface of the sample. First a platinum layer is deposited on to the target surface to preserve the surface. Then trench cuts of size 18 µm × 1.5Z µm× Z µm are made. Cleaning cross-sections are used to clean away the debris/redeposition near the lamella site and the lamella is then lifted out using Oxford Instrument's Omniprobe manipulator. The lifted-out lamella is welded onto a TEM Molybdenum (Mo) half grid rather than a Cu half grid as our alloy is also composed of Cu and would result in wrong statistics while doing any composition analysis. The lamella is mounted on one of the V shaped posts and thinned at different currents at 30 kV voltage up to a thickness of 100 nm. Further thinning is done at 5 kV voltage at 48 pA till a hole is formed in the lamella. The hole signifies that the areas around the hole are the thinnest. Following this the lamellas are cleaned at 2 kV steps to remove any Ga damage caused during the thinning process.

For microstructure characterization in the TEM, lamellas of size 18 µm × 2 µm × 10 µm for as-received sample and size 25 µm × 2 µm × 20 µm for irradiated sample are manufactured and

thinned to sub 100 nm thickness. The depth of the proton irradiated sample is significantly more than a normal TEM lamella size to be able to analyze the lamella along the damage profile as shown in Fig. 3.7.

3.4.2 Atom Probe Tomography (APT) needles

These samples were exclusively prepared on the FEI Quanta 3D FEG FIB at CAES, ID as the prepared APT needles need to be immediately moved to the Cameca Local Electrode Atom Probe (LEAP) 4000XR at CAES, ID to avoid oxidation of the needles. The lift-out process for the APT needles differs a little from the TEM lamella process as a wedge ended lamella needs to be lifted out to ease the process of welding the sample on to the APT coupon. For the as-received sample the sample wedges were lifted from the polished surface whereas for the proton irradiated sample the sample wedges were lifted-out from the side adjacent to the irradiated surface at a depth of ~12 µm at the targeted dose of 1 dpa. Sample wedges of 15 µm × 2 µm × 3 µm were prepared using rectangular cross-section milling at 30° stage tilt rather than at 52° to achieve the wedge shape as shown in Fig 8. This sample wedge is lifted out using the Omniprobe manipulator to weld tips on to the LEAP coupon. One lift-out results in around 8-10 needles. These welded tips undergo steps of annular milling to be sharpened to radius of 10-20 nm shown in Fig. 3.9. As it is a top view while milling the sample, care should be taken that your sample is still intact as well as not too make the tip too sharp.

3.4.3 TEM in situ mechanical sample

An initial prep is needed for these samples where a Cu half grid is mounted on a Cu Z-mount for the TEM in situ Hysitron (now Bruker) PI-95 holder using a silver epoxy as shown in Fig. 3.10(a). The epoxy can either be left to be cured for 6 hours or can be heat treated to use it

immediately. Like the lamella process, lamellas of size 40 µm × 3 µm × 15 µm are lifted-out. Before welding them on to the Cu grid on the Z-mount, the B post on the Cu half grid is milled to obtain a straight edge of 40 µm to make the welding of the lamella easier. Using the Omniprobe manipulator, a blind approach is used to mount the lamella on the B post as shown in Fig. 3.10(b) and is welded on the post before breaking off the Omniprobe. The lamella is secured by welding on the other side as well by rotating the stage (Fig. 3.11(a)). After this the Cu Z-mount is mounted on to a 45° pre-tilt stage to reduce the taper angle while thinning the indentation window sites. First, the lamella is kept perpendicular to the FIB ion beam to create 2-3 µm indentation window sites (Fig. 3.11(b)). After this the lamella is made parallel and thinned to a thickness of 150 nm. Around 7 to 8 window sites can be fabricated per lamella (Fig. 3.11(c)). Target thickness is set to 150 nm to find a balance between easily aligning the indenter tip with the window and being able to obtain a reliable diffraction pattern from the window site for crystal orientation mapping.

3.5 Microstructure characterization

This section outlines the various techniques used to characterize the microstructure of the material using various Transmission Electron Microscopy (TEM) and APT techniques.

3.5.1 Transmission Electron Microscopy (TEM)

For microstructure characterization, we used the FEI Tecnai TF30 STwin STEM TEM at CAES, ID. The TEM was used to characterize Cu grains, Ta phases, and irradiation induced defects. The techniques used for microstructure characterization have been outlined ahead.

Bright Field TEM mode

Bright Field imaging is the most basic type of imaging using the TEM where the objective aperture is used to selectively image the sample using just the transmitted bright beam. Even though the whole lamella is available for imaging the proton irradiated sample, analysis is performed between 12 µm to 15 µm as it corresponds to a dose of ~1 dpa. Basic imaging to compare the as-received microstructure to the proton irradiated microstructure is done in BFTEM and images are collected using Digital Micrograph later to be analyzed in ImageJ software.

BFTEM was used to image Cu grains at a magnification of 60kx and more. The size of the Cu grains was measured using the line intercept method. To do this, we first marked the Cu grains in the micrograph and drew lines of known length and measured the number of grain boundaries the line intercepted with. While doing so, if the line intercepted across a Ta phase then that much length of the line was subtracted from the original length. Based on this, the size of the Cu grain can be calculated using Eq. 3.2.

$$Size\ of\ Cu\ grain\ (nm) = \frac{Length\ of\ the\ line}{Number\ of\ intercepts} \qquad \text{(Eq. 3.2)}$$

Irradiation is known to induce defects such as stacking fault tetrehedra, dislocation loops and voids/cavities. These features can be imaged by aligning Cu grain or Ta phase to a low zone axis such as [001], [011] or [111] such that only one Bragg diffraction condition is only fulfilled for one reciprocal lattice resulting in max contrast for defects and dislocations. Due to the invisibility criteria where the dislocation/defect might not be seen due to weak contrast conditions, imaging should be performed on the same grain by aligning to different low zone axis. Due to the high contrast between Ta phase and Cu grain, where the Ta phase is extremely dark making it difficult to analyze any defects formed in it, defect imaging was done only for Cu grain. Due to the nanocrystallinity of the material, there is a lot of grain overlap even after thinning it to thickness

less than 100 nm, resulting in poor image conditions as well as tilting the sample results in moving of the sample resulting in losing track of the targeted Cu grain. Hence, we will be using a technique using Scanning TEM mode to overcome these practical challenges and image defects in this material which has been outlined in the next section.

Scanning TEM mode

Irradiation induced defects were imaged using STEM mode on the TEM at CAES following the procedure entailed in [127]. Before using the STEM mode, a Cu grain close to a distinct Ta phase is identified and tilted to [011] zone axis in BFTEM mode. This is done with the help of Kikuchi diffraction pattern formed in diffraction mode on the TEM. Before switching to STEM mode, the smallest condenser aperture is inserted to reduce the collection angle of the incident electron beam on the sample for better imaging conditions. After switching to STEM mode, the camera length is maximized to 4.5 m to minimize the convergence angle, such that the bright beam covers the High Angle Annular Dark Field (HAADF) detector entirely making it 'Bright-field' STEM imaging. This results in decrease in thickness contrast and results in much cleaner images for defect imaging. As both the as-received and the proton irradiated samples showed similar defects, chemical composition analysis for the defects needed to be done to identify if these defects were actually defects or Ta nanoclusters using Energy Filtered TEM mode which is described in the next section.

Elemental identification & Thickness Measurement

Electron Energy Loss Spectroscopy (EELS) can be used for elemental identification and thickness measurement as it records the energy lost by an electron after interacting with the sample. This analysis generates a spectrum of energies of electrons as shown in Fig. 3.12. As can be seen

there is a peak at 0 eV energy which signifies that these electrons have lost no energy and have essentially passed through the sample (basically BFTEM).

Energy Filtered TEM (EFTEM) mode is an extension of EELS and is generally used to form an image based on a kinetic energy of an electron usually intended to aid in chemical analysis when locating a particular element. Using EFTEM mode imaging can be done to create a region of interest in the EELS to perform imaging based on electrons which have lost a certain amount of energy, in our case it would be for Ta – L edge ~ 11 keV. A zero-loss image and the corresponding Ta – L edge image is taken to characterize the Ta atoms.

EELS has also been used for measuring the thickness of the lamella at several points to help in determining the volume and the number density of defects and phases. To do this the Digital Micrograph software integrates the counts in the graph shown in Fig. 3.12 with the help of other parameters such as condenser aperture which was 100 nm, objective aperture which was 50 nm and the average atomic number of the sample which was 33 and calculated using the Eq. 3.3.

$$Z_{avg} = 0.9(Z_{Cu}) + 0.1(Z_{Ta}) \quad \text{(Eq. 3.3)}$$

Where Z_{avg}, Z_{Cu}, and Z_{Ta} are the average atomic number of the sample, atomic number of Cu and atomic number of Ta, respectively.

3.5.2 APT analysis

Due to the resolution limits of the TEM to confidently characterize the size and of nanoclusters smaller than the size of 5 nm, we used Atom Probe Tomography to characterize the Ta nanoclusters. Also, completely characterize nanoclusters i.e., obtain number density, cluster size, and composition a combination of different techniques between STEM, EELS and EFTEM would have to be used. Whereas APT analysis allows us to characterize and represent the spatial distribution of nanoclusters all in one place.

The APT experiments were performed on the CAMECA Local Electrode Atom Probe 4000X-HR and the tip reconstruction and cluster analysis were performed on Integrated Visualization and Analysis Software (IVAS) 3.8.4 at CAES, Idaho Falls. The following section outlines the APT experiments followed by tip reconstruction and cluster analysis in IVAS.

LEAP Experiment

Multiple needles were fabricated for each sample to be experimented on in the LEAP. The LEAP uses a high frequency voltage or a pulsed laser to ionize and evaporate the atoms off the surface of the needles. Once the atoms are evaporated, they are picked up by a X-Y detector which records the position of the atoms and the order of evaporation of the ions determine the Z position of the atoms shown in Fig. 3.13. This process is repeated to record millions of evaporated atoms until the tip fractures and is stored in a .RHIT file. The file stores the atom coordinates, time of flight of each ion, and uses the time-of-flight data to perform spectroscopy for elemental identification using mass to charge ratio of the incident ions.

The LEAP experiment can be performed either in voltage mode or laser pulsed mode which depends on the material being analyzed. The voltage mode imparts a lot of stress on the needle if the sample comprises of a lot of interfaces (precipitates, grain boundaries, non-magnetic elements) i.e. where the laser pulse mode helps out as it applies less amount of stress due to the pulse nature of the laser. Due to the nanocrystallinity and high volume of interface boundaries in the Cu-Ta alloy, we used laser pulse mode to perform the experiment. To find the optimum conditions for performing atom probe tomography, multiple tips were subjected to energies between 50 pJ to 140 pJ. If the energy were too low, the tip would fracture very soon resulting in a very low count and if the energy were too high, the atoms would get evaporated too fast resulting in loss of information as it would result in a homogeneous solid solution. The optimum laser energy was found to be at

100 pJ with the pulse repetition rate at 200 kHz as the clusters can be clearly seen in the reconstruction as shown in Fig. 3.14.

Tip reconstruction

After the experiment in the LEAP 4000X HR, the generated .RHIT file is exported to an external computer on which the tip reconstruction and further analysis is performed using IVAS 3.8.4.

Once the file is opened, information about the experiment for the tip can be seen. Past this window, the reconstruction of the tip starts. First, the atoms which are to be used for reconstruction are determined. This is determined from a profile of where the hits on the detector have taken place as seen in Fig. 4.15. A region of interest is chosen from this detector histogram, based on which a voltage history of LEAP ion evaporation is plotted against sequence of the ions evaporated shown in Fig. 3.16(a,b). To select the appropriate ions for reconstruction from the voltage history, the region at the start of the profile should be avoided as the LEAP operator is optimizing the parameters of the experiment at the start and also any atoms recorded after a discontinuity in the voltage profile should also be avoided as this generally signifies fracture of the tip as shown in Fig. 3.16(b). The atoms used for reconstruction should be maximized for more volume and better statistics for tip reconstruction and analysis.

After the atoms for reconstruction are determined, a time-of-flight corrections are performed by the software to generate the mass to charge histogram for spectroscopy. After the histogram is generated the elements need to be identified for correcting the zero error in the histogram. Here, some knowledge about the composition of the alloy is valuable. Because Cu-Ta alloy is a binary alloy, the peaks were relatively simple to identify as shown in Fig. 3.17. Other peaks which were observed were of Ga, Pt and Si, which appear due to Ga deposition during

milling and partial ionization of the Pt weld and Si tip post during the LEAP experiment. The software gives a visual representation of the peaks which would be observed for that element in different charge states. For Cu, the most charge state identified is Cu^{+} hence a peak can be seen at 63 eV (63/1) though multiple Cu peaks are observed due to the different isotopes present. Ta peaks for Ta^{3+} were also identified. After the peak corrections, a full mass spectrum is calibrated and generated. The peaks can be ranged in two ways, one between the Full Width Half Maximum (FWHM) or at Full width as shown in Fig. 3.18. To maximize the counts, all peaks were ranged at full width for the analysis.

Next step is to define the shape of the tip, which is dependent on three factors, a) Image Compression Factor (ICF), b) the k-factor (*k*) and c) the evaporation field (*F*). The ICF is based on the voltage profile of the evaporation and is the compression of the trajectory of the ions travelling towards the detector. The default value for ICF is at 1.65 and is for a collection voltage of 2.8 kV. Prosa et. al. [128] has shown that the ICF value can be determined based on the ICF vs Collection Voltage graph generated by the software. The collection voltage changes throughout the experiment as the tip radius keeps changing, so an ideal sample would be cylinder shaped in which the radius would stay constant throughout. As fabricating a cylinder is difficult and depends on the material and operator, ICF value should either be chosen from the constant voltage dataset or just chose the ICF value for the midpoint. This value was different for each tip as per their collection voltage profile.

The k-factor decides the reconstruction geometry of the tip and is dependent on the shape of the tip, shank angle and distance of the tip from the electrode. As all the tips were fabricated in the same way as well as consistently located at 40 µm from the electrode, the value of k-factor decided by the software at 3.30 was constant for all the tips.

Lastly, the evaporation field parameter is decided which is dependent on the material being analyzed. As our material majorly consists of Cu, evaporation field value for Cu (30 V/nm) was chosen. As there is a difference in the evaporation fields of Cu and Ta (44 V/nm), where Cu gets more easily evaporated as compared to Ta, this leads to trajectorial and local magnification problems during reconstructions [129–133] due to which even after optimizing the three parameters, loss in spherical curvature of Ta nanoclusters is experienced which has been outlined in [134].

After optimizing these three parameters, the tip is ready for reconstruction and can be reconstructed in voltage mode, shank mode or tip profile mode

As the tip radius (R_0) can be related to the collection voltage by the following formula [135]:

$$R_0 = \frac{V}{kF} \qquad \text{(Eq. 3.4)}$$

Where, k is the k-factor (3.30), F is the evaporation field for Cu (30 V/nm) and V is the collection voltage. Therefore, for all three modes the initial tip radius is calculated based on the voltage profile.

In the Voltage mode, the whole tip is constructed in this particular manner, resulting in evolution of the tip radius which is directly proportional to the voltage profile. This mode is the easiest and most straightforward way to use if there are no discontinuities in the voltage profile as they would also be reflected in the reconstruction. In such cases where discontinuities prevail, shank mode or tip profile mode are to be used for reconstruction.

In the shank mode, the shank angle needs to be defined which is the angle between the vertical axis of the tip and the slope of the tip. Therefore, the tip radius starts with the initial tip radius based on the voltage profile and then grows linearly based on the shank angle. This

eliminates the influence of discontinuities in the voltage profile on the geometry of the reconstruction.

In the tip profile mode, we must manually define the change in tip radius. This can be done by taking measurements of the tip radius at several depths as per the image taken in the FIB before the LEAP experiment. Based on our manual input the tip is reconstructed. This mode is particularly useful for large data sets so that the tip radius evolution is consistent with the original APT needle. As the experiment parameters were optimized and the data sets consisted of less than 20 million ions, the voltage profile was continuous allowing the reconstruction to be done in voltage mode for the tips.

Finally, after dialing in all the parameters, a preview of the reconstruction is prepared. This reconstruction is saved, after which the final mass spectrum is generated. The operator now can range all peaks and proceed with composition and cluster analysis on the Ta nanoclusters. The following section explains the cluster analysis on Ta nanoclusters.

Cluster analysis

IVAS allows to perform cluster analysis using inbuilt functions which are based on the maximum separation of solutes method [136]. After ranging of all the appropriate Cu and Ta peaks in the mass spectrum, the cluster analysis for Ta nanoclusters can be started. For the maximum separation method, a few parameters need to be determined such as:

- d_{max} – Maximum distance between two solute atoms for them to be considered as a cluster.
- N_{min} – Minimum number of atoms in a cluster for the group of clustered atoms to be considered as a cluster.

- L – Maximum distance of non-solute atoms surrounding the confirmed clustered atoms for them to be considered as part of the cluster.
- $d_{erosion}$ – Erosion distance for maximum distance of atoms near the matrix interface to be removed.
- Order – Number of ions within d_{max} distance for the ion to be considered as a part of a cluster.

The maximum separation method is highly sensitive to the values of d_{max} and N_{min} and should be carefully determined using an iterative method. For each tip we first estimate the d_{max} value by using the "Nearest Neighbor Distribution" function, which calculates the number of atoms which are at a certain distance from each other and generates a histogram. The function requires two parameters, d_{pair} (1.0 - 1.2 nm) which is the maximum limit of the distance between solute atoms from each other and sampling interval (0.05 – 0.10 nm). The sampling interval is varied for better resolution or faster calculation. The Nearest Neighbor Distribution performs two calculations, first it calculates number of events when two solute atoms are within the d_{pair} distance and second is for how the histogram would look like if the solute atoms were randomly distributed through the tip as shown in Fig. 3.19. Therefore, if there is any amount of solute segregation, the histogram for the sample and for the random distribution will be different. A good guess for the initial value of d_{max} is the crossover point between the random distribution histogram and the sample distribution histogram.

Next step is to use the "Cluster size distribution analysis" function which is used to estimate the value of N_{min}. The initial value of d_{max} is used as well as Order (2 ions) for this calculation. Like the Nearest Neighbor Distribution function, the cluster size distribution analysis also calculates cluster size for the solute distribution in the sample and for random distribution of the

solute. In this case, we iterate the d_{max} value such that the randomized distribution histogram and the solute distribution in the sample histograms match as shown in Fig. 3.20. This ensures that random cluster formations due to random distribution are completely filtered out. Therefore, the point at which the histogram first crosses the x-axis is taken to be as a good estimate for N_{min} as shown in Fig. 3.20.

Next step is to use the iterated N_{min} value to finalize the d_{max} value using the "Cluster count distribution analysis" function. The function inputs are d_{pair} (~ 1.0 nm), sampling interval, order (2 ions) and the N_{min} value. Again, two separate histograms are generated by the function, one is for the random distribution and one is for the solute distribution in our sample as shown in Fig. 3.21. A good d_{max} value to choose based on this process is where the black line in the histogram experiences a maximum and the red line experiences a minimum shown in Fig. 3.21.

After successfully determining d_{max} at 0.95 nm and N_{min} at 20 ions the "Cluster analysis" can be performed. All the parameters such as d_{max} (0.95 nm), N_{min} (20 ions), Order (2 ions), L (0.5 nm) and $d_{erosion}$ (0.5 nm) are inputted into this function and the software calculates and indexes all the different clusters present in the dataset. A .csv file can be exported, which contains the composition and spatial data about the cluster. The radius of gyration (R_g) of the cluster can be calculated from the radius of gyration information in x,y and z direction provided in the output file using the following formula in [137]:

$$R_g = \sqrt{R_{gx}^2 + R_{gy}^2 + R_{gz}^2} \quad \text{(Eq. 3.5)}$$

The radius of gyration can then be used to calculate the Guinier diameter (D_g) as given in [138]:

$$D_G = 2\sqrt{\frac{5}{3}}R_g \quad \text{(Eq. 3.6)}$$

After determining their size, the average size of Ta nanoclusters can be found for $D_g < 20$ nm and the number density (N_{nc}) can be calculated using the following formula:

$$N_{nc} = \frac{N_C}{V_T} \quad \text{(Eq. 3.7)}$$

Where, N_c is the number of clusters with a composition of > 60at% Ta and D_g < 20 nm and V_T is the volume of the analyzed tip dataset. The cluster analysis also yields a .pos file with only the indexed clusters which can be used for visualizing the nanoclusters and performing spatial distribution of ions in the nanoclusters. Analyzing the spatial distribution of solutes in the nanoclusters has been outlined in the next section.

Spatial distribution analysis

After the cluster analysis, the .pos file for indexed cluster can be opened separately in IVAS and the corresponding range file is associated with it. This allows visual representation of the clusters alone in the dataset as the matrix is completely removed. Next step is to define the clusters, such that we can easily analyze individual clusters in the data set. This is where we use the "Create Isosurfaces" function in the 3d grid to create interfaces which can be easily analyzed as shown in Fig. 3.22. After selecting the solute ions for which the isosurfaces need to be created, the isosurfaces are created based on the concentration percentage. A concentration percentage adjustable bar helps in creating the isosurfaces. Based on the cluster analysis, the number of interfaces created should match the number of clusters obtained from cluster analysis by maximum separation method.

Creation of the interfaces allows us to individually analyze the nanoclusters. Different nanoclusters are identified to create a .pos file for that cluster on which the distribution of solute ions is analyzed using the ROI feature in IVAS. The ROI can be made in three different geometry. For this analysis, the cylinder geometry was used and after creating the ROI, the "1D concentration

profile" can be created for the cylinder along its z-axis. A .csv file is generated containing the at% of each ion in the nanocluster along the z-axis.

3.6 TEM *in situ* mechanical testing

This experiment was performed on the FEI Tecnai TF30 STwin STEM at CAES with the Bruker/Hysitron PI-95 picoindenter with the diamond Berkovich tip. Before loading the sample into the TEM, coarse alignment of the indenter tip with the tip is done. Fine adjustments are done using the indenter software once the holder has been inserted into the TEM. The indenter is operated in displacement-controlled mode.

For normal indents, the indentation depth is kept 600 nm with a loading rate of 1 nm/s followed by a hold period of 10 secs and unloading time of 30 secs. Whereas for the intermitted crystal orientation mapping indents the loading rate is kept at 1 nm/s and the depths increase per indent but the hold period and unloading time is kept the same. The loading rate is kept at such a low value to be able to observe and record any load drops during the indentation. Post indentation, the software generates load vs displacement data which can be exported to Microsoft Excel for further analysis and generates a video file of the indentation which is saved without any compression to preserve the timeline of the indent.

3.7 Micro Visual Background Extractor (ViBE) Motion Algorithm

The MicroViBE motion algorithm is based on the principle of identifying primary foreground pixels (pixels associated with objects which are moving) and distinguishing them from the background picture (pixels associated with stationary objects). The MicroViBE algorithm developed by [34] works on the basis of background subtraction technique to overcome challenges faced in capturing videos in the TEM such as changing image conditions, motion of the sample

during indentation, change of focus and motion at timescales lower than the video frame rate. The traditional ViBE algorithm uses techniques such as binarization, edge detection and blob analysis which are difficult to execute due to the intricate microstructure and changing contrasts conditions in the TEM.

In the background subtraction technique, each pixel in the video frame is compared to a background reference image to determine the motion in the video, hence this method is not reliant on determining the stationary object. The algorithm works several different parameters such as R which is the threshold value for deciding the resemblance of pixels between current frame and the background frame, ϕ which is a time subsampling factor, 'N' which is the number of samples stored for each pixel in the background frame and $\#_{min}$ which is the number of close pixels needed to classify a new pixel as background. These parameters can be optimized for each sample to derive a better output.

The MicroViBE algorithm has a five-step process which has been illustrated in Fig. 3.23 [34]. In the first step, the starting frame of the video is set as the background reference frame. In the second step, the next frame is selected and binarily segmented based on the subtraction of pixels in gray scale. 0 determines a black pixel and 255 is a white pixel. This histogram is generated for both the current frame and the background frame and is then subtracted from each other and the segmented image is generated as shown in Fig. 3.23 which shows movement between the two frames. In the third step a heatmap histogram signifying the motion in the video is generated and a heatmap image on the background reference frame is created with a pixel storage size of 16 bits. Each time the pixel is detected as a moving pixel the counter is iterated for each pixel in the frame. Due to the restriction of storage space for each pixel, videos up to 36 mins with a frame rate of 30 can be analyzed. In the fourth step, the 16-bit image of the heatmap is normalized to completely

fill the per pixel quota i.e is up to a maximum value of 65536 to create a heatmap with maximum contrast to show movement of features. As these values are based on a gray scale, in the fifth step the gray scale is converted to a color scheme to generate a false heatmap where blue pixel shows least movement and red shows maximum displacement. This process is iterated again for the next frame with the previous frame as the background reference frame. Frames for each iteration are generated and then can be used for compiling a false heatmap video.

3.7.1 Installing & Running MicroViBE algorithm application

The MicroViBE application was installed on a Linux based Operating system Ubuntu 20.10. The application is installed by cloning the following git repository by executing the following bash commands:

git clone https://amburan@bitbucket.org/amburan/atomicvibe.git
git checkout master

After downloading the git repository to the local drive, another application named QTCreator and OpenCV needs to be installed. The application was found to work only with the QT 5 version. The following commands can be used to install QTCreator:

sudo apt-get install qtcreator
sudo apt-get install qt5-default
sudo apt-get install libopencv-dev

Open the master folder which was downloaded and open the file named AtomicViBe.pro in QTCreator to build the application. This will allow us to then run the MicroViBE algorithm on our videos. Once the UI is launched for the AtomicViBe, we can load our indentation video files and press play. Three output windows pop up and a real time generation of a heat map based on our input video can be seen. The application outputs still frame of the heatmap which were later combined using Adobe PremierPro to create a video file of the ViBE generated heatmap for the

indentation process. The installation files can also be downloaded from the link provided in Appendix C.

3.8 Automated Crystal Orientation Mapping (ACOM)

The ACOM analysis was performed using the NanoMEGAS ASTAR system installed on the FEI Tecnai TF30 STwin STEM at CAES, Idaho. This system was used to map and track evolution in Cu grains and Ta particles before, during and after deformation due to the TEM *in situ* pico-indentation.

3.8.1 Acquiring Maps

The NanoMEGAS ASTAR system captures Selective Area Electron Diffraction patterns using an external camera mounted on the viewing screen in place of the binoculars shown in Fig. 3.24. The TEM is operated in BFTEM mode, where first, normal beam alignments are done. For this analysis, the objective aperture is retracted, and the smallest condenser aperture is used for obtaining the diffraction patterns. A spot size of 6 with a camera length of 135 mm was used for this analysis. The system uses a proprietary software called TOPSPIN to make alignments and set up the map. The system uses Precession Electron Diffraction (PED) method where the diffraction pattern is obtained by integrating diffraction patterns over different diffraction collection conditions caused due to rotation of the tilted electron beam around the central axis of the microscope as shown in Fig. 3.25. A precession angle of 0.48° was used for collecting the diffraction patterns. The TOPSPIN software generates virtual BFTEM images which help us set up the maps. Maps of size 1 μm × 1.5 μm with a step size of 3 nm around the indentation site were made shown in Fig. 3.26. The diffraction pattern collection time for these maps were around ~45 mins. After the software finishes mapping, a .BLO file is generated which stores the integrated

diffraction patterns for each pixel in the map along with the location of the diffraction pattern on the virtual BFTEM image. These .BLO files need to be indexed for analyzing the crystal orientation of Cu grains, Ta phases and Ta nanoclusters which has been outlined in the next section.

3.8.2 Analyzing Block files

The .BLO files are exported to an external analysis computer which has a diffraction pattern indexing software. After the .BLO is opened in the software the file is indexed using diffraction pattern banks for Cu and Ta. Various image enhancement techniques can be used on the diffraction patterns to increase the confidence in the indexed diffraction patterns.

After indexing, a .RES and .ANG file is generated. The .RES file needs to be analyzed using the ASTAR proprietary software whereas the .ANG file can be used to analyze the data in EDAX OIM Analysis software. Care should be taken to correct the scale bar while analyzing the .ANG files in the OIM analysis software as it changes the units from nm to µm. During this analysis, the Cu and Ta maps can be differentiated to generate separate orientation maps for each. Also, phase maps allow to just view where the Ta is present in the system. The OIM software provides us with various data outputs such as grain size distribution, Euler angles, grain ellipticity, grain diameters, misorientation angles and grain circularity.

The Euler angles can be converted to hkl indices using the following formula in Eq. 3.8:

$$h = \sin(\varphi)\sin(\varphi_2)$$

$$k = \sin(\varphi)\cos(\varphi_2)$$

$$l = \cos(\varphi) \qquad \text{(Eq. 3.8)}$$

Where, φ and φ_2 are Euler angles which are obtained from text file generated from the OIM files. The obtained hkl indices can be used for graphing the Orientation density function.

Table 3.1: Irradiation conditions for proton irradiation of Cu-10at%Ta alloy

Irradiating Particle	Energy of Particle	Dose	Temperature	Dose Rate
Protons	2 MeV	1 dpa	500°C	1.2×10^{-5} dpa/sec

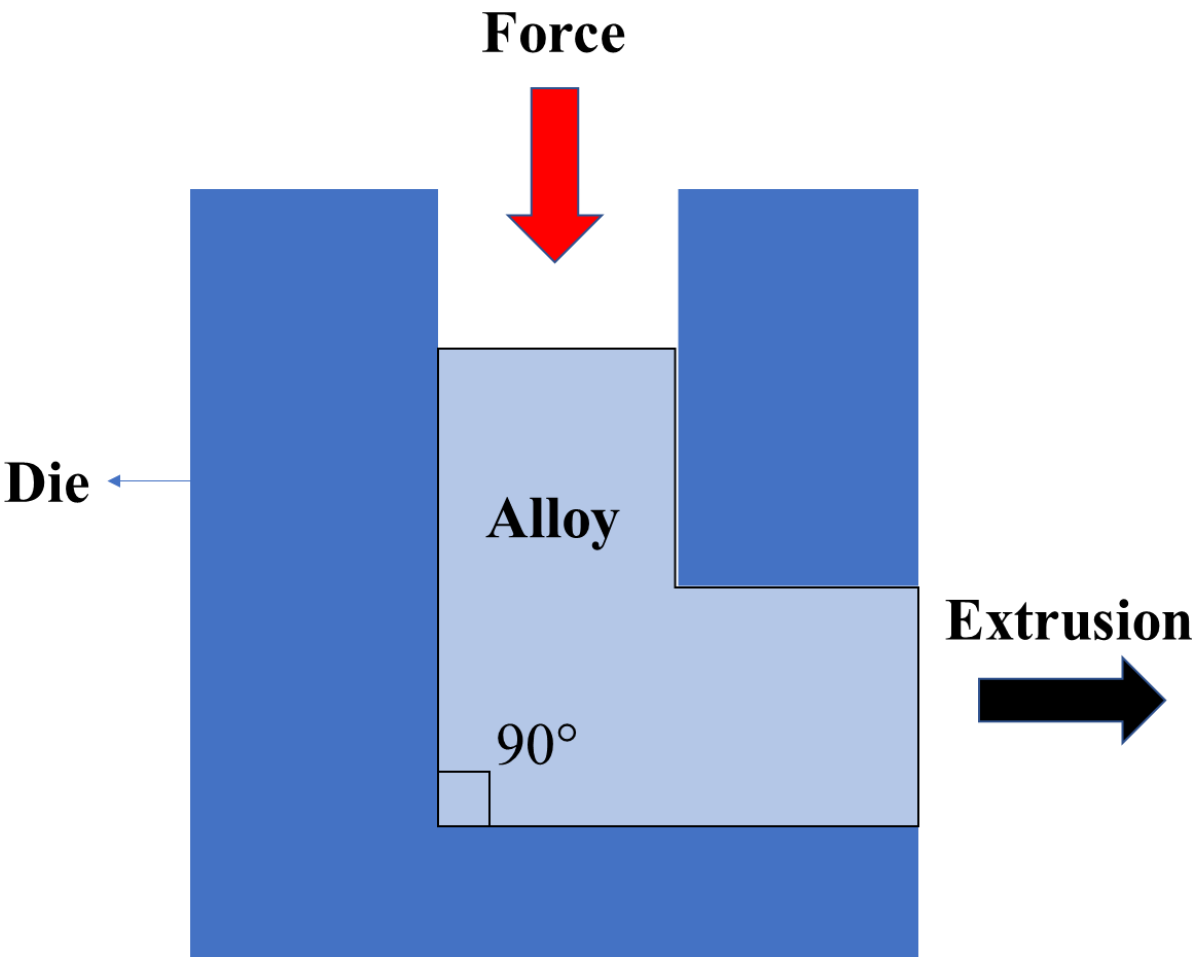

Figure 3.1: A schematic of Equal Channel Angular Extrusion performed at an extrusion angle of 90°

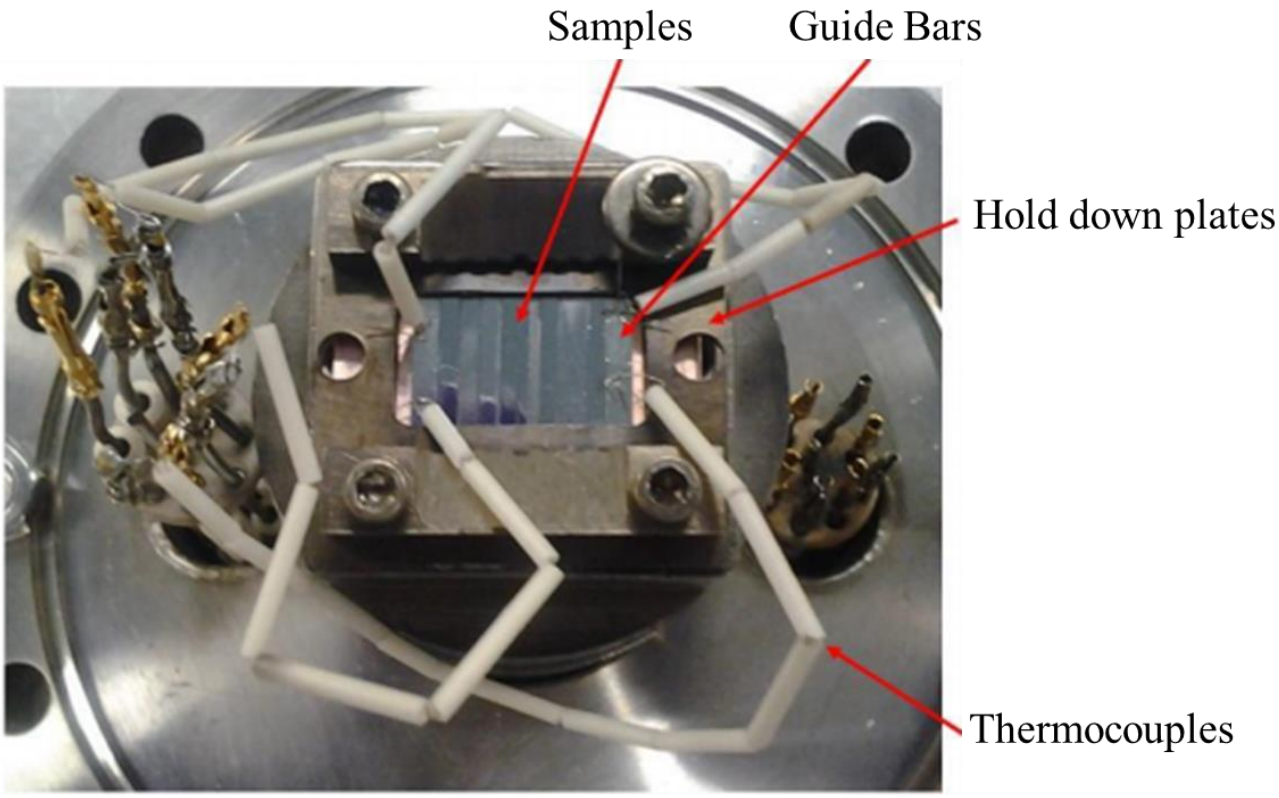

Figure 3.2: Sample stage assembly for proton irradiation at Michigan Ion Beam Laboratory [139]

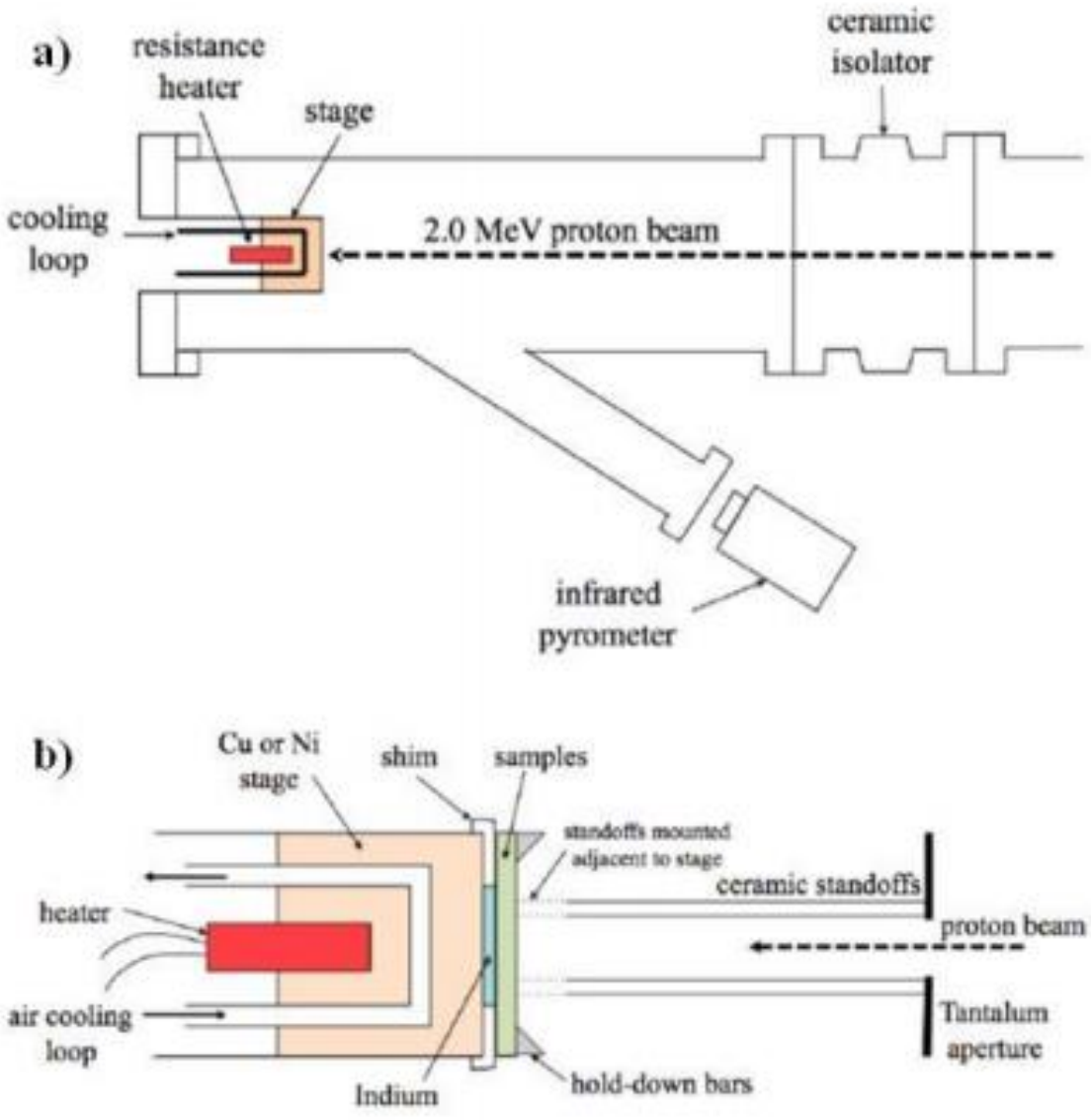

Figure 3.3: A schematic of sample stage assembly mounted at the end of the accelarator chamber as shown in [139]

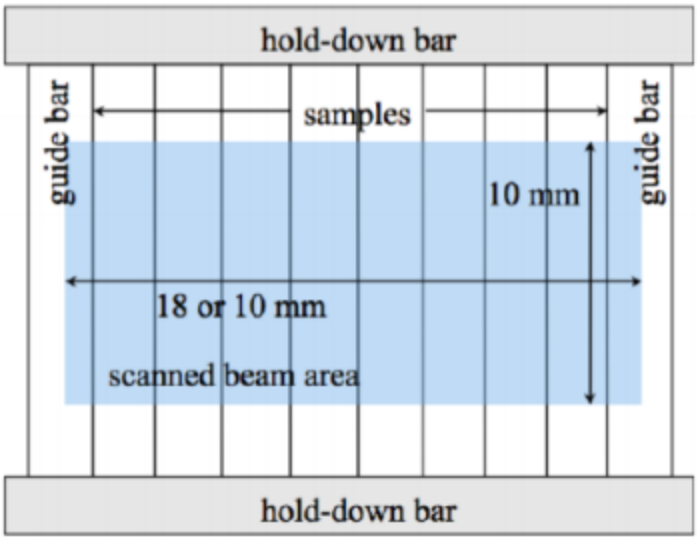

Figure 3.4: A schematic of the irradiated zone for samples due to the Ta plate apertures [139]

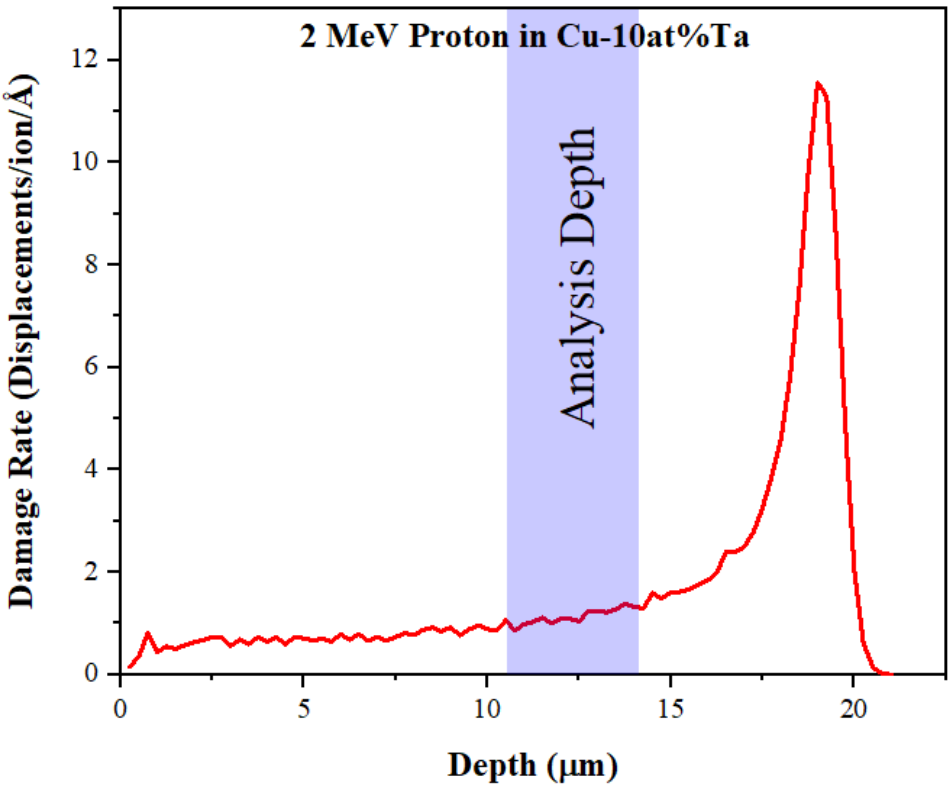

Figure 3.5: Damage profile calculated using SRIM calculations for 2 MeV proton irradiation of Cu-10at%Ta alloy [140]

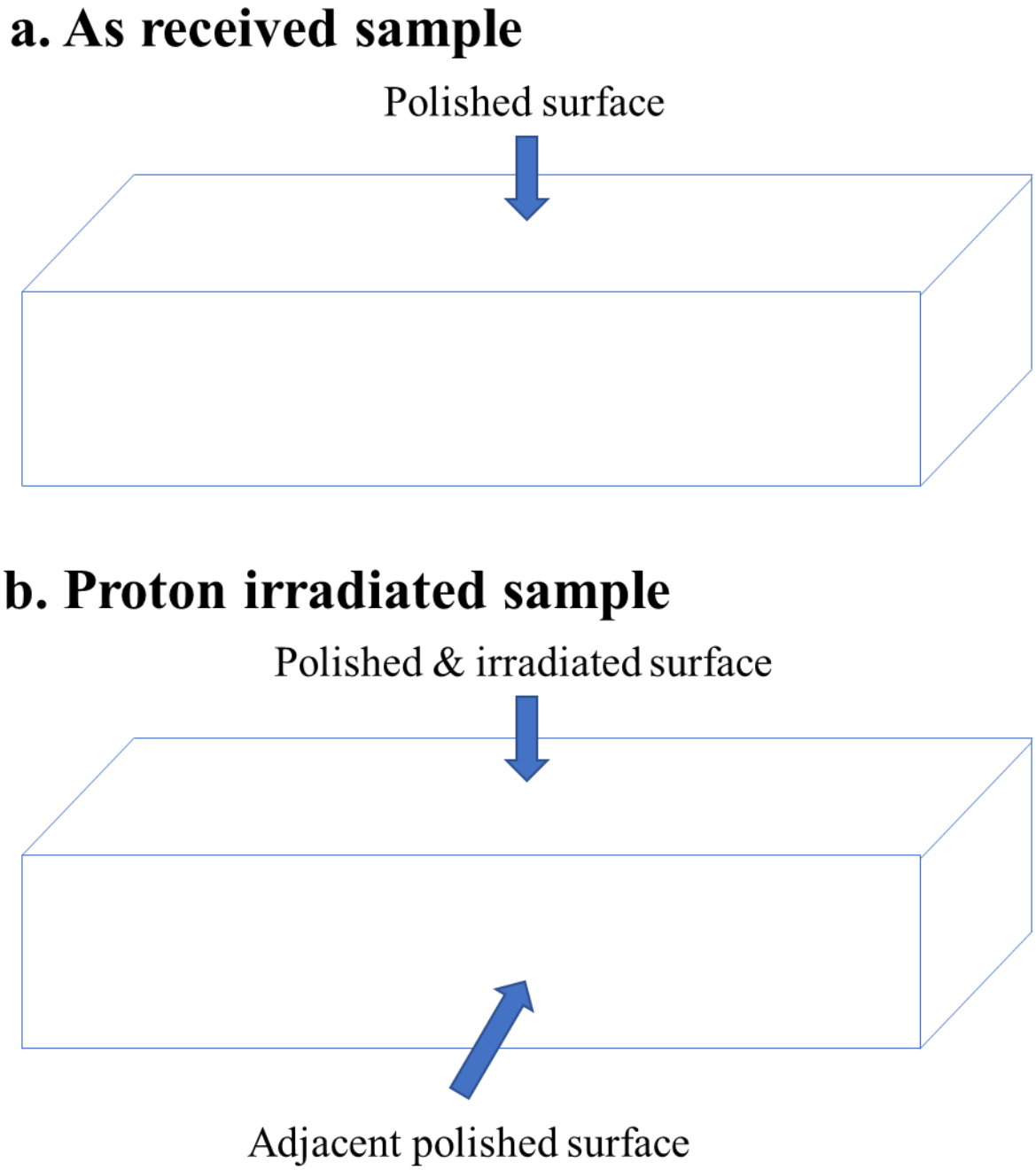

Figure 3.6: A schematic showing the polished surfaces for both the sample conditions

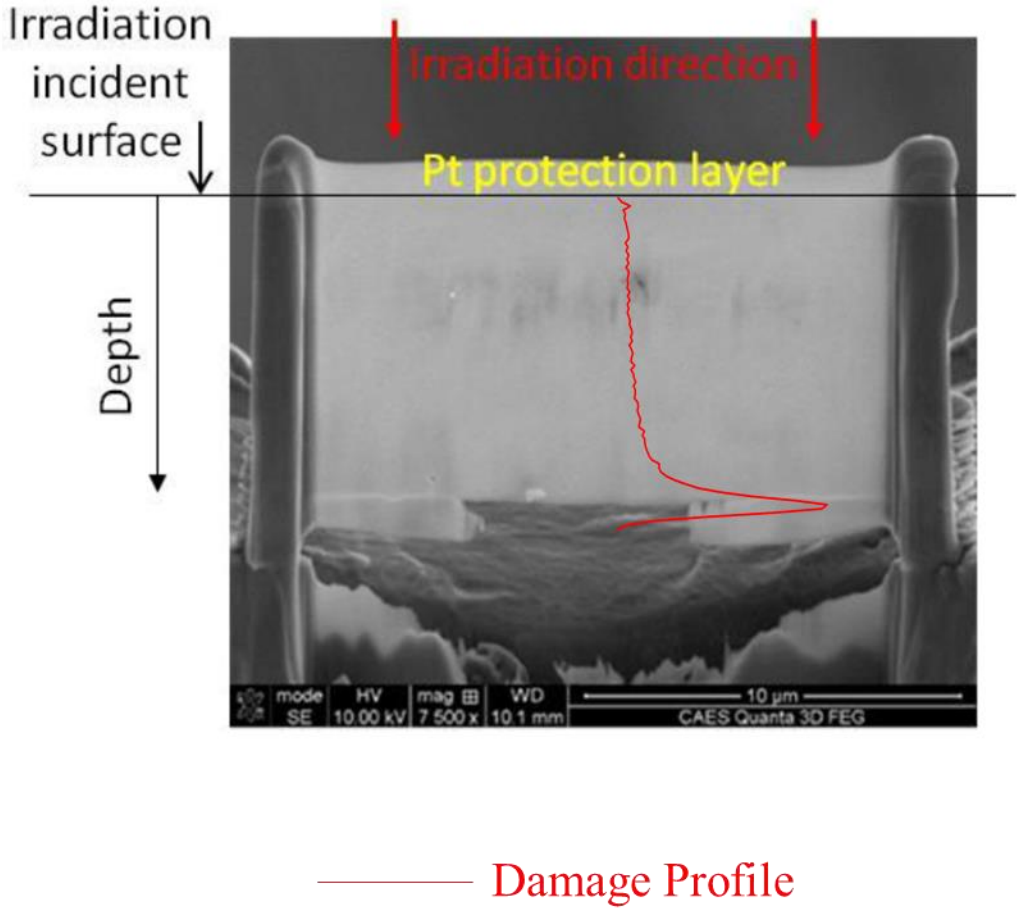

Figure 3.7: TEM lamella for the proton irradiated sample showing the irradiation damage profile

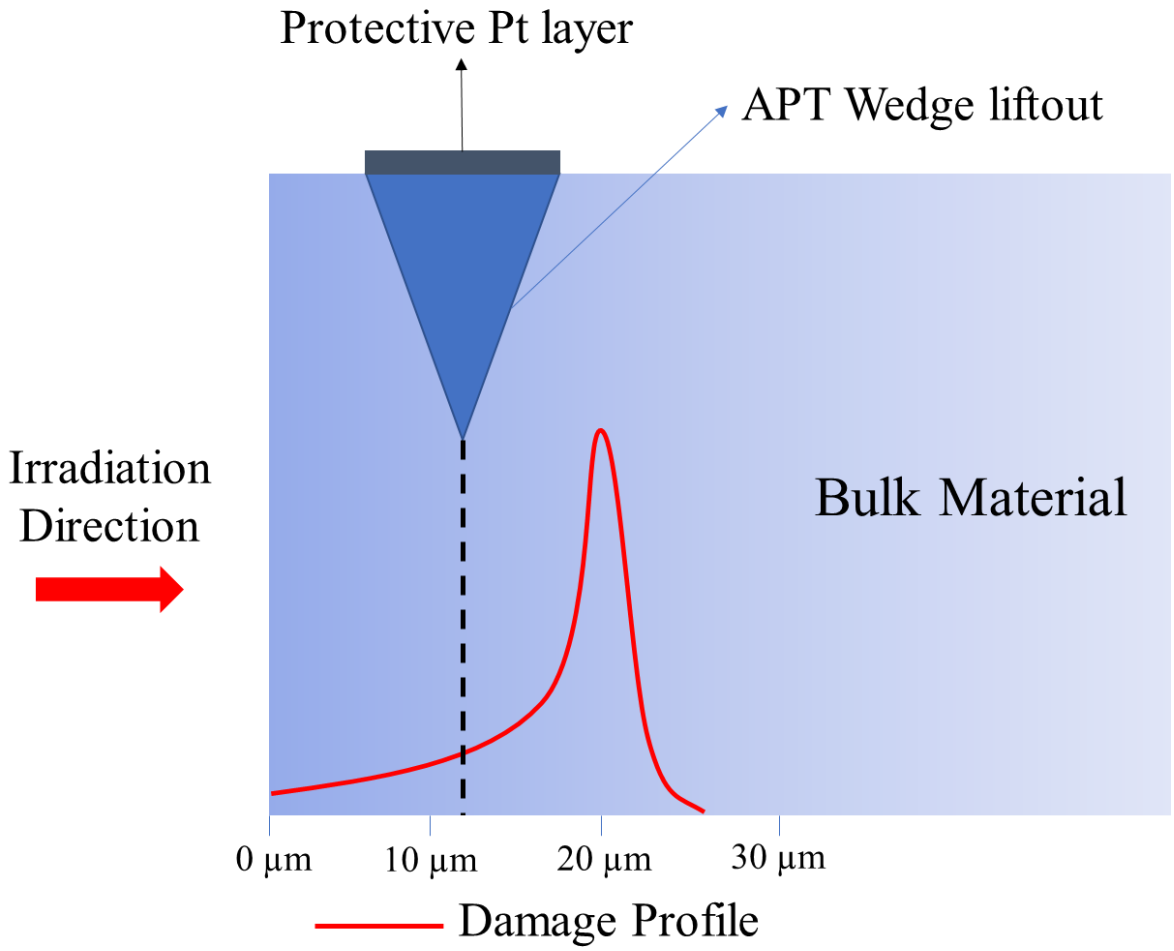

Figure 3.8: A schematic image of the wedge liftout from the depth corresponding to a damage dose of 1 dpa.

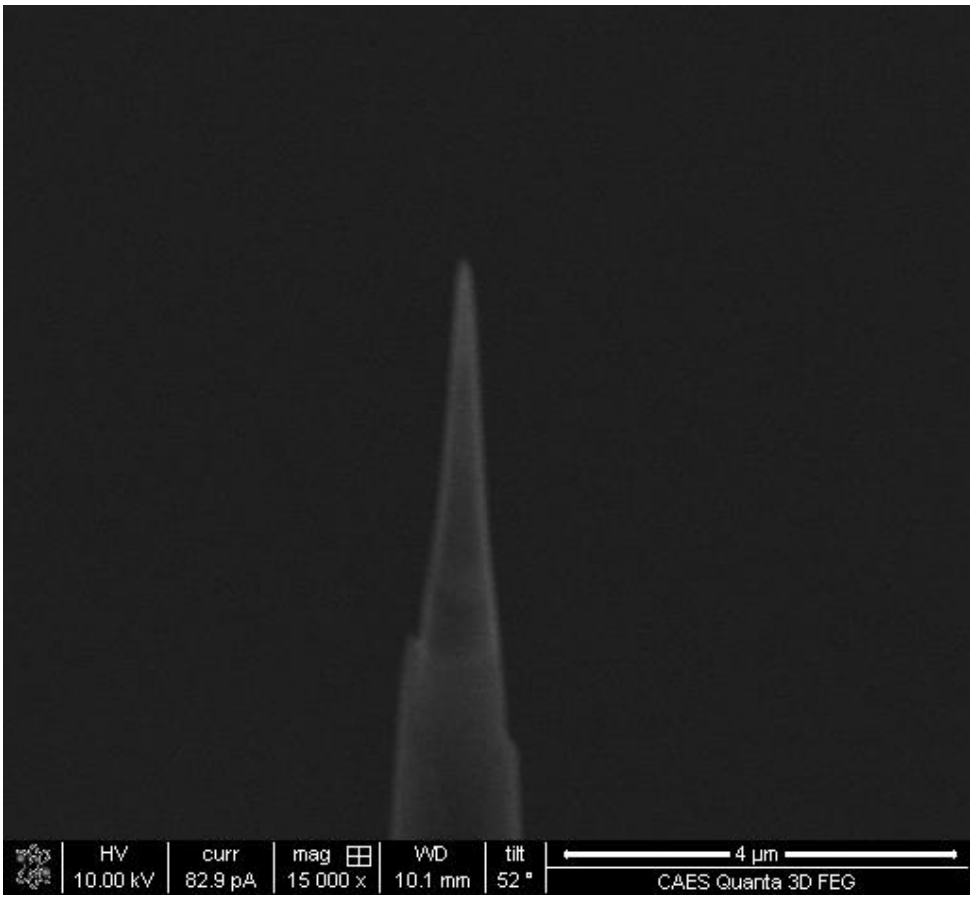

Figure 3.9: Scanning Electron Microscope image of a FIB prepared APT tip for proton irradiated Cu-10at%Ta alloy

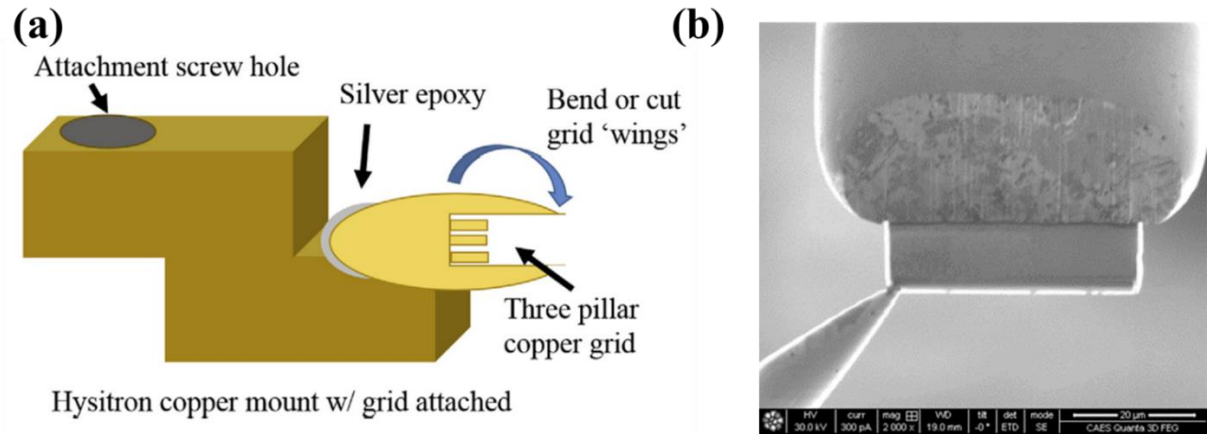

Figure 3.10: (a) A schematic of the Cu Z-mount for PI-95 holder with the mounted Cu half grid (b) Mounting of the lifted out lamella using a blind approach on to the B post of the Cu half grid

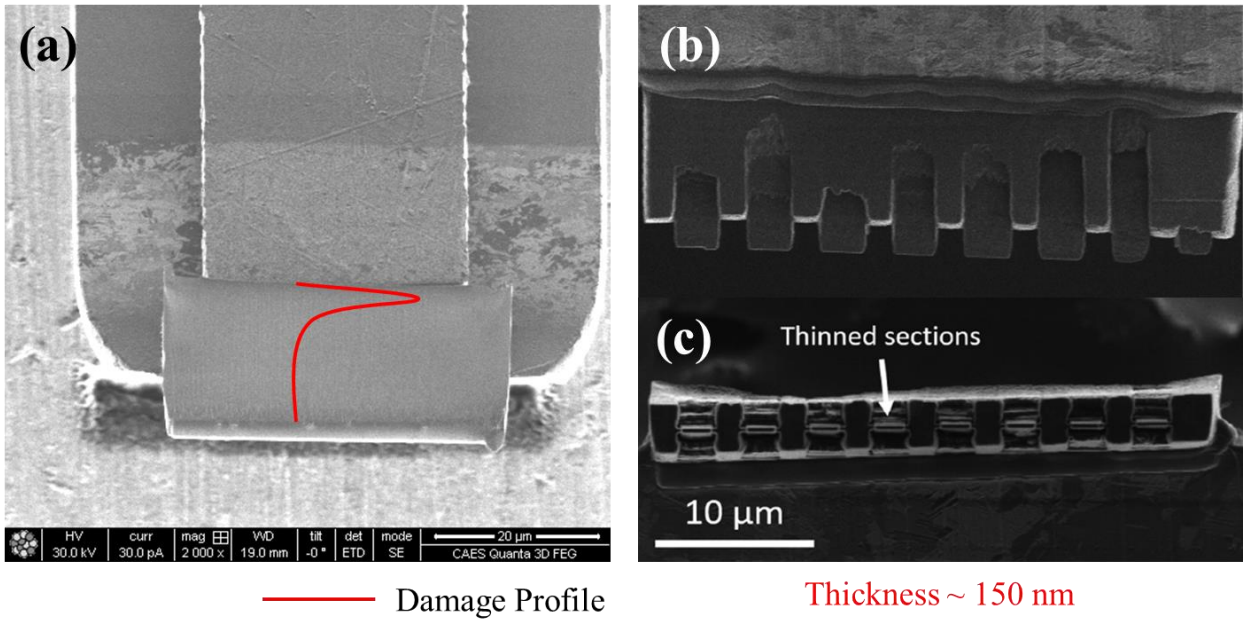

Figure 3.11: (a) Top view of the lamella after breaking off the Omniprobe needle which is secured with Pt welds. (b),(c) SEM image of the shaped and thinned pico-indentation sites.

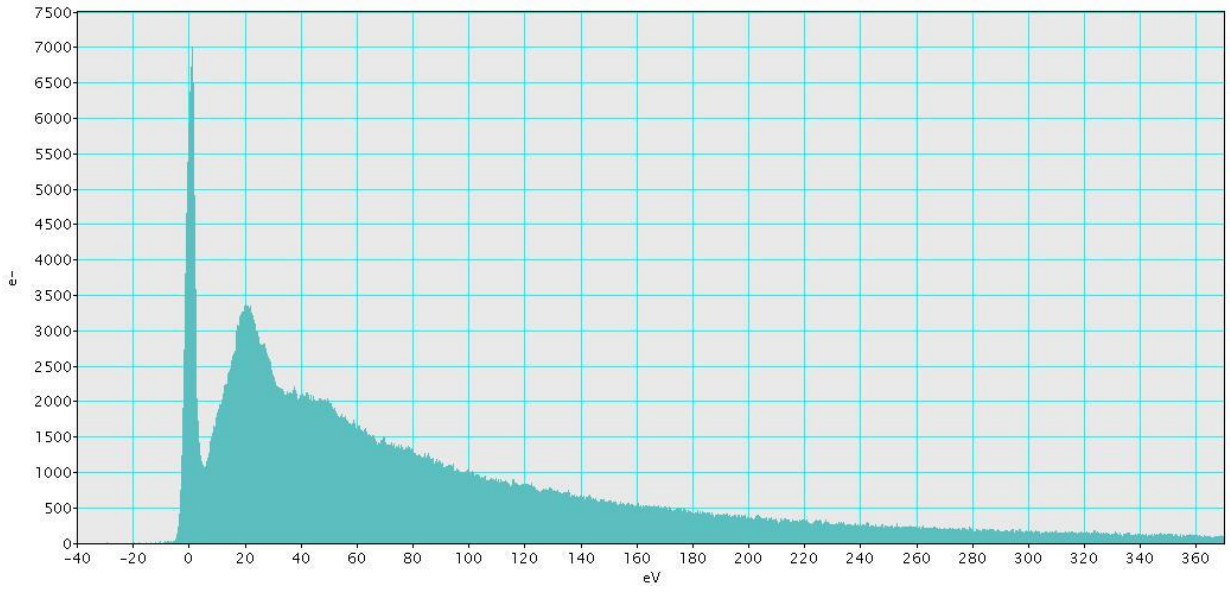

Figure 3.12: Counts vs Energy lost by electron spectrum obtained during EELS

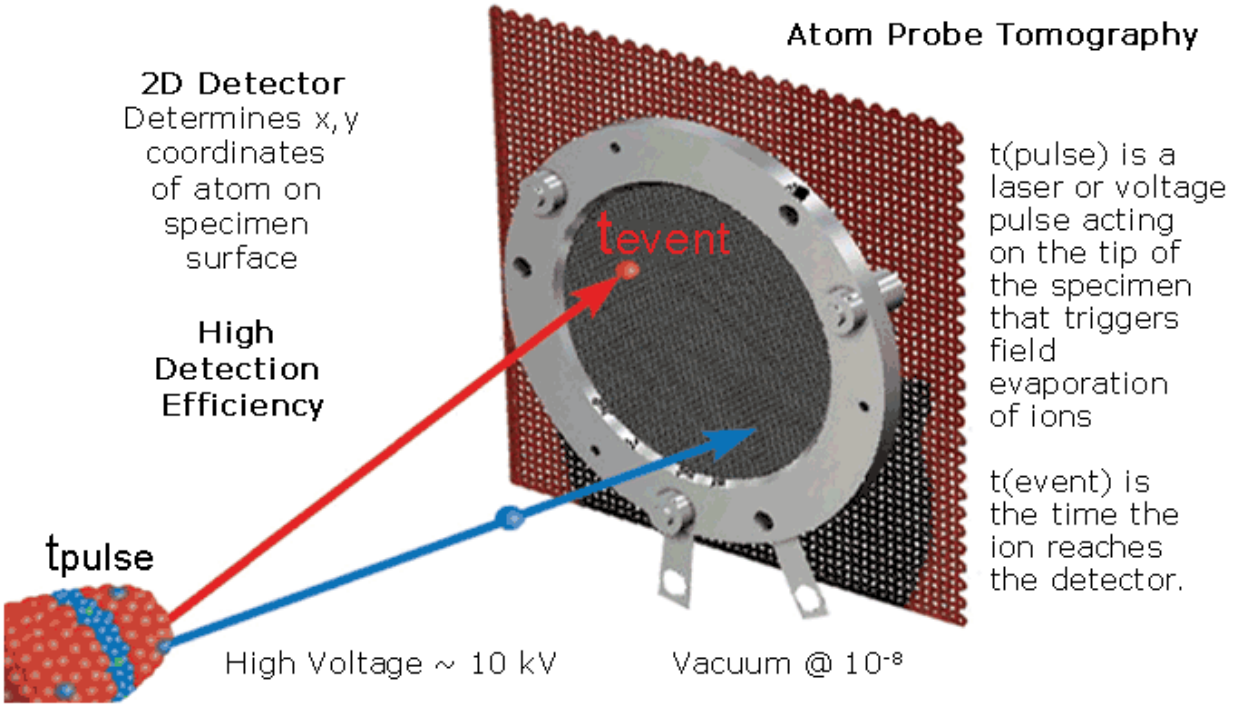

Figure 3.13: A schematic showing the evaporation of atoms from the APT needle to the 2D detector [141]

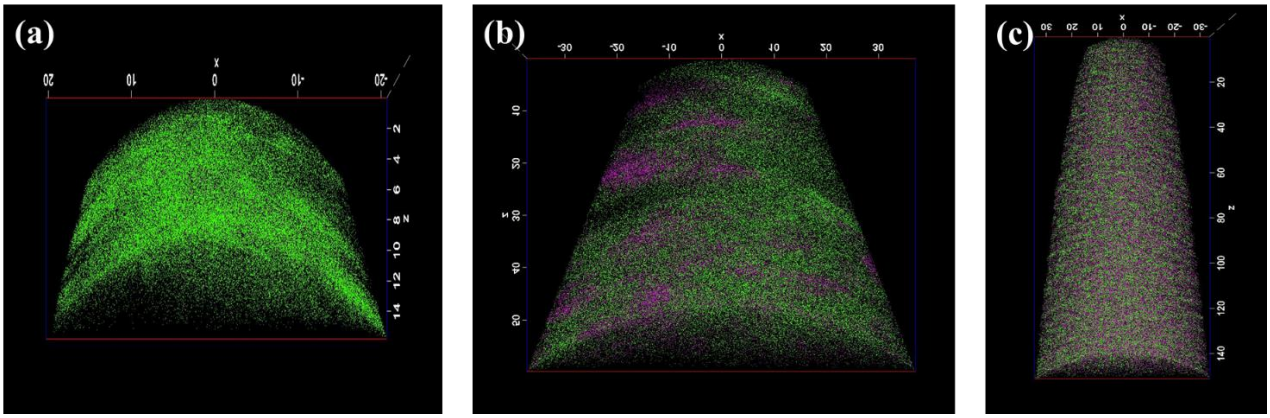

Figure 3.14: Tip reconstructions at different laser energies. (a) At 60 pJ, the stress created at interfaces is far too much during evaporation leading to early fracture of the tip, (b) At 100 pJ, the clusters can be observed nicely and the resulting dataset is good for statistical confidence and (c) At 140 pJ, though the dataset is big, the features in the tip are completely lost due to the aggressiveness of the laser.

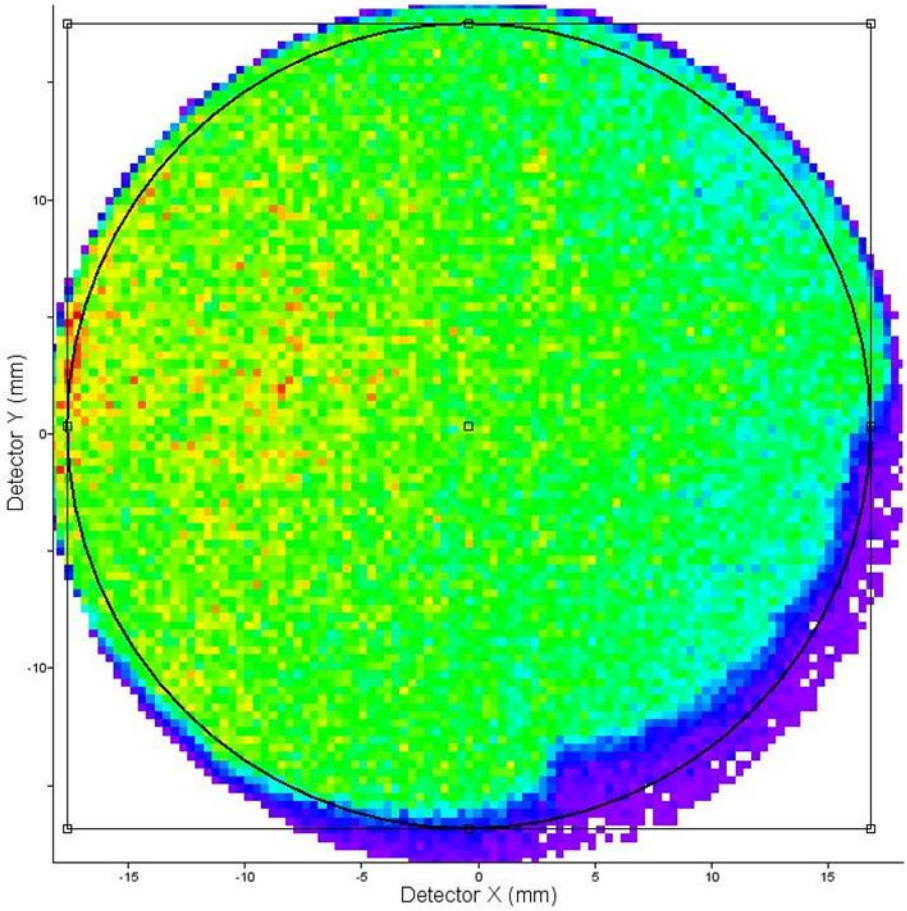

Figure 3.15: Histogram of events detected by the detector. Blue to Red color code signifies increase in number of events.

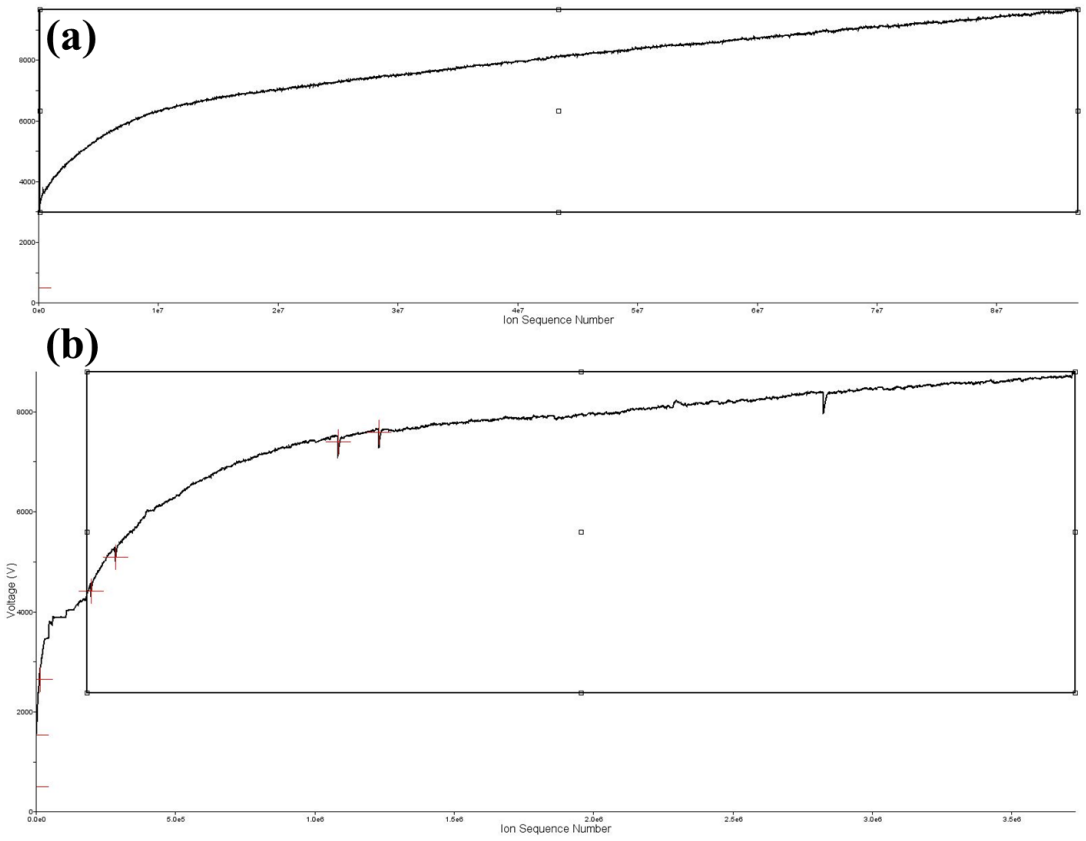

Figure 3.16: Voltage profile for two separate APT tips. (a) Ideal voltage profile and (b) Voltage profile with discontinuities due to fracturing of tip

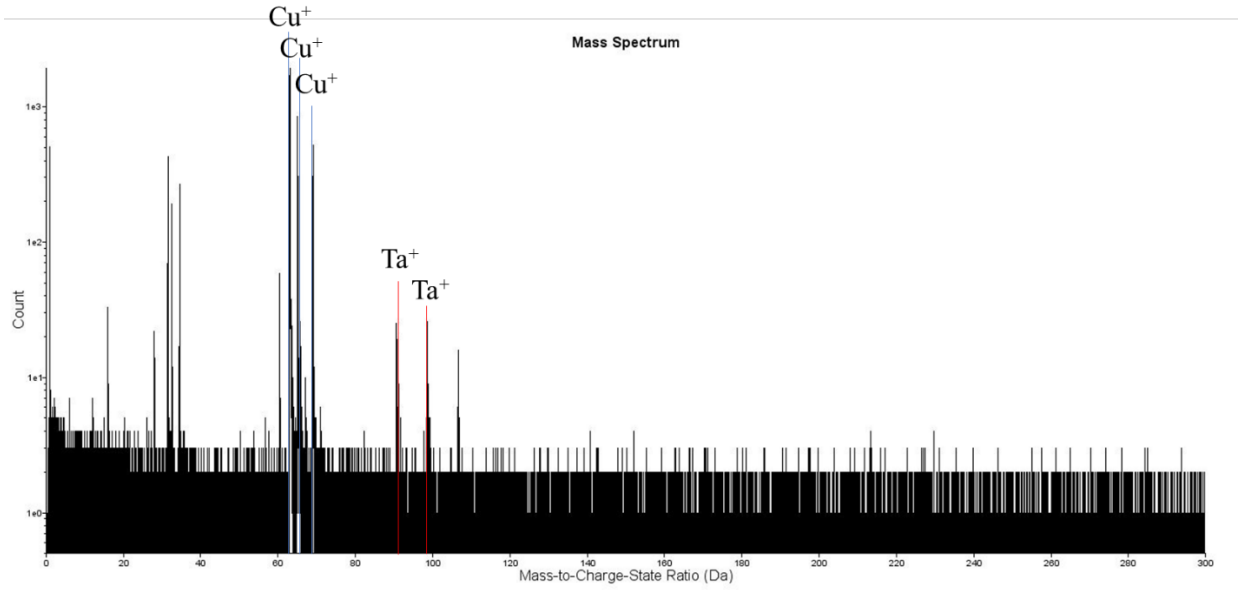

Figure 3.17: Mass spectrum generated by IVAS after time of flight corrections. The software overlays the peaks for the element for ease of identification.

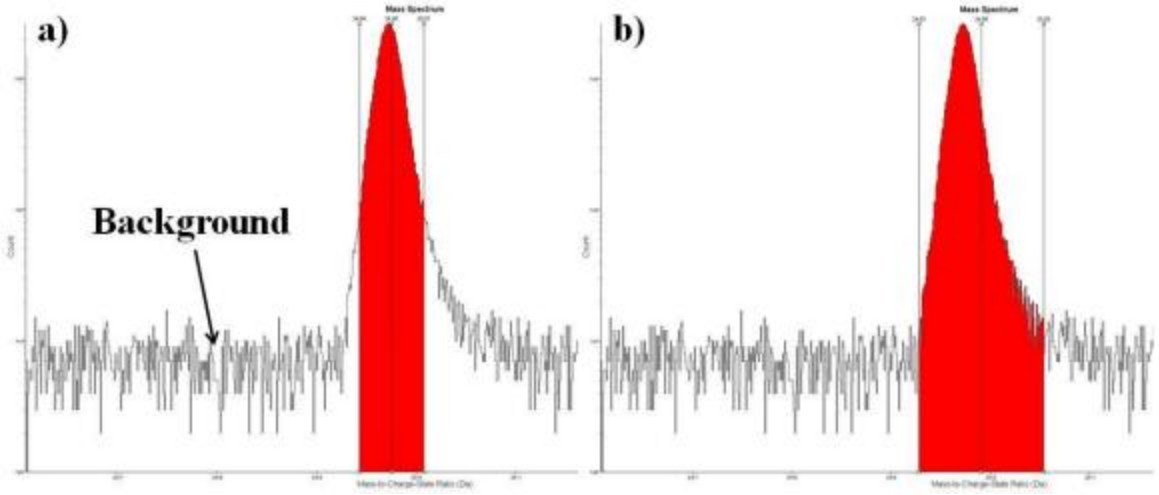

Figure 3.18: A schematic of how the peaks were ranged, (a) FWHM to FWHM and (b) Full width

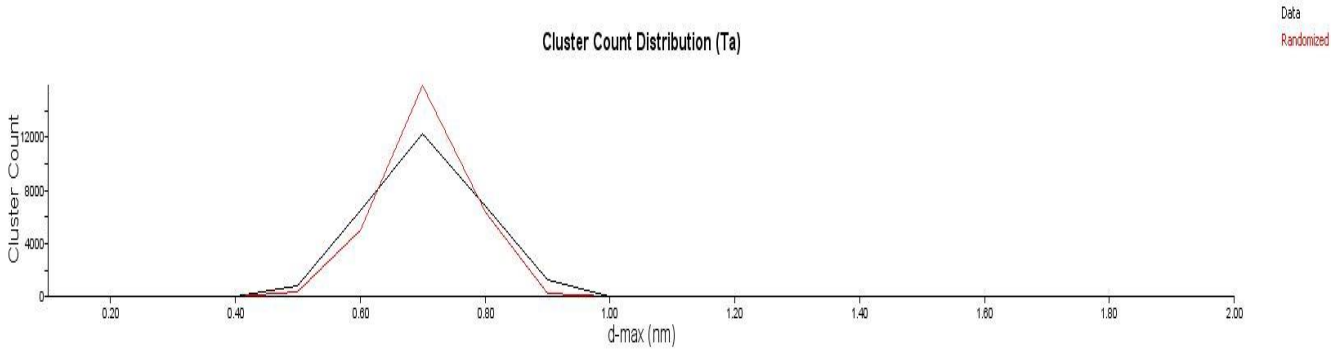

Figure 3.19: *Image needs to be updated* Nearest neighbour distribution histogram to estimate the initial guess value for d_{max}

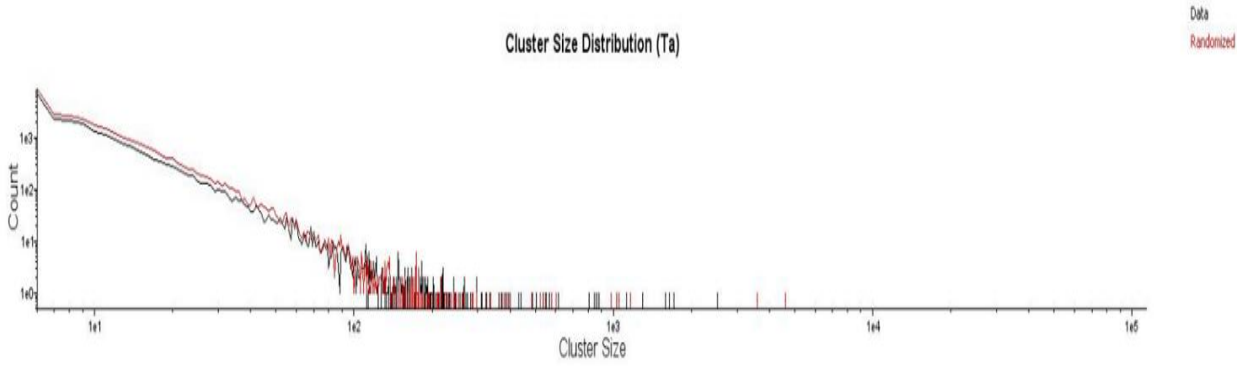

Figure 3.20: Cluster size distribution histogram which gives us the N_{min} value

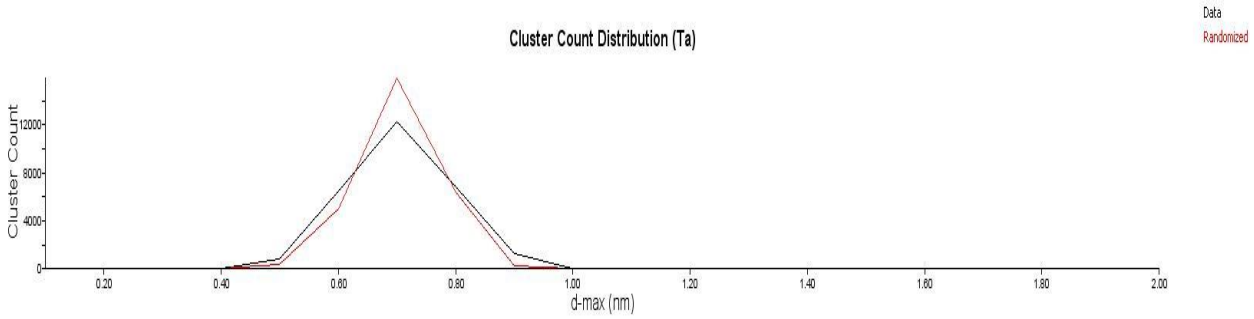

Figure 3.21: Cluster count distribution histogram to finalize the d_{max} value

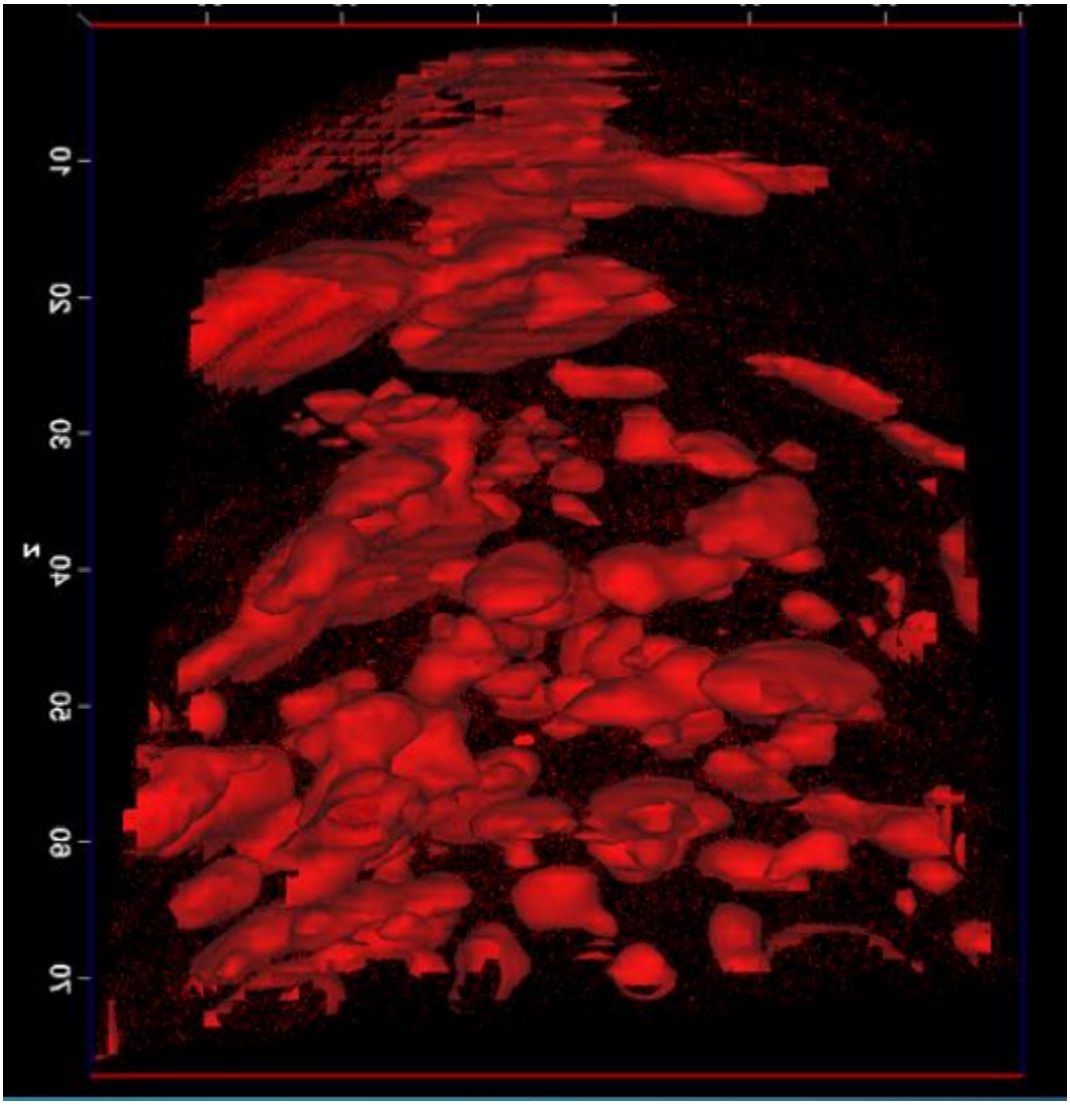

Figure 3.22: Isosurface function for analyzing the Ta nanoclusters present in the dataset

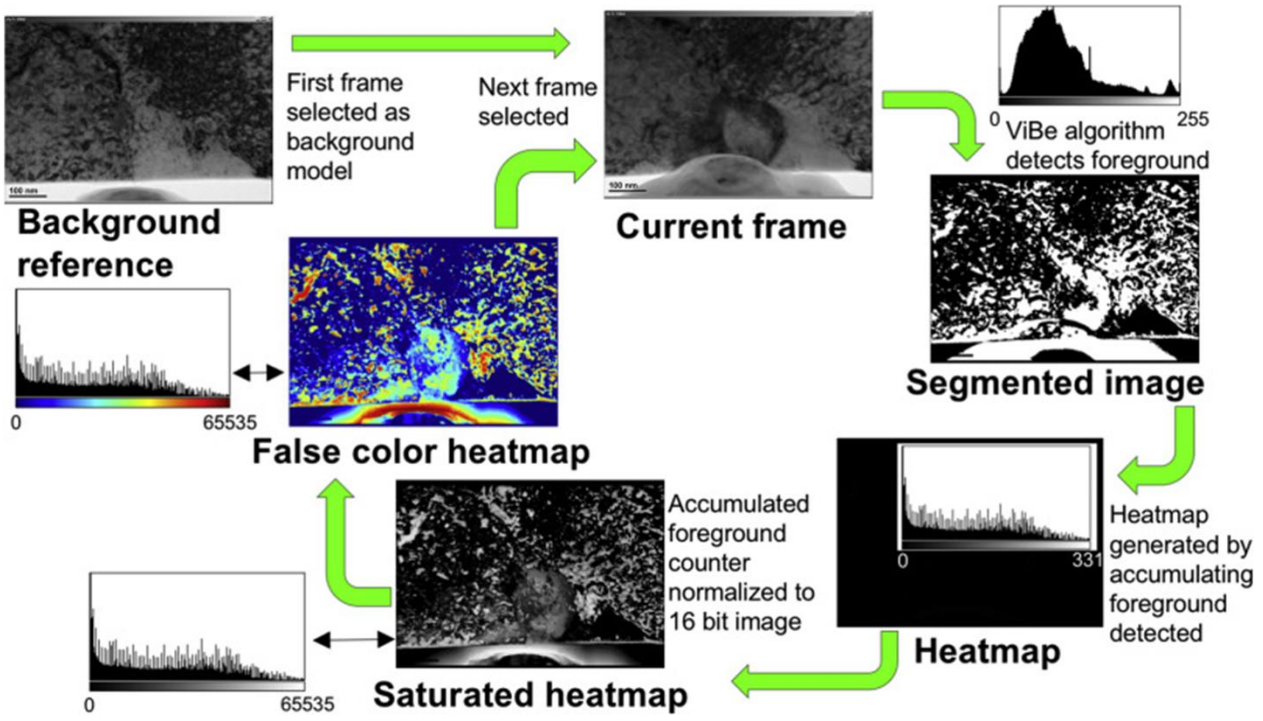

Figure 3.23: An illustrative figure to understand the logic flow of the MicroViBE motion capture application adapted from [34]

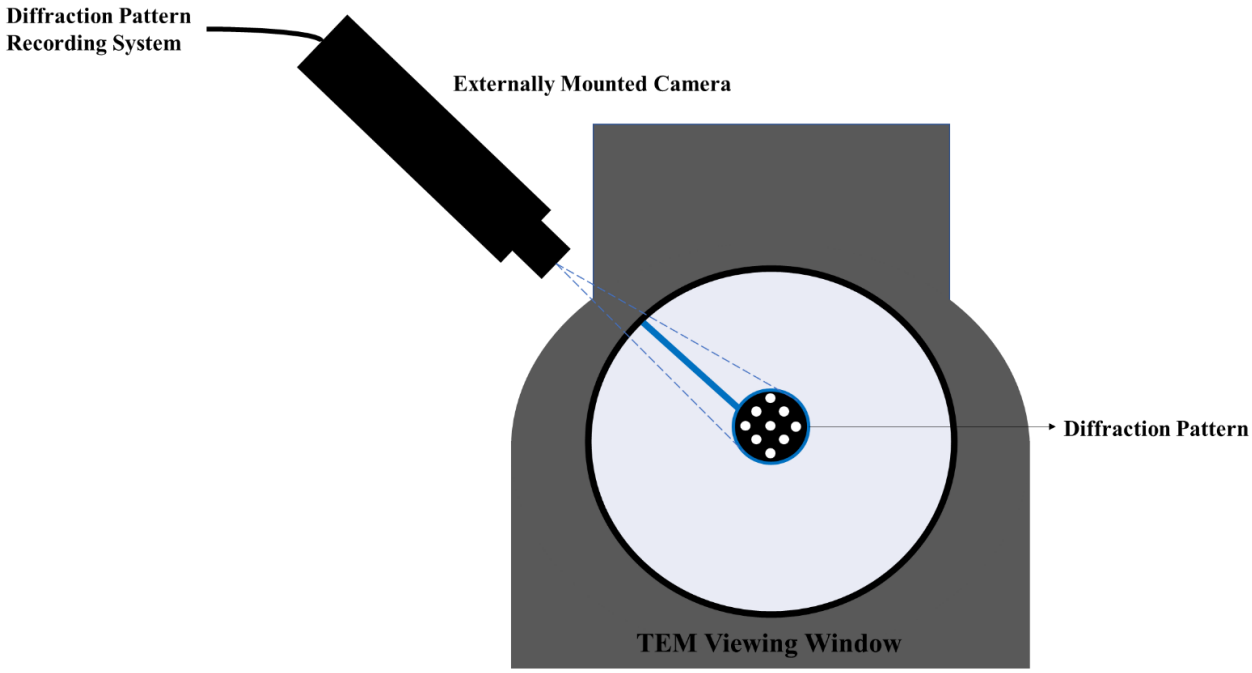

Figure 3.24: Schematic diagram of the ACOM system for recording diffraction patterns obtained in the TEM.

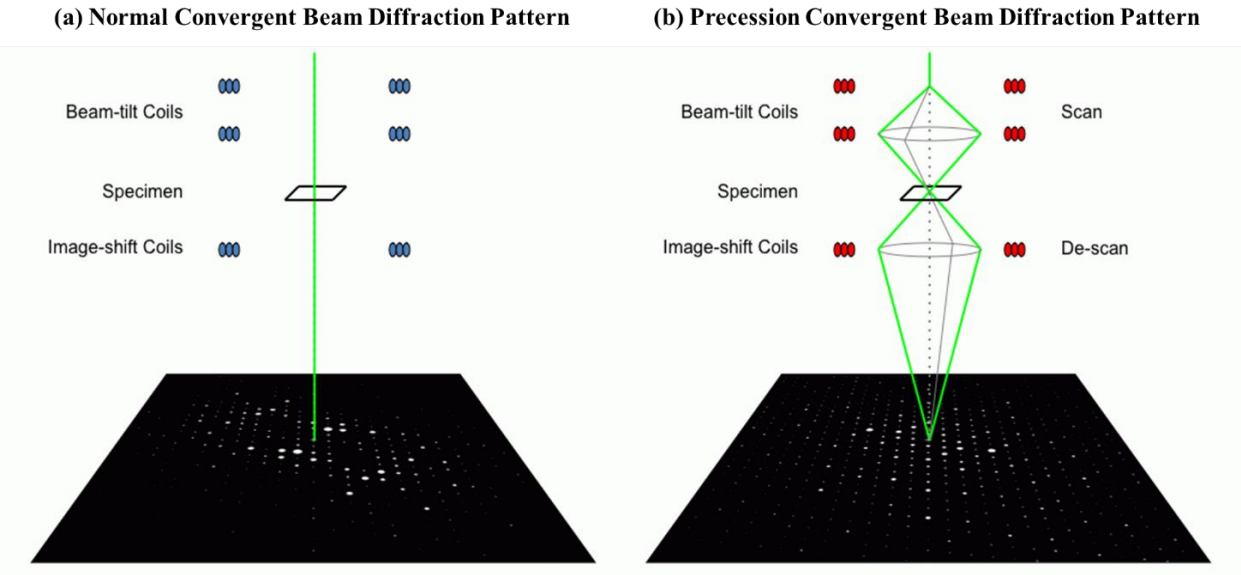

Figure 3.25: (a) Diffraction pattern obtained by normal method in the TEM (b) Precession diffraction pattern obtained in the TEM by deflecting and rotating the electron beam and integrating the multiple normal diffraction patterns obtained to output a precise diffraction pattern for that region

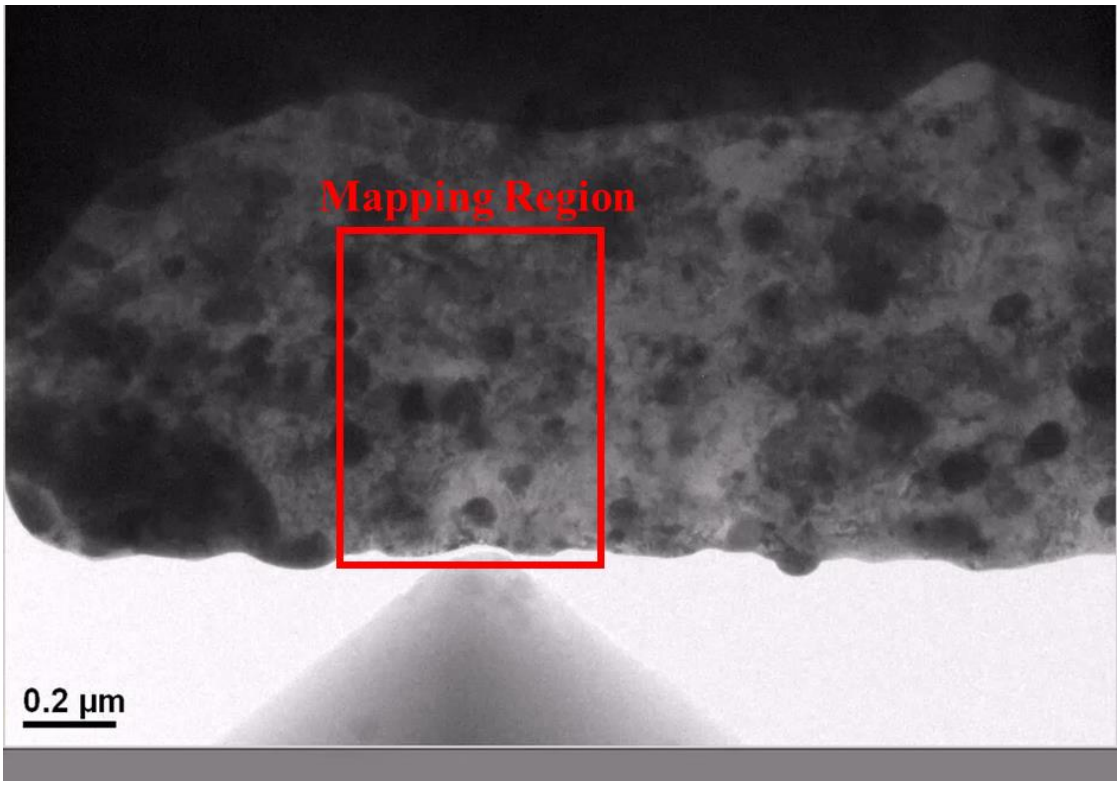

Figure 3.26: A representative image of the region mapped for ACOM analysis from the Pico-indentation experiment

4. RESULTS

A part of this section has already been published in the following journal article:

- P. V. Patki, Y. Wu, J.P. Wharry, Effects of proton irradiation on microstructure and mechanical properties of nanocrystalline Cu–10at%Ta alloy, Materialia. 9 (2020) 100597. https://doi.org/10.1016/j.mtla.2020.100597.

In this section, we would be first comparing the before irradiation and after irradiation, microstructure using TEM techniques and then compare the nanocluster morphology in the as-received sample and proton irradiated sample using the APT technique. We would then be gauging the change in mechanical properties using nanoindentation and, finally, see the effect of deformation on the microstructure of the material using TEM *in situ* pico-indentation intermitted with ACOM analysis.

4.1 TEM Microstructure Characterization

TEM analysis allows us to look at the basic microstructure in the material. BFTEM imaging shows us the general microstructure of the alloy. The microstructure comprises of Cu grains with Ta particles embedded in them. Ta particles of size greater than the Cu grains also exist at grain boundaries rather than inside the Cu grain. Throughout this thesis we will be referring to Ta particles < 20 nm as Ta nanoclusters and Ta particles > 20 nm as Ta phases. In this section, we would be using techniques mentioned in Section 3.5 for TEM to determine the change in morphology of Cu grains and Ta phases and the production of irradiation induced defects.

4.1.1 Cu grain evolution

Using BFTEM, the Cu grains were imaged. The grain boundaries were marked in the micrograph to use line intercept method to calculate the Cu grain size. In the line intercept method, a line of known length is drawn across the micrograph and the number of intercepts with the grain boundaries are calculated as shown in Fig. 4.1. Due to the presence of Ta phases, the length of line passing through the Ta phases should be subtracted. This has been shown in Fig. 4.1 where the line designated by blue color should be subtracted and the number of intercepts should be calculated with the Eq. 4.1.

$$No.of\ intercepts = (No.of\ red\ intercepts \times 1) + (No.of\ blue\ intercepts \times 0.5) \quad \text{(Eq. 4.1)}$$

The number of blue intercepts is halved as they are counted twice due to the interface boundary between the Cu grain and Ta phase which in absence of Ta phases would only be one. After counting the number of intercepts, the Cu grain size is calculated with the following Eq. 4.2.

$$Cu\ grain\ size\ (nm) = \frac{Length\ of\ line}{No.of\ intercepts} \quad \text{(Eq. 4.2)}$$

The Cu grain size was counted across several different areas, based on which the standard deviation in size of the Cu grain was calculated. In the as-received sample, Cu grains observed by bright-field TEM are equiaxed with an average grain size of 70 ± 25 nm, Fig. 4.2(a). Following irradiation, the Cu grains remain equiaxed and exhibit an average size of 77 ± 15 nm, Fig. 4.2(b), which signifies grain size stability throughout irradiation [140]. Additional micrographs used for calculating the grain size for each sample can be found in Appendix B in Fig. B.1 and Fig. B.2.

4.1.2 Irradiation-induced defects

To image irradiation-induced defects, we used the BFSTEM imaging technique. The Cu grains are tilted to their zone axis by utilizing the α and β tilt on the TEM. The beam is condensed to the smallest size using the intensity knob on the TEM controller panel, and the TEM is switched to diffraction mode to generate a Kikuchi pattern, as shown in Fig. 4.3(a) which provides a road map to a particular crystallographic direction.

With the help of the Kikuchi patterns, the Cu grains are aligned to a low zone axis in bright-field STEM to examine for pre-existing or irradiation-induced defects and dislocations (Fig. 4.4(a, b)). The nanocrystallinity of the alloy made it difficult to align the Cu grains to their zone axis hence, two Cu grains were analyzed for each condition. In the as-received specimen, presumed defects <10 nm in size with a number density of $6.1 \pm 2.0 \times 10^{22}$ m^{-3} are observed in a Cu grain on the (011) zone axis (Fig. 4.4(a)). Similarly, in an irradiated Cu grain on the (011) zone axis, defects <10 nm are observed at a number density of $3.3 \pm 1.5 \times 10^{22}$ m^{-3} (Fig. 4.4(b)). Combining these bright-field STEM images with the EELS zero-loss image (Fig. 4.4(c)) and its subsequent EFTEM image (Fig. 4.4(d)) confirms that these questioned defects correspond to locations of Ta nanoclusters. As both the samples show similarly shaped features with similar number density, it is implied that irradiation does not create defects resolvable by TEM. Table 4.1 summarizes all the quantitative microstructure data obtained from the TEM for both the as-received and irradiated microstructures. Additional micrographs used for characterizing defects in grains can be in Appendix B in Fig. B.3 and Fig. B.4.

4.1.3 Ta phase evolution

In BFTEM, due to the diffraction contrast, even some of the Cu grains appear as dark as the Ta phases. So due to the difference in the atomic number (Z) between Cu and Ta, STEM imaging

allows us to successfully distinguish the Ta phases as they appear brighter than the Cu grains. As the Ta phases do not seem perfectly circular, the size was calculated by averaging the shortest diameter of the phase and the longest diameter of the phase, as shown in Fig. 4.5.

The Ta phases (≥ 20 nm) are confirmed by STEM to be spread uniformly throughout the as-received and irradiated microstructures (Fig. 4.6(a)-(b), respectively). Although most Ta phases are round, a few Ta phases appear elongated heterogeneously, due to the extrusion process. A total of 227 Ta phases in the as-received sample and 810 Ta phases in the irradiated sample were analyzed. The huge discrepancy in the sampling set between the two samples is due to availability of more area to analyze in the proton irradiated sample as the lamella size was bigger. The Ta phases in the as-received sample have an average size of 57 ± 48 nm at a number density of $1 \pm 0.13 \times 10^{21}$ m^{-3} (Fig. 4.6(c)) while the irradiated sample has an average Ta phase size of 62 ± 31 nm at a number density of $1 \pm 0.4 \times 10^{21}$ m^{-3} (Fig. 4.6(d)). These results indicate that the Ta phases are statistically unchanged with irradiation. Though the average size of the Ta phases seems stable, the histogram observed in Fig. 4.6(d) compared to Fig. 4.6(c) seems to have shifted slightly to the right, signifying little growth in the Ta phase size. Fig. 4.7 compares both the size distribution and the skewness of the distribution for both the samples can be determined. Skewness dictates how further apart the distribution is from normal distribution. A normal distribution has a skewness value of 0. Positive value indicates a positively skewed (Most of the data points lie on the left side of the average value) data. For the as-received sample the skewness is found to be +4.8 whereas for the proton irradiated sample the skewness was found to be +1.8 signifying the shift of distribution from left to right after irradiation. Additional STEM micrographs used for characterization of Ta phases can be found in Appendix B in Fig. B.5 and Fig. B.6. As we calculated the minimum and maximum diameter of each of the Ta phase, we were also able to

determine the average ellipticity of the Ta phases in each sample based on the following formula in Eq. 4.3:

$$Ellipticity = \sqrt{\frac{a^2-b^2}{a^2}} \quad where\ a > b \qquad \text{(Eq. 4.3)}$$

Where a and b are the maximum and minimum diameter of the measured Ta phase. An ellipticity of 0 signifies a perfect circle whereas as we deviate from 0 the ellipticity increases. The increase in probability of higher ellipticity in the proton irradiated sample when compared to as-received sample as seen in Fig. 4.8 signifies irradiation induced change in shape of the Ta phases.

Hence, we can say that the Ta phases exhibit an overall increase in size after irradiation.

4.2 APT Nanocluster Analysis

APT analysis is performed to overcome the resolution limits of the TEM to study the morphology of the Ta nanoclusters. After completing the cluster analysis in IVAS, an excel workbook is generated with information on the radius of gyrations and the composition of the identified nanoclusters. The size of the nanoclusters is calculated using Eq. 3.6 and 3.7 in Section 3.6 and the nanoclusters are filtered according to their size (D_g < 20 nm) and their composition (Ta at% > 60 at%).

An aggregate of 167 as-received and 60 irradiated Ta nanoclusters are analyzed across three APT tips for each of the sample conditions and are summarized in Table 4.2. Cluster analysis data for each sample tip can be found in Appendix B. in Table B.1. Representative APT tip reconstructions show the atomic allocations (Figs. 4.9(a), 4.10(a)), indexed clusters (Figs.4.9(b), 4.10(b)), and cluster morphologies (Figs.4.9(c), 4.10(c)) for both the as-received and irradiated conditions. All other tips used for cluster analysis for both the samples can be found in Appendix B in Fig. B.7 and Fig. B.8. The quantitative size distribution of Ta nanocluster in both samples is

shown in Fig. 4.11. Even though nanoclusters in both the as-received and irradiated sample appear spherical in the TEM images (Fig. 4.2(a)-(b)), APT analysis shows them to exhibit complex morphologies (Fig. 4.9 & 4.10). The number density of the nanoclusters decreases from 5.7 ± 1.4 × 10^{23} m-3 in the as-received sample to 1.3 ± 1.7 × 10^{23} m-3 in the irradiated sample, indicating irradiation-induced dissolution of Ta nanoclusters. And although the average nanocluster size remains statistically unaffected with irradiation (3.3 ± 1.2 nm in the as-received specimens and 5.0 ± 3.3 nm in the irradiated specimens), the frequency probability of Ta nanoclusters < 2.5 nm diminishes to zero in the irradiated sample. This signifies the favored dissolution of the smallest Ta nanoclusters during irradiation.

The average Ta composition in the nanoclusters is also statistically unchanged with irradiation, at 91 ± 10% in the as-received material and 86 ± 12% in the irradiated material. Though, the composition of Ta in the Cu matrix (i.e., not grouped) increases from 0.36 ± 0.01% in the as-received sample to 0.70 ± 0.28% in the irradiated sample. Additionally, the APT reconstructions show that Cu is spread around the boundary of as-received nanoclusters, while Cu and Ta are more blended in the irradiated nanoclusters (Fig. 4.9(c), 4.10(c)). These observed chemistry changes are coherent with the variations in nanocluster number density and are suggestive of irradiation-induced Ta nanocluster disordering and dissolution.

4.3 TEM *in situ* pico-indentation intermitted with ACOM analysis

During pico-indentation, in both samples, deformation only in the Cu grains was observed, whereas the observable Ta phases did not show any signs of deformation (Fig. 4.12). The videos when coupled with the MicroViBE motion detection algorithm shows us the change in position of the features in the microstructure due to indentation. Due to the background subtraction method of ViBE algorithm, different contrast modes were used to track the Ta phases and Cu matrix

separately. In the videos obtained in BFTEM mode, due to the dark contrast of Ta particles movement of the Ta particles was captured. The Ta particles did not show any signs of compression but only showed displacement parallel to the indenter tip signified by the red region crown formed on the Ta particle in the heat map as shown in Fig. 4.13. In the STEM mode, due to the dark contrast of the Cu matrix, deformation in the Cu matrix was captured. Fig. 4.14 shows the heat map generated for the video taken in STEM video and it can be observed that the Cu matrix deforms throughout the window due to indentation. The ViBE analyzed videos in both BFTEM mode and STEM mode can be found in Appendix C. link.

The mechanical response from both the samples was similar as well as load drops were observed in both the samples signifying dislocation burst events as shown in Fig. 4.15. Due to the low magnification for TEM *in situ* pico-indentation experiment, we intermitted ACOM analysis to observe the response of the nanostructured alloy at the nanometer scale. The ACOM analysis allows us to analyze the crystallographic direction of the Cu matrix and the Ta particles. It will enable us to separately analyze the Ta particles to examine any changes in their shape or size as shown in Fig. 4.16(a-d). Two separate experiments were performed for the as-received condition and the proton irradiated sample. Post experiments, the Cu grain orientation maps, Ta particle orientation maps, and Ta phase maps were exported to high-resolution .png files to be analyzed in ImageJ software and Adobe Photoshop software. Due to the drawback of the software in which the maps are analyzed, which was mainly developed for Electron Beam Scattering Diffraction in Scanning Electron Microscope, the scale on these exported maps is in μm even though it should be nm. This difference should be corrected before any analysis on size of particles is done on these maps.

The ImageJ software was used to calculate the no. of Ta particles smaller than 20 nm. The analysis was done by first setting the scale on the .png file using the line feature to draw a line that fits the scale bar shown on the image, after which the set scale feature to known length is used to calibrate the dimensions on the image. After doing so, a circle with a diameter of 20 nm was drawn and Ta particles smaller than the circle were counted. For calculating the Ta area before and after indentation, Adobe Photoshop is used to calculate the pixels belonging to the Ta particles based on their color. The magic wand feature in Photoshop allows us to select pixels of the same color based on their unique Red, Green, and Blue intensities. As all the Ta particles are of the same color, the magic wand features allow us to isolate all pixels belonging to the Ta particles and then can be counted based on the histogram shown in Fig. 4.17.

In the as-received sample, the maps were taken at indent depths of 0 nm, 200 nm, 400 nm, and 600 nm whereas in the proton irradiated sample, the maps were taken at indents depths of 0 nm, 150 nm, 300 nm, and 450 nm. The Cu orientation maps and Ta phase maps for each indentation depth for each sample can be found in Appendix B between Fig. B.9 – B.15. A sample series of TEM in situ pico-indentation videos for ACOM analysis on the irradiated sample can be found at the link provided in Appendix C. Based on the Cu orientation maps, the OIM software calculates the size of the Cu grains in the sample. The Cu grain size in the as-received sample was found to be 12.6 nm ± 12.8 nm and 9.4 nm ± 12 nm in the proton irradiated sample. The Cu grain size obtained from the ACOM analysis varies from the grain size calculated by the line intercept method due to the error present in indexing the grains due to overlapping of multiple grains due to the use of thick (~150 nm thickness window) sample. Hence, a stronger diffraction pattern from either of the overlapped grains would result in the system counting the grain as two different small grains. Size distribution of the Cu grains in both the samples at 0 nm has been shown in Fig. 4.18.

This average grain size has been calculated based on the orientation maps taken at an indentation depth of 0 nm. Even though we have an error in indexing of the Cu grains due to overlapping of grains, comparing the Cu grain size distribution at 0 nm indentation depth in Fig. 4.18, both samples show similar Cu grain size distribution confirming our TEM analysis of the Cu grains stating no change in grain size is observed after irradiation. The Cu grains in both the samples show a decreasing grain size with respect to increasing indentation depth signifying compression of the Cu grains due to indentation as seen in Fig. 19(a, b). As this is a selective area analysis, Cu grains above the size 200 nm should not be taken into consideration while comparing the grain size distribution in both the samples at different indentation depths. Similar analysis on just the Ta particles gives us an average size of 9 nm ± 3.7 nm in the as-received sample and of 8.43 nm ± 8 nm in the proton irradiated sample. This average size of Ta particles is inclusive of Ta nanoclusters and Ta phases. The average size leans towards the Ta nanoclusters as the number density of these clusters was found to be higher than the number density of Ta phases by an order of magnitude. As the Ta particles sampling size is from a particular area, the conclusions drawn about the size of the Ta particles is skewed towards the analyzed area. Looking at the Cu orientation maps for both the samples, no change in orientation was observed with increasing deformation in Fig. 4.20. This can also be seen in the hkl indices distribution in both the samples in Fig. 4.21 and Fig. 4.22. Based on these unchanged distributions in Cu grain orientations with increasing indentation depth in both the samples, it can be concluded that deformation via grain rotation is absent in this material.

Looking at the number density of the Ta particles (Fig. 4.23) at different indentation depths it can be observed that there is a slight increase in number density of Ta particles in the proton irradiated sample when compared to the as-received sample after indentation. Using the photoshop – magic wand technique area of Ta particles in the Ta phase maps for both the samples was

calculated as shown in Fig. 4.24. The error bars were based on the reliability index for the diffraction patterns. Reliability of 100 indicates a perfect match and unique solution for indexing of the diffraction pattern whereas a reliability of 0 indicates no unique solution for the diffraction pattern. Normally, a reliability index of 15 is enough to give a unique solution for the diffraction pattern. Due to the curvature of the Ta particles in the microstructure, the diffraction patterns obtained at the Cu-Ta interface had a low reliability due to the overlapping of Cu grains and Ta particles and the reliability was found to be less than 15. Therefore, based on the reliability factor the error bars for all the Ta particle area is taken to be ± 15%. Both samples show decrease in area of Ta particles post deformation but the decrease in Ta particle area in the as-received sample is way higher than that of in the proton irradiated sample. Hence, we decided to examine the Ta phases separately and the Ta nanoclusters separately.

First, we examine the density of the Ta phases in both the samples. The Ta phase number density at different indentation depths in both the samples as shown in Fig. 4.25 show stability of the existing Ta phases. The Ta phase maps can be used to judge the phase evolution visually, and it is observed that both samples tend to show a decrease in the Ta phase area with increasing indentation depth as shown in Fig. 4.26(a) and Fig. 4.27(a). The visual output was also confirmed with calculation of Ta phase area and it was seen that all the Ta phases showed a negative slope for area with increasing indentation depth as shown in Fig. 4.26(b) and Fig. 4.27(b). Both samples showed refining of the Ta phase with deformation. Visually, Ta maps for the proton irradiated samples showed formation of newer Ta clusters. After counting the number of Ta particles less than the size of 20 nm in both the samples at each indentation depth, it was found that the number of Ta clusters in the as-received sample stayed stable whereas in the irradiated sample the number density seemed to increase with increasing indentation depth as shown in Fig. 4.28. This signifies

nucleation of Ta clusters with deformation in the proton irradiated sample. We performed the area calculation for Ta nanoclusters in both the samples. In the as-received sample the slope of the Ta area can be seen to be negligible for Ta particles smaller than 20 nm signifying no change in size with indentation shown in Fig. 4.29(a-b). In the proton irradiated sample, it can be observed in the circled region in Fig. 4.30(a) which shows the Ta phase maps, there is formation and enlargement of newer Ta particles smaller than the size of 20 nm. The positive slope of the Ta area with respect to indentation depth in Fig. 4.30(b) shows that the newly formed clusters also undergo growth with deformation. By analyzing the formation of Ta clusters in the orientation maps it is observed that the sites of formation of these Ta particles seem to be at the Cu grain boundaries as shown in Fig. 4.31(a-d) and no new Ta clusters are formed within the grain.

Table 4.1: Summary of microstructural analysis done on the TEM [140]

		As-received	**Proton Irradiated**
Cu grains	Diameter (nm)	70 ± 25	77 ± 15
	No. of grains measured	84	149
Ta phases (size > 20 nm)	No. of phases measured	227	810
	Diameter (nm)	57 ± 48	62 ± 31
	Density (10^{21} m^{-3})	1.0 ± 0.1	1.0 ± 0.4
	Volume fraction (*f*)	0.13	0.14
Defects in Cu grains	No. of grains analyzed	2	2
	Density (10^{22} m^{-3})	6.1 ± 2.0	3.3 ± 1.5

Table 4.2: Summary of cluster analysis performed on the Local Electrode Atom Probe [140].

		As-received	**Proton Irradiated**
Ta nanoclusters (size < 20 nm)	No. of APT tips analyzed	3	5
	No. of clusters analyzed	167	60
	Diameter (nm)	3.3 ± 1.2	5 ± 3.3
	Density (10^{23} m^{-3})	5.7 ± 1.4	1.3 ± 1.7
	Ta composition in nanoclusters (at %) (balance Cu)	91 ± 10	86 ± 12
	Ta composition in matrix (at %) (balance Cu)	0.36 ± 0.01	0.70 ± 0.28
	Volume fraction (*f**)	0.014	0.001

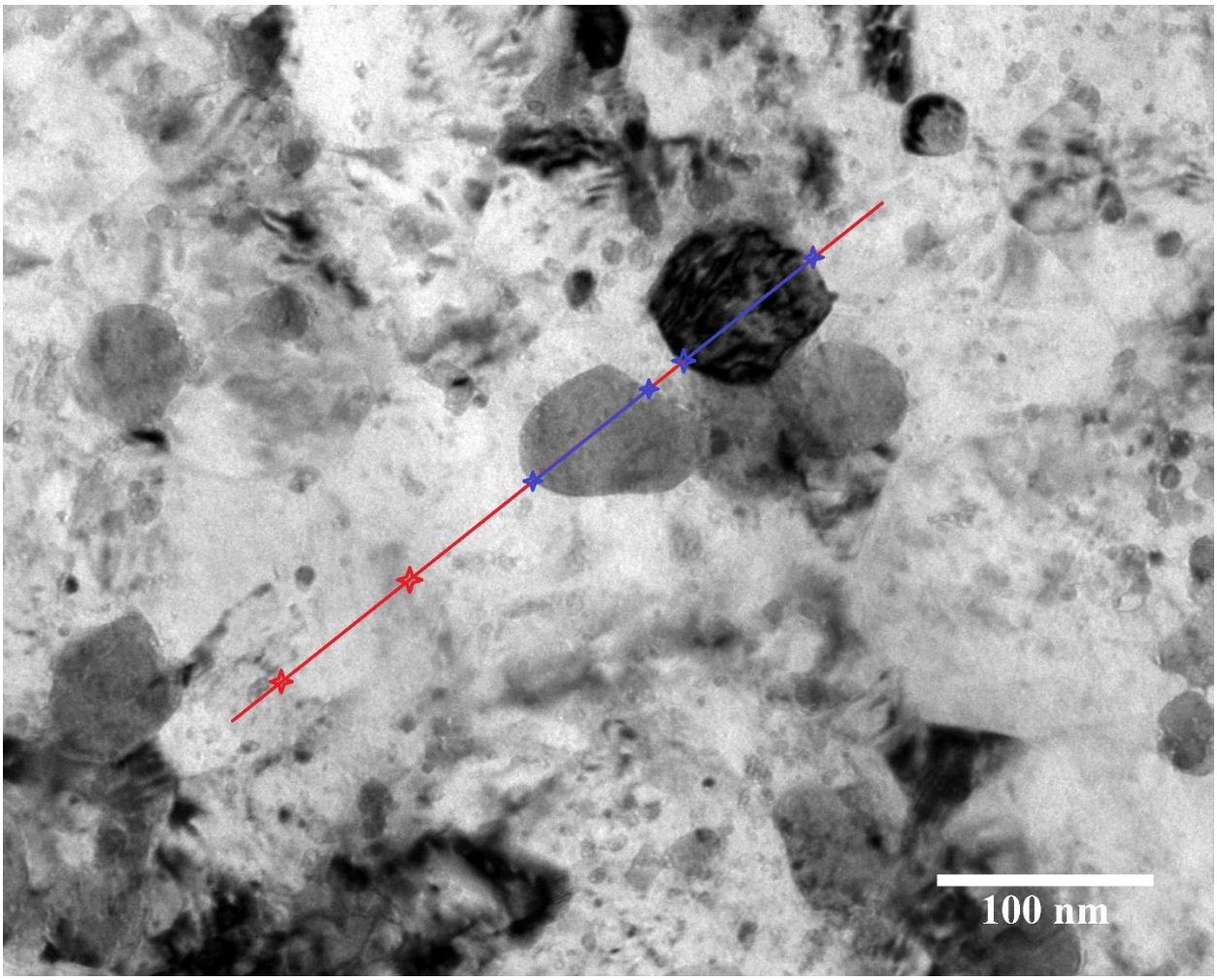

Figure 4.1: The line intercept method for counting Cu grain size. The blue line indicates length of line that needs to be subtracted from the original length of the line and the blue crosses indicate the Cu-Ta interface boundary.

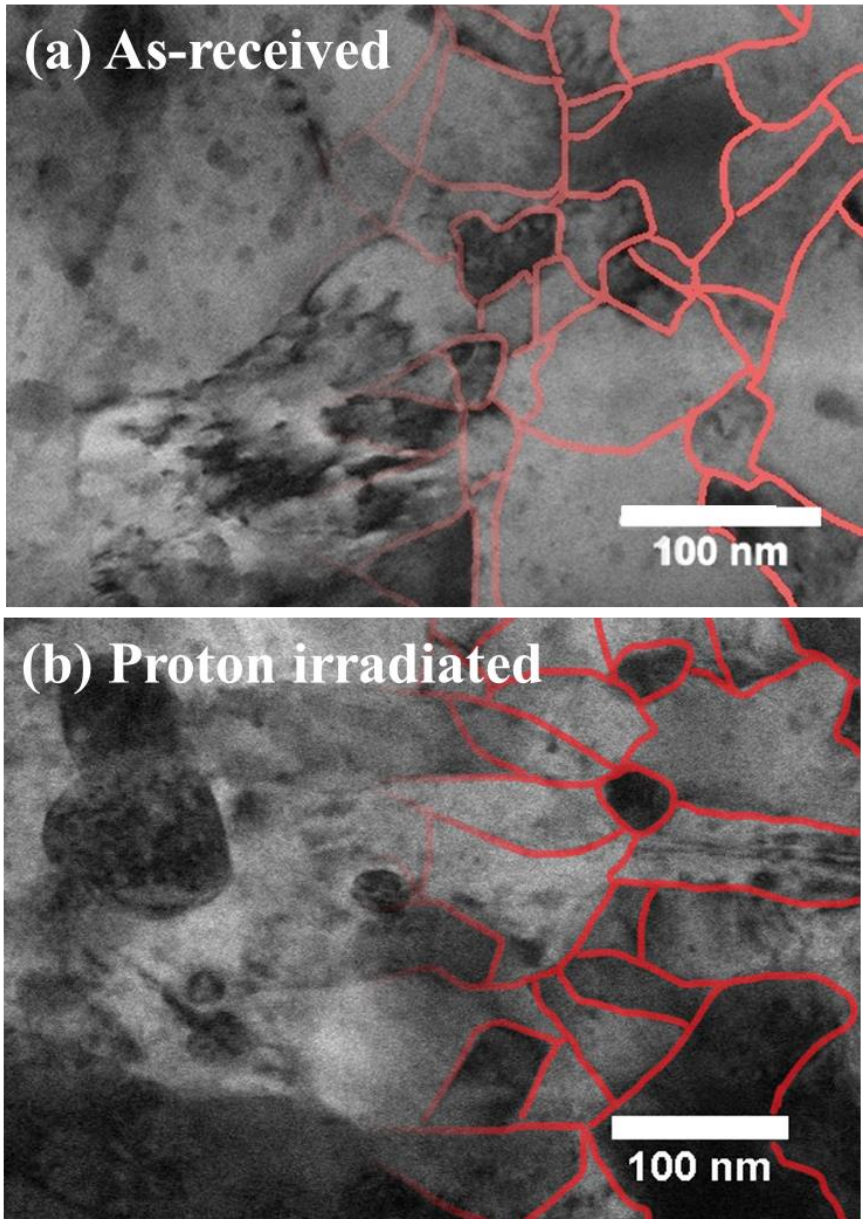

Figure 4.2: Bright field TEM micrographs showing Cu grains in (a) as-received and (b) proton irradiated Cu-10%Ta; the micrographs are marked for ease of visualizing the grain boundaries [140]. The Cu grains are observed to show stability after irradiation.

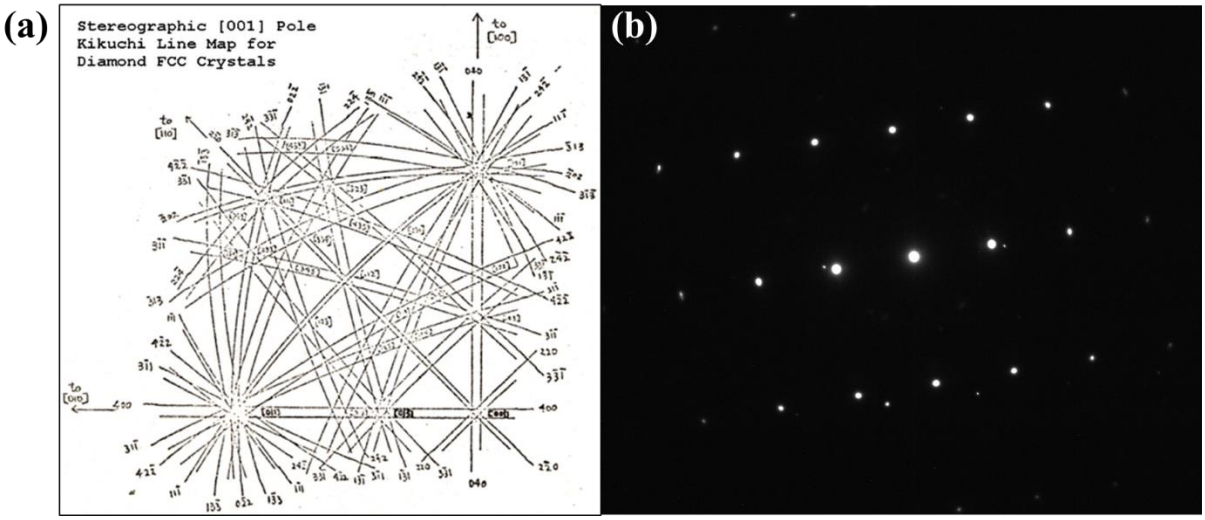

Figure 4.3: (a) Kikuchi diffraction pattern for Diamond FCC single crystals. Kikuchi diffraction patterns provide the microscopist with a road map to a crystallographic direction. (b) Convergent Beam Diffraction Pattern (CBED) for one of the Cu grains aligned to its zone axis in the Cu-Ta alloy system.

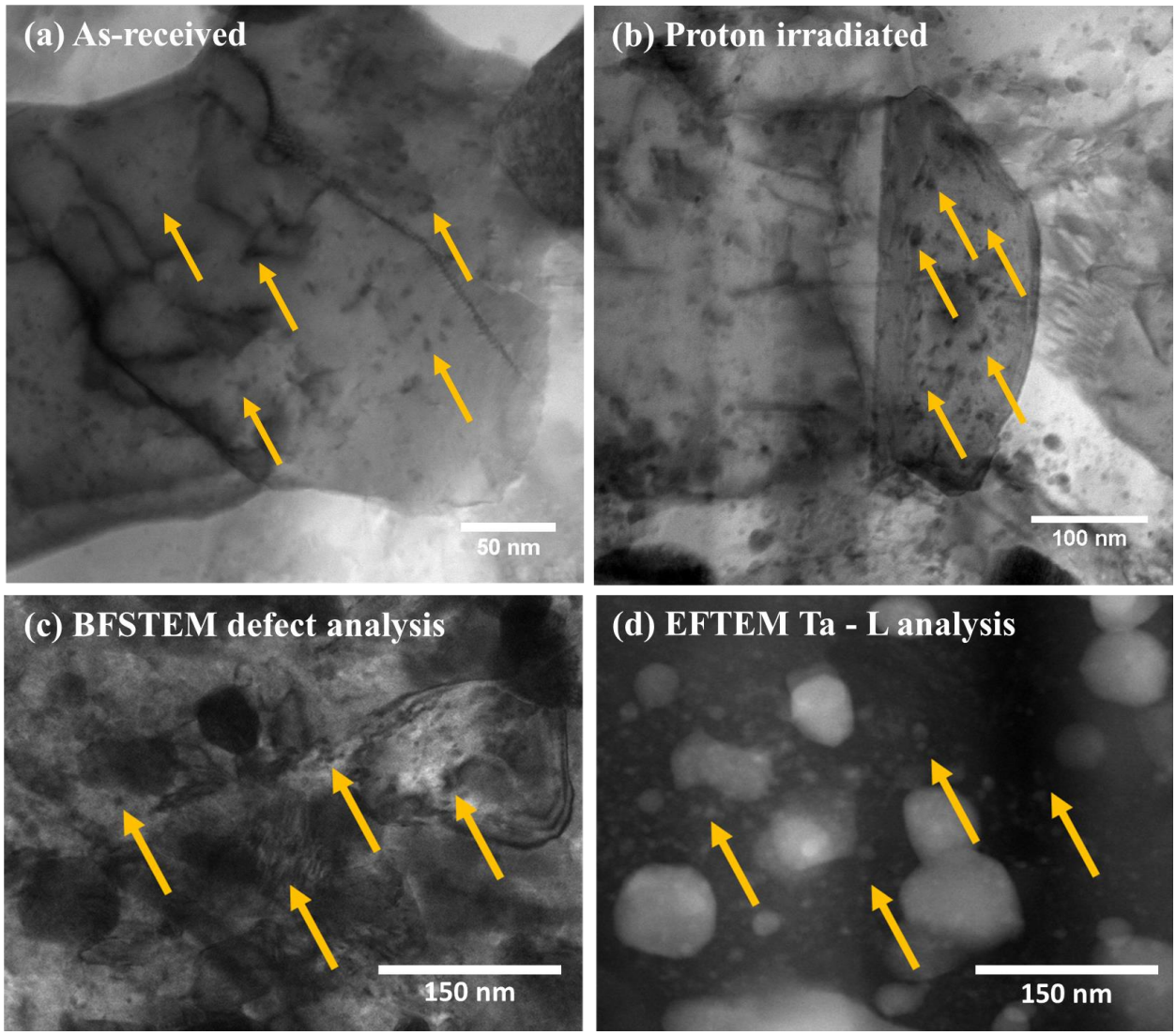

Figure 4.4: (a) As-received sample - Cu grain aligned to its zone axis, (b) Proton irradiated sample - Cu grain aligned to its zone axis. Both the samples show the presence of similar defects marked by yellow arrows. (c) BFSTEM image from the proton irradiated sample is correlated to (d) EFTEM image showing Ta nanocluster's presence at the yellow arrows. It is observed that these defects/features seen in BFSTEM images are actually Ta nanoclusters [140].

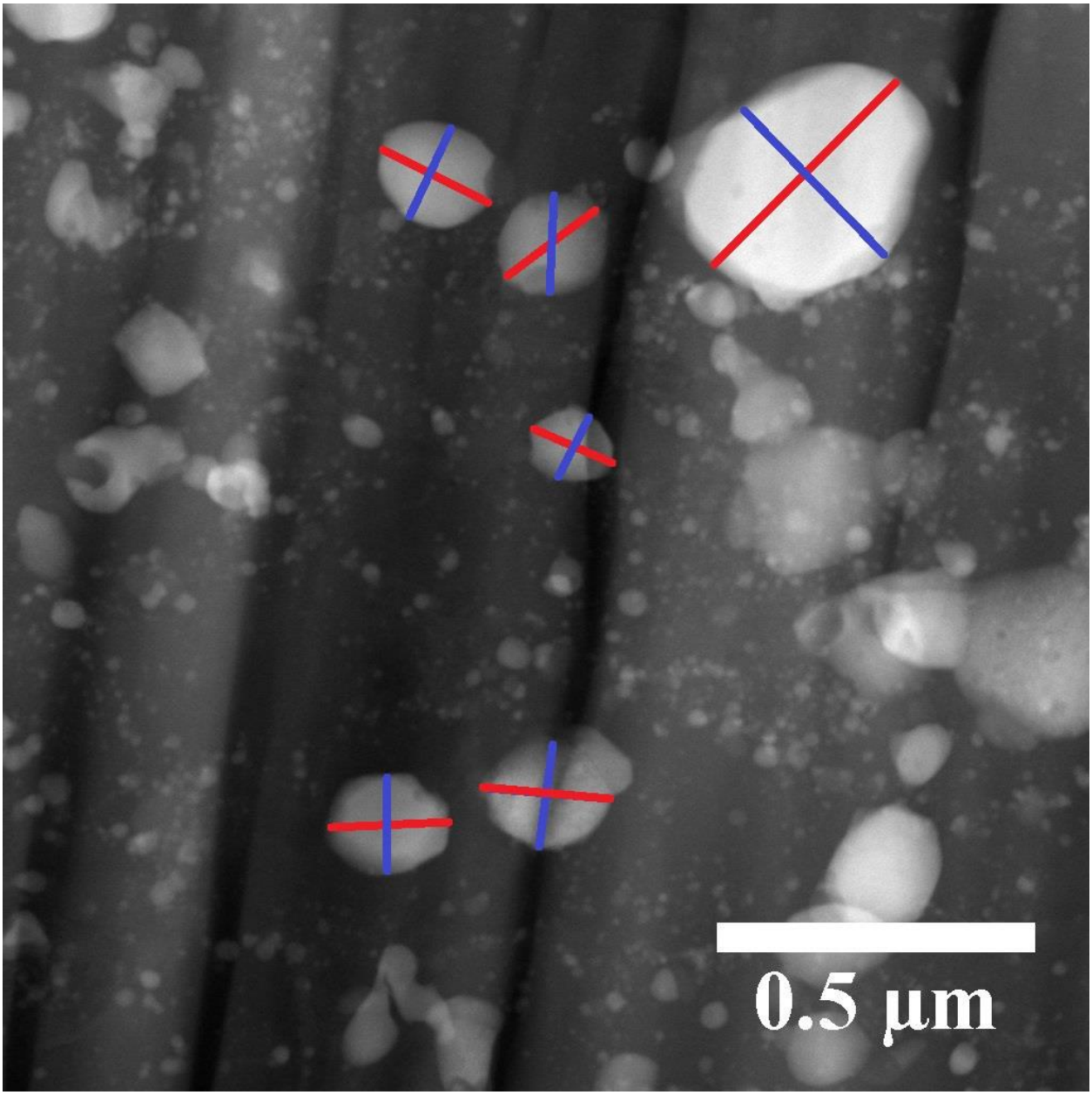

Figure 4.5: Representative image for calculating the size of the Ta phase. Redline represents the longest diameter, whereas the blue line represents the shortest diameter.

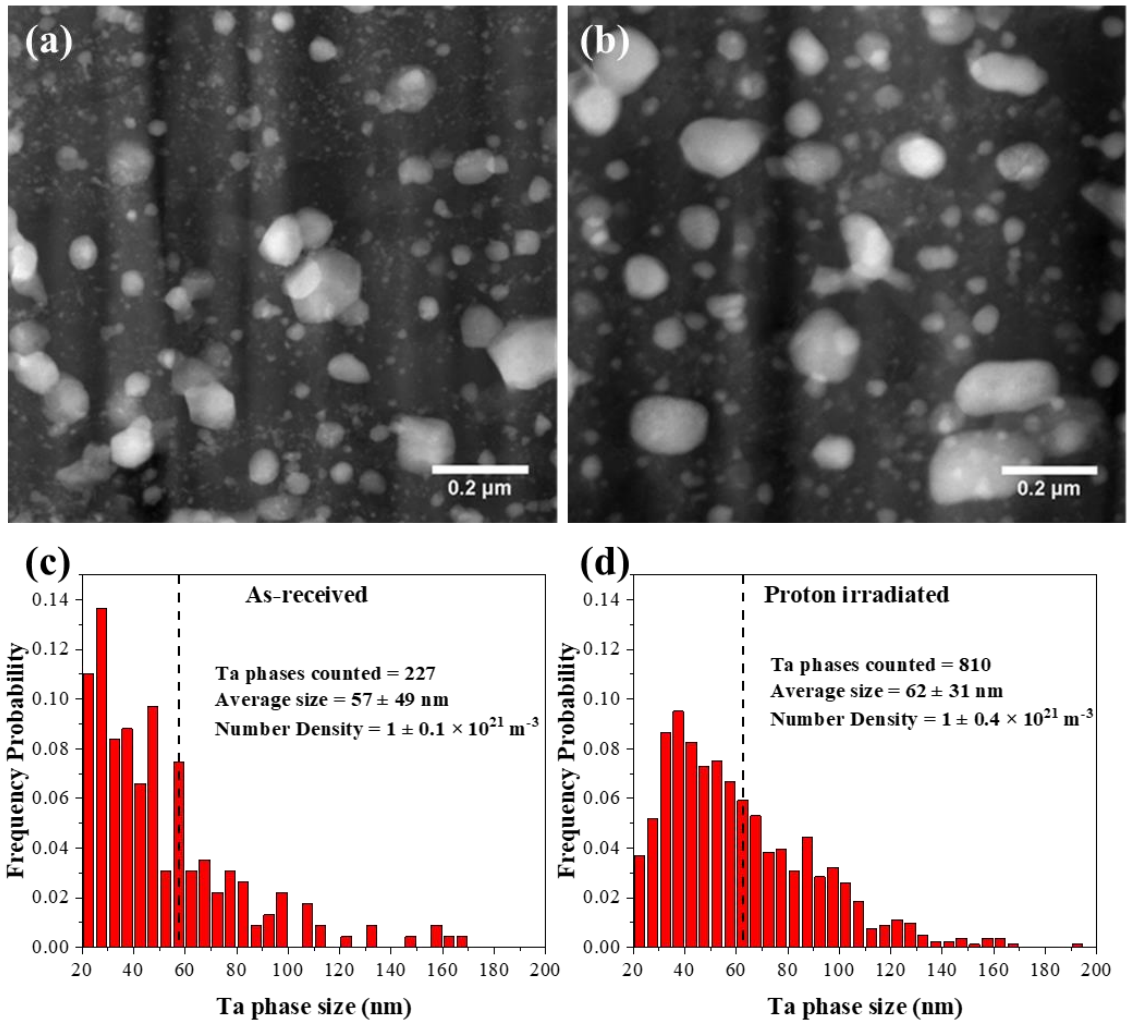

Figure 4.6: STEM images is used to take advantage of the high Z-contrast between Ta and Cu to discern Ta particles from Cu grains in (a) as-received and (b) proton irradiated Cu-10at%Ta; size distribution of Ta phases in (c) as-received and (d) proton irradiated Cu-10at%Ta [140].

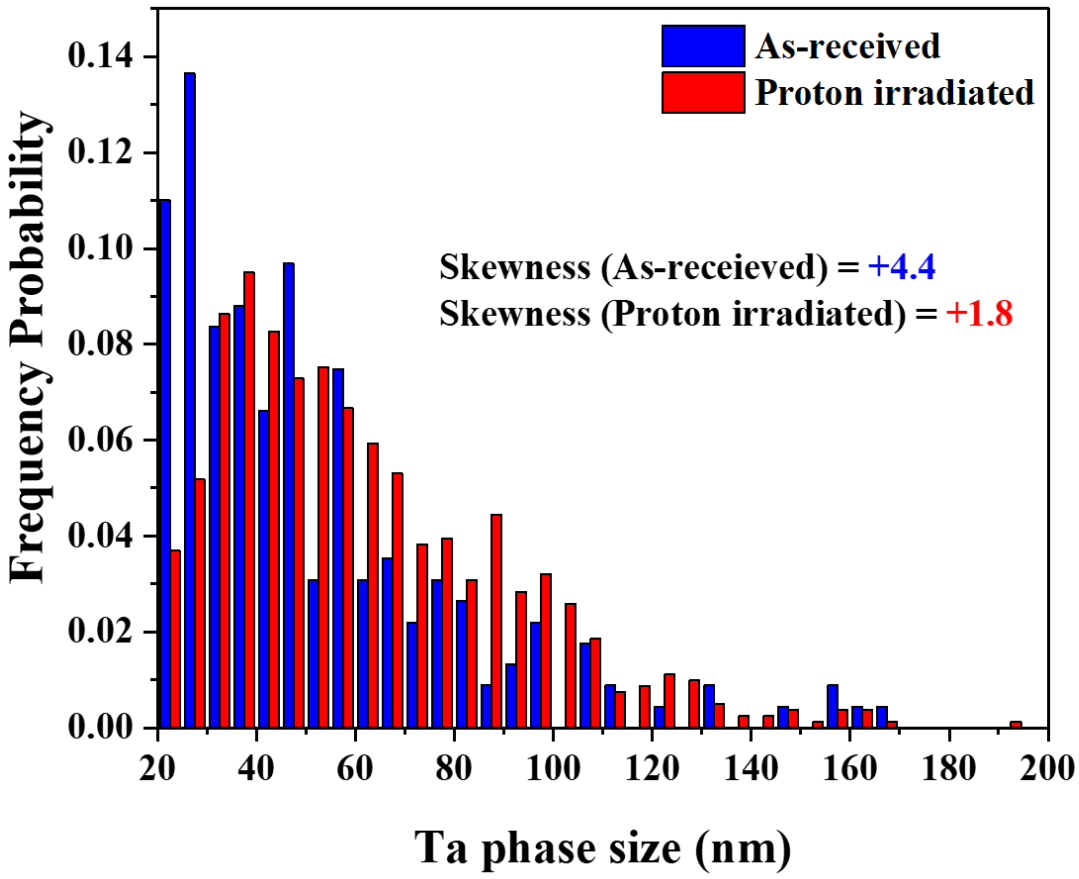

Figure 4.7: Comparison of Ta phase size distribution from both the samples. The decrease in skewness indicates the Ta phase size distribution shifting from left to right after irradiation, which means an overall increase in the size of the Ta phases.

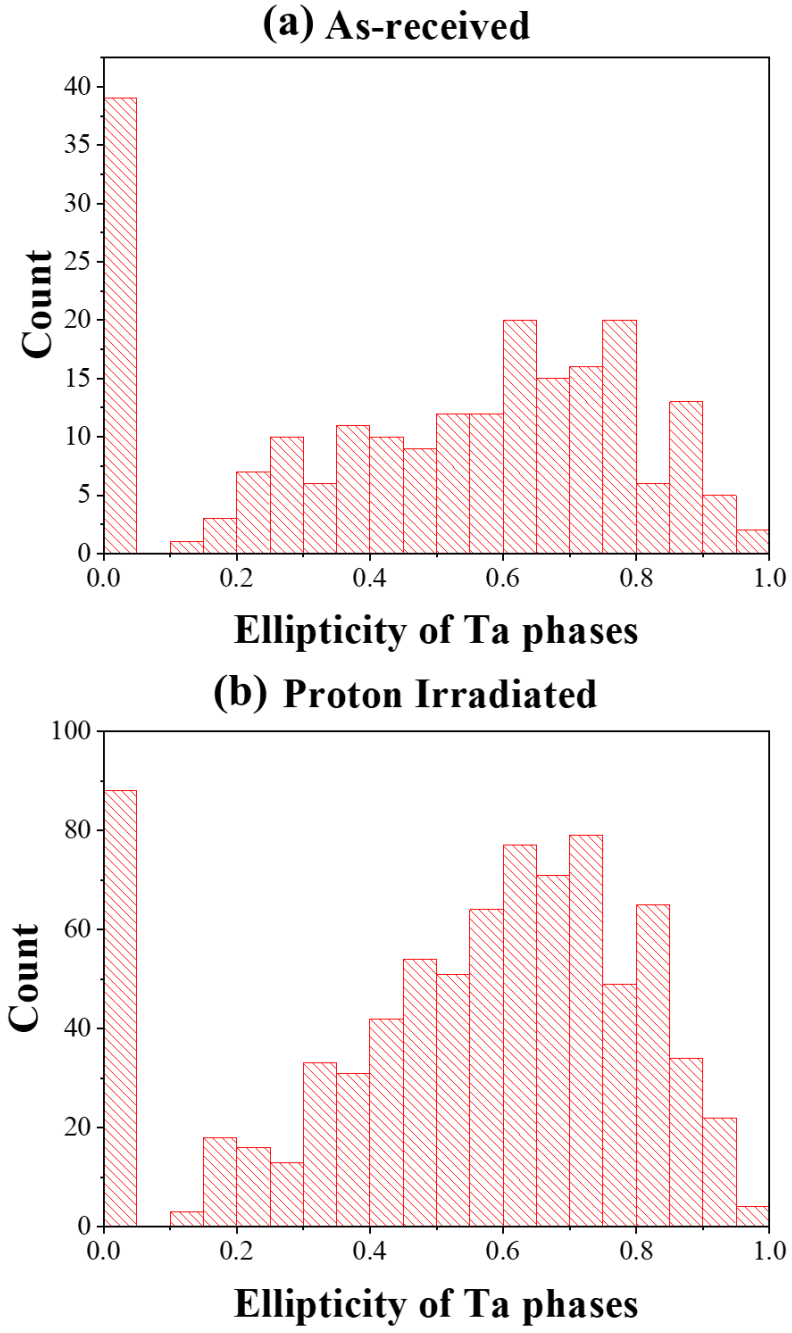

Figure 4.8: Ellipticity distribution of Ta phases in (a) As-received sample and (b) Proton irradiated sample. The increase in probability of higher ellipticity phases in the proton irradiated sample suggests loss of circular shape in the material after irradiation

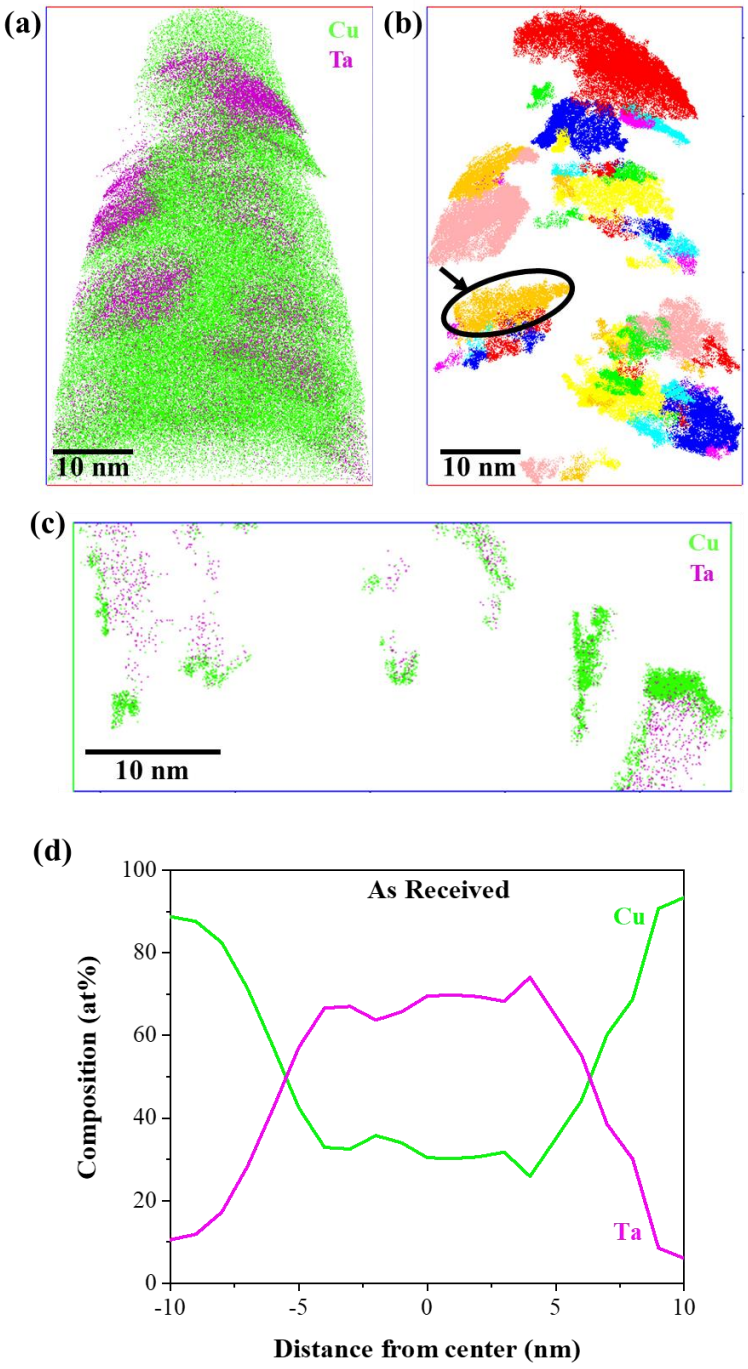

Figure 4.9: Representative APT tip from the as-received Cu-10at%Ta, showing (a) Reconstructed APT needle, (b) color coded indexed clusters in the reconstructed tip, (c) Spacial distribution of Cu and Ta around the cluster in a 5 nm thick slice, and (d) composition profile of cluster as marked in (b) [140].

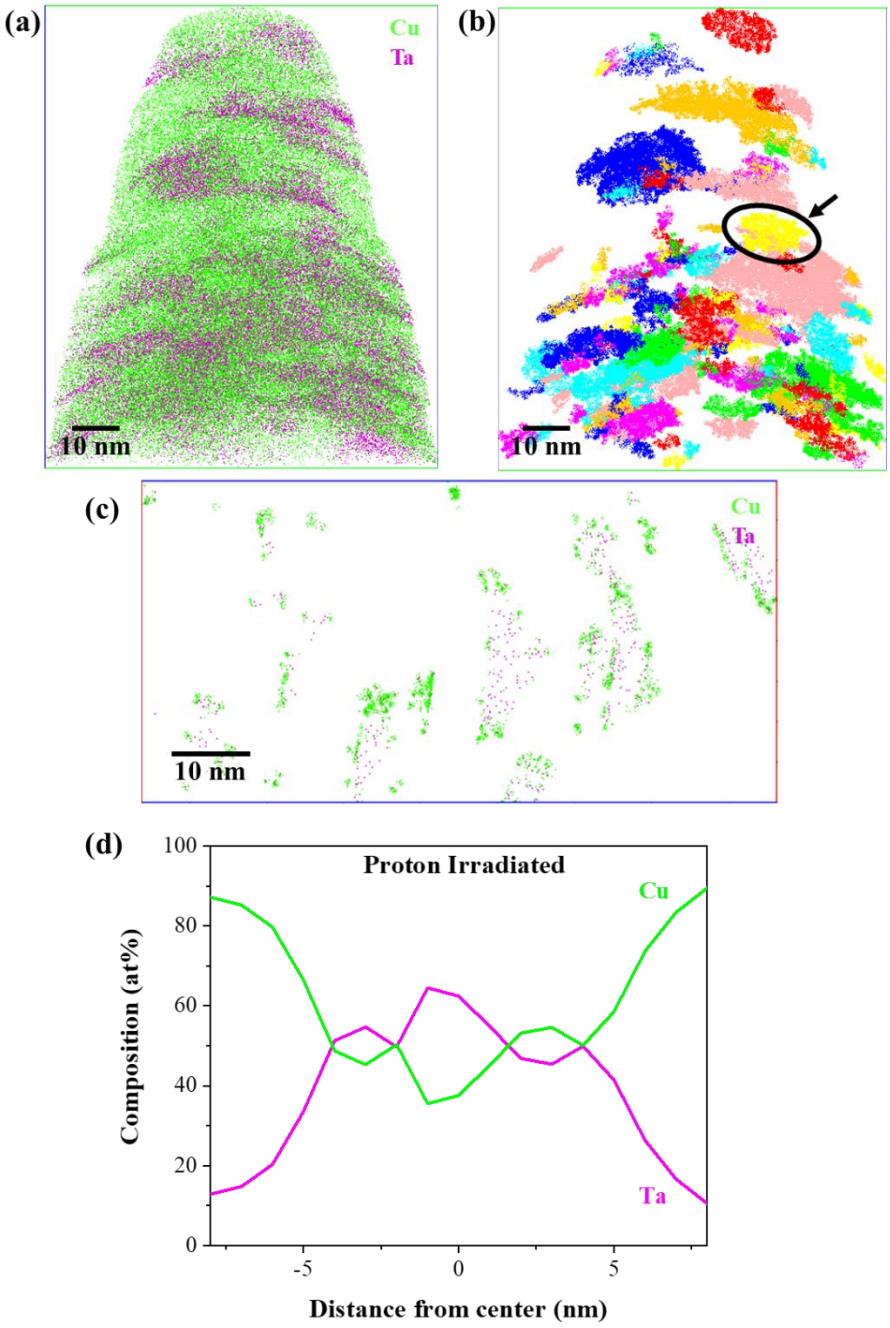

Figure 4.10: Representative APT tip from the proton irradiated Cu-10at%Ta, showing (a) Reconstructed APT needle, (b) color coded indexed clusters in the reconstructed tip, (c) Spacial distribution of Cu and Ta around the cluster in a 5 nm thick slice, and (d) composition profile of cluster as marked in (b) [140].

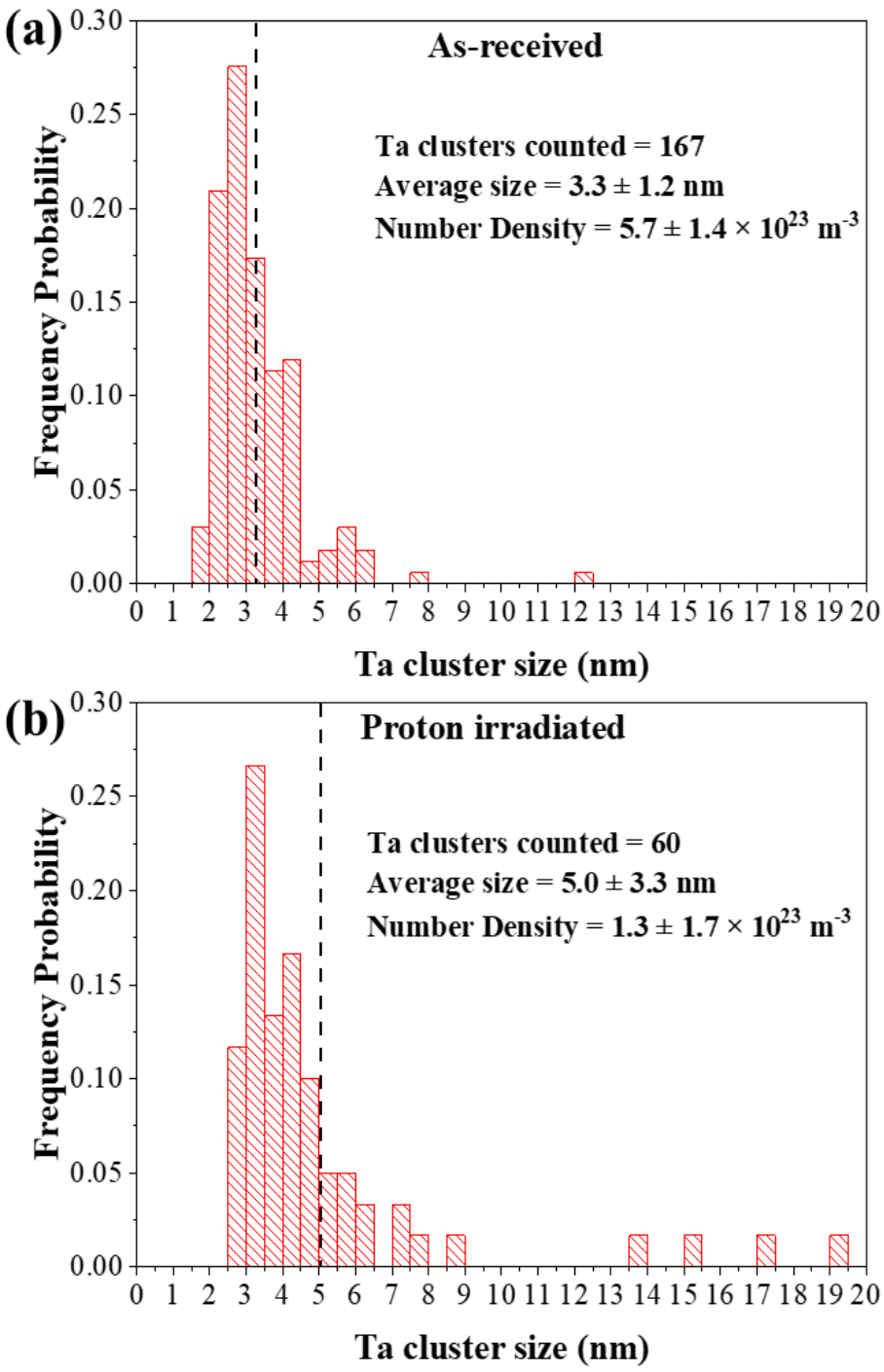

Figure 4.11: Size distribution of Ta nanoclusters in (a) as-received and (b) irradiated Cu-10at%Ta [140].

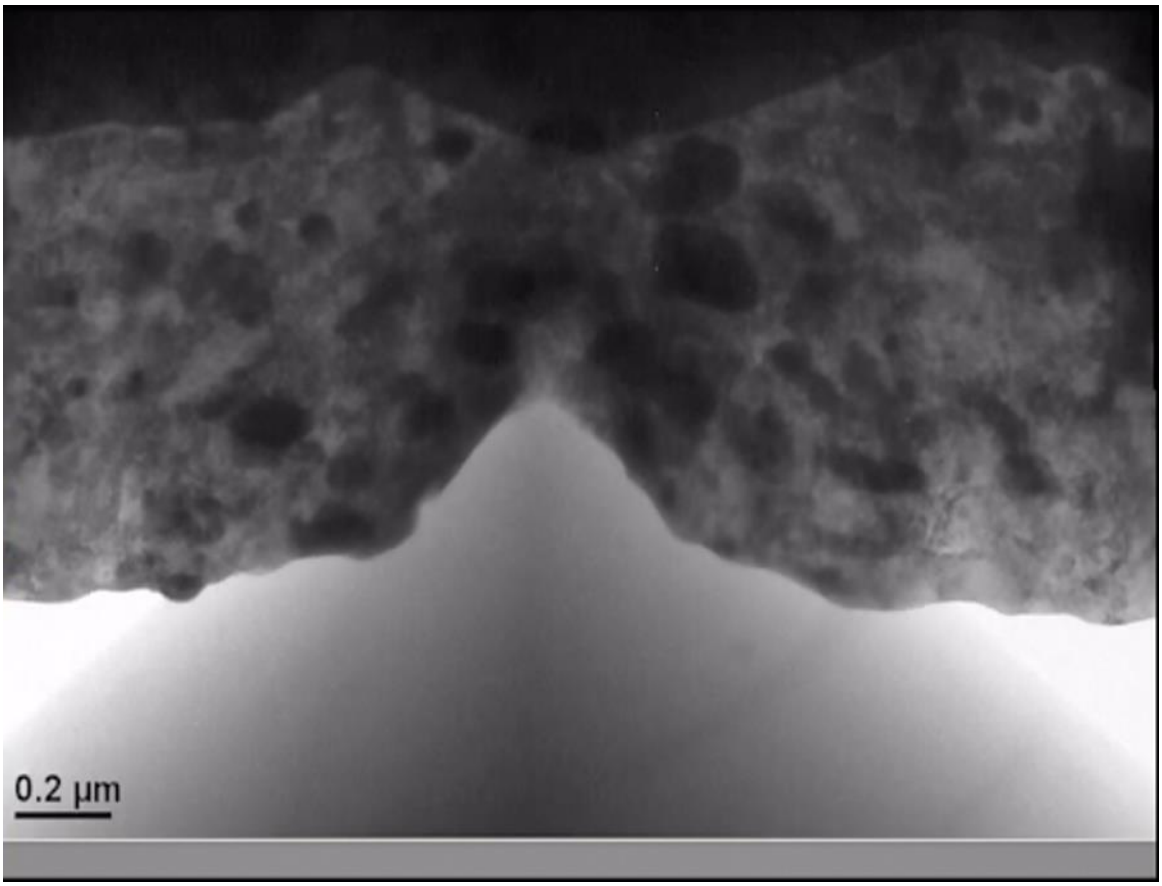

Figure 4.12: A pico-indentation experiment snapshot showing the deformation in the pico-indentation window. The dark contrast is from the Ta phases.

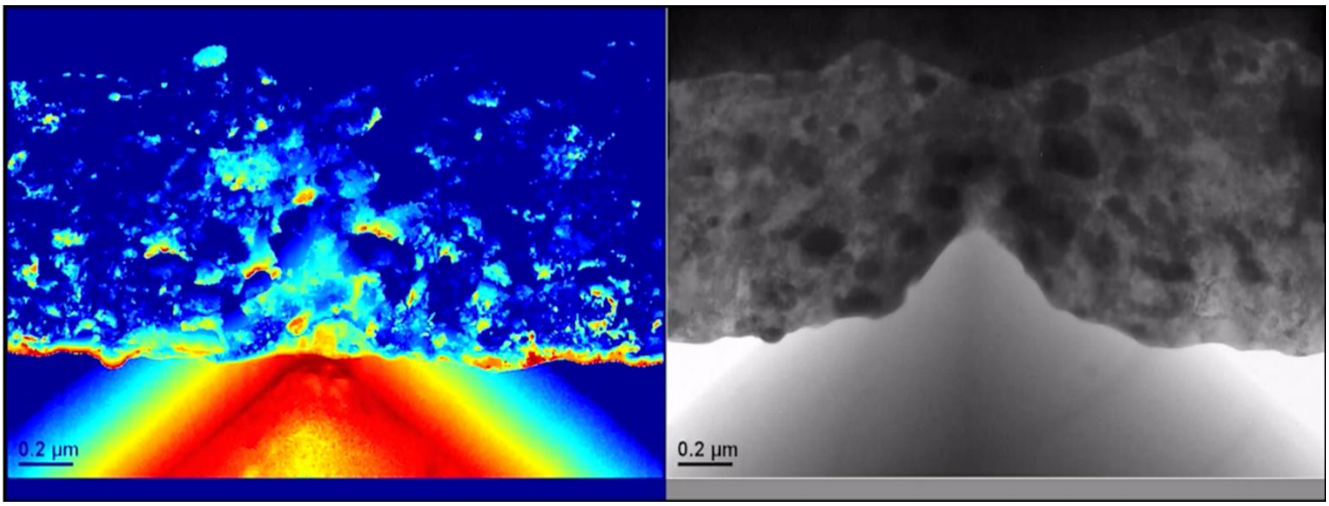

Figure 4.13: ViBE motion detection analysis of TEM *in situ* pico-indentation video taken in BFTEM mode. The crowns forming on the Ta phases after indentation indicate Ta phases moving through the microstructure parallel to the indenter tip without any signs of deformation.

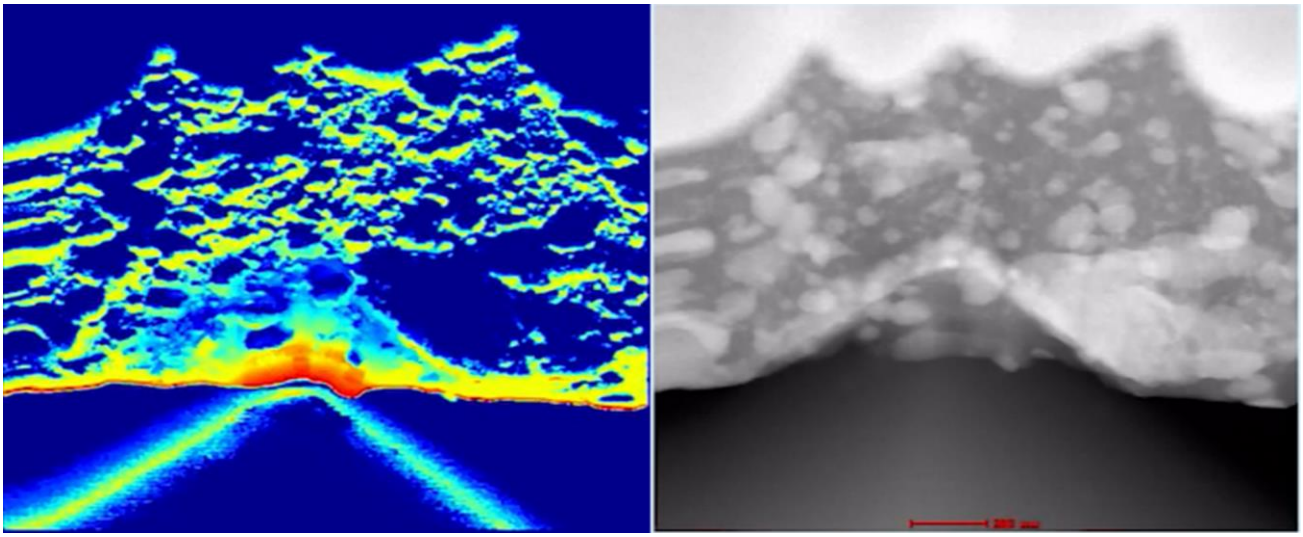

Figure 4.14: ViBE motion detection analysis of TEM *in situ* pico-indentation video taken in STEM mode. The formation of yellow regions in the Cu matrix signify deformation of the Cu matrix during pico-indentation.

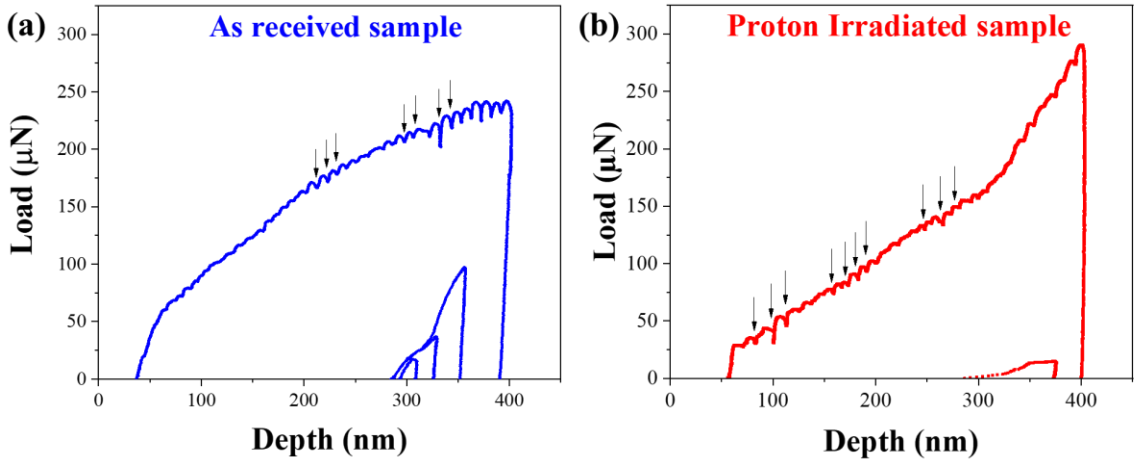

Figure 4.15: Mechanical response obtained from the nanoindentation experiments for (a) As-received sample and (b) Proton irradiated sample. The arrows indicate the load drops observed during the indentation.

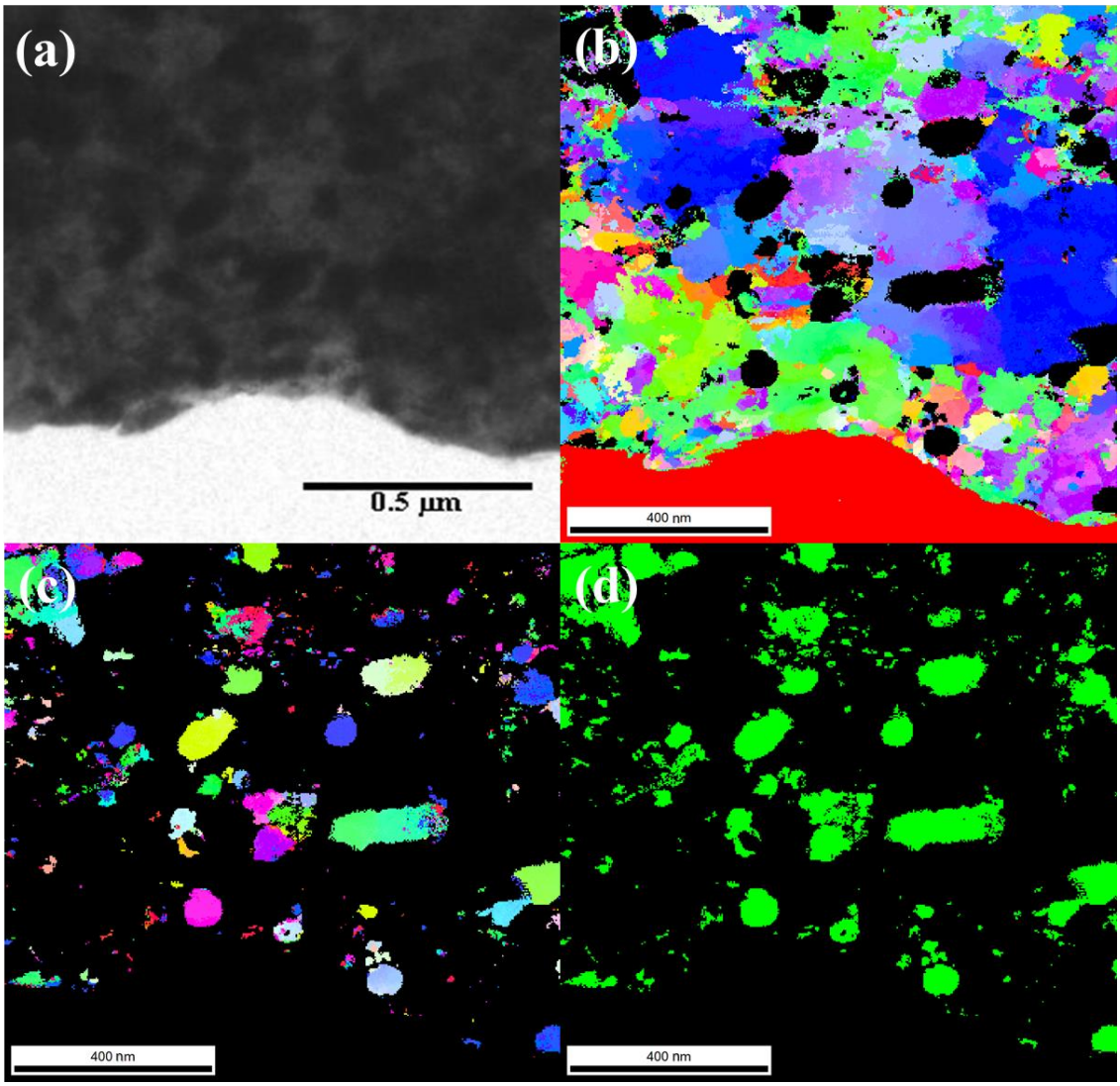

Figure 4.16: ACOM analysis during the picoindentation experiment. (a) Picoindentation window (b) Cu matrix orientation map (c) Ta particles orientation map and (d) Ta particles phase map. This particular set of data is for the proton irradiated sample.

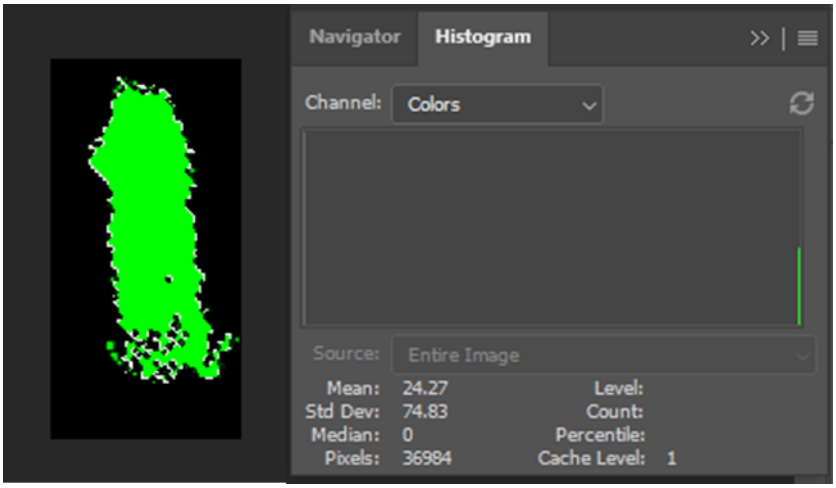

Figure 4.17: The magic wand feature in photoshop allows us to selectively choose the Ta particles and obtain the number of pixels to analyze the area of the Ta phase.

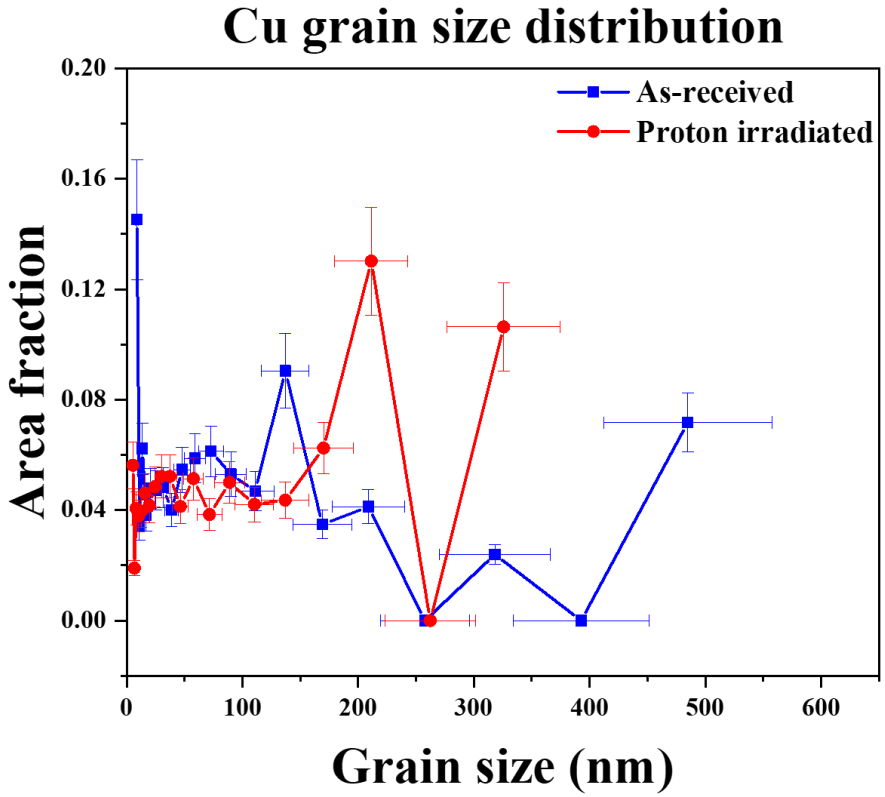

Figure 4.18: Cu grain size distribution calculated based on the Cu matrix orientation maps obtained from the ACOM analysis. Both samples show similar distribution signifying no changes were observed after irradiation in the Cu grain size.

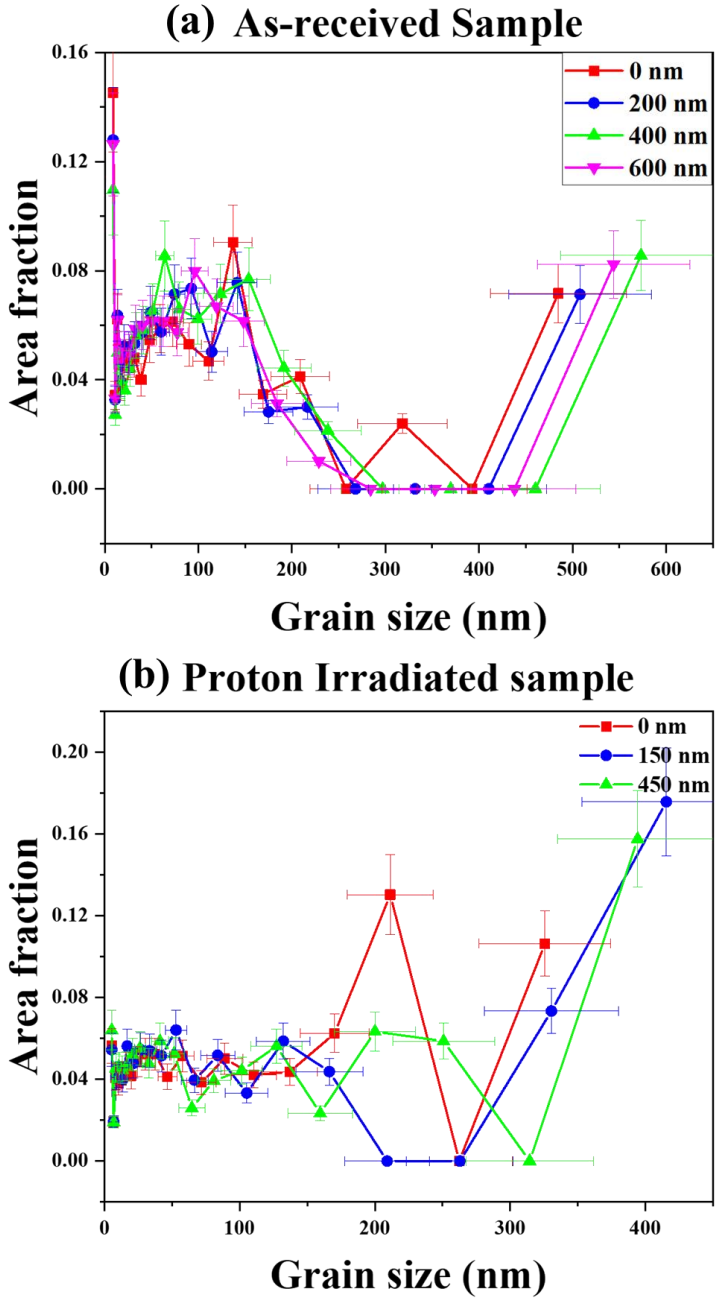

Figure 4.19: Cu grain size distribution calculated at different indentation depths based on the Cu matrix orientation maps obtained from the ACOM analysis. In both the samples, the distribution stays fairly the same but the larger grains show decrease in size with increasing indentation depth signified by the distribution shifting towards the left.

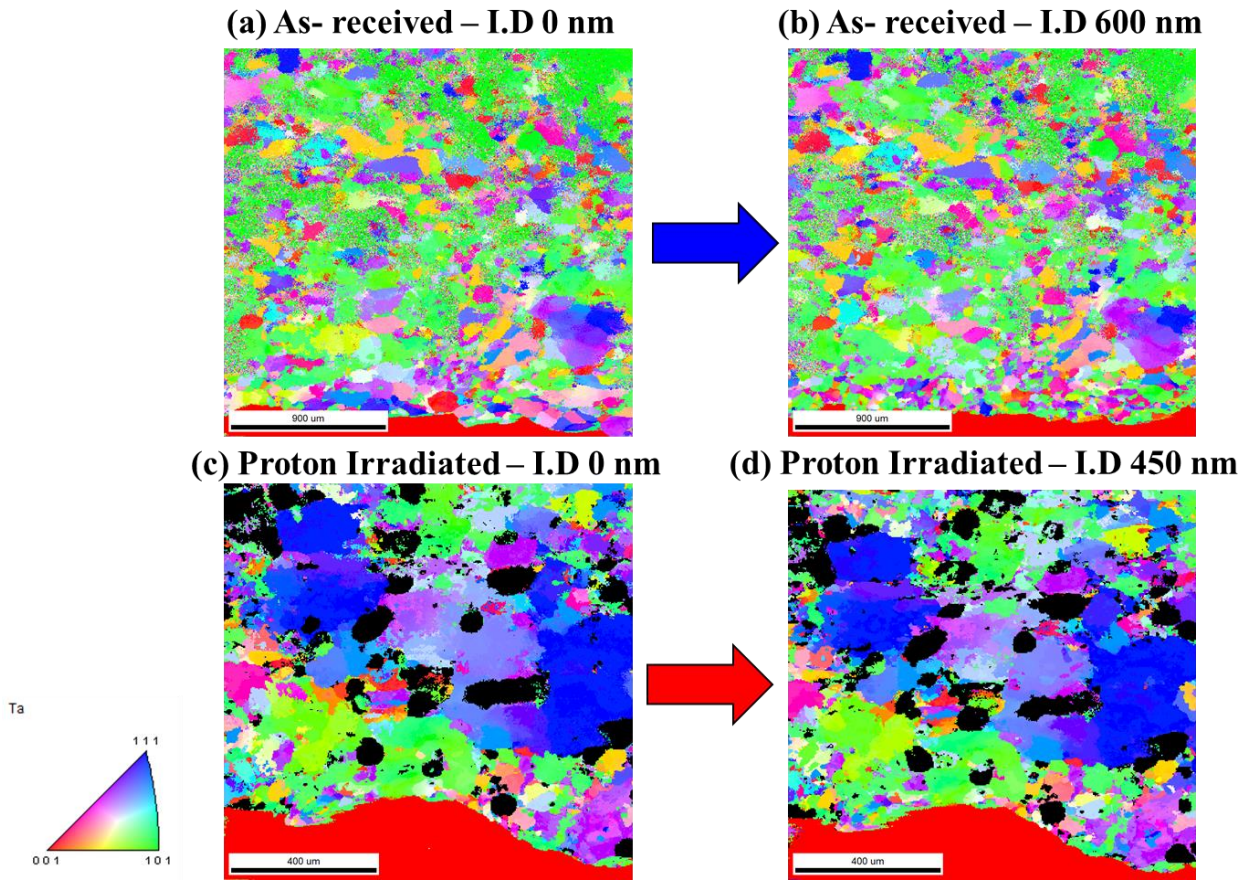

Figure 4.20: (a), (b) Orientation maps from the as-received sample at the indentation depth of 0 nm and 600 nm, respectively. (c), (d) Orientation maps of proton irradiated sample at the indentation depth of 0 nm and 450 nm, respectively. Both instances show there is no evidence of change in orientations after deformation.

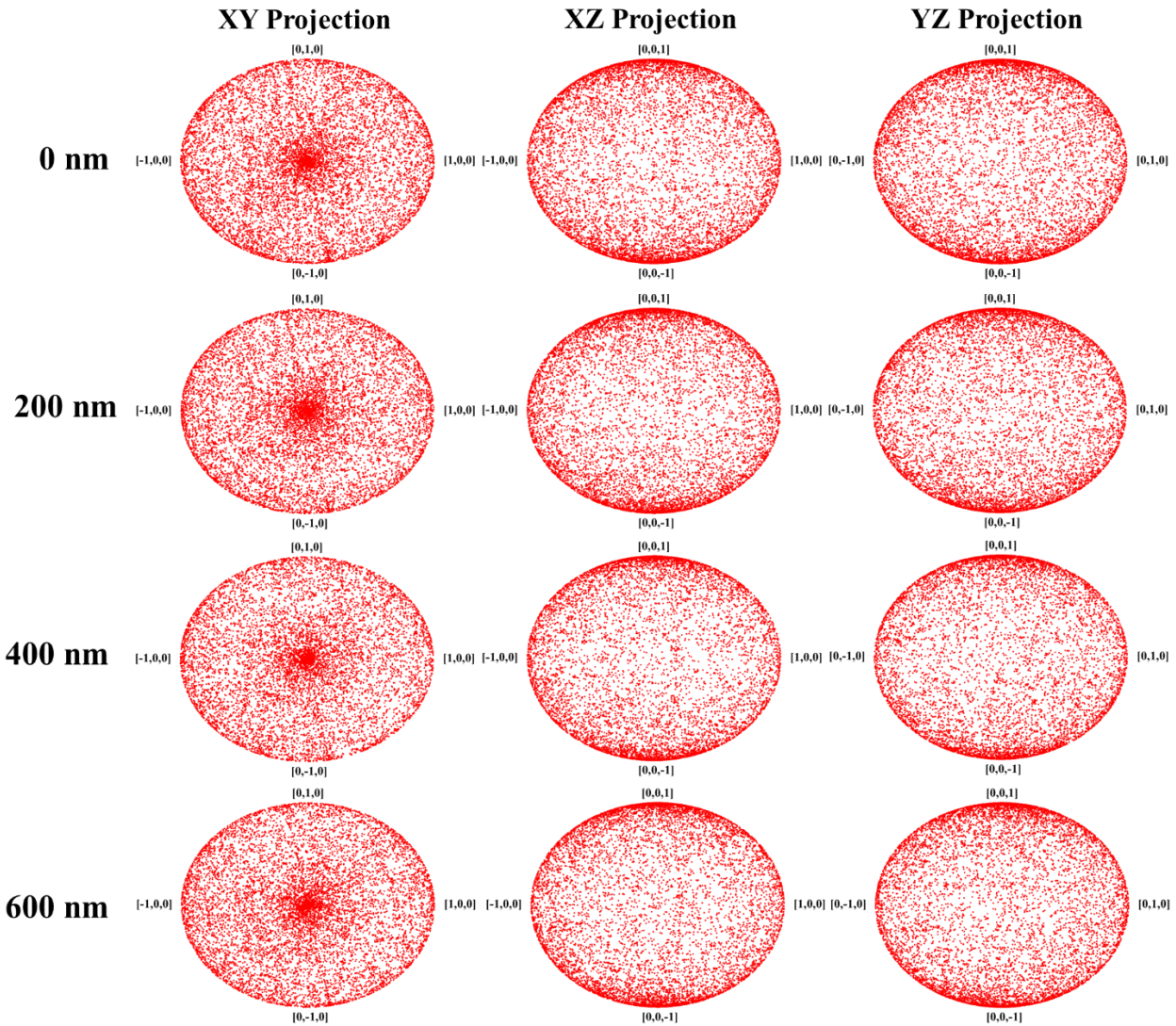

Figure 4.21: Cu grain orientation distribution in the as-received sample at different indentation depths. The orientation distributions stay the same throughout the indentation depth signifying absence of grain rotation after indentation.

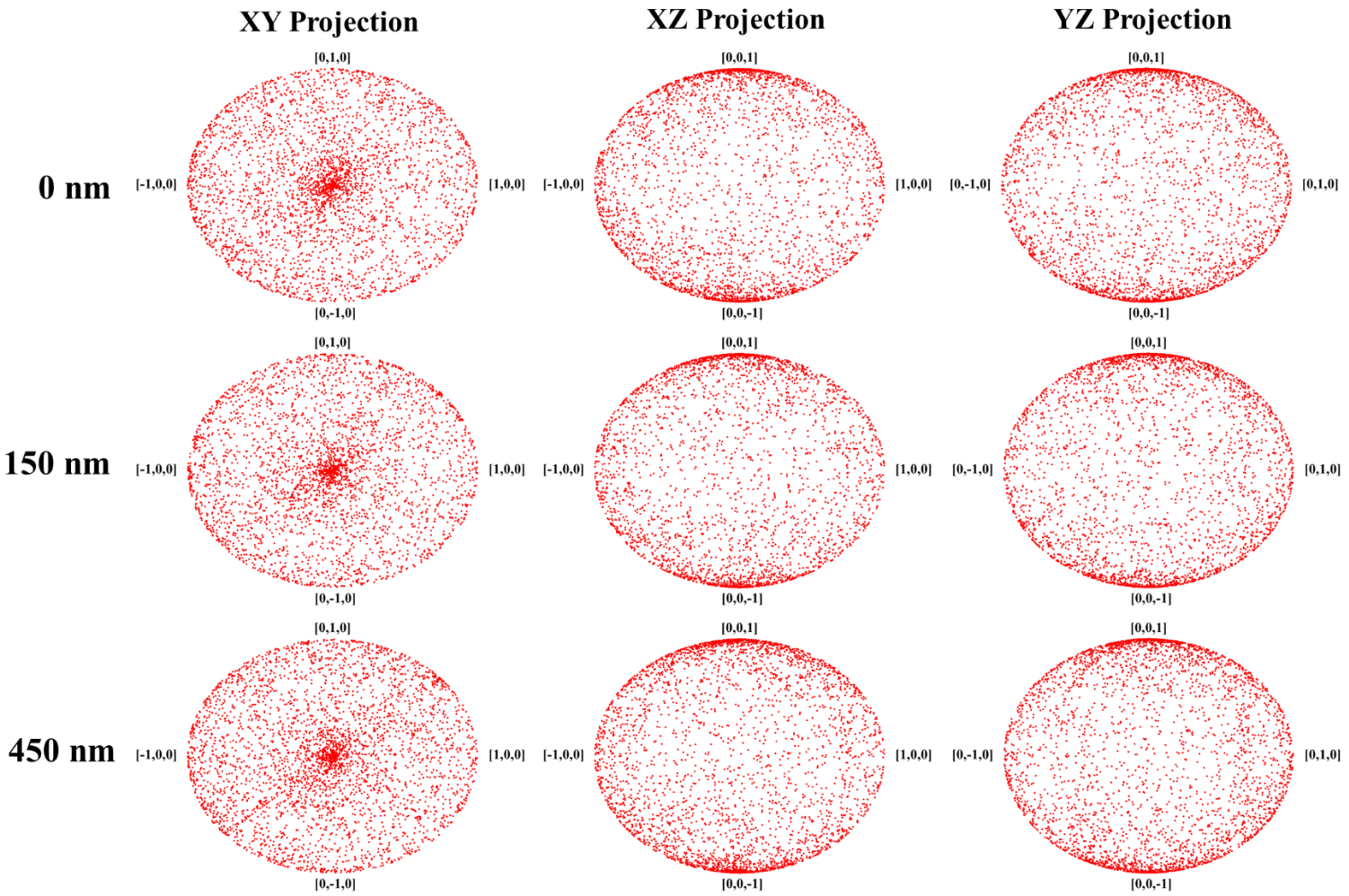

Figure 4.22: Cu grain orientation distribution in the proton irradiated sample at different indentation depths. The orientation distributions stay the same at the different indentation depths signifying absence of grain rotation due to indentation.

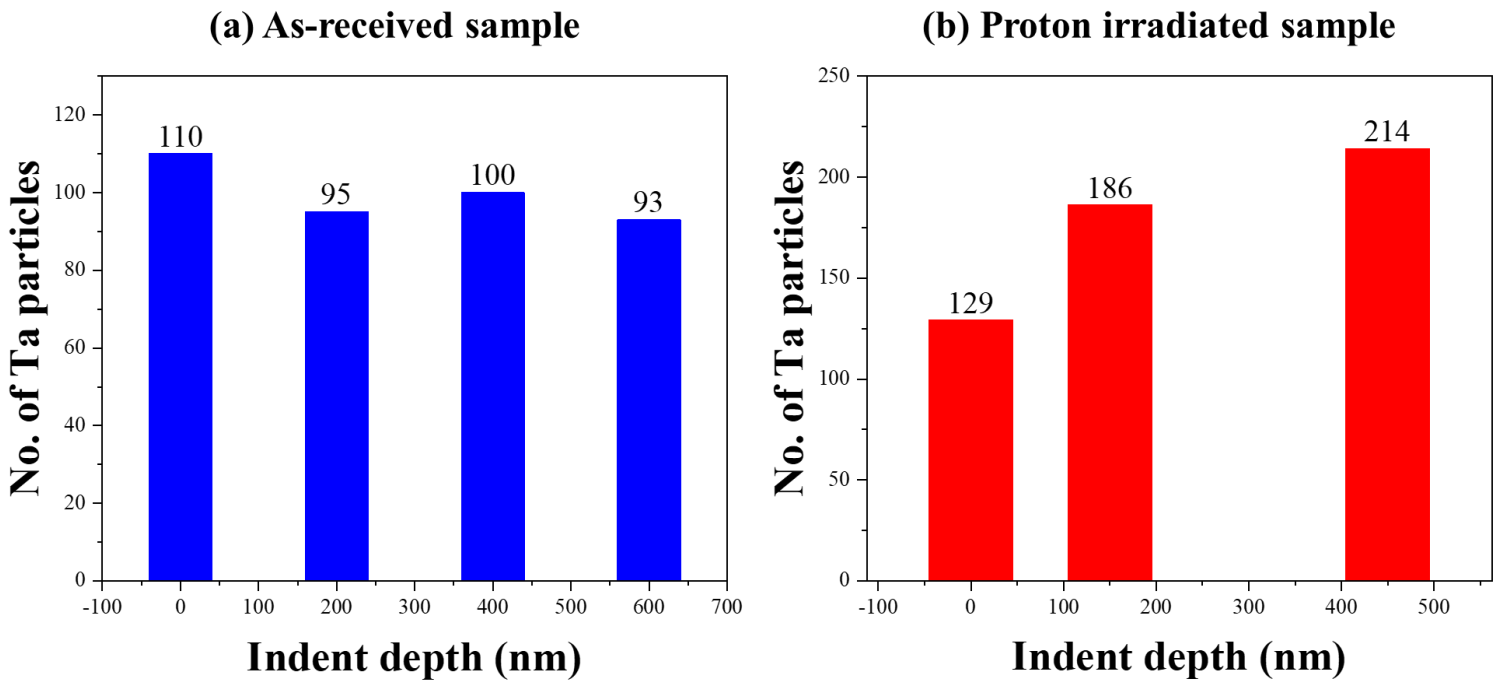

Figure 4.23: Ta particle density observed at different indentation depths in (a) As-received sample and (b) Proton irradiated sample.

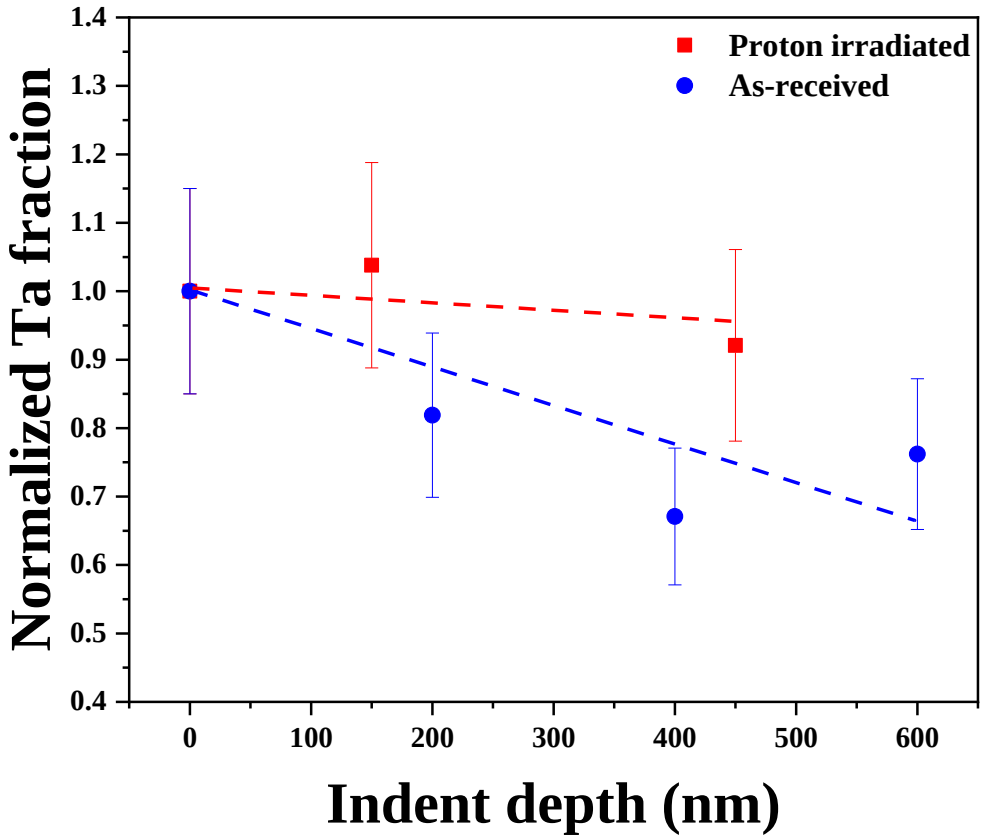

Figure 4.24: Overall Ta area fraction at different indentation depths obtained from the Ta phase maps from the ACOM analysis for both samples. The Ta area fraction decrease in the as-received sample is much higher than that in the proton irradiated sample.

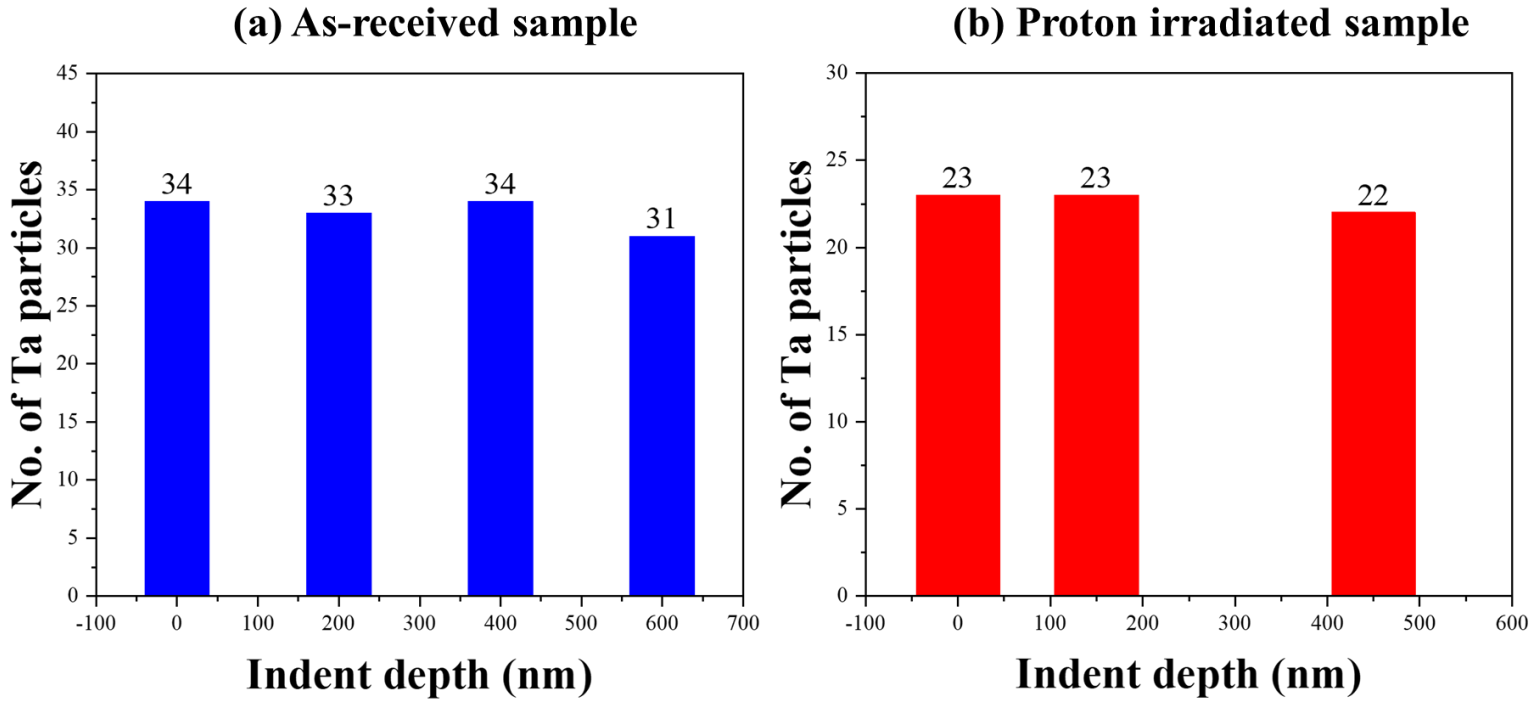

Figure 4.25: Number density of Ta particles > 20 nm in (a) As-received sample and (b) Proton irradiated sample. Both samples show stability in the number density of Ta particles > 20 nm after indentation.

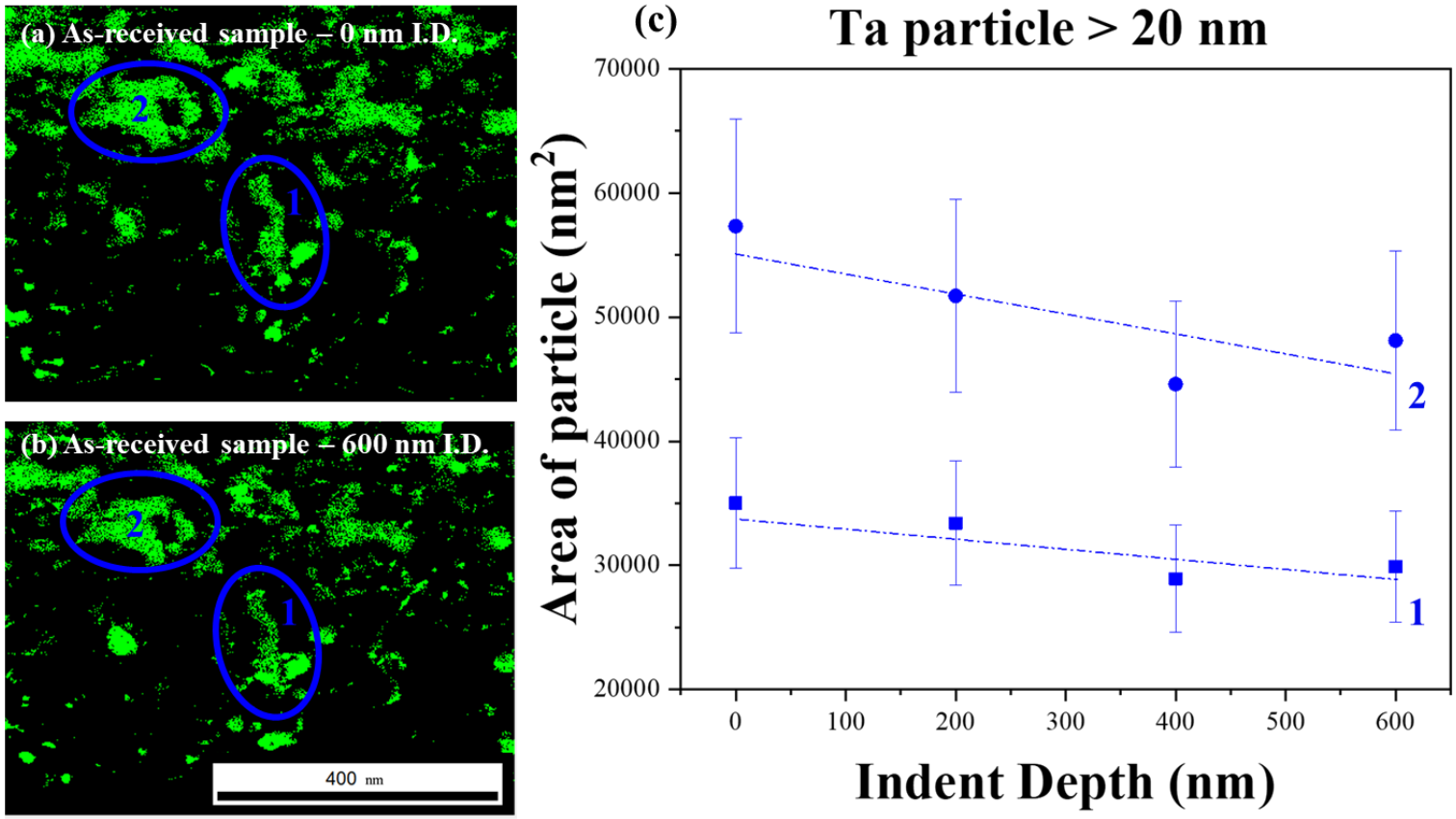

Figure 4.26: (a), (b) Ta phase maps for the as-received sample at indentation depths of 0 nm and 600 nm, respectively. (c) Change in Ta area fraction with increasing indentation depth for phases marked in (a), (b). The refining of Ta phases is observed with increasing indentation depth.

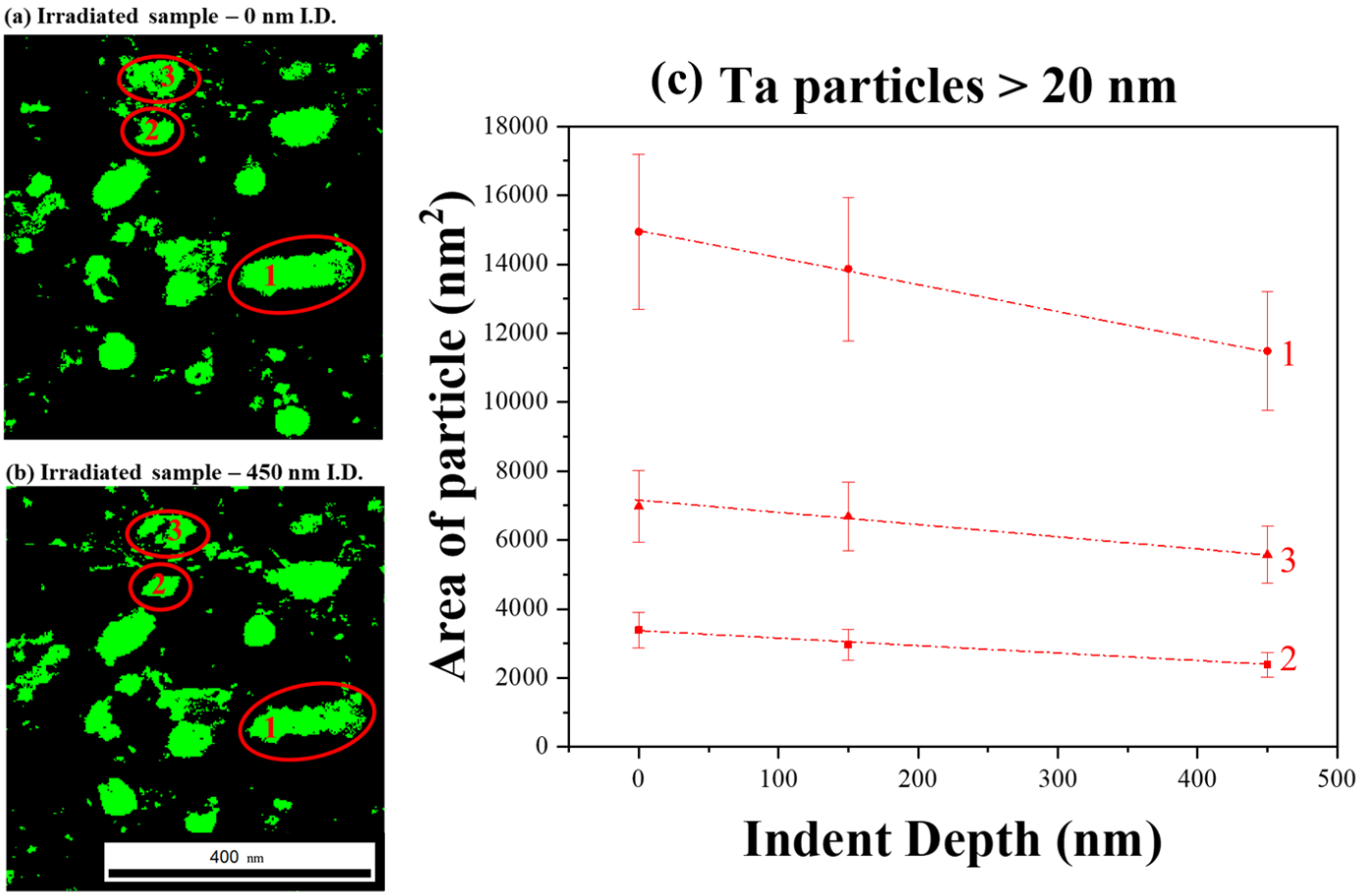

Figure 4.27: (a), (b) Ta phase maps for the proton irradiated sample at indentation depths of 0 nm and 450 nm, respectively. (c) Change in Ta area fraction with increasing indentation depth for phases marked in (a), (b). The refining of Ta phases is observed with increasing indentation depth.

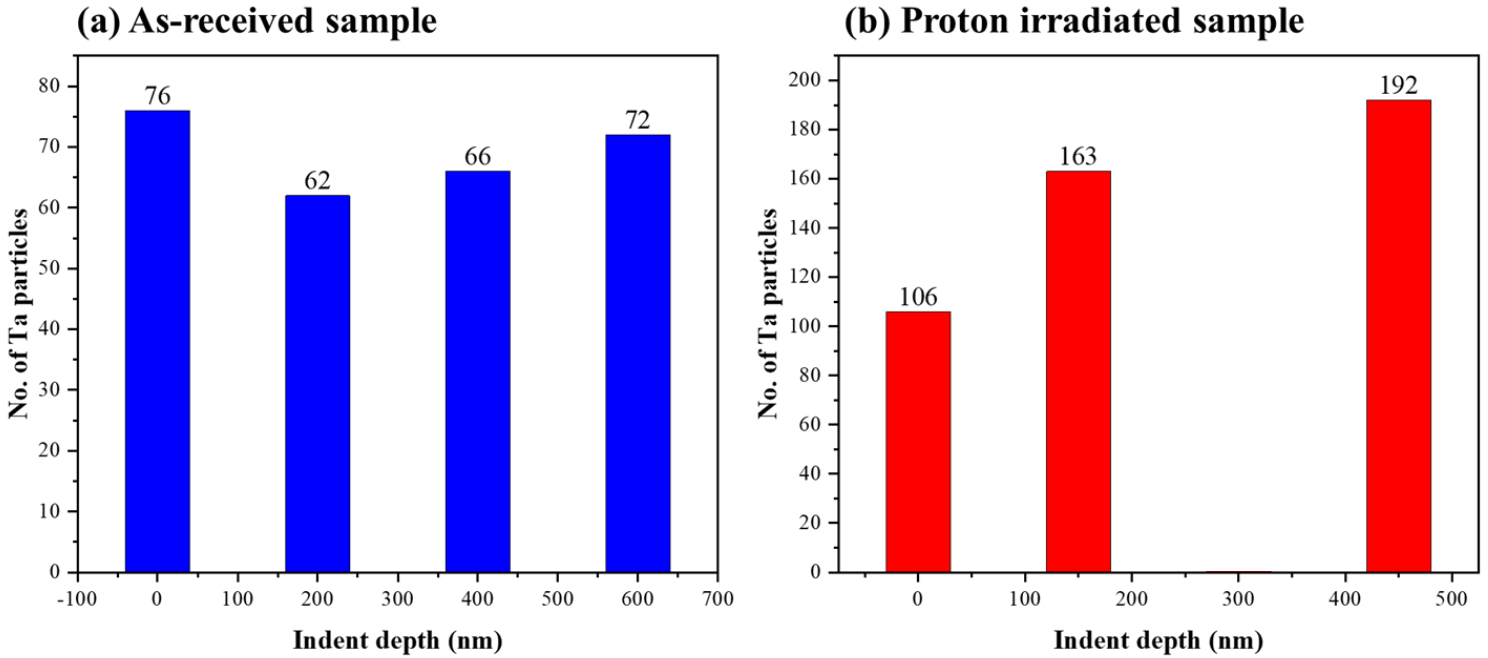

Figure 4.28: Density of Ta nanoclusters in (a) As-received sample and (b) Proton irradiated sample. The Ta nanoclusters in the as-received sample do not change with indentation depth signifying the nanoclusters stability, whereas the Ta nanoclusters in the proton irradiated sample increase with indentation depth, indicating the formation of newer Ta nanoclusters.

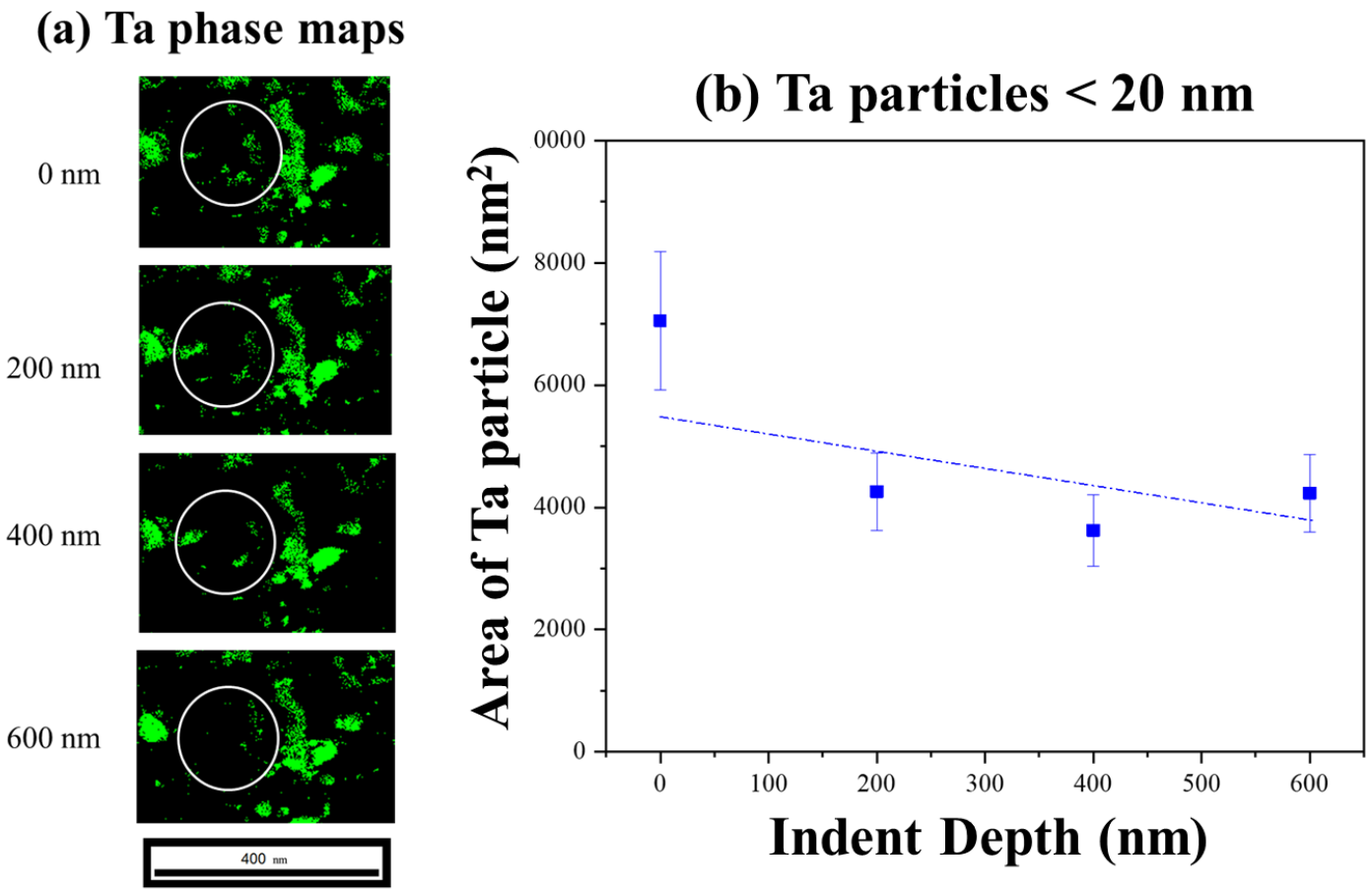

Figure 4.29: (a) Ta phase maps for the as-received sample at different indentation depths. The circled region indicates the particles counted for the Ta particle area for Ta nanoclusters. (b) The graph shows the change in the Ta nanocluster area with increasing indentation depth. The Ta nanoclusters exhibit stability and do not display any appreciable difference in the as-received sample.

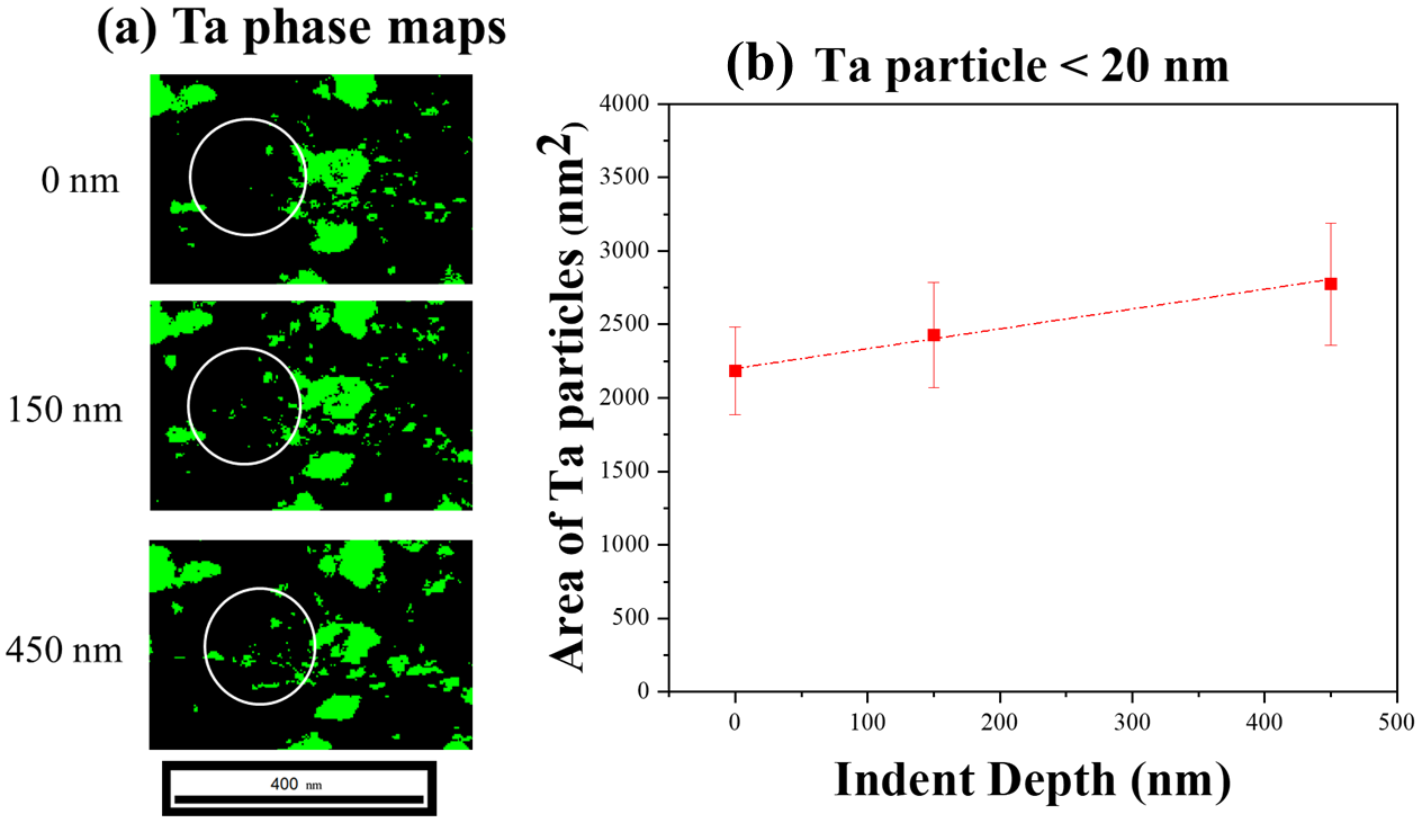

Figure 4.30: (a) Ta phase maps for the proton irradiated sample at different indentation depths. The circled region indicates the particles counted for the Ta particle area for Ta nanoclusters. (b) The graph shows the change in the Ta nanocluster area with increasing indentation depth. The existing Ta nanoclusters exhibit stability and do not display any appreciable difference, but the Ta nanoclusters area increases as newer clusters are formed with the indentation in the proton irradiated sample.

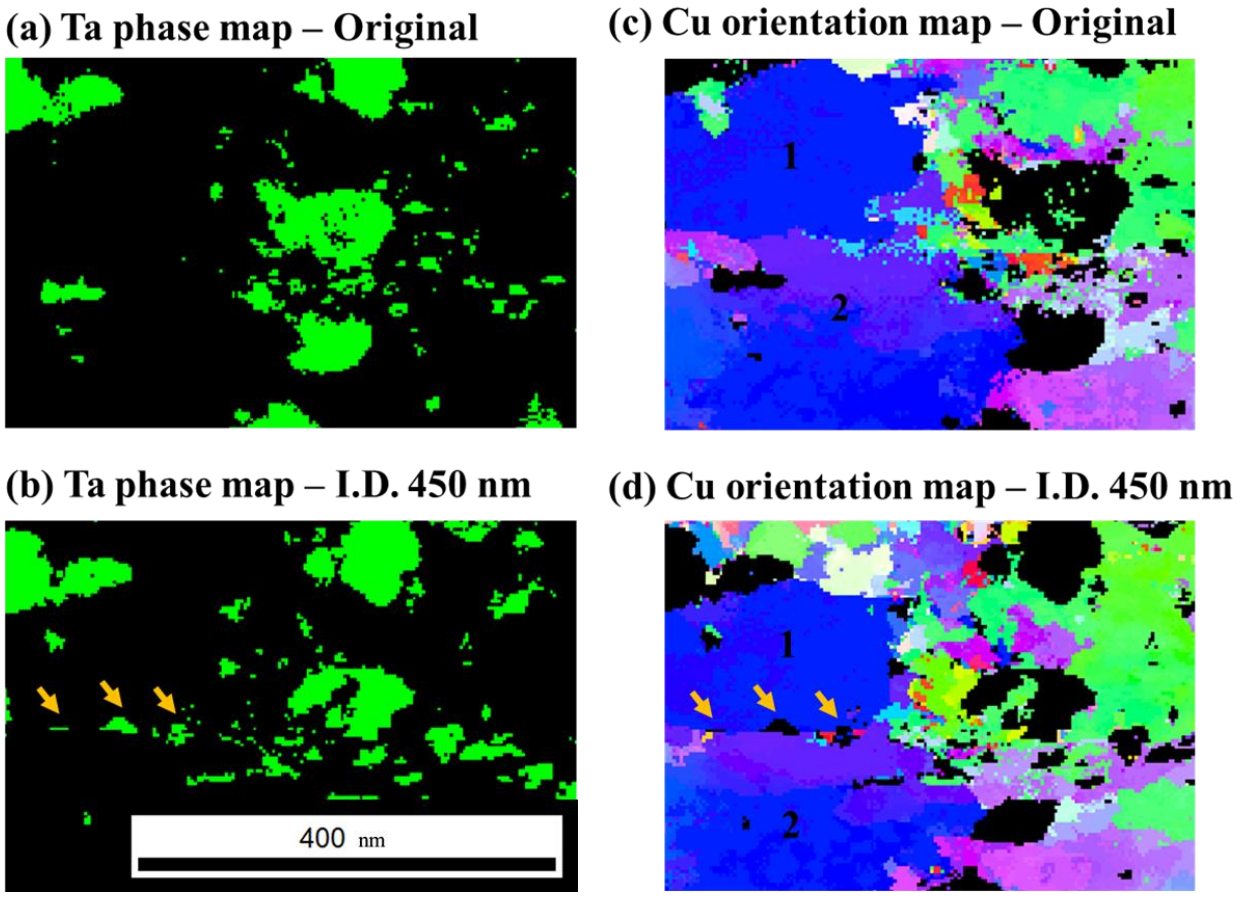

Figure 4.31: (a), (b) Ta phase maps for proton irradiated sample showing the newly formed Ta nanoclusters at indentation depths of 0 nm and 450 nm, respectively. The yellow arrows in (b) indicate the newly formed Ta nanoclusters. (c) Cu matrix orientation maps showing the Cu grains 1 and 2 at indentation depth of 0 nm. (d) At the indentation depth of 450 nm, the Cu matrix orientation map shows that the newly formed Ta nanoclusters form at the Cu grain boundaries of Cu grain 1 and 2 after deformation.

5. DISCUSSION

In this section, we will be discussing the changes in microstructure in the Cu-10at%Ta alloy after proton irradiation, effect of irradiation on the mechanical properties of the alloy and the alleviation of irradiation induced changes in the microstructure post deformation. A part of this section has already been published in the following journal article:

- P. V. Patki, Y. Wu, J.P. Wharry, Effects of proton irradiation on microstructure and mechanical properties of nanocrystalline Cu–10at%Ta alloy, Materialia. 9 (2020) 100597. https://doi.org/10.1016/j.mtla.2020.100597.

As discussed in the previous chapter, after proton irradiation, Cu grains do not show any irradiation induced defects, dissolution of Ta nanoclusters and Ostwald ripening of the Ta phases is observed. TEM in situ pico-indentation reveals, deformation leads to Ta phase thinning and recovery of Ta nanoclusters resulting in alleviation of irradiation induced defects. This section discusses the mechanisms behind these phenomena and helps establish proof based on previous literature studies.

5.1 Microstructure Evolution

5.1.1 Cu grain stability and irradiation-induced defects

Numerous nanocrystalline Cu alloys and nanocomposites show irradiation-induced grain growth, even at irradiation temperatures as small as ~$0.2T_m$ [13]. The preservation of nanocrystallinity in the Cu-10at%Ta is credited to the stabilizing effects of the Ta phases and nanoclusters, much like these phases and nanoclusters exhibit Zener pinning of Cu grain boundaries under only thermal extremes [6,11]. Though after irradiation we have dissolution of Ta nanoclusters which would mean the Cu grains aren't as effectively pinned as they were before,

grain growth should be observed. We can calculate the equilibrium grain size associated with Zener pinning of the Ta nanoclusters, using Eq. 5.1:

$$D = \alpha 4r/3f \quad \text{(Eq. 5.1)}$$

Where r is the radius of the Ta nanoclusters, f is the volume fraction of the nanoclusters, and α is a constant dependent on grain boundary energy, average curvature of the nanoclusters, nanocluster distribution, and shape, and normally ranges between 0.25 to 0.5. Bear in mind, however, that both r and f have relatively large measurement error associated with the values, which propagate through the above equation according to error propagation rules. Based on Eq. 5.1, the equilibrium grain size in the as-received sample is found to range between 58 nm ± 149 nm and 115 nm ± 299 nm whereas for the proton irradiated sample the equilibrium grain size ranges from 90 nm ± 278 nm and 180 nm ± 557 nm.

Clearly, the error bars are larger than the equilibrium grain size values themselves. As such, we cannot have statistical confidence in the calculated change in grain size due to irradiation-induced dissolution of nanoclusters. But even if one ignores the uncertainty and interprets the above table to predict grain growth due to nanocluster dissolution, this contradicts our TEM observations. We believe this can be reconciled as an artifact of the APT cluster analysis. That is, during APT cluster analysis, we set N_{min} = 20 atoms (for both the as-received and irradiated specimens), so any clusters containing fewer than 20 atoms are not counted as clusters. It is expected that the irradiated specimen will have more sub-20-atom clusters than the as-received specimen, which would result in a more extreme under-accounting of nanocluster volume fraction (f) in the irradiated specimen. Consequently, the calculated equilibrium grain size D would artificially increase for the irradiated specimen. For reference, Koju *et al*. [142] show that Ta nanoclusters as small as r = 0.43 nm can effectively pin the grain boundary, but a cluster of this

diameter contains fewer than 20 atoms (based on the Ta bcc crystal structure), and would thus be overlooked during APT cluster analysis.

The absence of irradiation-induced defects in Cu grains is attributed to the irradiation temperature and the nanocrystallinity of the material. It is well-known that irradiation causes the formation of stacking fault tetrahedra (SFT) in Cu and Cu alloys at extremely low doses [87–89,94]. However, the number density of SFTs and defects declines dramatically at irradiation temperatures ≥150°C, due to the swift diffusion of point defects from defect clusters developed during the displacement cascade [87,92,143,144]. Hence, few defects would be expected at the 500°C irradiation temperature. Furthermore, the nanocrystalline microstructure provides a high density of interfaces, including both Cu grain boundaries and Cu-Ta (fcc-bcc) phase boundaries. Nanocrystalline interfaces are a widely-used approach for engineering irradiation tolerance in materials by creating a high density of sinks for irradiation-induced defects [19,145]. Recently, Jin *et al*. [146] have described the process through which defect clusters, including SFTs, preferentially migrate to grain boundaries, where they are annihilated. But on the other hand, several studies have advocated that grain boundaries in Cu and other metals with similar stacking fault energy, are fairly weak defect sinks [41,42]. However, Han *et al*. [43], Fu *et al*. [44], and Demkowicz, *et al*. [45] have shown fcc-bcc phase interfaces can be effectively limitless sinks for irradiation-induced defects, enabling efficient Frenkel pair recombination. Hence, the defect-free microstructure seen in this study is attributed due to the existence of large number densities of bcc-fcc Cu-Ta interfaces. Defect-free irradiated microstructures analogous to those observed here, have also been noticed in comparable material systems, including dual-phase, immiscible, nanocrystalline Cu-Mo and Cu-W alloys irradiated with 1.8 MeV Kr^+ over a wide temperature range ~20-1000°C [22–24], immiscible Cu-Nb nanolayered composites irradiated with ~20-400

keV He^+ ions [147–150] and a Cu-Al_2O_3 nanocomposite irradiated with 590 MeV protons [13]. Recent study by Srinivasan et al. also observed defect free structure and stable Cu grain size for the same Cu-10at%Ta irradiated with 4 MeV Cu^{2+} to a dose of 200 dpa at temperatures ranging from room temperature to 723K signifying enhanced stability of the microstructure at even higher doses and denser damage cascades.

5.1.2 Ta particles evolution

Stability of the particle size and number density of Ta particles in *in situ* annealing studies up to 400°C by Rajagopalan *et al*. [151] and 600°C creep tests from Darling *et al*. [53] on the same Cu-10at%Ta alloys, have both been observed. Hence, the development of Ta particles seen herein can be attached to irradiation. In order to comprehend mechanisms of irradiation evolution of Ta particles, it may be useful to consider the irradiation evolution of the nanoclusters in oxide dispersion strengthened (ODS) alloys, which have comparable sizes and number densities as the Ta particles herein. A latest review of ODS irradiation experiments has discovered significant mechanisms that influence the irradiation evolution of nanoclusters: (a) ballistic dissolution, (b) irradiation enhanced diffusion, which result in phenomenon such as Ostwald ripening, and heterogeneous nucleation [25]. One or more of these processes can be active simultaneously, reliant on the alloy and the irradiation conditions. The observed increase in size of Ta phases is attributed to the phenomenon of Ostwald ripening where the Ta phases grow due to the ballistically dissolved Ta nanoclusters which contribute towards the growth of the phases. The observed Ta nanocluster disordering and dissolution may be credited to the ballistic dissolution mechanism, in which ballistic collisions from irradiation damage cascades cause recoil displacement and disordering of nanoclusters [108,152–154].

Because Cu and Ta are immiscible [155], the studied behaviors can be related to the comparably immiscible binary Cu-W alloys. When irradiated with Kr^+ ions at temperatures $\lessapprox 0.8T_m$, nanocrystalline Cu-W alloys display irradiation-induced nucleation and growth of W-rich nanoclusters [22,23]. These observations of heterogeneous nucleation and Ostwald ripening of W nanoclusters may originally appear contradictory to the dissolution of Ta nanoclusters in the Cu-10at%Ta herein. But molecular dynamics (MD) simulations predict that the interdiffusion coefficient for Ta into Cu is lower than that for Cu into Ta [156]. On The Contrary, the interdiffusion coefficient for W into Cu is higher than that for Cu into W [157]. This implies that W atoms knocked out from W nanoclusters can diffuse through Cu to re-join a nanocluster through the Ostwald ripening mechanism. On the other hand, Ta atoms knocked out from Ta nanoclusters cannot diffuse as easily through crystalline Cu to re-join a Ta nanocluster (some studies have even indicated that Ta interdiffusion in Cu must occur along accelerated routes such as dislocations or grain boundaries [10]). Hence, Ostwald ripening competes with ballistic dissolution, leading to the irradiation-induced nucleation and growth of W nanoclusters in Cu.

But in the Cu-Ta system, due to the bimodal distribution of Ta particles, we have two opposite behaviors. As the smaller nanoclusters have a higher interfacial energy (hence, less stable) due to the thermodynamic drive to minimize surface area and surface tension, Ostwald ripening is less significant, leading to a supremacy of ballistic dissolution and the observed irradiation-induced reduction of Ta nanocluster number density. Whereas in the Ta phases, as these phases are incoherent, they are thermodynamically more stable and hence with irradiation Ostwald ripening becomes more prominent as compared to ballistic dissolution hence an overall increase in the Ta phase size is observed. A study by Srinivasan et al. [158] showed that after irradiation of Cu-Ta system with Cu^{2+} ions at 450°C, segregation of Ta atoms at the grain boundaries was found due to

irradiation enhanced diffusion. Due to the size difference between a Cu and Ta atom, it is energetically more favorable for a Ta atom to sit at the grain boundary. Hence, Ta atoms which are ballistically ejected from the Ta nanoclusters sit at the grain boundary and can then contribute towards the growth of Ta phases by diffusion along the grain boundaries.

5.2 Deformation-based alleviation of irradiation induced changes

5.2.1 Mechanical test response

In the pico-indentation experiments, we can observe that the Ta phases remain undeformed, whereas most deformation occurs in the Cu matrix. This is expected as the Ta particles of size ~ 56 nm exhibits a hardness of 4.1 GPa, which is way higher as compared to pure nanocrystalline Cu of grain size ~ 70 nm having a hardness of 1.35 GPa. Similarly, Verhoeven et al. [159] studied the powder processed Cu – Nb immiscible system in which they only observed deformation of the Cu matrix, whereas the Nb particles showed no signs of co-deformation after the wire drawing process. Though at higher deformation rates of those implied in processes such as Severe Plastic Deformation and High-Pressure Torsion, co-deformation of Nb particles has been observed [100,102,103]. The deformation of Ta particles was not observed during tensile testing of the Cu-3at%Ta alloy system [160]. As the strain rates and deformation created during picoindentation are not like SPD/HPT methods, the absence of co-deformation of the Ta phase is expected. The load drops observed in both the samples represent dislocations burst events due to the dislocations exiting through the surface of the window. Similar serrated load-displacement curves have been observed during TEM *in situ* pillar compression of Fe-9%Cr and Cu-10at%Ta [31,32].

Many studies show that nanocrystalline materials deform via grain rotation [161–164]. Still, the Cu matrix ACOM analysis reveals no change in orientation of the Cu grains surrounding the heavily deformed region, signifying the absence of grain rotation in the nanocrystalline Cu-

10at%Ta alloy system. Koju et al. [10,142] determined this to be due to the heavy pinning of the Cu grain due to the Ta nanoclusters. They also found with increasing Ta nanocluster concentration; the grain took an extended amount of time to be unpinned.

5.2.2 Ta phase refinement

Irradiation of the Cu -Ta alloy leads to an overall increase in the size of the Ta phases signifying Ostwald ripening of the Ta phases[25]. The effect of Ostwald ripening of the Ta phases on the mechanical properties of the material can be understood with the Hall-Petch relationship combined with the rule of mixture strengthening of the material. The contribution of Ta phases is mainly through the Rule of mixtures strengthening in which the hardness of the alloy is dependent on the alloying fraction of the secondary element and the hardness of the material. Patki et al. [140] did not observe a significant change in the phase fraction of the Ta phases. Therefore, a change in hardness of the Ta phases would affect the mechanical properties of the alloy. The difference in hardness of Ta phases can be calculated via the Hall-Petch relationship, which is dependent on $d^{-1/2}$, where '*d'* is the size of the Ta phase. Therefore, an overall increase in the size of the Ta phase would lead to the softening of the material.

Deformation leads to refinement of Ta phases and is seen in both the as-received sample and the proton irradiated sample. This process of thinning of the Ta phase in the Cu – Ta system has been described by Ashkenazy et al. [26] via dislocation glide mediated random walk process as observed in molecular dynamics simulations. Ashkenazy et al. state that at the Cu – Ta interface, the Ta atoms are carried away by dislocation glide, facilitated due to the increase in shear stress at the FCC – BCC interface. To accommodate this stress, metastable amorphous regions develop around the Ta particle. Though metastable amorphous regions weren't observed during this experiment, a decrease in confidence levels in diffraction patterns was observed at the Cu – Ta

interface in the crystal orientation maps during intermediate indentation steps. It is also stated that these atoms are not carried away by tangential dislocations as such but relatively move by dislocation glide, causing the Ta atoms to be way away from the parent particle. This phenomenon has been observed in Cu – Nb alloy systems during rolling [101,102], ultimately resulting in the refinement of the Nb precipitate, which is similar to the compression based deformation in the indentation process.

In Fig. 4.26 and 4.27, it is observed with decreasing Ta phase area in both the samples, the thinning rate for deformation decreases. Meaning larger particles are prone to thin quickly as compared to smaller Ta particles and would suggest the system going towards a certain equilibrium Ta phase size due to deformation. High-Pressure Torsion experiments on Cu – Nb system showed refinement of Nb particles to an equilibrium size of 10 nm, which was independent of the initial state of the system [29]. Self-selection of an equilibrium size explains particle refinement in the proton irradiated sample based on Ostwald ripening of the Ta phases after irradiation. The particle refinement in the as-received sample can be understood based on the fabrication temperature during the ECAE process. Studies show the effect of various temperatures used during the ECAE process on the microstructure of the Cu – 10 at%Ta system [11,165]. At a fabrication temperature of 700℃, the average Ta nanocluster size is found to be 7 nm, and Ta phase size is found to be 40 nm, whereas at a fabrication temperature of 900℃, the average Ta nanocluster size is found to be 17 nm and Ta phase size is found to be 122 nm [11]. This observation suggests with decreasing temperature, the equilibrium size of Ta particles after deformation would reduce as well. The acquired sample was processed through ECAE at 700℃ and then deformed at room temperature; hence refinement in the as-received sample was observed.

5.2.3 Recovery of Ta nanoclusters

The formation of nanosized Ta particles is only seen in the proton irradiated system due to the increased matrix concentration of Ta due to the dissolution of the nanoclusters during irradiation. Ashkenazy et al. [27] performed multiple simulations for the deformation in the Cu – Ta system with varying initial Ta concentrations. They found that under deformation, any Ta composition below 0.3at%Ta tends to stay in a single homogeneous distribution, whereas above 0.3at%Ta and up to 24at%Ta, under deformation, both the phases tend to separate out. In our case in the as-received sample, before deformation, the Ta matrix composition is 0.36at%Ta, and hence we do not see an appreciable recovery of nanosized Ta particles. In contrast, the proton irradiated sample has a Cu matrix composition of 0.7at%Ta, resulting in supersaturation of the Cu matrix with Ta, which under deformation results in the formation of Ta nanosized particles. Also, Ashkenazy et al. [27] tracked atoms separated from the Ta phases and found that even these atoms tend to segregate and contribute towards forming Ta nanoclusters, due to their affinity towards each other as they are immiscible in Cu.

In our experiment, nucleation of the Ta nanoclusters is only seen at the Cu grain boundaries, and no clusters develop inside the Cu grain. As during deformation, due to dislocation glide in the Cu matrix, the newly formed Ta nanoclusters would successively get separated, resulting in these nanoclusters being unstable. Therefore, stable clusters tend to form at the Cu grain boundaries as grain boundaries are excellent diffusion pathways for oversized atoms. Kale et al. observed the coarsening of Ta nanoclusters, which were along the grain boundary in the Cu-3at%Ta alloy system during tensile testing. They also simulated the tensile loading of the same sample to examine the coarsening of the Ta nanoclusters and found this to be due to accelerated diffusion of Ta atoms along the grain boundary during deformation. Though an appreciable amount of grain boundary segregation isn't observed in this irradiation experiment, Srinivasan et al. [158] observed

grain boundary segregation of Ta atoms after Cu^{2+} irradiation at 300℃ up to a dose of 200 dpa, signifying that the ballistically dissolved nanoclusters release atoms to the grain boundaries. Due to the dissolution of nanoclusters after irradiation, the grain boundary is not as efficiently pinned as it is in the as-received sample. Hence, grain boundary motion by as small as 1 nm might occur during which Ta atoms agglomerate at the grain boundary by diffusion to re-pin it, after which no movement in the grain boundary is observed. This phenomenon has been simulated by Koju et al. [142], where they imitated the pinning and unpinning of grain boundaries by Ta nanoclusters. They observed that after a grain boundary is unpinned, the grain boundary motion is slowed down due to solute drag and the formation of newer nanoclusters at the grain boundary, which pin the grain boundary even stronger than before. During this process, the newly formed Ta nanocluster would grow through pipe diffusion of Ta atoms along the grain boundary. The simulation also showed that this process is more likely to take place during grain boundary motion at low temperatures as it provides enough time for the nanocluster to grow whereas at high-temperature deformation the grain boundary would easily unpin from the nanocluster without getting enough time for the nanoclusters to grow. Hence, formation of nanoclusters at the grain boundaries is observed during TEM *in situ* pico-indentation at room temperature.

Though recovery of the Ta nanoclusters is possible by deformation, the main concern arises because the recovered clusters are only at the grain boundaries. During irradiation, uniform dissolution of Ta nanoclusters is expected between the Ta nanoclusters at the grain boundary as well as those clusters within the grain. As Ta nanoclusters would only be recovered at the grain boundaries, there would be lesser obstacles for dislocations present inside the grain even after recovering some of the nanoclusters. Given the average Cu grain size of 70 nm in the material, the material is still in the plastic deformation via dislocation glide regime rather than grain boundary

sliding regime [161]. This would mean, recovery of mechanical strength lost due to dissolution of nanoclusters under irradiation would not be completely possible under these experimental parameters.

6. CONCLUSION & FUTURE WORK

In this thesis, we were able to mitigate irradiation induced ballistic dissolution of Ta nanoclusters and Ostwald Ripening of Ta phases via deformation. Proton irradiation of the Cu-10at%Ta caused the following changes in the microstructure:

- Cu grains retained their grain size and did not show any irradiation induced defects owing to a combination of high irradiation temperature and high volume of defect sinks.
- Ta phases (size > 20 nm) exhibit an overall increase in size indicating Ostwald ripening of the phase
- Ta nanoclusters (size < 20 nm) exhibit a decrease in the number density indicating ballistic dissolution of the clusters resulting in increase in Ta concentration in the Cu matrix

When subjected to deformation using TEM *in situ* pico-indentation, both as-received sample and proton irradiated sample show refining of the Ta phase arising from the dislocation glide mediated random walk of Ta atoms at the fcc/bcc interface. Ta cluster formation is only observed in the proton irradiated sample owing to supersaturated microstructure after irradiation. Stable Ta clusters formed at the grain boundaries due to deformation assisted diffusion of Ta atoms along the grain boundaries.

Based on the findings of this thesis, future work entails:

- Examination of irradiation induced defects at low irradiation temperature, to study the resistance of the material to irradiation induced defects based on the defect sink volume to tailor make radiation resistant microstructure

- Examination of irradiation induced defect development using different irradiating ion species to study the swelling of the material
- Examination of recovery of irradiation induced changes in Ta particles using surface treatment techniques such as laser shock peening to engineer a real-world solution to irradiation effects in this material

APPENDIX A. NANOINDENTATION

A.1 Method:

These experiments were performed on the Nanomechanic's iMicro nanoindenter at Purdue University, West Lafayette, IN. Initially the samples need to be mounted on to a puck provided with the sample, using superglue. Care needs to be taken that the superglue is around the sample to keep it in place and not under the sample to avoid compression of the glue layer during the indentation. The puck is loaded in the loading tray. The loading tray has 4 pillars to assist in loading the puck properly at the proper height and ensures that the indenter tip is exactly perpendicular to the sample surface.

Using the Inview software to control the nanoindenter equipment, we select the E & H to Load method. The maximum load the system can go up to is 1000 mN. We then select the point where the indent needs to be done and then the equipment performs the indent. The loading time for each indent is different but there is a 1 sec hold at 1000 mN and then the load is reduced to 100 mN for 30 secs to deal with system creep. The system uses Oliver-Pharr's Method to gauge the hardness and elastic modulus of the material. The software generates a hardness and elastic modulus data with respect to indentation depth which can be exported to Microsoft Excel for further analysis. 8 indents were carried out for each material, with each indent being placed 50 μm away from the first one to avoid overlapping of the plastic zone.

Surface effects are prominent at depths < 500 nm as the contact area of the indenter tip is assumed to be more than it is resulting in enlargement of the hardness and elastic modulus values. Hence, to avoid surface effects which are overwhelmed at a deeper indent depth, the hardness and elastic modulus values reach a plateau. As the plastic zone caused due to the indent is 4 to 5 times the size of the indent depth, the hardness and modulus values [166]. So, an indentation depth of 3

μm allows us to evaluate properties of the material up to 12-15 μm allowing us to evaluate properties for ion irradiated material as shown in Fig. A.1.

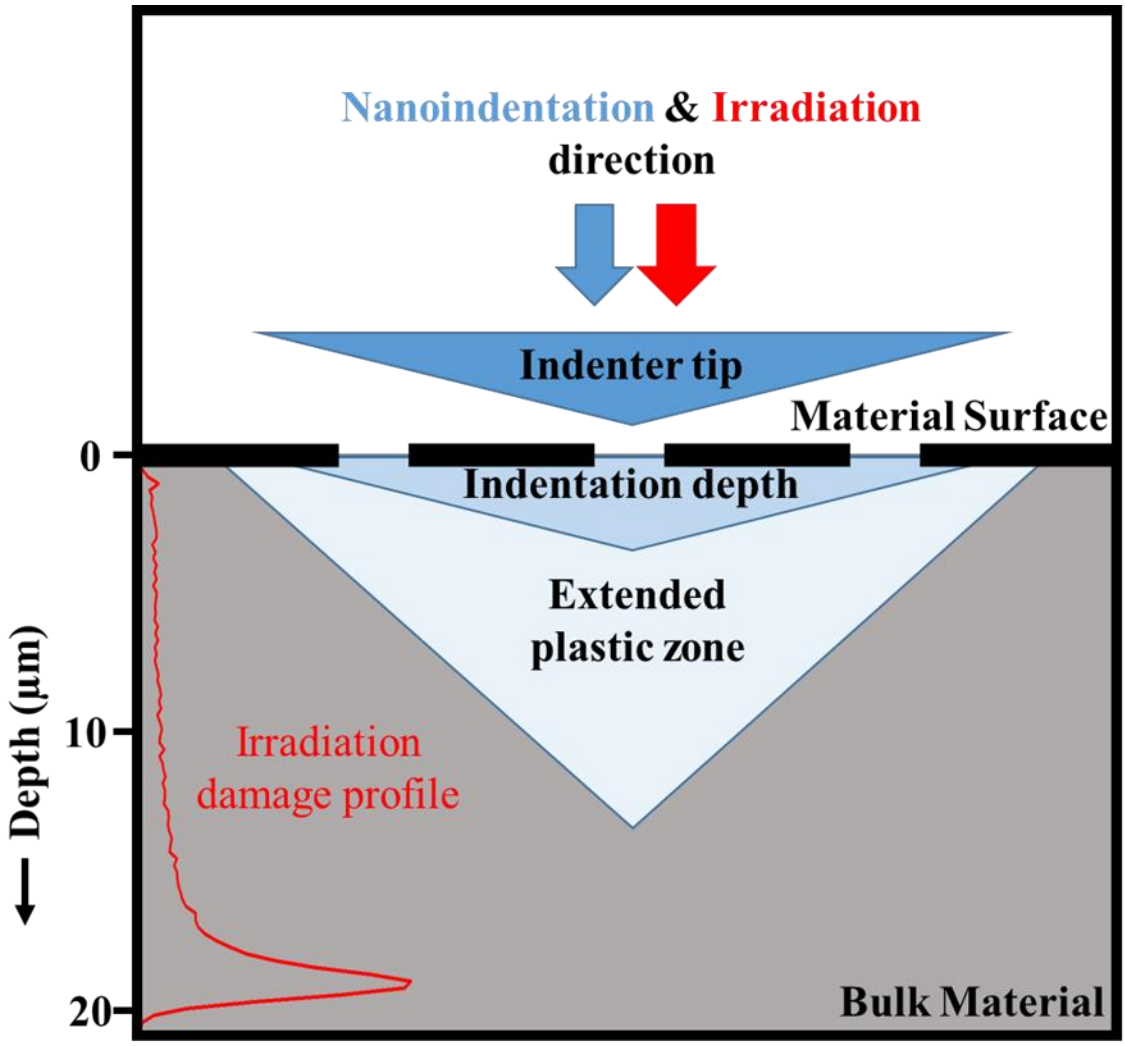

Figure A.1.1: A schematic of the nanoindentation experiment showing the extended plastic zone formed due to the indentation which allows us to sample properties at a much higher depth than the indentation depth [140].

A.2 Results:

Nanoindents exhibit an equilateral triangle geometry without any sink-in or pile-up at the specimen surface, signifying an appropriate selection of nanoindentation experiment parameters for the material, Fig. A.2 (embedded). All indents made on each of the as-received and irradiated specimens exhibit self-consistent depth profiles of hardness and elastic modulus (Fig. A.2). Surface effects are evident at indent depths ≤ 500 nm. Average depth profiles of hardness and elastic modulus are taken over all indents from a given specimen condition, Fig. A.2(c), A.2(f). Note that the average hardness and modulus values corresponding to the shallowest depths are truncated during the averaging process in Origin Pro 2019, which only considers the common depth range over which to calculate the averages. The average hardness and moduli are greater in the irradiated specimen than in the as-received specimen at all depths, but there is a significant overlap of error bars throughout the entire nanoindentation depth range probed. Average hardness values taken from the plateau regions are 4.0 ± 0.1 GPa and 4.3 ± 0.2 GPa for the as-received and irradiated specimens, respectively. The average elastic moduli, also taken from the plateau regions, are 135 ± 2.6 GPa and 141 ± 5.0 GPa for the as-received and irradiated specimens, respectively. The results from the nanoindentation experiment have been summarized in Table A.1. These measurements indicate that hardness and modulus are statistically unchanged with irradiation, even though the loss of nanoclusters would suggest loss in strength of the material.

Table A.2.1: Summary of hardness and modulus results obtained from nanoindentation experiments [140].

		As-received	**Proton Irradiated**
Nanoindentation	Number of indents	8	8
	Hardness (GPa)	4.0 ± 0.1	4.3 ±0.2
	Elastic modulus (GPa)	135 ± 2.6	141 ± 5.0

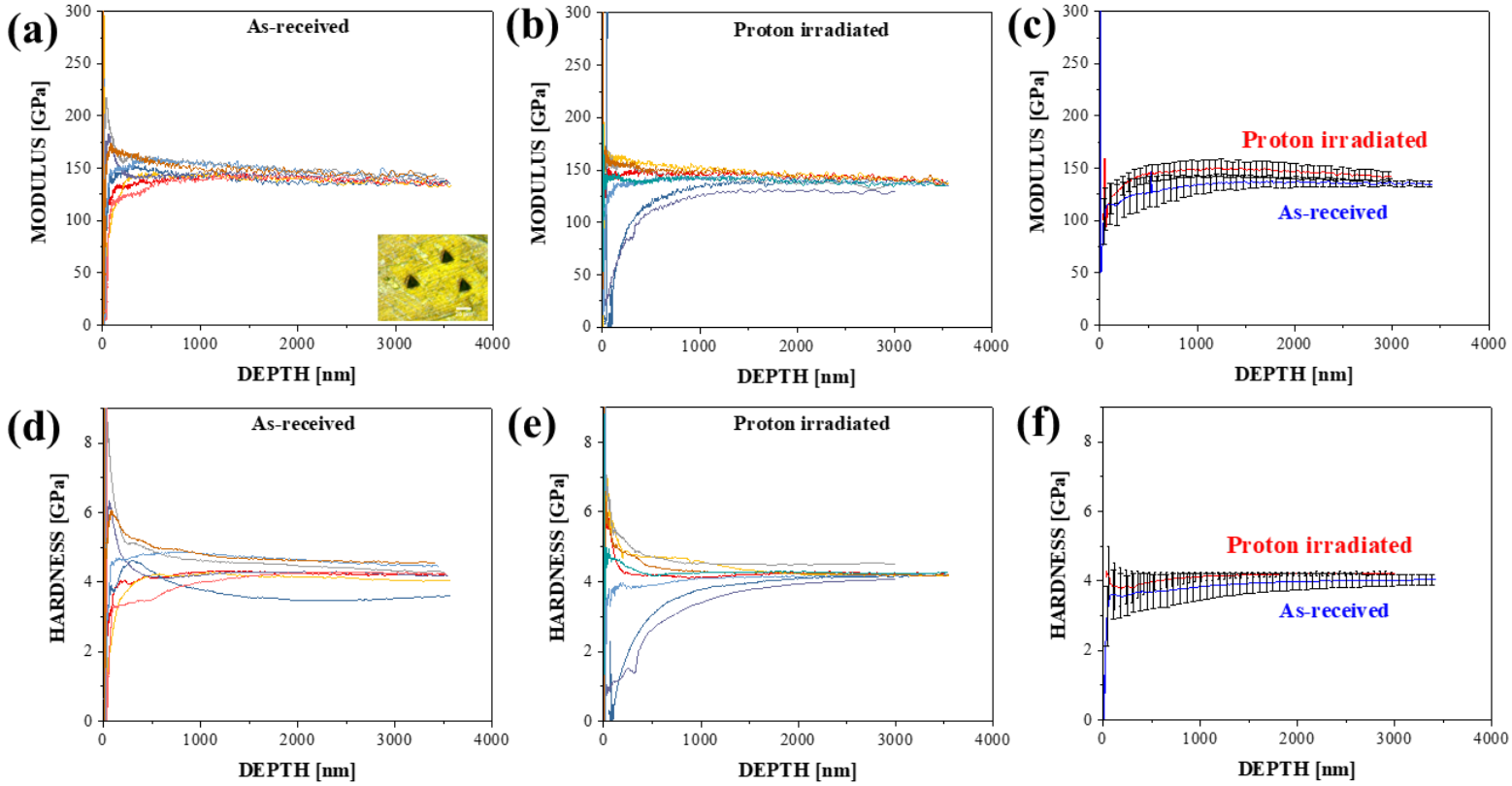

Figure A.2.2: (a - embedded) Representative indents from the Berkovich tip indenter for both the as-received and irradiated conditions for Cu-10at%Ta. Indents are more than 50 um apart from each other to avoid overlapping of the plastic region and no sink-in or pile-up can be observed at the indent sites. Nanoindentation modulus depth profiles for all indents on the (a) as-received and (b) irradiated samples, and (c) average overall indents; nanoindentation hardness depth profiles for all indents on the (d) as-received and (e) irradiated samples, and (f) average overall indents [140]

A.3 Discussion: Effect on mechanical properties

The total hardness of the as-received Cu-10%Ta has previously been determined to be the sum of the hardness contributions from the active strengthening mechanisms [83,167]. Specifically, the hardness associated with the Cu grain size can be quantified using the Hall-Petch relationship [36,37]; the effect of Ta phase volume fraction by the rule of mixtures relationship [81]; and the effect of Ta nanoclusters by the Orowan strengthening relationship [80]. To quantitatively corroborate the irradiated microstructure with irradiation-induced changes in nanoindentation hardness, one must consider all features of the microstructure undergoing evolution [83–85]. Since the irradiation-induced dissolution of the Ta nanoclusters leads to an increase in Ta concentration in the Cu matrix, this hardening contribution must also be considered. Hence, the total irradiation hardening of the Cu-10%Ta can be expressed as:

$$\Delta H = \Delta H_{HP} + \Delta H_{Oro} + \Delta H_{ROM} + \Delta H_{Ta} \tag{A.3.1}$$

where ΔH_{HP} is the Hall-Petch hardening, ΔH_{Oro} the Orowan hardening, ΔH_{ROM} the rule of mixtures hardening, and ΔH_{Ta} the hardening from Ta in the Cu matrix. Since the Cu grains and Ta phases exhibit statistically insignificant changes with irradiation, the terms ΔH_{HP} and ΔH_{ROM} are negligible, and Eq. 4 can be reduced to:

$$\Delta H = \Delta H_{Oro} + \Delta H_{Ta}$$

Tabor's relation between hardness and yield stress ($H=3\sigma_y$) [168] and the von Mises plastic flow rule ($\tau = \sigma_y/\sqrt{3}$) [169] are combined to obtain the change in Orowan strengthening due to the interaction of Ta nanoclusters and dislocations:

$$\Delta H_{Oro} = \frac{3\sqrt{3}Gb}{2\pi}\left\{\frac{\ln(\lambda_{AR})}{\lambda_{AR}}\left[\frac{\ln(2r_{AR})}{\ln(\lambda_{AR})}\right]^{1.5} - \frac{\ln(\lambda_{Irr})}{\lambda_{Irr}}\left[\frac{\ln(2r_{Irr})}{\ln(\lambda_{Irr})}\right]^{1.5}\right\} \tag{A.3.2}$$

where G is the shear modulus of Cu (48 GPa), b is the Burgers vector (0.25 nm), r_{AR} and r_{Irr} are the radii of the Ta nanoclusters in the as-received and proton irradiated sample, respectively, and λ is the interparticle spacing given by:

$$\lambda = 2r\left(\sqrt{\frac{\pi}{4f^*}} - 1\right) \tag{A.3.3}$$

where f^* represents the effective volume fraction of Ta nanoclusters, and r is the average radius of the Ta nanoclusters. Carrying through the Orowan hardening calculation, with the propagation of error from the measured Ta nanocluster volume fraction, the irradiation-induced decrease in Ta nanocluster number density leads to ΔH_{Oro} of -98 ± 317 MPa. There is no well-established expression for ΔH_{Ta}, although this contribution is akin to solid solution strengthening of miscible species. Given the irradiation-induced increase in matrix Ta, the magnitude of ΔH_{Ta} will be positive, potentially offsetting ΔH_{Oro} and yielding a positive net ΔH consistent with nanoindentation measurements. However, the large error bars on calculated hardening contributions and measured nanoindentation hardening are self-consistent with the conclusion that there is no significant irradiation-induced change in the strength of the Cu-10at%Ta.

The Orowan hardening contribution from nanoclusters (*nc*) can also be expressed in terms of a barrier strength, α_{nc} [170]:

$$\Delta H_{nc} = 3\alpha_{nc} M \mu b \sqrt{N_{nc} d_{nc}} \tag{A.3.4}$$

where M represents the Taylor Factor [90] taken to be 3.06 for the fcc lattice, N_{nc} represents the number density of Ta nanoclusters, and d_{nc} is the average diameters of Ta nanoclusters in the as-received or irradiated condition. Equating the two Orowan expressions, Eqs. 5 and 7, enables calculation of the barrier strength for Ta nanoclusters, α_{nc}, which are found to be 0.07 and 0.09 in the as-received and proton irradiated samples, respectively. These barrier strengths are consistent in magnitude and follow the same size dependence (Fig. A.3.1) as barrier strengths determined for

coherent Y-Ti-O nanoclusters in Fe-9Cr ODS steel alloy [66] and α′ nanoclusters in FeCrAl alloys [171,172]. APT results have observed the preferential dissolution of Ta nanoclusters having initial diameters ≲2.5 nm (Fig. 8). Considering the size dependence of the barrier strength, the preferential dissolution of the ≲ 2.5 nm nanoclusters during irradiation produces little change in the hardness of the alloy.

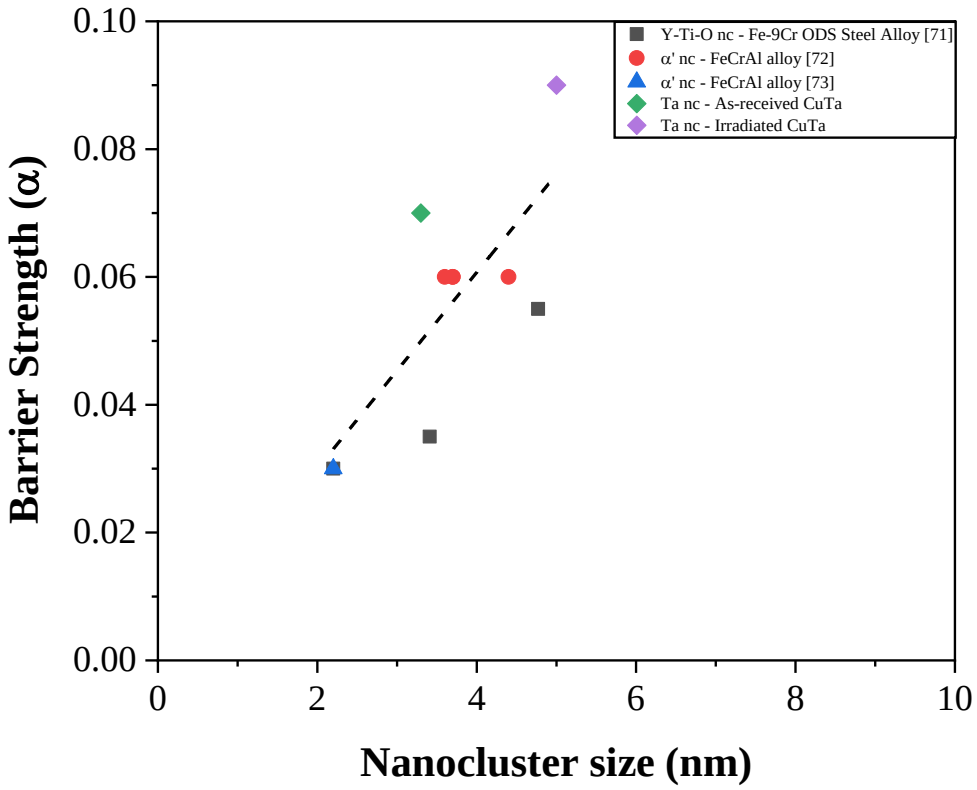

Figure A.3.1: A plot of barrier strengths vs nanocluster as reported in literature showing the decreasing barrier strength with decreasing size.

APPENDIX B. ADDITIONAL DATA

Table B.1: Data obtained from APT cluster analysis for tips in each of the samples.

	NO. OF TIPS	NO. OF CLUSTERS	TIP VOLUME (nm^3)	CLUSTER DENSITY ($\times 10^{23}$ m^{-3})	TA MATRIX CONCENTRATION (at%)	AVERAGE CLUSTER DENSITY ($\times 10^{23}$ m^{-3})
AS-RECEIVED SAMPLE	1	129	216670	5.95	0.36	5.65
	2	38	84372	4.5	0.37	
	3	167	256923	6.5	0.3	
PROTON IRRADIATED SAMPLE	1	12	272879	0.44	0.7	1.34
	2	23	53721	4.28	0.65	
	3	4	52715	0.76	0.88	
	4	2	230472	0.09	0.5	
	5	19	168856	1.13	0.9	

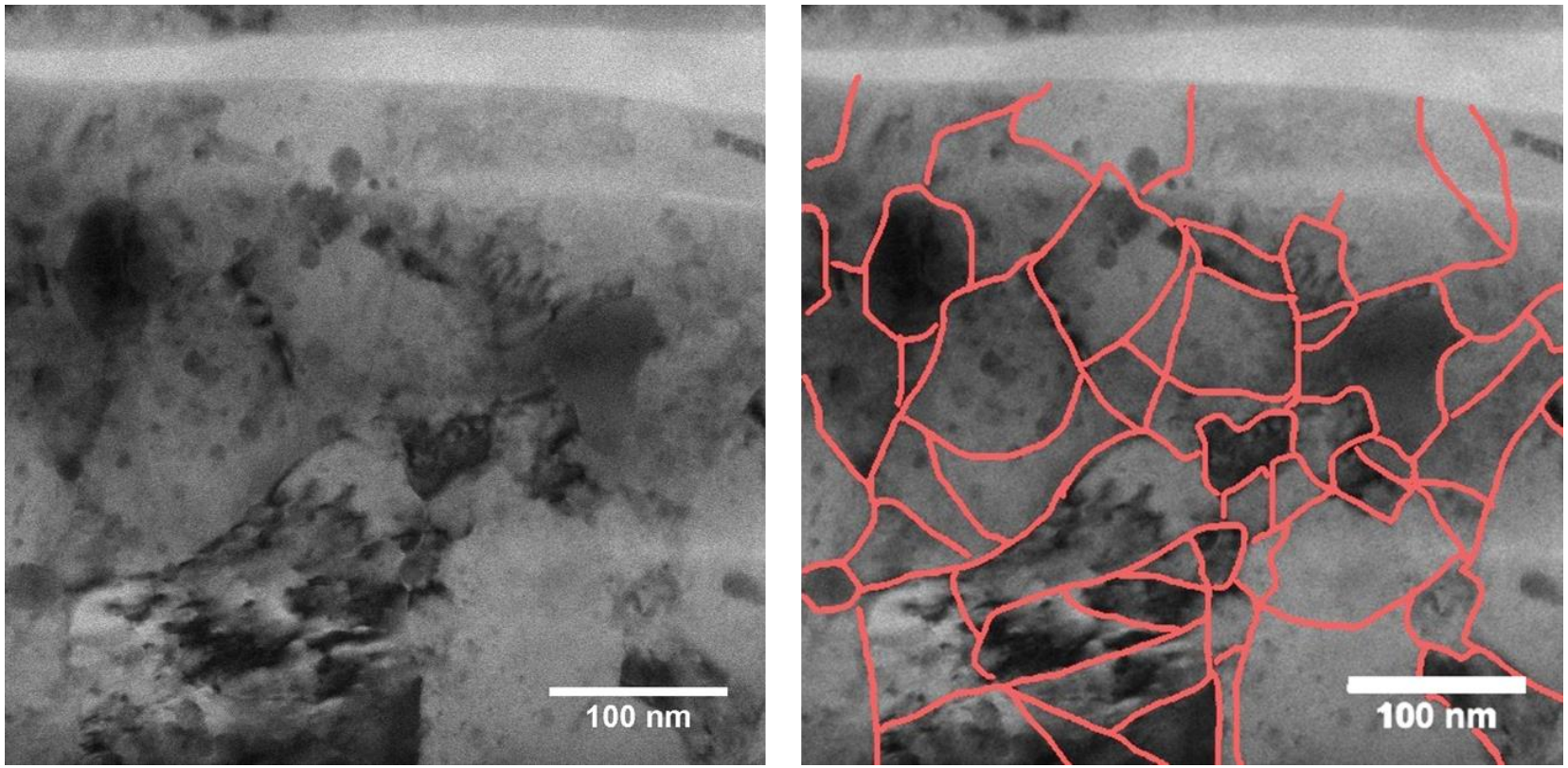

Figure B.1: BFSTEM image of microstructure in as-received sample used to calculate grain size. The bottom image shows the marked grain boundaries on the top image micrograph.

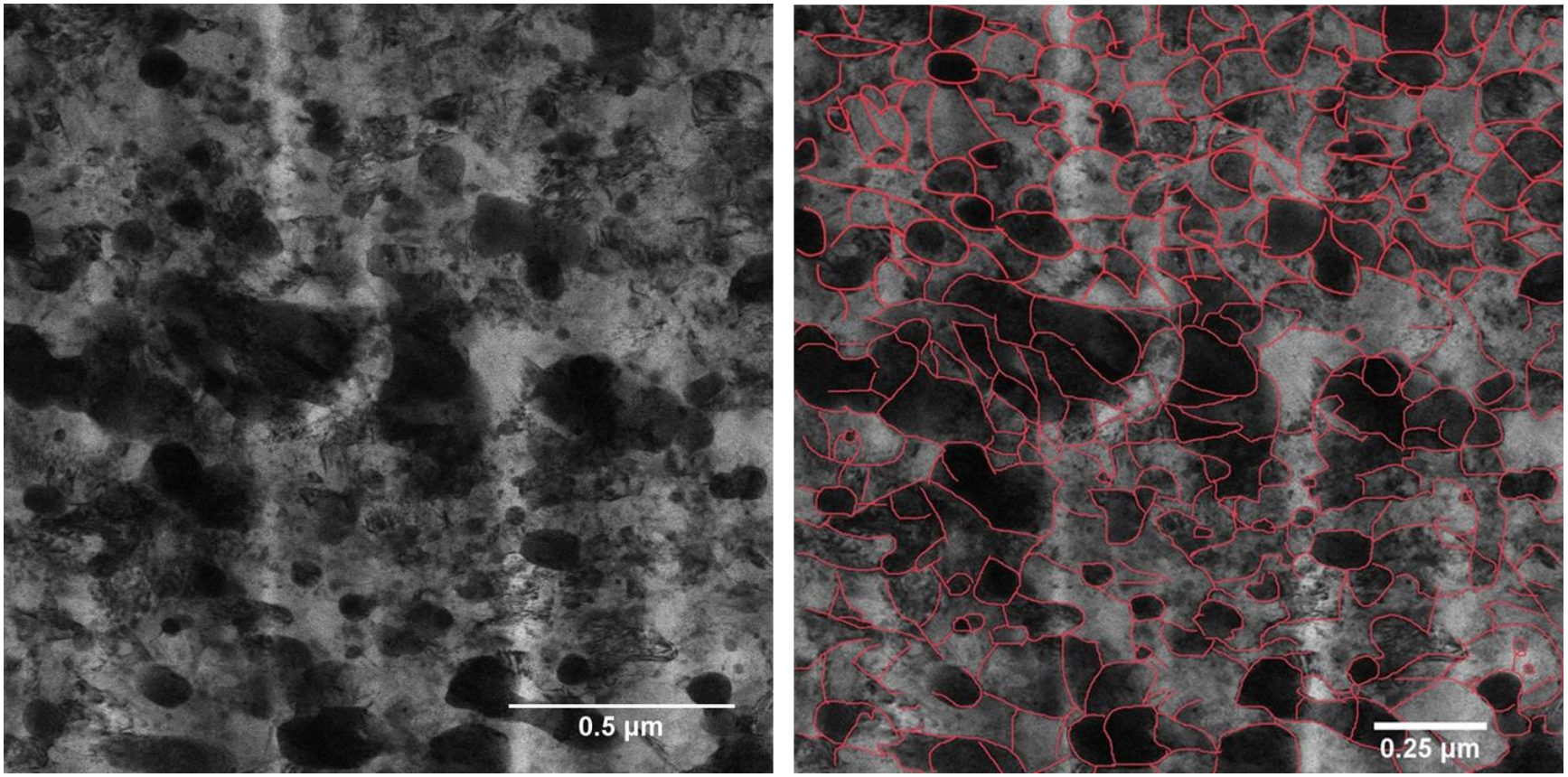

Figure B.2: BFSTEM image of microstructure in proton irradiated sample used to calculate grain size. The bottom image shows the marked grain boundaries on the top image micrograph

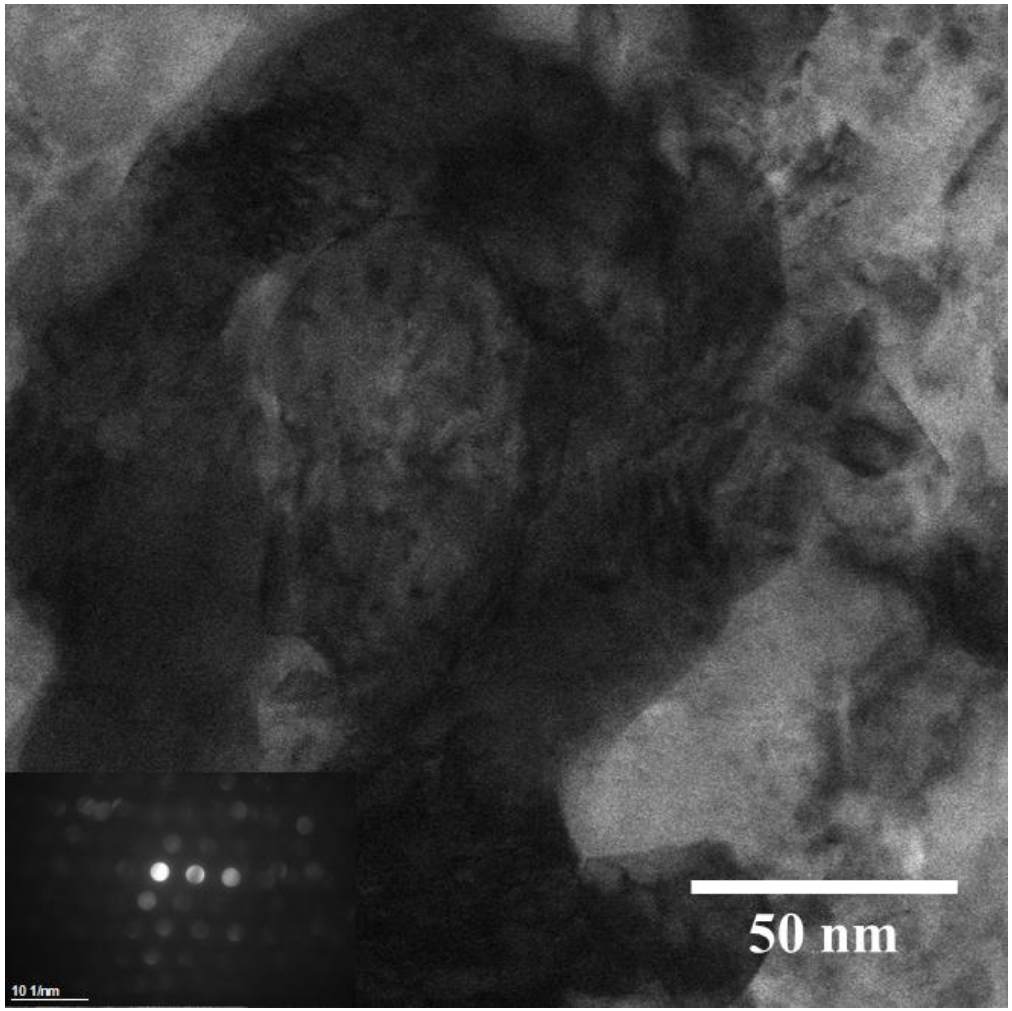

Figure B.3: Additional grain analyzed in the as-received sample for irradiation induced defects with the indexed diffraction pattern.

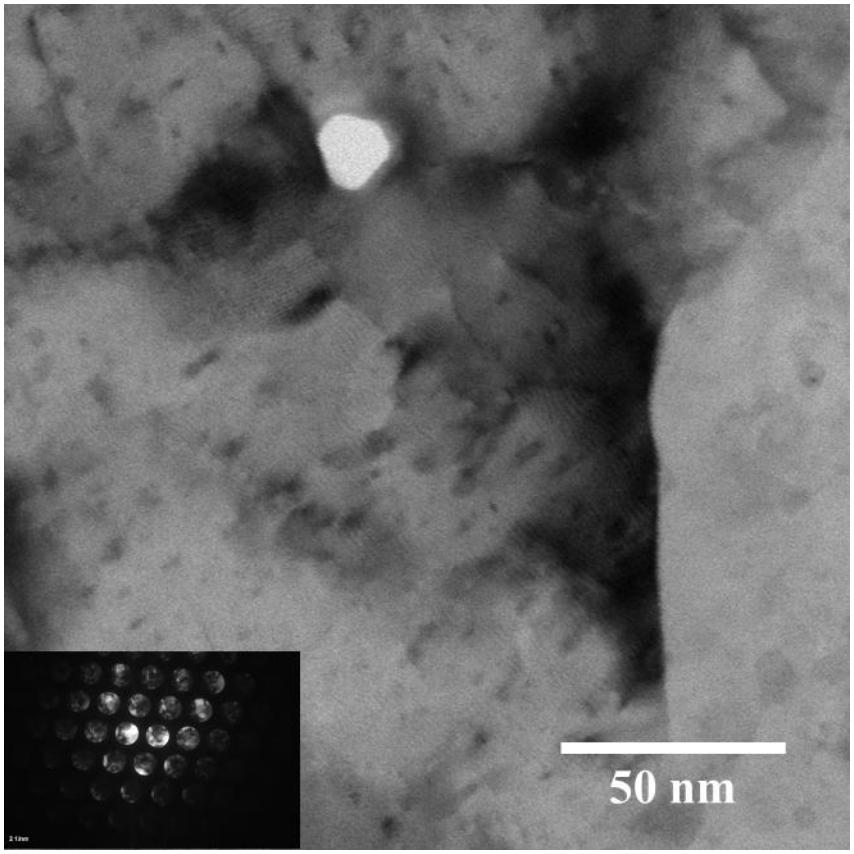

Figure B.4: Additional grain analyzed in the proton irradiated sample for irradiation induced defects with the indexed diffraction pattern.

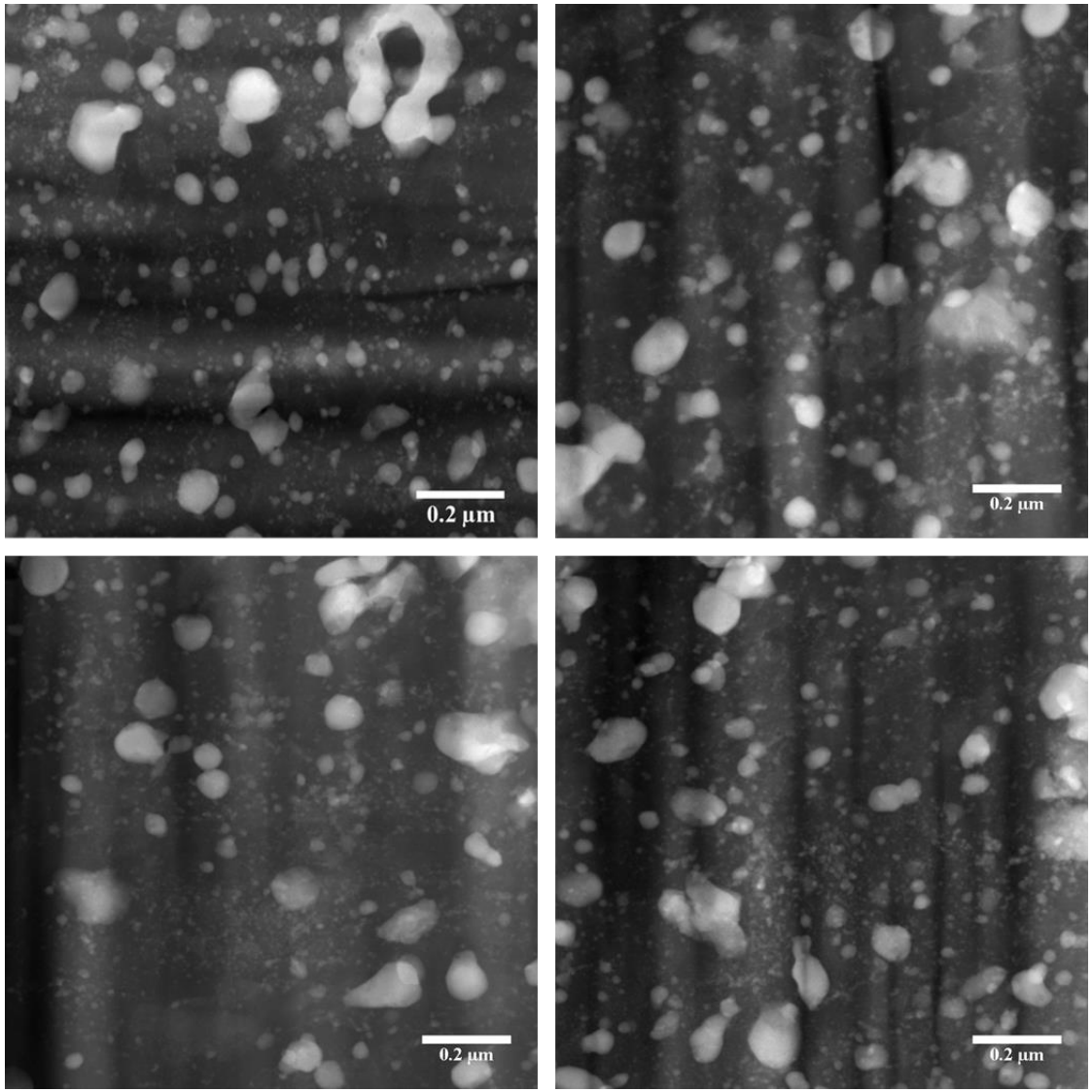

Figure B.5: STEM images used for calculating the size distribution of Ta phases in the as-received sample.

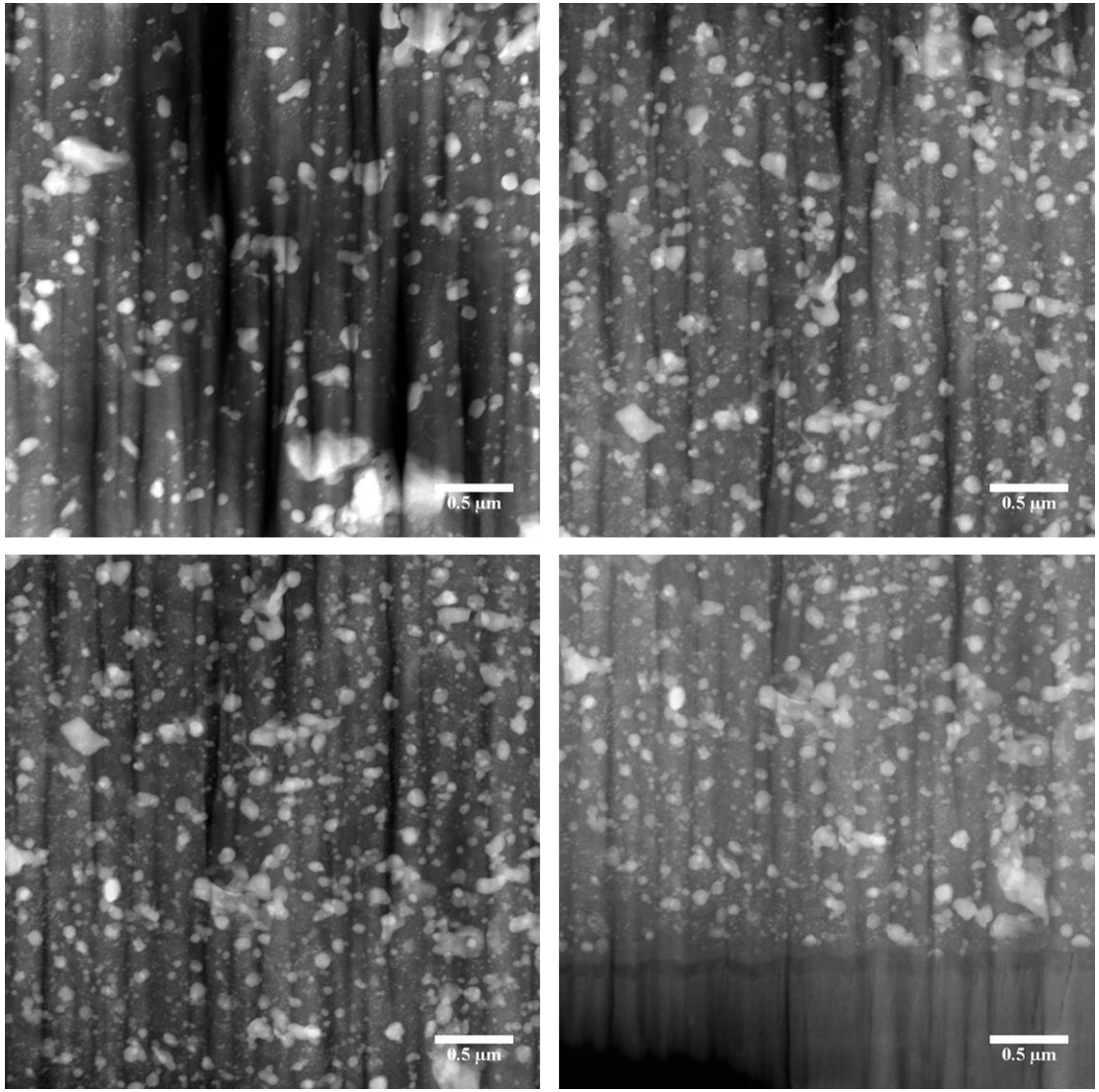

Figure B.6: STEM images used for calculating the Ta phase size distribution in the proton irradiated sample.

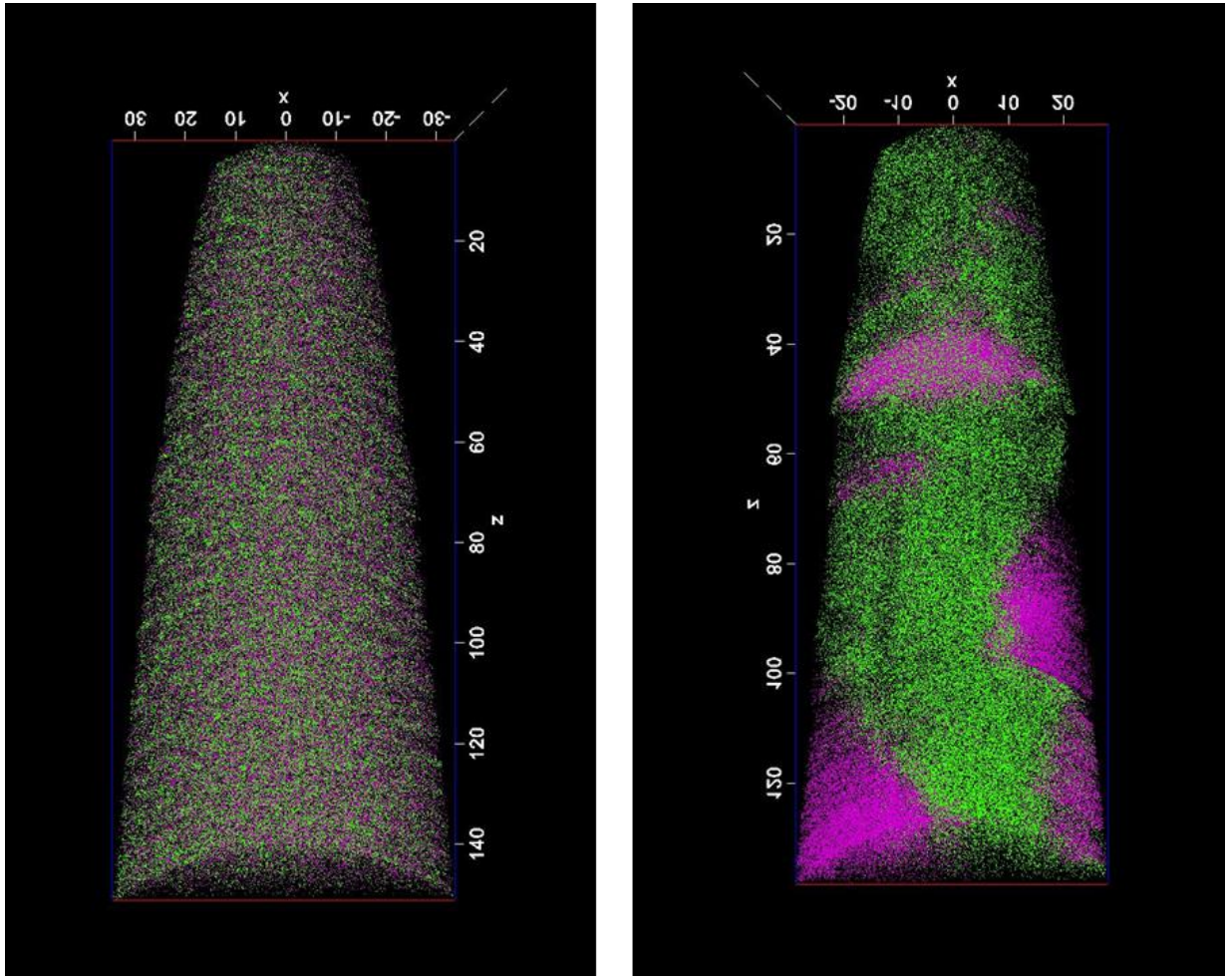

Figure B.7: Tip reconstructions for as-received samples used for performing cluster analysis.

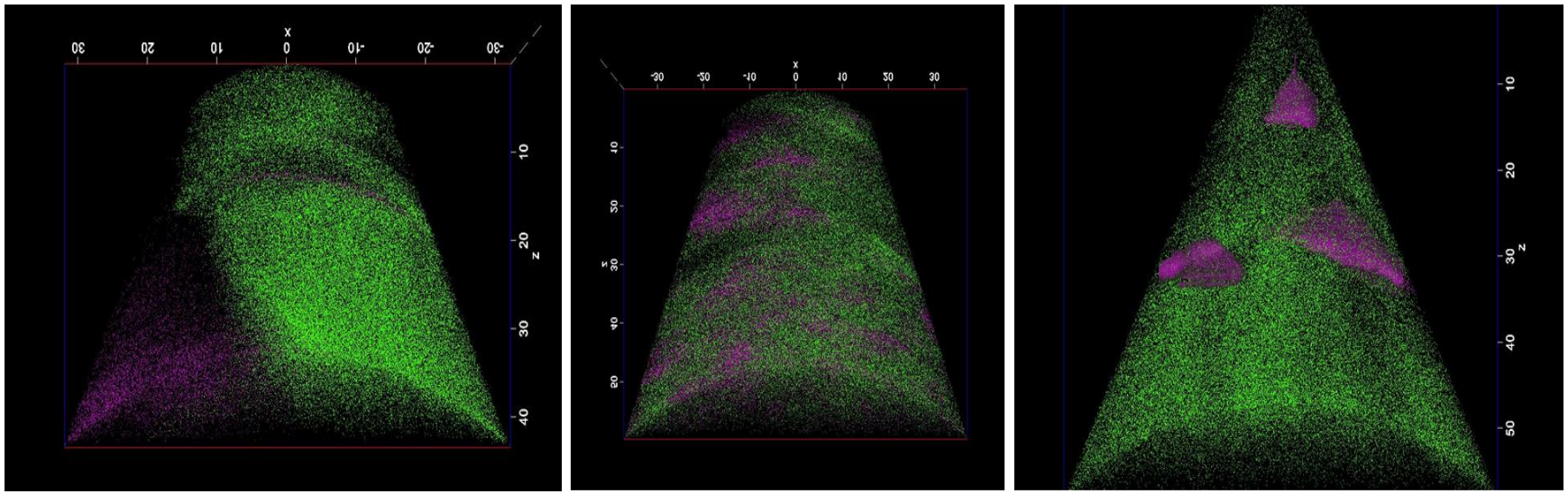

Figure B.8: Tip reconstructions for proton irradiated samples used for performing cluster analysis.

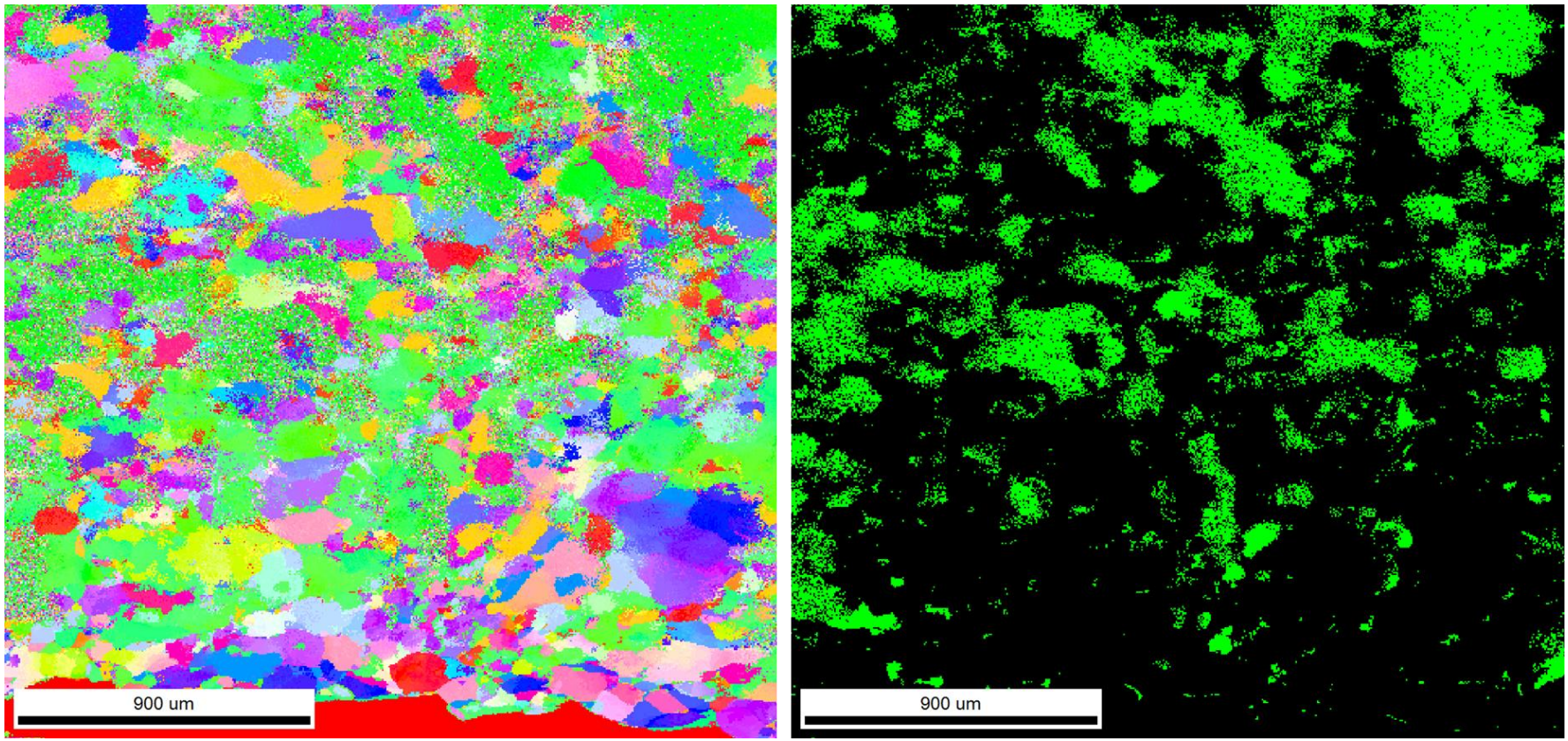

Figure B.9: ACOM analysis showing the orientation map (left) and Ta particles map (right) at 0 nm indentation depth in the as-received sample. The scale is in nanometer and not micrometer.

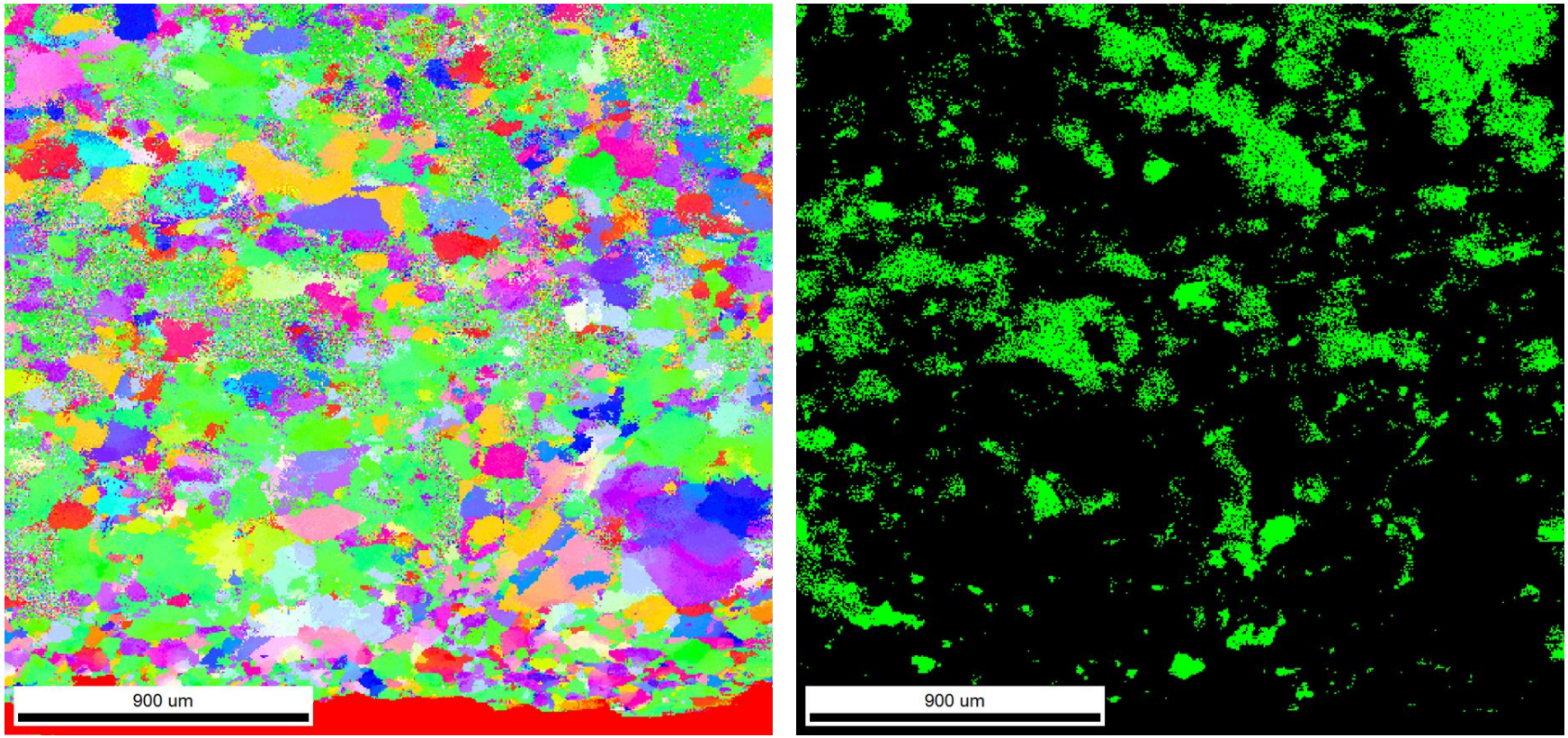

Figure B.10: ACOM analysis showing the orientation map (left) and Ta particles map (right) at 200 nm indentation depth in the as-received sample. The scale is in nanometer and not micrometer.

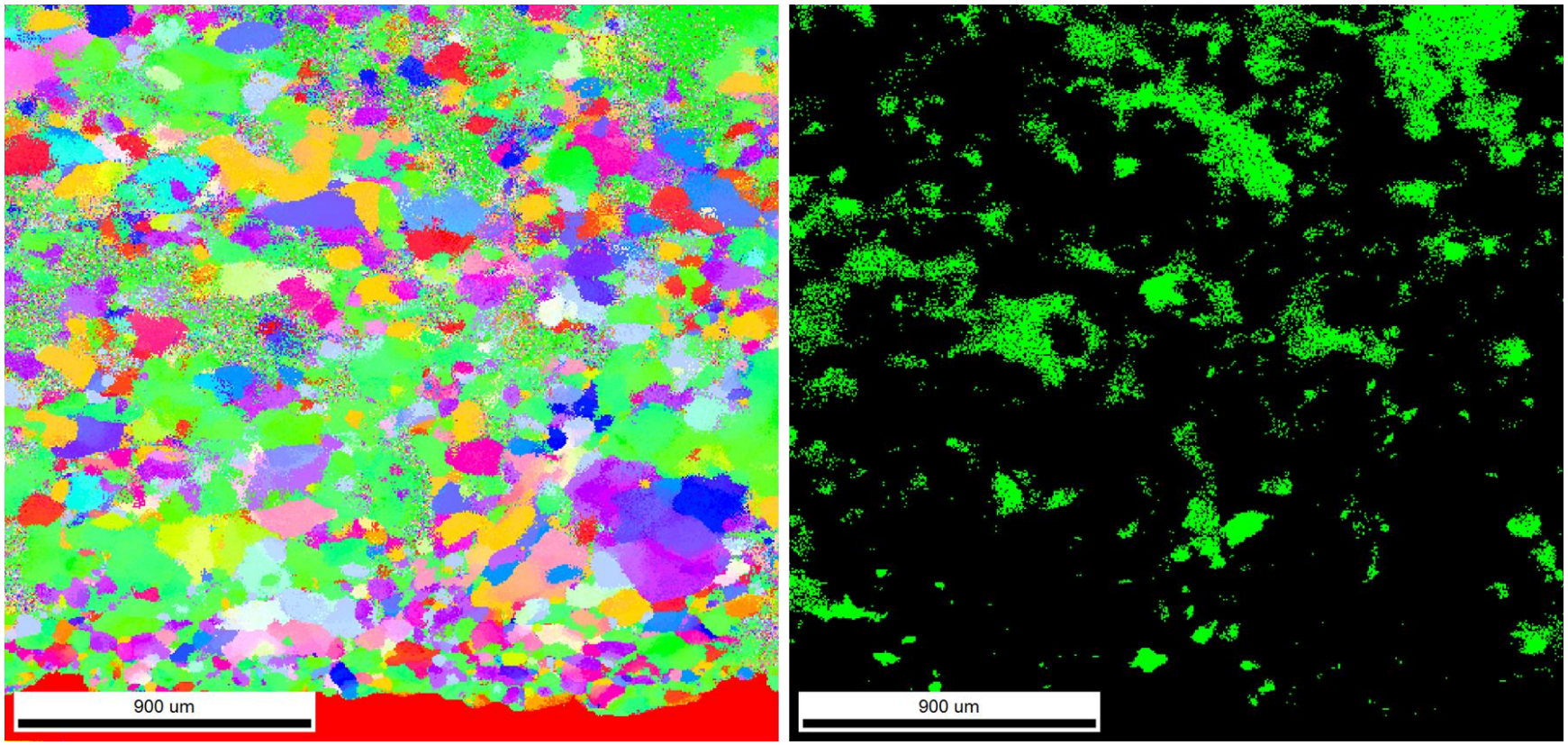

Figure B.11: ACOM analysis showing the orientation map (left) and Ta particles map (right) at 400 nm indentation depth in the as-received sample. The scale is in nanometer and not micrometer.

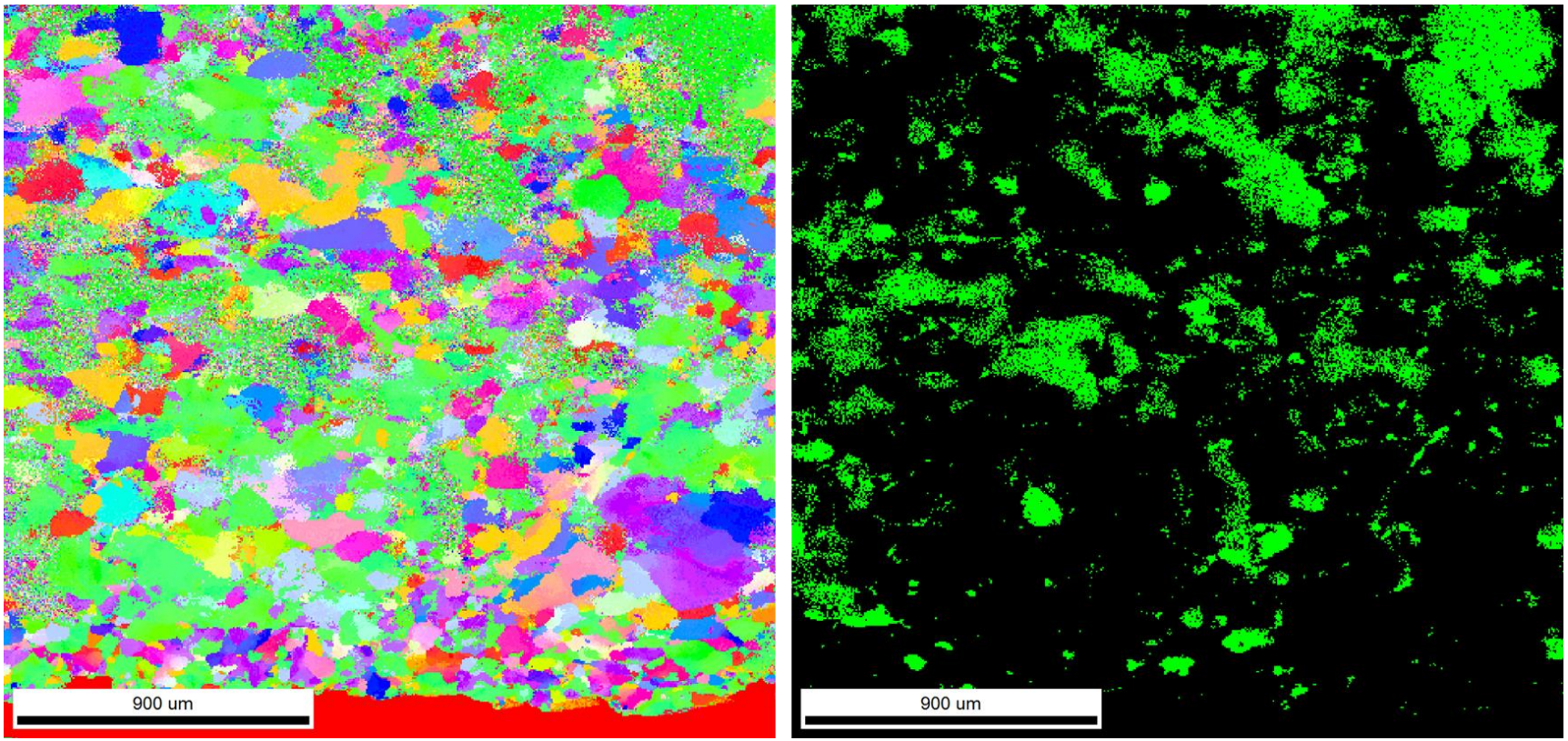

Figure B.12: ACOM analysis showing the orientation map (left) and Ta particles map (right) at 600 nm indentation depth in the as-received sample. The scale is in nanometer and not micrometer.

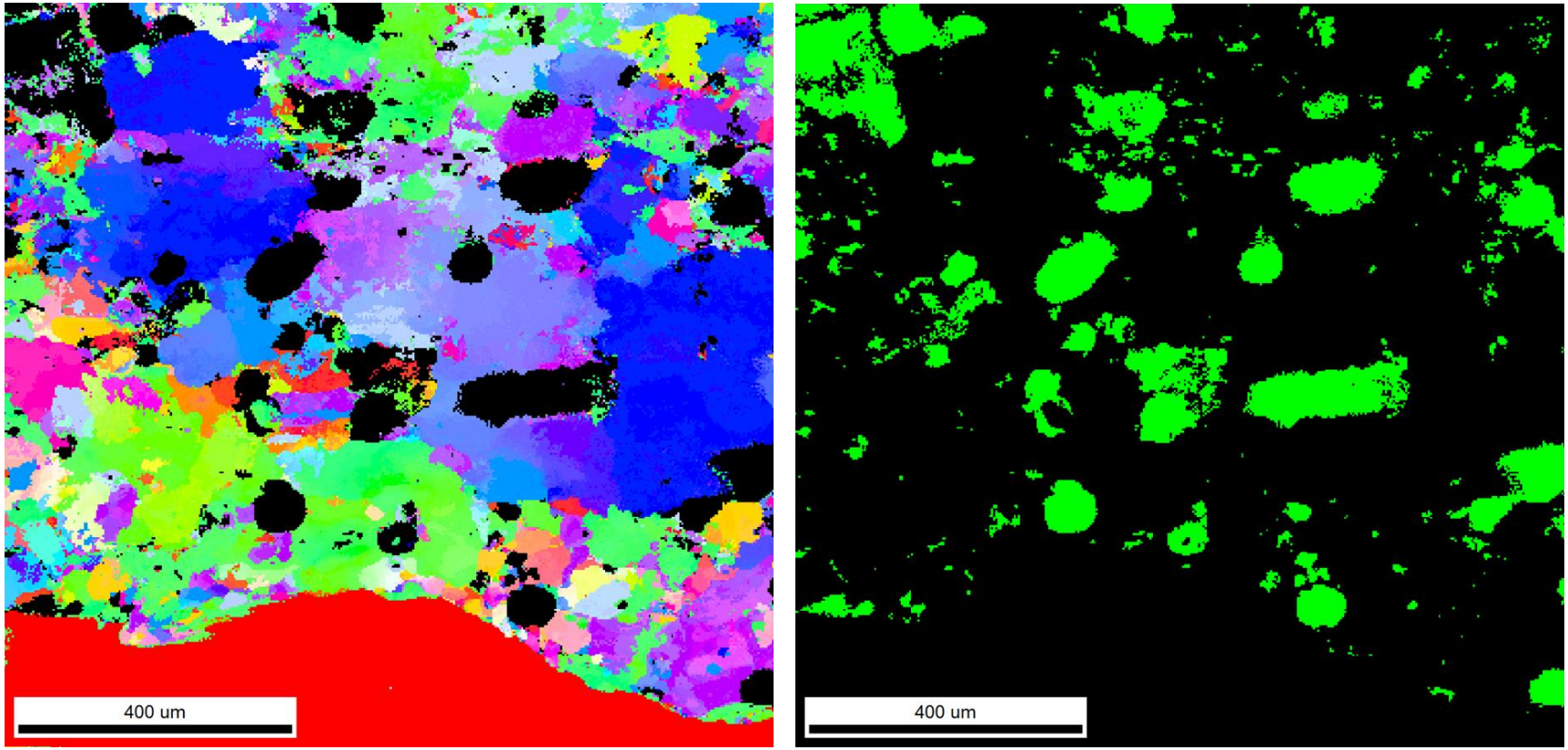

Figure B.13: ACOM analysis showing the orientation map (left) and Ta particles map (right) at 0 nm indentation depth in the proton irradiated sample. The scale is in nanometer and not micrometer.

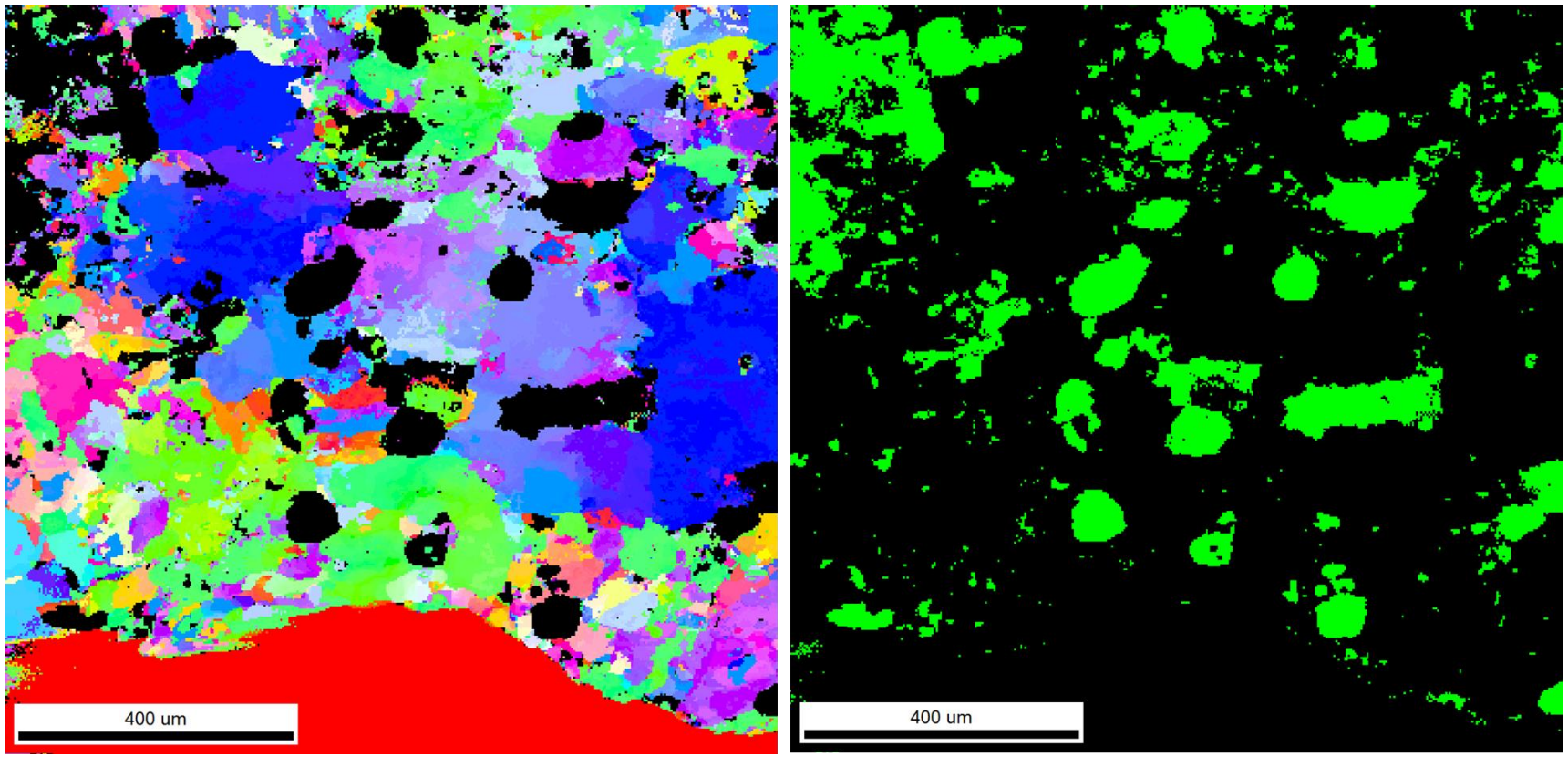

Figure B.14: ACOM analysis showing the orientation map (left) and Ta particles map (right) at 150 nm indentation depth in the proton irradiated sample. The scale is in nanometer and not micrometer.

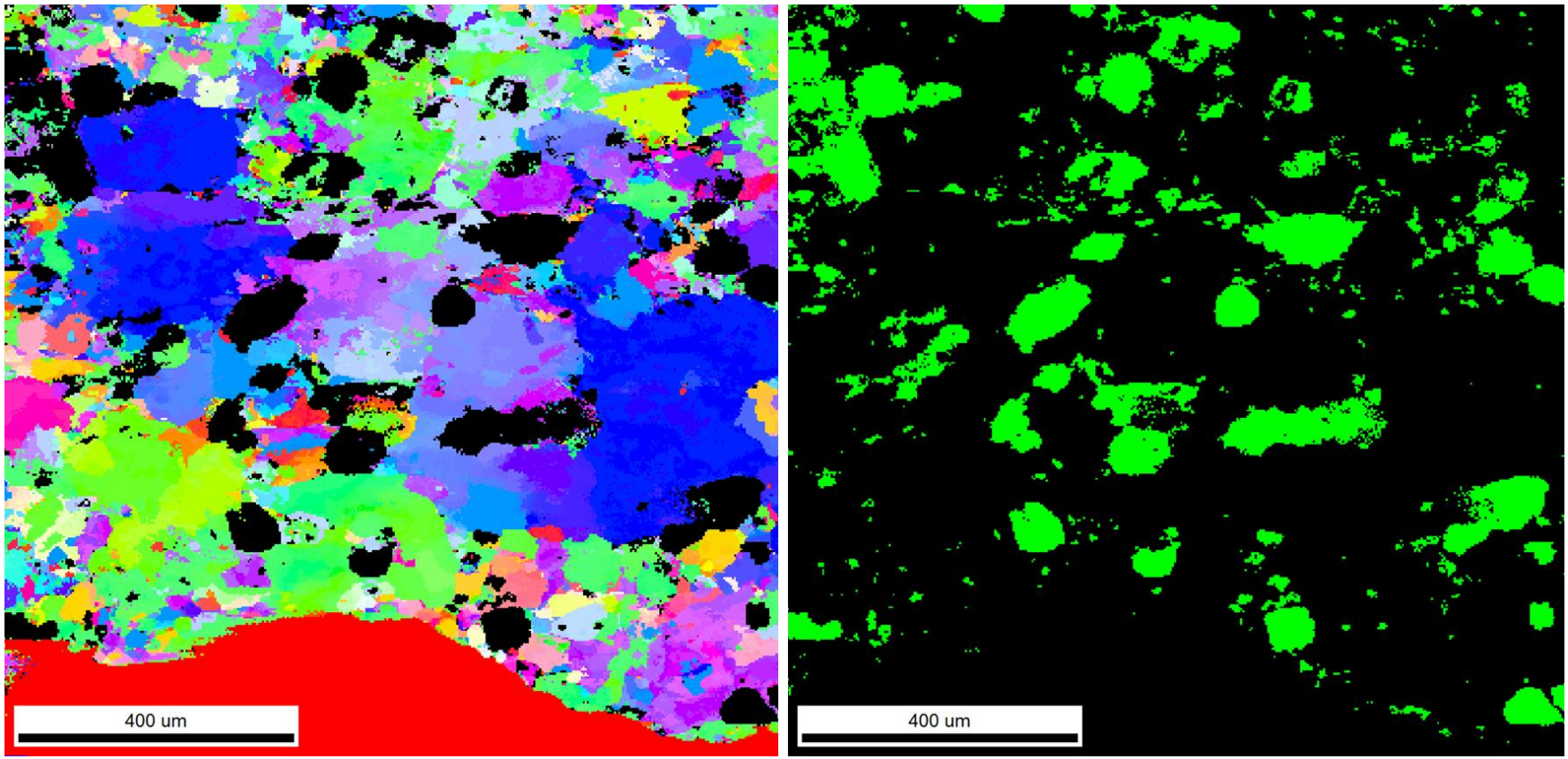

Figure B.15: ACOM analysis showing the orientation map (left) and Ta particles map (right) at 450 nm indentation depth in the proton irradiated sample. The scale is in nanometer and not micrometer.

APPENDIX C. TEM *in situ* VIDEOS

The OneDrive link for ViBE installation files, ViBE analyzed indentation videos and a sample video of the TEM in situ pico-indentation intermitted with ACOM analysis for the irradiated sample can be found.

https://purdue0-my.sharepoint.com/:f:/g/personal/patkip_purdue_edu/EpyQPIF6sihHgkIDeIsHAfoBzBaVQsQfEOm7NpbkkkEsbQ?e=uJnwDe

REFERENCES

[1] C. Suryanarayana, Nanocrystalline materials, Int. Mater. Rev. 40 (1995) 41–63. https://doi.org/10.1179/imr.1995.40.2.41.

[2] C. Suryanarayana and C.C. Koch., Nanocrystalline materials – Current research and future Directions, Hyperfine Interact. 130 (2000) 5–44.

[3] C. Suryanarayana, Structure and properties of nanocrystalline materials, Bull. Mater. Sci. 17 (1994) 307–346. https://doi.org/10.1007/BF02745220.

[4] M. Ames, J. Markmann, R. Karos, A. Michels, A. Tschöpe, R. Birringer, Unraveling the nature of room temperature grain growth in nanocrystalline materials, Acta Mater. 56 (2008) 4255–4266. https://doi.org/10.1016/j.actamat.2008.04.051.

[5] K. Pantleon, M.A.J. Somers, Interpretation of microstructure evolution during self-annealing and thermal annealing of nanocrystalline electrodeposits-A comparative study, Mater. Sci. Eng. A. 528 (2010) 65–71. https://doi.org/10.1016/j.msea.2010.04.077.

[6] M.A. Tschopp, H.A. Murdoch, L.J. Kecskes, K.A. Darling, Bulk nanocrystalline metals: Review of the current state of the art and future opportunities for copper and copper alloys, Jom. 66 (2014) 1000–1019. https://doi.org/10.1007/s11837-014-0978-z.

[7] H.A. Murdoch, C.A. Schuh, Stability of binary nanocrystalline alloys against grain growth and phase separation, Acta Mater. 61 (2013) 2121–2132. https://doi.org/10.1016/j.actamat.2012.12.033.

[8] T. Chookajorn, H.A. Murdoch, C.A. Schuh, Design of stable nanocrystalline alloys, Science (80-.). 337 (2012) 951–954. https://doi.org/10.1126/science.1224737.

[9] T. Chookajorn, C.A. Schuh, Thermodynamics of stable nanocrystalline alloys: A monte carlo analysis, Phys. Rev. B - Condens. Matter Mater. Phys. 89 (2014). https://doi.org/10.1103/PhysRevB.89.064102.

[10] R.K. Koju, K.A. Darling, L.J. Kecskes, Y. Mishin, Zener Pinning of Grain Boundaries and Structural Stability of Immiscible Alloys, JOM. 68 (2016) 1596–1604. https://doi.org/10.1007/s11837-016-1899-9.

[11] K.A. Darling, M.A. Tschopp, R.K. Guduru, W.H. Yin, Q. Wei, L.J. Kecskes, Microstructure and mechanical properties of bulk nanostructured Cu-Ta alloys consolidated by equal channel angular extrusion, Acta Mater. 76 (2014) 168–185. https://doi.org/10.1016/j.actamat.2014.04.074.

[12] M. Samaras, W. Hoffelner, M. Victoria, Irradiation of pre-existing voids in nanocrystalline iron, J. Nucl. Mater. 352 (2006) 50–56. https://doi.org/10.1016/J.JNUCMAT.2006.02.041.

[13] N. Nita, R. Schaeublin, M. Victoria, Impact of irradiation on the microstructure of nanocrystalline materials, J. Nucl. Mater. 329–333 (2004) 953–957. https://doi.org/10.1016/J.JNUCMAT.2004.04.058.

[14] M. Rose, A.G. Balogh, H. Hahn, Instability of irradiation induced defects in nanostructured materials, Nucl. Instruments Methods Phys. Res. B. 127128 (1997) 119–122. https://ac.els-cdn.com/S0168583X96008634/1-s2.0-S0168583X96008634-main.pdf?_tid=d13c0157-e52e-4ba6-bcea-38dd288fecaf&acdnat=1523513794_6899a9cd213434db42a04552c615ebd4 (accessed April 12, 2018).

[15] C. Sun, K.Y. Yu, J.H. Lee, Y. Liu, H. Wang, L. Shao, S.A. Maloy, K.T. Hartwig, X. Zhang, Enhanced radiation tolerance of ultrafine grained Fe–Cr–Ni alloy, J. Nucl. Mater. 420 (2012) 235–240. https://doi.org/10.1016/J.JNUCMAT.2011.10.001.

[16] Y. Chimi, A. Iwase, N. Ishikawa, M. Kobiyama, T. Inami, T. Kambara, S. Okuda, Swift heavy ion irradiation effects in nanocrystalline gold, Nucl. Instruments Methods Phys. Res. Sect. B Beam Interact. with Mater. Atoms. 245 (2006) 171–175. https://doi.org/10.1016/J.NIMB.2005.11.096.

[17] Y.-Q. Chang, Q. Guo, J. Zhang, L. Chen, Y. Long, F.-R. Wan, Irradiation effects on nanocrystalline materials, Front. Mater. Sci. 7 (2013) 143–155. https://doi.org/10.1007/s11706-013-0199-3.

[18] A. Taylor, C.W. Allen, E.A. Ryan, The HVEM-Tandem Accelerator Facility at Argonne National Laboratory, Nucl. Instruments Methods Phys. Res. Sect. B Beam Interact. with Mater. Atoms. 24–25 (1987) 598–602. https://doi.org/10.1016/0168-583X(87)90718-X.

[19] X. Zhang, K. Hattar, Y. Chen, L. Shao, J. Li, C. Sun, K. Yu, N. Li, M.L. Taheri, H. Wang, J. Wang, M. Nastasi, Radiation damage in nanostructured materials, Prog. Mater. Sci. 96 (2018) 217–321. https://doi.org/10.1016/j.pmatsci.2018.03.002.

[20] W. Mohamed, B. Miller, D. Porter, K. Murty, The Role of Grain Size on Neutron Irradiation Response of Nanocrystalline Copper, Materials (Basel). 9 (2016) 144. https://doi.org/10.3390/ma9030144.

[21] D. Kaoumi, A.T. Motta, R.C. Birtcher, Grain Growth in Nanocrystalline Metal Thin Films under In Situ Ion-Beam Irradiation, 2007. www.astm.org (accessed November 11, 2019).

[22] N.Q. Vo, S.W. Chee, D. Schwen, X. Zhang, P. Bellon, R.S. Averback, Microstructural stability of nanostructured Cu alloys during high-temperature irradiation, Scr. Mater. 63 (2010) 929–932. https://doi.org/10.1016/j.scriptamat.2010.07.009.

[23] K. Tai, R.S. Averback, P. Bellon, Y. Ashkenazy, B. Stumphy, Temperature dependence of irradiation-induced creep in dilute nanostructured Cu-W alloys, J. Nucl. Mater. 422 (2012) 8–13. https://doi.org/10.1016/j.jnucmat.2011.11.068.

[24] K. Tai, R.S. Averback, P. Bellon, Y. Ashkenazy, Irradiation-induced creep in nanostructured Cu alloys, Scr. Mater. 65 (2011) 163–166. https://doi.org/10.1016/j.scriptamat.2011.04.001.

[25] J.P. Wharry, M.J. Swenson, K.H. Yano, A review of the irradiation evolution of dispersed oxide nanoparticles in the b.c.c. Fe-Cr system: Current understanding and future directions, J. Nucl. Mater. 486 (2017) 11–20. https://doi.org/10.1016/J.JNUCMAT.2017.01.009.

[26] Y. Ashkenazy, N.Q. Vo, D. Schwen, R.S. Averback, P. Bellon, Shear induced chemical mixing in heterogeneous systems, Acta Mater. 60 (2012) 984–993. https://doi.org/10.1016/j.actamat.2011.11.014.

[27] Y. Ashkenazy, N. Pant, J. Zhou, P. Bellon, R.S. Averback, Phase evolution of highly immiscible alloys under shear deformation: Kinetic pathways, steady states, and the lever-rule, Acta Mater. 139 (2017) 205–214. https://doi.org/10.1016/j.actamat.2017.08.014.

[28] X. Sauvage, W. Lefebvre, C. Genevois, S. Ohsaki, K. Hono, Complementary use of transmission electron microscopy and atom probe tomography for the investigation of steels nanostructured by severe plastic deformation, Scr. Mater. 60 (2009) 1056–1061. https://doi.org/10.1016/J.SCRIPTAMAT.2009.02.019.

[29] J.A. Beach, M. Wang, P. Bellon, S. Dillon, Y. Ivanisenko, T. Boll, R.S. Averback, Self-organized, size-selection of precipitates during severe plastic deformation of dilute Cu-Nb alloys at low temperatures, Acta Mater. 140 (2017) 217–223. https://doi.org/10.1016/j.actamat.2017.08.041.

[30] H.J. Qu, K.H. Yano, P. V. Patki, M.J. Swenson, J.P. Wharry, Understanding plasticity in irradiated alloys through TEM in situ compression pillar tests, J. Mater. Res. (2019). https://doi.org/10.1557/jmr.2019.295.

[31] K.H. Yano, M.J. Swenson, Y. Wu, J.P. Wharry, TEM in situ micropillar compression tests of ion irradiated oxide dispersion strengthened alloy, J. Nucl. Mater. 483 (2017) 107–120. https://doi.org/10.1016/j.jnucmat.2016.10.049.

[32] J.P. Wharry, K.H. Yano, P. V. Patki, Intrinsic-extrinsic size effect relationship for micromechanical tests, Scr. Mater. 162 (2019) 63–67. https://doi.org/10.1016/J.SCRIPTAMAT.2018.10.045.

[33] P.H. Warren, G. Warren, M. Dubey, J. Burns, Y.Q. Wu, J.P. Wharry, Method for Fabricating Depth-Specific TEM In Situ Tensile Bars, JOM. 72 (2020) 2057–2064. https://doi.org/10.1007/s11837-020-04105-8.

[34] K.H. Yano, S. Thomas, M.J. Swenson, Y. Lu, J.P. Wharry, TEM in situ cube-corner indentation analysis using ViBe motion detection algorithm, J. Nucl. Mater. 502 (2018) 201–212. https://doi.org/10.1016/J.JNUCMAT.2018.02.003.

[35] K.H. Yano, IN SITU TEM MECHANICAL TESTING OF IRRADIATED OXIDE DISPERSION STRENGTHENED ALLOYS, Purdue University Graduate School, 2019. https://doi.org/10.25394/PGS.8041817.V1.

[36] E.O. Hall, The Deformation and Ageing of Mild Steel: III Discussion of Results, Proc. Phys. Soc. B (1951) 747.

[37] PETCH, N. J., The Cleavage Strengh of Polycrystals, J. Iron Steel Inst. 174 (1953) 25–28. http://ci.nii.ac.jp/naid/10005741787/en/ (accessed March 31, 2018).

[38] T. Allen, J. Busby, M. Meyer, D. Petti, Materials challenges for nuclear systems, Mater. Today. 13 (2010) 14–23. https://doi.org/10.1016/S1369-7021(10)70220-0.

[39] S.J. Zinkle, J.T. Busby, Structural materials for fission & fusion energy, Mater. Today. 12 (2009) 12–19. https://doi.org/10.1016/S1369-7021(09)70294-9.

[40] G.S. WAS, Fundamentals of Radiation Materials Science, Springer New York, New York, NY, 2017. https://doi.org/10.1007/978-1-4939-3438-6.

[41] N. Li, K. Hattar, A. Misra, In situ probing of the evolution of irradiation-induced defects in copper, J. Nucl. Mater. 439 (2013) 185–191. https://doi.org/10.1016/j.jnucmat.2013.04.013.

[42] C.M. Barr, O. El-Atwani, D. Kaoumi, K. Hattar, Interplay Between Grain Boundaries and Radiation Damage, JOM. 71 (2019) 1233–1244. https://doi.org/10.1007/s11837-019-03386-y.

[43] W. Han, M.J. Demkowicz, N.A. Mara, E. Fu, S. Sinha, A.D. Rollett, Y. Wang, J.S. Carpenter, I.J. Beyerlein, A. Misra, Design of Radiation Tolerant Materials Via Interface Engineering, Adv. Mater. 25 (2013) 6975–6979. https://doi.org/10.1002/adma.201303400.

[44] E.G. Fu, A. Misra, H. Wang, L. Shao, X. Zhang, Interface enabled defects reduction in helium ion irradiated Cu/V nanolayers, J. Nucl. Mater. 407 (2010) 178–188. https://doi.org/10.1016/j.jnucmat.2010.10.011.

[45] M.J. Demkowicz, R.G. Hoagland, J.P. Hirth, Interface structure and radiation damage resistance in Cu-Nb multilayer nanocomposites, Phys. Rev. Lett. 100 (2008). https://doi.org/10.1103/PhysRevLett.100.136102.

[46] E. Ma, Alloys created between immiscible elements, Prog. Mater. Sci. 50 (2005) 413–509. https://doi.org/10.1016/j.pmatsci.2004.07.001.

[47] N.Q. Vo, J. Schäfer, R.S. Averback, K. Albe, Y. Ashkenazy, P. Bellon, Reaching theoretical strengths in nanocrystalline Cu by grain boundary doping, Scr. Mater. 65 (2011) 660–663. https://doi.org/10.1016/J.SCRIPTAMAT.2011.06.048.

[48] J. M. Rigsbee, Development of Nanocrystalline Copper-Refractory Metal Alloys | Scientific.Net, Mater. Sci. Forum. 561–565 (2007) 2373–2378. https://www.scientific.net/MSF.561-565.2373 (accessed May 24, 2020).

[49] R.J. Comstock, T.H. Courtney, Elevated-temperature stability of mechanically alloyed Cu-Nb powders, Metall. Mater. Trans. A. 25 (1994) 2091–2099. https://doi.org/10.1007/BF02652310.

[50] I. Budai, G. Kaptay, A new class of engineering materials: Particle-Stabilized metallic emulsions and monotectic alloys, Metall. Mater. Trans. A Phys. Metall. Mater. Sci. 40 (2009) 1524–1528. https://doi.org/10.1007/s11661-009-9857-6.

[51] P.A. Manohar, M. Ferry, T. Chandra, Five Decades of the Zener Equation., 1998. https://doi.org/10.2355/isijinternational.38.913.

[52] K.A. Darling, E.L. Huskins, B.E. Schuster, Q. Wei, L.J. Kecskes, Mechanical properties of a high strength Cu–Ta composite at elevated temperature, Mater. Sci. Eng. A. 638 (2015) 322–328. https://doi.org/10.1016/J.MSEA.2015.04.069.

[53] K.A. Darling, M. Rajagopalan, M. Komarasamy, M.A. Bhatia, B.C. Hornbuckle, R.S. Mishra, K.N. Solanki, Extreme creep resistance in a microstructurally stable nanocrystalline alloy, Nature. 537 (2016) 378–381. https://doi.org/10.1038/nature19313.

[54] T. Frolov, K.A. Darling, L.J. Kecskes, Y. Mishin, Stabilization and strengthening of nanocrystalline copper by alloying with tantalum, Acta Mater. 60 (2012) 2158–2168. https://doi.org/10.1016/j.actamat.2012.01.011.

[55] M. Rajagopalan, K. Darling, S. Turnage, R.K. Koju, B. Hornbuckle, Y. Mishin, K.N. Solanki, Microstructural evolution in a nanocrystalline Cu-Ta alloy: A combined in-situ TEM and atomistic study, Mater. Des. 113 (2017) 178–185. https://doi.org/10.1016/j.matdes.2016.10.020.

[56] R.K. Guduru, K.L. Murty, K.M. Youssef, R.O. Scattergood, C.C. Koch, Mechanical behavior of nanocrystalline copper, Mater. Sci. Eng. A. 463 (2007) 14–21. https://doi.org/10.1016/j.msea.2006.07.165.

[57] Q. Wei, Z.L. Pan, X.L. Wu, B.E. Schuster, L.J. Kecskes, R.Z. Valiev, Microstructure and mechanical properties at different length scales and strain rates of nanocrystalline tantalum produced by high-pressure torsion, Acta Mater. 59 (2011) 2423–2436. https://doi.org/10.1016/J.ACTAMAT.2010.12.042.

[58] Q. Wei, B.E. Schuster, S.N. Mathaudhu, K.T. Hartwig, L.J. Kecskes, R.J. Dowding, K.T. Ramesh, Dynamic behaviors of body-centered cubic metals with ultrafine grained and nanocrystalline microstructures, Mater. Sci. Eng. A. 493 (2008) 58–64. https://doi.org/10.1016/j.msea.2007.05.126.

[59] B. Farrokh, A.S. Khan, Grain size, strain rate, and temperature dependence of flow stress in ultra-fine grained and nanocrystalline Cu and Al: Synthesis, experiment, and constitutive modeling, Int. J. Plast. 25 (2009) 715–732. https://doi.org/10.1016/j.ijplas.2008.08.001.

[60] M.A. Meyers, A. Mishra, D.J. Benson, Mechanical properties of nanocrystalline materials, Prog. Mater. Sci. 51 (2006) 427–556. https://doi.org/10.1016/j.pmatsci.2005.08.003.

[61] J. Ribis, E. Bordas, P. Trocellier, Y. Serruys, Y. de Carlan, A. Legris, Comparison of the neutron and ion irradiation response of nano-oxides in oxide dispersion strengthened materials, J. Mater. Res. 30 (2015) 2210–2221. https://doi.org/10.1557/jmr.2015.183.

[62] J. Ribis, S. Lozano-Perez, Nano-cluster stability following neutron irradiation in MA957 oxide dispersion strengthened material, J. Nucl. Mater. 444 (2014) 314–322. https://doi.org/10.1016/J.JNUCMAT.2013.10.010.

[63] J. Ribis, Structural and chemical matrix evolution following neutron irradiation in a MA957 oxide dispersion strengthened material, J. Nucl. Mater. 434 (2013) 178–188. https://doi.org/10.1016/J.JNUCMAT.2012.11.038.

[64] J. He, F. Wan, K. Sridharan, T.R. Allen, A. Certain, Y.Q. Wu, Response of 9Cr-ODS steel to proton irradiation at 400 °C, J. Nucl. Mater. 452 (2014) 87–94. https://doi.org/10.1016/J.JNUCMAT.2014.05.004.

[65] M.J. Swenson, J.P. Wharry, The comparison of microstructure and nanocluster evolution in proton and neutron irradiated Fe–9%Cr ODS steel to 3 dpa at 500 °C, J. Nucl. Mater. 467 (2015) 97–112. https://doi.org/10.1016/J.JNUCMAT.2015.09.022.

[66] M.J. Swenson, C.K. Dolph, J.P. Wharry, The effects of oxide evolution on mechanical properties in proton- and neutron-irradiated Fe-9%Cr ODS steel, J. Nucl. Mater. 479 (2016) 426–435. https://doi.org/10.1016/J.JNUCMAT.2016.07.022.

[67] J.J. Kai, R.D. Lee, Effects of proton irradiation on the microstructural and microchemical evolution of Inconel 600 alloy, J. Nucl. Mater. 207 (1993) 286–294. https://doi.org/10.1016/0022-3115(93)90271-Y.

[68] T. Chen, J.G. Gigax, L. Price, D. Chen, S. Ukai, E. Aydogan, S.A. Maloy, F.A. Garner, L. Shao, Temperature dependent dispersoid stability in ion-irradiated ferritic-martensitic dual-phase oxide-dispersion-strengthened alloy: Coherent interfaces vs. incoherent interfaces, Acta Mater. 116 (2016) 29–42. https://doi.org/10.1016/J.ACTAMAT.2016.05.042.

[69] Y. Bazarbayev, M. Kattoura, K.S. Mao, J. Song, V.K. Vasudevan, J.P. Wharry, Effects of corrosion-inhibiting surface treatments on irradiated microstructure development in Ni-base alloy 718, J. Nucl. Mater. 512 (2018) 276–287. https://doi.org/10.1016/j.jnucmat.2018.10.006.

[70] M.L. Lescoat, I. Monnet, J. Ribis, P. Dubuisson, Y. De Carlan, J.M. Costantini, J. Malaplate, Amorphization of oxides in ODS materials under low and high energy ion irradiations, in: J. Nucl. Mater., 2011: pp. 266–269. https://doi.org/10.1016/j.jnucmat.2011.01.065.

[71] A. Certain, S. Kuchibhatla, V. Shutthanandan, D.T. Hoelzer, T.R. Allen, Radiation stability of nanoclusters in nano-structured oxide dispersion strengthened (ODS) steels, J. Nucl. Mater. 434 (2013) 311–321. https://doi.org/10.1016/J.JNUCMAT.2012.11.021.

[72] B. Sencer, G. Bond, F. Garner, S. Maloy, W. Sommer, M. James, Microstructural Alteration of Structural Alloys by Low Temperature Irradiation with High Energy Protons and Spallation Neutrons, in: Eff. Radiat. Mater. 20th Int. Symp., ASTM International, 100 Barr Harbor Drive, PO Box C700, West Conshohocken, PA 19428-2959, n.d.: pp. 588-588–24. https://doi.org/10.1520/STP10559S.

[73] M. Song, Y. Yang, M. Wang, W. Kuang, C.R. Lear, G.S. Was, Probing long-range ordering in nickel-base alloys with proton irradiation, Acta Mater. (2018). https://doi.org/10.1016/j.actamat.2018.06.043.

[74] M.-L. Lescoat, J. Ribis, Y. Chen, E.A. Marquis, E. Bordas, P. Trocellier, Y. Serruys, A. Gentils, O. Kaïtasov, Y. de Carlan, A. Legris, Radiation-induced Ostwald ripening in oxide dispersion strengthened ferritic steels irradiated at high ion dose, Acta Mater. 78 (2014) 328–340. https://doi.org/10.1016/J.ACTAMAT.2014.06.060.

[75] T. Lazauskas, S.D. Kenny, R. Smith, G. Nagra, M. Dholakia, M.C. Valsakumar, Simulating radiation damage in a bcc Fe system with embedded yttria nanoparticles, J. Nucl. Mater. 437 (2013) 317–325. https://doi.org/10.1016/j.jnucmat.2013.02.016.

[76] T.R. Allen, J. Gan, J.I. Cole, S. Ukai, S. Shutthanandan, S. Thevuthasan, The stability of 9Cr-ODS oxide particles under heavy-ion irradiation, Nucl. Sci. Eng. 151 (2005) 305–312. https://doi.org/10.13182/NSE05-A2549.

[77] T.R. Allen, J. Gan, J.I. Cole, M.K. Miller, J.T. Busby, S. Shutthanandan, S. Thevuthasan, Radiation response of a 9 chromium oxide dispersion strengthened steel to heavy ion irradiation, J. Nucl. Mater. 375 (2008) 26–37. https://doi.org/10.1016/j.jnucmat.2007.11.001.

[78] N. Akasaka, S. Yamashita, T. Yoshitake, S. Ukai, A. Kimura, Microstructural changes of neutron irradiated ODS ferritic and martensitic steels, J. Nucl. Mater. 329–333 (2004) 1053–1056. https://doi.org/10.1016/J.JNUCMAT.2004.04.133.

[79] R.O. Scattergood, C.C. Koch, K.L. Murty, D. Brenner, Strengthening mechanisms in nanocrystalline alloys, Mater. Sci. Eng. A. 493 (2008) 3–11. https://doi.org/10.1016/j.msea.2007.04.132.

[80] D.J. Bacon, U.F. Kocks, R.O. Scattergood, The effect of dislocation self-interaction on the orowan stress, Philos. Mag. 28 (1973) 1241–1263. https://doi.org/10.1080/14786437308227997.

[81] J.B. Ferguson, H. Lopez, D. Kongshaug, B. Schultz, P. Rohatgi, Revised orowan strengthening: Effective interparticle spacing and strain field considerations, Metall. Mater. Trans. A Phys. Metall. Mater. Sci. 43 (2012) 2110–2115. https://doi.org/10.1007/s11661-011-1029-9.

[82] R. Labusch, A Statistical Theory of Solid Solution Hardening, Phys. Status Solidi. 41 (1970) 659–669. https://doi.org/10.1002/pssb.19700410221.

[83] M.A. Atwater, D. Roy, K.A. Darling, B.G. Butler, R.O. Scattergood, C.C. Koch, The thermal stability of nanocrystalline copper cryogenically milled with tungsten, Mater. Sci. Eng. A. 558 (2012) 226–233. https://doi.org/10.1016/j.msea.2012.07.117.

[84] K. Mao, H. Wang, Y. Wu, V. Tomar, J.P. Wharry, Microstructure-property relationship for AISI 304/308L stainless steel laser weldment, Mater. Sci. Eng. A. 721 (2018) 234–243. https://doi.org/10.1016/j.msea.2018.02.092.

[85] S.A. Turnage, M. Rajagopalan, K.A. Darling, P. Garg, C. Kale, B.G. Bazehhour, I. Adlakha, B.C. Hornbuckle, C.L. Williams, P. Peralta, K.N. Solanki, Anomalous mechanical behavior of nanocrystalline binary alloys under extreme conditions, Nat. Commun. 9 (2018). https://doi.org/10.1038/s41467-018-05027-5.

[86] J.T. Lloyd, High-rate dislocation motion in stable nanocrystalline metals, J. Mater. Res. 34 (2019) 2252–2262. https://doi.org/10.1557/jmr.2019.59.

[87] S.J. Zinkle, Microstructure and properties of copper alloys following 14-mev neutron irradiation, J. Nucl. Mater. 150 (1987) 140–158. https://doi.org/10.1016/0022-3115(87)90070-5.

[88] R. Schäublin *, Z. Yao, N. Baluc, M. Victoria, Irradiation-induced stacking fault tetrahedra in fcc metals, Philos. Mag. 85 (2005) 769–777. https://doi.org/10.1080/14786430412331319929.

[89] M.J. Caturla, N. Soneda, E. Alonso, B.D. Wirth, T. Díaz De La Rubia, J.M. Perlado, Comparative study of radiation damage accumulation in Cu and Fe, J. Nucl. Mater. 276 (2000) 13–21. https://doi.org/10.1016/S0022-3115(99)00220-2.

[90] R.E. Stoller, S.J. Zinkle, On the relationship between uniaxial yield strength and resolved shear stress in polycrystalline materials, J. Nucl. Mater. 283–287 (2000) 349–352. https://doi.org/10.1016/S0022-3115(00)00378-0.

[91] S.J. Zinkle, K. Farrell, Void swelling and defect cluster formation in reactor-irradiated copper, J. Nucl. Mater. 168 (1989) 262–267. https://doi.org/10.1016/0022-3115(89)90591-6.

[92] S.J. Zinkle, A. Horsewell, B.N. Singh, W.F. Sommer, Defect microstructure in copper alloys irradiated with 750 MeV protons, J. Nucl. Mater. 212–215 (1994) 132–138. https://doi.org/10.1016/0022-3115(94)90043-4.

[93] D. Kiener, P. Hosemann, S.A. Maloy, A.M. Minor, In situ nanocompression testing of irradiated copper, Nat. Mater. 10 (2011) 608. http://dx.doi.org/10.1038/nmat3055.

[94] S.J. Zinkle, A. Horsewell, B.N. Singh, W.F. Sommer, Defect microstructure in copper alloys irradiated with 750 MeV protons, J. Nucl. Mater. 212–215 (1994) 132–138. https://doi.org/10.1016/0022-3115(94)90043-4.

[95] D. Schwen, M. Wang, R.S. Averback, P. Bellon, Compositional patterning in immiscible alloys subjected to severe plastic deformation, J. Mater. Res. 28 (2013) 2687–2693. https://doi.org/10.1557/jmr.2013.224.

[96] S. Odunuga, Y. Li, P. Krasnochtchekov, P. Bellon, R.S. Averback, Forced chemical mixing in alloys driven by plastic deformation, Phys. Rev. Lett. 95 (2005) 045901. https://doi.org/10.1103/PhysRevLett.95.045901.

[97] P. Bellon, R.S. Averback, Nonequilibrium roughening of interfaces in crystals under shear: Application to ball milling, Phys. Rev. Lett. 74 (1995) 1819–1822. https://doi.org/10.1103/PhysRevLett.74.1819.

[98] S. Zghal, R. Twesten, F. Wu, P. Bellon, Electron microscopy nanoscale characterization of ball milled Cu-Ag powders. Part II: Nanocomposites synthesized by elevated temperature milling or annealing, Acta Mater. 50 (2002) 4711–4726. https://doi.org/10.1016/S1359-6454(02)00286-0.

[99] C. Suryanarayana, Mechanical alloying and milling, Prog. Mater. Sci. 46 (2001) 1–184. https://doi.org/10.1016/S0079-6425(99)00010-9.

[100] A. Bachmaier, R. Pippan*, Generation of metallic nanocomposites by severe plastic deformation, Int. Mater. Rev. 58 (2013) 41–62. https://doi.org/10.1179/1743280412Y.0000000003.

[101] D. Raabe, S. Ohsaki, K. Hono, Mechanical alloying and amorphization in Cu-Nb-Ag in situ composite wires studied by transmission electron microscopy and atom probe tomography, Acta Mater. 57 (2009) 5254–5263. https://doi.org/10.1016/j.actamat.2009.07.028.

[102] J.S. Carpenter, S.C. Vogel, J.E. Ledonne, D.L. Hammon, I.J. Beyerlein, N.A. Mara, Bulk texture evolution of Cu-Nb nanolamellar composites during accumulative roll bonding, Acta Mater. 60 (2012) 1576–1586. https://doi.org/10.1016/j.actamat.2011.11.045.

[103] E.H. Ekiz, T.G. Lach, R.S. Averback, N.A. Mara, I.J. Beyerlein, M. Pouryazdan, H. Hahn, P. Bellon, Microstructural evolution of nanolayered Cu-Nb composites subjected to high-pressure torsion, Acta Mater. 72 (2014) 178–191. https://doi.org/10.1016/j.actamat.2014.03.040.

[104] A.G. Certain, K.G. Field, T.R. Allen, M.K. Miller, J. Bentley, J.T. Busby, Response of nanoclusters in a 9Cr ODS steel to 1 dpa, 525 °C proton irradiation, J. Nucl. Mater. 407 (2010) 2–9. https://doi.org/10.1016/J.JNUCMAT.2010.07.002.

[105] F. Carsughi, H. Derz, P. Ferguson, G. Pott, W. Sommer, H. Ullmaier, Investigations on Inconel 718 irradiated with 800 MeV protons, J. Nucl. Mater. 264 (1999) 78–88. https://doi.org/10.1016/S0022-3115(98)00475-9.

[106] B.H. Sencer, G.M. Bond, F.A. Garner, M.L. Hamilton, B.M. Oliver, L.E. Thomas, S.A. Maloy, W.F. Sommer, M.R. James, P.D. Ferguson, Microstructural evolution of Alloy 718 at high helium and hydrogen generation rates during irradiation with 600-800 MeV protons, J. Nucl. Mater. 283–287 (2000) 324–328. https://doi.org/10.1016/S0022-3115(00)00308-1.

[107] A.J. London, B.K. Panigrahi, C.C. Tang, C. Murray, C.R.M. Grovenor, Glancing angle XRD analysis of particle stability under self-ion irradiation in oxide dispersion strengthened alloys, Scr. Mater. 110 (2016) 24–27. https://doi.org/10.1016/J.SCRIPTAMAT.2015.07.037.

[108] M.-L. Lescoat, J. Ribis, A. Gentils, O. Kaïtasov, Y. de Carlan, A. Legris, In situ TEM study of the stability of nano-oxides in ODS steels under ion-irradiation, J. Nucl. Mater. 428 (2012) 176–182. https://doi.org/10.1016/J.JNUCMAT.2011.12.009.

[109] V. de Castro, M. Briceno, S. Lozano-Perez, P. Trocellier, S.G. Roberts, R. Pareja, TEM characterization of simultaneous triple ion implanted ODS Fe12Cr, J. Nucl. Mater. 455 (2014) 157–161. https://doi.org/10.1016/J.JNUCMAT.2014.05.064.

[110] C.K. Dolph, D.J. da Silva, M.J. Swenson, J.P. Wharry, Plastic zone size for nanoindentation of irradiated Fe–9%Cr ODS, J. Nucl. Mater. 481 (2016) 33–45. https://doi.org/10.1016/J.JNUCMAT.2016.08.033.

[111] H. Kishimoto, K. Yutani, R. Kasada, O. Hashitomi, A. Kimura, Heavy-ion irradiation effects on the morphology of complex oxide particles in oxide dispersion strengthened ferritic steels, J. Nucl. Mater. 367-370 A (2007) 179–184. https://doi.org/10.1016/j.jnucmat.2007.03.149.

[112] C. Liu, C. Yu, N. Hashimoto, S. Ohnuki, M. Ando, K. Shiba, S. Jitsukawa, Micro-structure and micro-hardness of ODS steels after ion irradiation, in: J. Nucl. Mater., 2011: pp. 270–273. https://doi.org/10.1016/j.jnucmat.2011.01.067.

[113] C.A. Williams, E.A. Marquis, A. Cerezo, G.D.W. Smith, Nanoscale characterisation of ODS–Eurofer 97 steel: An atom-probe tomography study, J. Nucl. Mater. 400 (2010) 37–45. https://doi.org/10.1016/J.JNUCMAT.2010.02.007.

[114] N. Hashimoto, J.D. Hunn, T.S. Byun, L.K. Mansur, Microstructural analysis of ion-irradiation-induced hardening in inconel 718, in: J. Nucl. Mater., 2003: pp. 300–306. https://doi.org/10.1016/S0022-3115(03)00013-8.

[115] T. Kaito, S. Ohtsuka, Y. Yano, … T.T.-F.R. and, undefined 2015, Irradiation performance of oxide dispersion strengthened (ODS) ferritic steel claddings for fast reactor fuels, Inis.Iaea.Org. (n.d.). https://inis.iaea.org/search/search.aspx?orig_q=RN:46091127 (accessed July 3, 2019).

[116] M.K. Miller, D.T. Hoelzer, Effect of neutron irradiation on nanoclusters in MA957 ferritic alloys, J. Nucl. Mater. 418 (2011) 307–310. https://doi.org/10.1016/J.JNUCMAT.2011.07.031.

[117] A. Alamo, V. Lambard, X. Averty, M.. Mathon, Assessment of ODS-14%Cr ferritic alloy for high temperature applications, J. Nucl. Mater. 329–333 (2004) 333–337. https://doi.org/10.1016/J.JNUCMAT.2004.05.004.

[118] N.A. Bailey, E. Stergar, M. Toloczko, P. Hosemann, Atom probe tomography analysis of high dose MA957 at selected irradiation temperatures, J. Nucl. Mater. 459 (2015) 225–234. https://doi.org/10.1016/J.JNUCMAT.2015.01.006.

[119] M. Perrut, S.-Y. Zhong, S. Jiao, M.H. Mathon, M. Perrut, S.Y. Zhong, Y. De Carlan, Small angle neutron scattering study of martensitic/ferritic ODS alloys, Artic. J. Nucl. Mater. (2012). https://doi.org/10.1016/j.jnucmat.2011.12.010.

[120] P. Dubuisson, R. Schill, M.-P. Hugon, I. Grislin, J.-L. Séran, Behavior of an Oxide Dispersion Strengthened Ferritic Steel Irradiated in Phenix, in: Eff. Radiat. Mater. 18th Int. Symp., ASTM International, 100 Barr Harbor Drive, PO Box C700, West Conshohocken, PA 19428-2959, n.d.: pp. 882-882–17. https://doi.org/10.1520/STP13910S.

[121] D. Menut, J.-L. Béchade, S. Cammelli, S. Schlutig, B. Sitaud, P.L. Solari, Synchrotron radiation investigations of microstructural evolutions of ODS steels and Zr-based alloys irradiated in nuclear reactors, J. Mater. Res. 30 (2015) 1392–1402. https://doi.org/10.1557/jmr.2015.74.

[122] I. Monnet, P. Dubuisson, Y. Serruys, M.O. Ruault, O. Kaı¨tasov, B. Jouffrey, Microstructural investigation of the stability under irradiation of oxide dispersion strengthened ferritic steels, J. Nucl. Mater. 335 (2004) 311–321. https://doi.org/10.1016/J.JNUCMAT.2004.05.018.

[123] S. Yamashita, K. Oka, S. Ohnuki, N. Akasaka, S. Ukai, Phase stability of oxide dispersion-strengthened ferritic steels in neutron irradiation, J. Nucl. Mater. 307–311 (2002) 283–288. https://doi.org/10.1016/S0022-3115(02)01077-2.

[124] S. Rogozhkin, A. Bogachev, … O.K.-N.M. and, undefined 2016, Nanostructure evolution in ODS steels under ion irradiation, Elsevier. (n.d.). https://www.sciencedirect.com/science/article/pii/S2352179116300035 (accessed July 3, 2019).

[125] S.V. Rogozhkin, A.A. Aleev, A.G. Zaluzhnyi, A.A. Nikitin, N.A. Iskandarov, P. Vladimirov, R. Lindau, A. Möslang, Atom probe characterization of nano-scaled features in irradiated ODS Eurofer steel, J. Nucl. Mater. 409 (2011) 94–99. https://doi.org/10.1016/J.JNUCMAT.2010.09.021.

[126] L.A. Giannuzzi, J.L. Drown, S.R. Brown, R.B. Irwin, F.A. Stevie, Applications of the FIB lift-out technique for TEM specimen preparation, Microsc. Res. Tech. 41 (1998) 285–290. https://doi.org/10.1002/(SICI)1097-0029(19980515)41:4<285::AID-JEMT1>3.0.CO;2-Q.

[127] C.M. Parish, K.G. Field, A.G. Certain, J.P. Wharry, Application of STEM characterization for investigating radiation effects in BCC Fe-based alloys, J. Mater. Res. 30 (2015) 1275–1289. https://doi.org/10.1557/jmr.2015.32.

[128] T.J. Prosa, D. Olson, B. Geiser, D.J. Larson, K. Henry, E. Steel, Analysis of implanted silicon dopant profiles, Ultramicroscopy. 132 (2013) 179–185. https://doi.org/10.1016/j.ultramic.2012.10.005.

[129] M.K. Miller, THE EFFECTS OF LOCAL MAGNIFICATION AND TRAJECTORY ABERRATIONS ON ATOM PROBE ANALYSIS THE EFFECTS O F LOCAL MAGNIFICATION AND TRAJECTORY ABERRATIONS ON ATOM PROBE ANALYSIS, ATOM PROBE Anal. J. Phys. Colloq. 48 (1987) 565–570. https://doi.org/10.1051/jphyscol:1987692ï.

[130] M.K. Miller, M.G. Hetherington, Local magnification effects in the atom probe, Surf. Sci. 246 (1991) 442–449. https://doi.org/10.1016/0039-6028(91)90449-3.

[131] B. Gault, M.P. Moody, F. De Geuser, A. La Fontaine, L.T. Stephenson, D. Haley, S.P. Ringer, Spatial resolution in atom probe tomography, n.d.

[132] E.A. Marquis, F. Vurpillot, Chromatic aberrations in the field evaporation behavior of small precipitates, Microsc. Microanal. 14 (2008) 561–570. https://doi.org/10.1017/S1431927608080793.

[133] F. Vurpillot, A. Bostel, D. Blavette, Trajectory overlaps and local magnification in three-dimensional atom probe, Appl. Phys. Lett. 76 (2000) 3127–3129. https://doi.org/10.1063/1.126545.

[134] D.J. Larson, B. Gault, B.P. Geiser, F. De Geuser, F. Vurpillot, Atom probe tomography spatial reconstruction: Status and directions, Curr. Opin. Solid State Mater. Sci. 17 (2013) 236–247. https://doi.org/10.1016/j.cossms.2013.09.002.

[135] D.J. Larsonn·, T.J. Prosa, R.M. Ull, B.P. Geiser, T.F. Kelly, C.J. Humphreys, Local Electrode Atom Probe Tomography A User's Guide, n.d.

[136] J.M. Hyde, E.A. Marquis, K.B. Wilford, T.J. Williams, A sensitivity analysis of the maximum separation method for the characterisation of solute clusters, Ultramicroscopy. 111 (2011) 440–447. https://doi.org/10.1016/J.ULTRAMIC.2010.12.015.

[137] M.K. Miller, R.G. Forbes, Atom-Probe Tomography, Springer US, Boston, MA, 2014. https://doi.org/10.1007/978-1-4899-7430-3.

[138] P. Pareige, M.K. Miller, R.E. Stoller, D.T. Hoelzer, E. Cadel, B. Radiguet, Stability of nanometer-sized oxide clusters in mechanically-alloyed steel under ion-induced displacement cascade damage conditions, J. Nucl. Mater. 360 (2007) 136–142. https://doi.org/10.1016/J.JNUCMAT.2006.09.011.

[139] M.J. Swenson, THE MECHANISM OF RADIATION-INDUCED NANOCLUSTER EVOLUTION IN OXIDE DISPERSION STRENGTHENED AND FERRITIC-MARTENSITIC ALLOYS, 2017.

[140] P. V. Patki, Y. Wu, J.P. Wharry, Effects of proton irradiation on microstructure and mechanical properties of nanocrystalline Cu–10at%Ta alloy, Materialia. 9 (2020) 100597. https://doi.org/10.1016/j.mtla.2020.100597.

[141] Atom Probe Tomography - Introduction to the technique, (n.d.). https://www.cameca.com/products/apt/technique (accessed May 8, 2020).

[142] R.K. Koju, K.A. Darling, K.N. Solanki, Y. Mishin, Atomistic modeling of capillary-driven grain boundary motion in Cu-Ta alloys, Acta Mater. 148 (2018) 311–319. https://doi.org/10.1016/j.actamat.2018.01.027.

[143] D.J. Bacon, F. Gao, Y.N. Osetsky, Primary damage state in fcc, bcc and hcp metals as seen in molecular dynamics simulations, J. Nucl. Mater. 276 (2000) 1–12. https://doi.org/10.1016/S0022-3115(99)00165-8.

[144] S.J. Zinkle, P.J. Maziasz, R.E. Stoller, Dose dependence of the microstructural evolution in neutron-irradiated austenitic stainless steel, J. Nucl. Mater. 206 (1993) 266–286. https://doi.org/10.1016/0022-3115(93)90128-L.

[145] X.M. Bai, A.F. Voter, R.G. Hoagland, M. Nastasi, B.P. Uberuaga, Efficient Annealing of Radiation Damage Near Grain Boundaries via Interstitial Emission, Science (80-.). 327 (2010) 1631–1634. https://doi.org/10.1126/science.1183723.

[146] M. Jin, P. Cao, S. Yip, M.P. Short, Radiation damage reduction by grain-boundary biased defect migration in nanocrystalline Cu, Acta Mater. 155 (2018) 410–417. https://doi.org/10.1016/j.actamat.2018.05.071.

[147] X. Zhang, N. Li, O. Anderoglu, H. Wang, J.G. Swadener, T. Höchbauer, A. Misra, R.G. Hoagland, Nanostructured Cu/Nb multilayers subjected to helium ion-irradiation, Nucl. Instruments Methods Phys. Res. Sect. B Beam Interact. with Mater. Atoms. 261 (2007) 1129–1132. https://doi.org/10.1016/j.nimb.2007.03.098.

[148] X. Zhang, E.G. Fu, A. Misra, M.J. Demkowicz, Interface-enabled defect reduction in He ion irradiated metallic multilayers, JOM. 62 (2010) 75–78. https://doi.org/10.1007/s11837-010-0185-5.

[149] N. Li, M. Nastasi, A. Misra, Defect structures and hardening mechanisms in high dose helium ion implanted Cu and Cu/Nb multilayer thin films, Int. J. Plast. 32–33 (2012) 1–16. https://doi.org/10.1016/j.ijplas.2011.12.007.

[150] A. Misra, M.J. Demkowicz, X. Zhang, R.G. Hoagland, The radiation damage tolerance of ultra-high strength nanolayered composites, JOM. 59 (2007) 62–65. https://doi.org/10.1007/s11837-007-0120-6.

[151] M. Rajagopalan, K. Darling, S. Turnage, R.K. Koju, B. Hornbuckle, Y. Mishin, K.N. Solanki, Microstructural evolution in a nanocrystalline Cu-Ta alloy: A combined in-situ TEM and atomistic study, Mater. Des. 113 (2017) 178–185. https://doi.org/10.1016/j.matdes.2016.10.020.

[152] R.S. Nelson, J.A. Hudson, D.J. Mazey, The stability of precipitates in an irradiation environment, J. Nucl. Mater. 44 (1972) 318–330. https://doi.org/10.1016/0022-3115(72)90043-8.

[153] P. Wilkes, Phase stability under irradiation - a review of theory and experiment, J. Nucl. Mater. 83 (1979) 166–175. https://doi.org/10.1016/0022-3115(79)90602-0.

[154] G. Martin, Phase stability under irradiation: Ballistic effects, Phys. Rev. B. 30 (1984) 1424–1436. https://doi.org/10.1103/PhysRevB.30.1424.

[155] P.R. Subramanian, D.E. Laughlin, The Cu-Ta (Copper-Tantalum) system, Bull. Alloy Phase Diagrams. 10 (1989) 652–655. https://doi.org/10.1007/BF02877637.

[156] G. Li, H. Wu, H. Luo, Z. Chen, A.A.O. Tay, W. Zhu, Diffusion behavior of Cu/Ta heterogeneous interface under high temperature and high strain: An atomistic investigation, AIP Adv. 7 (2017). https://doi.org/10.1063/1.4997677.

[157] L. Xiu, J.F. Wu, Atomic diffusion behavior in W/Cu diffusion bonding process, J. Fusion Energy. 34 (2015) 769–773. https://doi.org/10.1007/s10894-015-9884-9.

[158] S. Srinivasan, C. Kale, B.C. Hornbuckle, K.A. Darling, M.R. Chancey, E. Hernández-Rivera, Y. Chen, T.R. Koenig, Y.Q. Wang, G.B. Thompson, K.N. Solanki, Radiation tolerance and microstructural changes of nanocrystalline Cu-Ta alloy to high dose self-ion irradiation, Acta Mater. 195 (2020) 621–630. https://doi.org/10.1016/j.actamat.2020.05.061.

[159] J.D. Verhoeven, W.A. Spitzig, F.A. Schmidt, C.L. Trybus, MATERIAL AND MANUFACTURING PROCESS DEFORMATION PROCESSED Cu-REFRACTORY METAL COMPOSITES DEFORMATION PROCESSED Cu-REFRACTORY METAL COMPOSITES, Mater. Manuf. Process. 4 (1989) 197–209. https://doi.org/10.1080/10426918908956284.

[160] C. Kale, S. Srinivasan, B.C. Hornbuckle, R.K. Koju, K. Darling, Y. Mishin, K.N. Solanki, An experimental and modeling investigation of tensile creep resistance of a stable nanocrystalline alloy, Acta Mater. 199 (2020) 141–154. https://doi.org/10.1016/j.actamat.2020.08.020.

[161] N.Q. Vo, R.S. Averback, P. Bellon, S. Odunuga, A. Caro, Quantitative description of plastic deformation in nanocrystalline Cu: Dislocation glide versus grain boundary sliding, Phys. Rev. B - Condens. Matter Mater. Phys. 77 (2008) 134108. https://doi.org/10.1103/PhysRevB.77.134108.

[162] M. Murayama, J.M. Howe, H. Hidaka, S. Takaki, Atomic-level observation of disclination dipoles in mechanically milled, nanocrystalline Fe, Science (80-.). 295 (2002) 2433–2435. https://doi.org/10.1126/science.1067430.

[163] I.A. Ovid'ko, Deformation of Nanostructures, Science (80-.). 295 (2002) 2386 LP – 2386. https://doi.org/10.1126/science.1071064.

[164] M.Y. Gutkin, A.L. Kolesnikova, I.A. Ovid'ko, N. V. Skiba, Rotational Deformation Mechanism in Fine-Grained Materials Prepared by Severe Plastic Deformation, J. Metastable Nanocrystalline Mater. 12 (2002) 47–58. https://doi.org/10.4028/www.scientific.net/jmnm.12.47.

[165] T. Rojhirunsakool, K.A. Darling, M.A. Tschopp, G.P. Purja Pun, Y. Mishin, R. Banerjee, L.J. Kecskes, Structure and thermal decomposition of a nanocrystalline mechanically alloyed supersaturated Cu–Ta solid solution, MRS Commun. 5 (2015) 333–339. https://doi.org/10.1557/mrc.2015.34.

[166] P. Hosemann, D. Kiener, Y. Wang, S.A. Maloy, Issues to consider using nano indentation on shallow ion beam irradiated materials, J. Nucl. Mater. 425 (2012) 136–139. https://doi.org/10.1016/J.JNUCMAT.2011.11.070.

[167] D. Srinivasan, R. Corderman, P.R. Subramanian, Strengthening mechanisms (via hardness analysis) in nanocrystalline NiCr with nanoscaled Y2O3 and Al2O3 dispersoids, Mater. Sci. Eng. A. 416 (2006) 211–218. https://doi.org/10.1016/j.msea.2005.09.109.

[168] D. Tabor, The physical meaning of indentation and scratch hardness, Br. J. Appl. Phys. 7 (1956) 159–166. https://doi.org/10.1088/0508-3443/7/5/301.

[169] J. Moon, S. Kim, J. il Jang, J. Lee, C. Lee, Orowan strengthening effect on the nanoindentation hardness of the ferrite matrix in microalloyed steels, Mater. Sci. Eng. A. 487 (2008) 552–557. https://doi.org/10.1016/j.msea.2007.10.046.

[170] A. Seeger, J. Diehl, S. Mader, H. Rebstock, Work-hardening and work-softening of face-centred cubic metal crystals, Philos. Mag. 2 (1957) 323–350. https://doi.org/10.1080/14786435708243823.

[171] K.G. Field, X. Hu, K.C. Littrell, Y. Yamamoto, L.L. Snead, Radiation tolerance of neutron-irradiated model Fe-Cr-Al alloys, J. Nucl. Mater. 465 (2015) 746–755. https://doi.org/10.1016/j.jnucmat.2015.06.023.

[172] F. Bergner, C. Pareige, M. Hernández-Mayoral, L. Malerba, C. Heintze, Application of a three-feature dispersed-barrier hardening model to neutron-irradiated Fe-Cr model alloys, J. Nucl. Mater. 448 (2014) 96–102. https://doi.org/10.1016/j.jnucmat.2014.01.024.